SLAC-R-949

A Study of $B \to c\bar{c}\gamma K$ in the *BABAR* Experiment

by

Bryan Gregory Fulsom

B.Sc., Queen's University at Kingston, 2000
M.Sc., Queen's University at Kingston, 2003

A THESIS SUBMITTED IN PARTIAL FULFILLMENT OF
THE REQUIREMENTS FOR THE DEGREE OF

DOCTOR OF PHILOSOPHY

in

The Faculty of Graduate Studies

(Physics)

THE UNIVERSITY OF BRITISH COLUMBIA

(Vancouver)

April 2009

Work supported in part by US Department of Energy contract DE-AC02-76SF00515.

SLAC National Accelerator Laboratory, Menlo Park, CA 94025

Abstract

The *BABAR* Collaboration is a high energy physics experiment located at the Stanford Linear Accelerator Center. The primary goal of the experiment is to study charge and parity violation in the B-meson sector, however the copious production of B mesons decaying to other final states allows for a wide-ranging physics program. In particular, one can access the charmonium system via colour-suppressed $b \to c$ decays of the type $B \to c\overline{c}K$.

This thesis presents a study of $B \to c\overline{c}\gamma K$ decays where $c\overline{c}$ includes J/ψ and $\psi(2S)$, and K includes $K^{\pm}$, K^0_S and $K^*(892)$. The particular emphasis is on a search for the radiative decays $X(3872) \to J/\psi\,\gamma$ and $X(3872) \to \psi(2S)\gamma$. The $X(3872)$ state is a recently-discovered resonance of undetermined quark composition, speculatively a conventional charmonium state or exotic four-quark di-meson molecule. This research is also sensitive to the well-known radiative charmonium decays $B \to \chi_{c1,2}K$, which are used as verification for the analysis technique.

This dissertation sets the best $B \to \chi_{c1}K$ branching fraction measurements to date, and sees the first evidence for factorization-suppressed $B^0 \to \chi_{c2}K^{*0}$ decay at a level of 3.6σ. It also provides evidence for $X(3872) \to J/\psi\gamma$ and $X(3872) \to \psi(2S)\gamma$ with 3.6σ and 3.3σ significance, respectively. The product of branching fractions $\mathcal{B}(B^{\pm} \to X(3872)K^{\pm}) \cdot \mathcal{B}(X(3872) \to J/\psi\gamma) = (2.8 \pm 0.8(stat.) \pm 0.2(syst.)) \times 10^{-6}$ and $\mathcal{B}(B^{\pm} \to X(3872)K^{\pm}) \cdot \mathcal{B}(X(3872) \to \psi(2S)\gamma) = (9.5 \pm 2.7(stat.) \pm 0.9(syst.)) \times 10^{-6}$ are measured. These results improve upon previous $X(3872) \to J/\psi\,\gamma$ measurements, and represent the first evidence for $X(3872) \to \psi(2S)\gamma$.

Table of Contents

Abstract ii

Table of Contents iii

List of Tables vii

List of Figures ix

Glossary xiv

Acknowledgements xx

Dedication xxii

1 Introduction 1

2 Background Information 4

2.1 The Charmonium Model 4

2.2 Charmonium Production 8

2.3 Charmonium Decay 10

2.4 Exotic Quarkonia 11

2.5 Recent Experimental Results 13

2.5.1 $X(3872)$ 14

2.5.2 The $X/Y/Z$ Family 16

2.5.3 States Produced in ISR 17

2.5.4 Charged Multiquark States 18

2.6 $X(3872)$ Phenomenology 18

2.7 Analysis Outlook 20

3 The *BABAR* Experiment 22
3.1 The Linear Accelerator and PEP-II Storage Rings 22
3.2 Detector Overview 24
3.3 The Silicon Vertex Tracker (SVT) 28
3.4 The Drift Chamber (DCH) 29
3.5 The Detector of Internally-Reflected Cherenkov Light (DIRC) 30
3.6 The Electromagnetic Calorimeter (EMC) 34
3.7 The Instrumented Flux Return (IFR) 37
3.8 Triggering and Software 41

4 Analysis Preliminaries 44
4.1 Data Set 44
4.2 B Candidate Reconstruction 45
4.2.1 "JpsitollTight" Skim 45
4.2.2 $J/\psi \to \ell^+\ell^-$ Reconstruction 47
4.2.3 $\psi(2S)$ Reconstruction 47
4.2.4 $X \to c\overline{c}\gamma$ Reconstruction 48
4.2.5 Kaon Reconstruction 48
4.2.6 $B \to XK$ Reconstruction 48
4.3 Event Variables 49
4.3.1 B Meson Variables 49
4.3.2 Event Topology Variables 50
4.3.3 Photon Variables 51
4.3.4 Kaon Variables 53
4.4 Event Selection 53
4.4.1 Cut Optimization Procedure 53
4.4.2 Optimization Results 54
4.4.3 Multiple Candidate Selection 70
4.4.4 Event Selection Efficiency 70

5 Analysis Methodology 75
5.1 Signal Extraction Procedure 75
5.1.1 Probability Density Functions 75

5.1.2 Choice of PDF shapes . . . 76
5.1.3 PDF Parametrization, m_{miss} . . . 77
5.1.4 PDF Parametrization, m_X . . . 80
5.1.5 PDF Parametrization, m_{K^*} . . . 88
5.1.6 PDF Correlations . . . 88
5.1.7 The $_s$Plot Technique . . . 100
5.2 $X(3872)$ Signal Extraction on Monte Carlo . . . 101
5.2.1 Monte Carlo Tests . . . 101
5.2.2 Bias . . . 102
5.2.3 Fit Efficiency . . . 104
5.2.4 Total Efficiency . . . 112
5.2.5 Cross-feed and Other Backgrounds . . . 112
5.2.6 Null Signal Tests . . . 113
5.3 The $\chi_{c1,2}$ Benchmark Modes . . . 114
5.3.1 χ_{c1} PDF Parametrization . . . 115
5.3.2 χ_{c2} PDF Parametrization . . . 116
5.3.3 PDF Correlations for χ_{cJ} . . . 121
5.3.4 Treatment of $B \to \chi_{c1} K\pi$ Non-Resonant (NR) Backgrounds . . . 127
5.3.5 χ_{c1} Cross-feed . . . 129
5.3.6 χ_{c1} Signal Extraction Efficiency . . . 133
5.3.7 χ_{c2} Signal Extraction Efficiency . . . 135

6 Signal Extraction from Data . . . 138
6.1 $\chi_{c1,2}$ Signal Extraction from Data . . . 138
6.2 $X(3872)$ Signal Extraction from Data . . . 150
6.2.1 $B \to X(3872)K$, $X(3872) \to J/\psi\gamma$ . . . 150
6.2.2 $B \to X(3872)K$, $X(3872) \to \psi(2S)\gamma$ . . . 161
6.2.3 $B \to X(any)K$, $X(any) \to c\bar{c}\gamma$ . . . 172
6.3 Systematic Uncertainties and Corrections . . . 173
6.3.1 B Counting . . . 173
6.3.2 Branching Fraction Uncertainties . . . 173
6.3.3 MC/Data Differences . . . 176

6.3.4 PDF Fit Parameter Uncertainty 176
6.3.5 True X Mass and Width Uncertainty 177
6.3.6 Bias and Efficiency 180
6.3.7 PID Correction and Systematics 181
6.3.8 Tracking Systematics 181
6.3.9 Photon Corrections 181
6.3.10 Total Systematic Error 182

7 Conclusions 185
7.1 Analysis Results 185
7.2 Discussion and Implications 187

Bibliography 194

List of Tables

4.1 Number of events and luminosity weighting. 46
4.2 Selection criteria optimization results. 56
4.3 Average number of B candidates per event. 70
4.4 Reconstruction and event selection efficiency. 71

5.1 m_{miss} PDF fit results for $X(3872)$ signal modes. 80
5.2 m_{miss} PDF fit results for $X(3872)$ background modes. 83
5.3 m_X PDF fit results for $X(3872)$ signal modes. 88
5.4 m_X PDF fit results for $X(3872)$ background modes. 91
5.5 m_{K^*} PDF fit results for the $X(3872)$ modes. 91
5.6 Test of signal extraction for truth-matched signal MC events with PDF-generated background events. 103
5.7 Test of signal extraction for all signal MC events with PDF-generated background events. 105
5.8 Total signal extraction efficiency for each signal mode based on MC samples. 112
5.9 Expected $B \to X(3872)(J\psi\pi^+\pi^-)K$ background. 114
5.10 Number of events returned by the signal extraction from a background-only toy data sample. 115
5.11 m_{miss} PDF fit results for χ_{c1} signal modes. 121
5.12 m_{miss} PDF fit results for χ_{c1} background modes. 121
5.13 m_X PDF fit results for χ_{c1} signal modes. 127
5.14 m_X PDF fit results for χ_{c1} background modes. 127
5.15 m_{K^*} PDF fit results for χ_{c1} modes. 128
5.16 m_X PDF fit results for χ_{c2} signal modes. 128
5.17 Cross-feed for the $B \to \chi_{cJ}K$ modes. 133

5.18 Reconstruction and event selection efficiency for $B \to \chi_{c1}K$ MC events. 134
5.19 Results of tests of signal extraction for $B \to \chi_{c1}K$. 135
5.20 Signal extraction efficiency for $B \to \chi_{c1}K$. 135
5.21 Reconstruction and event selection efficiency for $B \to \chi_{c2}K$ MC events. 136
5.22 Test of signal extraction for χ_{c2} with zero MC events. 136
5.23 Results of tests of signal extraction for $B \to \chi_{c2}K$. 137
5.24 Signal extraction efficiency for $B \to \chi_{c2}K$. 137

6.1 Results of $\mathcal{B}(B \to \chi_{c1,2}K)$ signal extraction. 146
6.2 Results of $\mathcal{B}(B \to X(3872)(J/\psi\,\gamma)K)$ signal extraction. 161
6.3 Results of $\mathcal{B}(B \to X(3872)(\psi(2S)\gamma)K)$ signal extraction. . . . 172
6.4 Values and uncertainties for the relevant daughter branching fractions. 173
6.5 Systematic uncertainties due to PDF parameter uncertainties for the $X(3872) \to J/\psi\gamma$ modes. 177
6.6 Systematic uncertainties due to PDF parameter uncertainties for the $X(3872) \to \psi(2S)\gamma$ modes. 178
6.7 Systematic uncertainties due to PDF parameter uncertainties for the $\chi_{c1,2}$ modes. 179
6.8 Summary of the systematic uncertainties due to uncertainties in the properties of $X(3872)$. 180
6.9 PID and tracking corrections and systematic uncertainties applied to the efficiency. 182
6.10 Total systematic uncertainties for the $X(3872) \to J/\psi\gamma$ decay modes. 183
6.11 Total systematic uncertainties for the $X(3872) \to \psi(2S)\gamma$ decay modes. 183
6.12 Total systematic uncertainties for the χ_{c1} decay modes. . . . 184
6.13 Total systematic uncertainties for the χ_{c2} decay modes. . . . 184

7.1 Comparison of $B \to \chi_{c1,2}K$ results with previous measurements. 191

List of Figures

2.1 Predicted and observed spectrum of the charmonium model. . 7
2.2 Feynman diagram of $B \to c\bar{c}K$. 8
2.3 Cartoon depiction of exotic QCD states. 12
2.4 Previous results of $X(3872) \to J/\psi\gamma$ from Belle and *BABAR*. . 15

3.1 Illustration of the linear accelerator and PEP-II collider. . . . 23
3.2 Integrated luminosity of the *BABAR* experiment. 25
3.3 Longitudinal view of the *BABAR* detector. 26
3.4 End view of the *BABAR* detector. 27
3.5 Transverse cross-sectional view of the SVT. 28
3.6 Longitudinal cross-sectional view of the SVT. 29
3.7 Longitudinal diagram of the DCH. 31
3.8 Layout of the DCH drift cells. 32
3.9 Diagram of the DIRC system. 33
3.10 Layout of the EMC barrel and forward endcap. 35
3.11 Diagram of a typical CsI(Tl) crystal in the EMC. 36
3.12 Layout of the IFR barrel and endcaps. 38
3.13 Cross section of Resistive Plate Chamber construction. 39
3.14 Diagram of a limited streamer tube. 40
3.15 Z-plane read-out strip diagram. 41
3.16 Muon identification efficiency by IFR region. 42

4.1 Optimized B mass for the $J/\psi\gamma$ modes. 55
4.2 Optimized J/ψ mass for the $J/\psi\gamma$ modes. 57
4.3 Optimized γ *LAT* and γA_{42} for the $J/\psi\gamma$ modes. 57
4.4 Optimized π^0 veto for the $J/\psi\gamma$ modes. 58

4.5 Optimized $\cos\theta_{thrust}$ and $\cos\theta_{sphericity}$ for the $J/\psi\gamma$ modes. . 58
4.6 Optimized $R2$ for the $J/\psi\gamma$ modes. 59
4.7 Optimized B χ^2 values for the $J/\psi\gamma$ modes. 60
4.8 Optimized K^0_S cuts for the $J/\psi\gamma$ modes. 61
4.9 Optimized $K^{*\pm}$ cuts for the $J/\psi\gamma$ modes. 62
4.10 Optimized K^{*0} cuts for the $J/\psi\gamma$ modes. 62
4.11 Optimized B mass for the $\psi(2S)\gamma$ modes. 63
4.12 Optimized J/ψ mass for the $\psi(2S) \to J/\psi\pi^+\pi^-$ modes. . . . 63
4.13 Optimized $\psi(2S)$ mass for the $\psi(2S)\gamma$ modes. 64
4.14 Optimized γ LAT and γA_{42} for the $\psi(2S)\gamma$ modes. 65
4.15 Optimized π^0 veto for the $\psi(2S)\gamma$ modes. 65
4.16 Optimized $\cos\theta_{thrust}$ and $\cos\theta_{sphericity}$ for the $\psi(2S)\gamma$ modes. 66
4.17 Optimized $R2$ for the $\psi(2S)\gamma$ modes. 66
4.18 Optimized B χ^2 values for the $\psi(2S)\gamma$ modes. 67
4.19 Optimized K^0_S cuts for the $\psi(2S)\gamma$ modes. 68
4.20 Optimized $K^{*\pm}$ cuts for the $\psi(2S)\gamma$ modes. 69
4.21 Optimized K^{*0} cuts for the $\psi(2S)\gamma$ modes. 69
4.22 m_X distribution of MC background events for $X(3872) \to J/\psi\gamma$. 72
4.23 m_X distribution of MC background events for $X(3872) \to \psi(2S)\gamma$. 73
4.24 m_X distribution of MC background events for $\chi_{c1} \to J/\psi\gamma$. . 74

5.1 m_{miss} PDF fits for the J/ψ signal modes. 78
5.2 m_{miss} PDF fits for the $\psi(2S)$ signal modes. 79
5.3 m_{miss} PDF fits for the J/ψ background modes. 81
5.4 m_{miss} PDF fits for the $\psi(2S)$ background modes. 82
5.5 m_X PDF fits for the J/ψ signal modes. 84
5.6 m_X PDF fits for the $\psi(2S)$ signal modes. 85
5.7 m_X PDF fits for the J/ψ background modes. 86
5.8 m_X PDF fits for the $\psi(2S)$ background modes. 87
5.9 m_{K^*} PDF fits for the J/ψ signal and background modes. . . 89
5.10 m_{K^*} PDF fits for the $\psi(2S)$ signal and background modes. . 90

5.11 Plots of m_{miss} versus m_X for the $X(3872) \to J/\psi\gamma$ signal modes. 92
5.12 Plots of m_{miss} versus m_{K^*} and m_X versus m_{K^*} for the $X(3872) \to J/\psi\gamma$ signal modes. 93
5.13 Plots of m_{miss} versus m_X for the $X(3872) \to \psi(2S)\gamma$ signal modes. 94
5.14 Plots of m_{miss} versus m_{K^*} and m_X versus m_{K^*} for the $X(3872) \to \psi(2S)\gamma$ signal modes. 95
5.15 Plots of m_{miss} versus m_X for the $X(3872) \to J/\psi\gamma$ background modes. 96
5.16 Plots of m_{miss} versus m_{K^*} and m_X versus m_{K^*} for the $X(3872) \to J/\psi\gamma$ background modes. 97
5.17 Plots of m_{miss} versus m_X for the $X(3872) \to \psi(2S)\gamma$ background modes. 98
5.18 Plots of m_{miss} versus m_{K^*} and m_X versus m_{K^*} for the $X(3872) \to \psi(2S)\gamma$ background modes. 99
5.19 Comparison of truth-matched and non-truth-matched MC for $B^\pm \to X(3872)(\psi(2S)\gamma)K^\pm$. 106
5.20 Comparison of truth-matched and non-truth-matched MC for $B^0 \to X(3872)(\psi(2S)\gamma)K^0_S$. 106
5.21 Comparison of truth-matched and non-truth-matched MC for m_X, m_{miss}, and $m_{K^{*\pm}}$ for $B^\pm \to X(3872)(\psi(2S)\gamma)K^{*\pm}$. . . . 107
5.22 Comparison of truth-matched and non-truth-matched MC for m_X, m_{miss}, and $m_{K^{*0}}$ for $B^0 \to X(3872)(\psi(2S)\gamma)K^{*0}$. 108
5.23 Comparison of truth-matched and non-truth-matched MC for $B^\pm \to X(3872)(J/\psi\gamma)K^\pm$. 109
5.24 Comparison of truth-matched and non-truth-matched MC for $B^0 \to X(3872)(J/\psi\gamma)K^0_S$. 109
5.25 Comparison of truth-matched and non-truth-matched MC for m_X, m_{miss}, and $m_{K^{*\pm}}$ for $B^\pm \to X(3872)(J/\psi\gamma)K^{*\pm}$. 110
5.26 Comparison of truth-matched and non-truth-matched MC for m_X, m_{miss}, and $m_{K^{*0}}$ for $B^0 \to X(3872)(J/\psi\gamma)K^{*0}$. 111
5.27 m_{miss} PDF fits for the χ_{c1} signal modes. 116

5.28 m_{miss} PDF fits for the χ_{c1} background. 117
5.29 m_X PDF fits for the χ_{c1} signal modes. 118
5.30 m_X PDF fits for the χ_{c1} background modes. 119
5.31 m_{K^*} PDF fits for the χ_{c1} signal and background modes. . . . 120
5.32 m_X PDF fits for the χ_{c2} signal modes. 122
5.33 Plots of m_{miss} versus m_X for the χ_{cJ} signal modes. 123
5.34 Plots of m_{miss} versus m_{K^*} and m_X versus m_{K^*} for the χ_{cJ} signal modes. 124
5.35 Plots of m_{miss} versus m_X for the χ_{cJ} background modes. . . 125
5.36 Plots of m_{miss} versus m_{K^*} and m_X versus m_{K^*} for the χ_{cJ} background modes. 126
5.37 m_X and $m_{K^{*\pm}}$ distributions for $\chi_{c1}K^{*\pm}$ background MC events 130
5.38 m_X and $m_{K^{*0}}$ distributions for $\chi_{c1}K^{*0}$ background MC events 131
5.39 m_X versus $m_{K^{*0}}$ for $\chi_{c1}K^{*0}$ background MC events peaking in m_{miss}. 132

6.1 Data/MC comparison for $B^{\pm} \to \chi_{c1}K^{\pm}$. 139
6.2 Data/MC comparison for $B^{\pm} \to \chi_{c1}K^0_S$. 139
6.3 Data/MC comparison for $B^{\pm} \to \chi_{c1}K^{*\pm}$. 140
6.4 Data/MC comparison for $B^{\pm} \to \chi_{c1}K^{*0}$. 141
6.5 Event type components for the fit to m_{miss} for $B^{\pm} \to \chi_{cJ}K^{\pm}$. 142
6.6 Event type components for the fit to m_{miss} for $B^0 \to \chi_{cJ}K^0_S$. 143
6.7 Event type components for the fit to m_{miss} and $m_{K^{*\pm}}$ for $B^{\pm} \to \chi_{cJ}K^{*\pm}$. 144
6.8 Event type components for the fit to m_{miss} and $m_{K^{*0}}$ for $B^0 \to \chi_{cJ}K^{*0}$. 145
6.9 ${}_s$Plots for $B \to \chi_{c1,2}K$ events from data. 147
6.10 ${}_s$Plots for $B^{\pm} \to \chi_{c1,2}K^{*\pm}$ events from data. 148
6.11 ${}_s$Plots for $B^0 \to \chi_{c1,2}K^{*0}$ events from data. 149
6.12 Data/MC comparison for $B^{\pm} \to X(J/\psi\gamma)K^{\pm}$. 150
6.13 Data/MC comparison for $B^{\pm} \to X(J/\psi\gamma)K^0_S$. 151
6.14 Data/MC comparison for $B^{\pm} \to X(J/\psi\gamma)K^{*\pm}$. 152
6.15 Data/MC comparison for $B^{\pm} \to X(J/\psi\gamma)K^{*0}$. 153

6.16 Event type components for the fit to m_{miss} for the $B^{\pm} \to X(J/\psi\gamma)K^{\pm}$ decay mode. 154
6.17 Event type components for the fit to m_{miss} for the $B^{0} \to X(J/\psi\gamma)K^{0}_{S}$ decay mode. 155
6.18 Event type components for the fit to m_{miss} and $m_{K^{*\pm}}$ for $B^{\pm} \to X(J/\psi\gamma)K^{*\pm}$. 156
6.19 Event type components for the fit to m_{miss} and $m_{K^{*0}}$ for $B^{0} \to X(J/\psi\gamma)K^{0}_{S}$. 157
6.20 ${}_s$Plots for $B \to X(3872)(J/\psi\gamma)K$ events from data. 158
6.21 ${}_s$Plots for $B^{\pm} \to X(3872)(J/\psi\gamma)K^{*\pm}$ events from data. 159
6.22 ${}_s$Plots for $B^{0} \to X(3872)(J/\psi\gamma)K^{*0}$ events from data. 160
6.23 Data/MC comparison for $B^{\pm} \to X(\psi(2S)\gamma)K^{\pm}$. 162
6.24 Data/MC comparison for $B^{\pm} \to X(\psi(2S)\gamma)K^{0}_{S}$. 162
6.25 Data/MC comparison for $B^{\pm} \to X(\psi(2S)\gamma)K^{*\pm}$. 163
6.26 Data/MC comparison for $B^{\pm} \to X(\psi(2S)\gamma)K^{*0}$. 164
6.27 Event type components for the fit to m_{miss} for the $B^{\pm} \to X(\psi(2S)\gamma)K^{\pm}$ decay mode. 165
6.28 Event type components for the fit to m_{miss} for the $B^{0} \to X(\psi(2S)\gamma)K^{0}_{S}$ decay mode. 166
6.29 Event type components for the fit to m_{miss} and $m_{K^{*\pm}}$ for $B^{\pm} \to X(\psi(2S)\gamma)K^{*\pm}$. 167
6.30 Event type components for the fit to m_{miss} and $m_{K^{*0}}$ for $B^{0} \to X(\psi(2S)\gamma)K^{0}_{S}$. 168
6.31 ${}_s$Plots for $B \to X(3872)(\psi(2S)\gamma)K$ events from data. 169
6.32 ${}_s$Plots for $B^{\pm} \to X(3872)(\psi(2S)\gamma)K^{*\pm}$ events from data. . . 170
6.33 ${}_s$Plots for $B^{0} \to X(3872)(\psi(2S)\gamma)K^{*0}$ events from data. . . . 171
6.34 ${}_s$Plots for $X \to J/\psi\gamma$ in the range $3.6 < m_X < 5.0\,\mathrm{GeV}/c^2$. . . 174
6.35 ${}_s$Plots for $X \to \psi(2S)\gamma$ in the range $3.6 < m_X < 5.0\,\mathrm{GeV}/c^2$. . 175

7.1 Results for the $\chi_{c1,2}$ decay modes. 188
7.2 Results for the $X(3872) \to J/\psi\gamma$ decay modes. 189
7.3 Results for the $X(3872) \to \psi(2S)\gamma$ decay modes. 190

Glossary

ARGUS - The name of a particle physics experiment conducted at the Deutsches Elektronen Synchrotron in Germany during the late 1980ies.

B Factories - Collective name for the *BABAR* and Belle experiments.

B meson - A particle consisting of a bottom quark (or anti-quark) and an anti-quark (quark), particularly of the up or down type.

BABAR - A particle physics experiment located at SLAC, designed primarily to explore CP violation in the decays of B mesons.

Belle - A particle physics experiment similar to *BABAR*, located in Japan.

C++ - A computer programming language.

$c\overline{c}$ - Shorthand notation for a charmonium state.

CDF - A particle physics experiment examining proton-antiproton collisions at Fermilab.

charmonium - The bound state of a charm and anti-charm quark.

Cherenkov light - Photons emitted by a particle traveling faster than the speed of light in a given medium.

$\chi_{c0,1,2}$ - Symbolic name for a series of charmonium states with an orbital

angular momentum $L = 1$, and total angular momentum of $J = 0, 1, 2$, respectively.

CKM matrix - Abbreviation for the Cabibbo-Kobayashi-Maskawa matrix. A 3×3 matrix describing the relationship between the weak and flavour eigenstates of the quarks.

CLEO - A particle physics experiment examining e^+e^- collisions located at Cornell University in New York.

CP violation - The concept that the laws of physics are not identical under the interchange of a particle to antiparticle and swapping the spatial definition of left and right.

Crystal Ball - A particle physics detector originally used at SLAC in the late 1970ies and early 1980ies.

D meson - A particle consisting of a charm quark (or anti-quark) and a light (up or down) anti-quark (quark).

DØ - A particle physics experiment examining proton-antiproton collisions at Fermilab.

Dalitz plot - The scatter plot of the invariant mass of a pair of particles versus that of another pair of particles in a three-body decay.

DCH - Abbreviation for drift chamber. In *BABAR*, a detector component consisting of multiple wires in a gas chamber used to track the passage of charged particles.

$D^0\overline{D}^{*0}$ molecule - A loosely-bound four-quark state consisting of a D^0 and $\overline{D}^{*0}$ meson.

DIRC - Abbreviation for Detector of Internally-Reflected Cherenkov light. A unique detector component in *BABAR* that uses Cherenkov light emitted and reflected inside of quartz bars for particle identification.

EMC - Abbreviation for electromagnetic calorimeter. In *BABAR*, a detector component composed of scintillating crystals used to detect electrons and photons.

factorization - A theoretical assumption that decays of the form $B \to c\overline{c}K$ can be simplified by considering only the interaction between the final state $c\overline{c}$ and the vacuum. One implication is the prediction of a decay rate of zero for $B \to \chi_{c0,2}K$

Fermilab - A U.S. national laboratory for particle physics located near Chicago, IL.

GEANT4 - A software package for simulating the interaction of particles with matter.

gluon - According to the Standard Model, the particle responsible for the strong force between quarks.

HER - Abbreviation for High Energy Ring. Refers to the ring used for circulating 9 GeV electrons in the PEP-II collider.

hybrid - Term used to describe a state consisting of a quark-antiquark pair (particularly a $c\overline{c}$ in this case) and a gluon.

IFR - Abbreviation for Instrumented Flux Return. In *BABAR*, it refers to a detector region consisting of metal plates sandwiching gas-filled particle detection chambers used both for managing the magnetic field and for muon detection.

ISR - Abbreviation for Initial State Radiation. Describes events in which the initial e^+e^- collision occurs at a reduced energy due to earlier emission of a photon.

J/ψ - Symbolic name for the lowest charmonium state with orbital angular momentum $L = 0$ and total angular momentum $J = 1$. The first experimentally-discovered $c\overline{c}$ state.

kaon - Short for "K meson". A particle consisting of a strange quark (or anti-quark) and a light (up or down) anti-quark (quark).

klystron - A vacuum tube used for microwave generation and particle acceleration.

LER - Abbreviation for Low Energy Ring. Refers to the ring used for circulating 3.1 GeV positrons in the PEP-II collider.

LST - Abbreviation for Limited Streamer Tubes. In *BABAR*, a detector component consisting of a gas-filled chamber with a sense wire, used for muon detection. Replaced failing resistive plate chambers in *BABAR*.

MC - Abbreviation for Monte Carlo.

Monte Carlo - A computational analysis method using many randomized detailed simulations of an experiment to understand and predict how it will perform in reality.

m_{K^*} - The invariant mass of a K^* candidate.

m_{miss} - The difference between the four-momentum of the e^+e^- system and that of the reconstructed B candidate with the mass constrained to the known value.

$\boldsymbol{m_X}$ - The invariant mass of the $X \to c\bar{c}\gamma$ candidate.

particle identification - Methods used to assign a particle type to an object reconstructed from primary information collected by a particle detector.

PDF - Abbreviation for Probability Density Function. A function describing the probability distribution of a given variable in an integral form.

PEP-II - A positron and electron particle accelerator located at SLAC.

PID - Abbreviation for particle identification.

PMT - Abbreviation for photomultiplier tube. Used to detect photons.

$\boldsymbol{\psi(2S)}$ - Symbolic name for the first excited charmonium state with orbital angular momentum $L = 0$ and total angular momentum $J = 1$. Analogous to the J/ψ.

QCD - Abbreviation for quantum chromodynamics, the theoretical description of the strong force of particle physics.

ROOT - A software package commonly used for particle physics analyses.

RPC - Abbreviation for Resistive Plate Chambers. In *BABAR*, a detector component consisting of a gas-filled gap under high voltage used for muon detection.

SLAC - Abbreviation for the Stanford Linear Acclerator Center, now known as the SLAC National Accelerator Center. A U.S. national particle physics laboratory located near Stanford University in California.

Standard Model - The basic modern theoretical description of all of par-

ticle physics.

$_s$Plot - A statistical technique for unfolding the distribution of a sample in one variable based on its distribution in another uncorrelated variable.

SVT - Abbreviation for Silicon Vertex Tracker. In *BABAR*, a detector component consisting of silicon strips under an applied voltage used for precise tracking of a B meson decay at its decay vertex.

tetraquark - Term used to describe a tightly-bound state of two quarks and two antiquarks.

TRIUMF - Abbreviation for TRI-University Meson Facility, a particle physics laboratory located in Vancouver, Canada.

$X(3872)$ - A recently discovered particle with a mass of $\sim 3872\,\mathrm{MeV}/c^2$ and unknown internal quark content.

$\Upsilon(4S)$ - Symbolic name for the bottomonium state produced at the B Factories that promptly decays to B mesons.

Acknowledgements

First and foremost, I wish to thank my supervisor, Chris Hearty. He has been incredibly supportive of my scientific pursuits, and I am very grateful for the many opportunities he has afforded me during my graduate work. He is an impressive physicist, and his advice and suggestions have been extremely valuable in advancing this analysis and my career. It has been a pleasure to work with him and have him as my academic mentor.

I wish to thank all of the members of the *BABAR* Charmonium Working Group, past and present, especially Claudia Patrignani, Philippe Grenier, Shuwei Ye, Tulay Cuhadar-Donszelmann, Arafat Gabareen Mokhtar, and Bill Dunwoodie. Their insight and help have been very important to me in my explorations of heavy quarkonium physics. I would also like to extend my thanks to the members of the *BABAR* review committees that oversaw the publications related to this work: Paul (Jack) Jackson, Nicolas Arnaud, Woochun Park, Georges Vasseur, Frank Winklmeier, and David Lopes Pegna.

Many thanks to the members of the LST team: Charlie Young, Peter Kim, Mark Convery, Stew Smith, Changguo Lu, Sanjay Swain, Gabriele Benelli, Wolfgang Menges (Ehrenfeld), and Sasha Telnov, to name only a few, whose expertise, friendship, and teamwork made the LST upgrade project one of my most rewarding graduate school experiences.

Thanks to professors Janis McKenna and Tom Mattison, and to Ph.D. committee members, Scott Oser, Javed Iqbal, and Vesna Sossi, for all of their helpful guidance and input over the course of my studies at UBC.

To fellow graduate students, Dave Asgeirsson, Tae Min Hong, Keith Ulmer, Dan Balick, Karsten Koeneke, Jim Hirschauer, Chris Schilling, Tim Piatenko, Andy Ruland, Grant MacGregor, Joe Tuggle, Jake Anderson,

and the many others I've worked with at SLAC: thank you for making my experience somewhat more intellectual and mostly a whole lot more fun.

Finally, a special thank you to my wife Melissa, without whose love, support, and sacrifice, this would not have been possible.

Dedication

For Mariposa Jane, with love.

Chapter 1

Introduction

The development of particle physics over the past century has led to what is called the Standard Model (SM) of particle physics. This framework encompasses the fundamental particles of matter, leptons (electrons, muons, taus, and their associated neutrinos) and quarks (with "flavours" up, down, charm, strange, top, and bottom), and their interactions via the electromagnetic, strong, and weak forces (mediated by photons, gluons, and the W and Z bosons, respectively). Weak interactions are capable of changing quark flavour, with the coupling between flavours described by the Cabbibo-Maskawa-Kobayashi (CKM) matrix. The Standard Model also predicts the existence of the Higgs boson, thought to be responsible for the masses of the other particles in the SM, and necessary to explain the symmetry breaking of the electromagnetic and weak forces. It is a highly successful theory, and represents our best description of how all known matter exists and interacts in the most fundamental way. The study of particle physics is the study of our universe at its deepest level.

In the Standard Model, quarks are massive point-like particles that interact with one another predominantly via the strong force. The strong force is mediated by gluons and acts between particles (i.e. quarks) that have colour, the strong force analogue of electromagnetic charge. The theory describing these processes is called quantum chromodynamics (QCD), and it essentially explains how quarks bind together to form matter. This work focuses primarily on bound states of a charm and anticharm quark, known as charmonium ($c\overline{c}$) mesons, whose interactions are described within the realm of QCD. By investigating particles in the charmonium system, one can indirectly test and improve the theory of quantum chromodynamics.

Charmonium was first discovered experimentally in 1973 [1]. This was

the first convincing evidence for the quark model. This system has been well described by a phenomenology analogous to that for hydrogen or positronium states. The so-called "charmonium model" [2] has successfully predicted and characterized all of the charmonium states expected up to a mass of $\sim 3.72\,\mathrm{GeV}/c^2$, above which the dominant decays are via the strong force to a pair of D mesons.

The *BABAR* experiment, located at the PEP-II e^+e^- collider at the Stanford Linear Accelerator Center, was designed to explore the violation of charge conjugation and parity (CP) symmetry in the decays of B mesons. In addition, the decays of B mesons provide a fertile ground for studying a broad range of particle physics topics, including the charmonium system. B mesons decaying via the weak interaction quark decay $b \to c$ produce charmonium states via $B \to c\bar{c}K$. This can be used to test the predictions of the charmonium model, and to search for yet-to-be-discovered exotic states.

In 2003, the Belle experiment discovered a signal in the decay $B^+ \to XK^+$, $X \to J/\psi\,\pi^+\pi^-$ [3]. Called the $X(3872)$, it was found to have a mass of $m_X = 3872.0 \pm 0.6(stat.) \pm 0.5(syst.)\,\mathrm{MeV}/c^2$ and a width of $\Gamma < 2.3\,\mathrm{MeV}/c^2$. This discovery was verified by *BABAR* [4], as well as by DØ [5] and CDF [6] at Fermilab. Angular analyses suggest a quantum number assignment of $J^{PC} = 1^{++}$ or 2^{-+} [7].

The $X(3872)$ displays some characteristics of a charmonium-like state, but its narrow width above the $D\overline{D}$ threshold and quantum numbers limit its possible assignment within the charmonium model. Its mass near $m_{D^0} + m_{\overline{D}^{*0}}$ has led to speculation that the $X(3872)$ may be the bound state of two D mesons. Other more exotic interpretations include a tetraquark (tightly bound state of four quarks) model, or charmonium-gluon hybrid bound states. If the $X(3872)$ is not a conventional charmonium state, it pushes the boundaries of the well-known framework of QCD.

A search for the radiative decays $X(3872) \to J/\psi\,\gamma$ and $X(3872) \to \psi(2S)\gamma$ provides a useful diagnostic for this particle. Decays of this type would confirm charge-parity to be positive ($C = +$). While some molecular theories can accommodate $X(3872) \to J/\psi\,\gamma$, the decay $X(3872) \to \psi(2S)\gamma$ is expected to be greatly suppressed. On the other hand, the charmonium

model predicts that the ratio of the branching fraction for the decay to $\psi(2S)\gamma$ compared to $J/\psi\,\gamma$ could be substantial for the $\chi_{c1}(2P)$ charmonium state, one of the few available charmonium options remaining for the $X(3872)$.

This thesis presents a study of $B \to c\overline{c}\gamma K$ decays where $c\overline{c}$ includes J/ψ and $\psi(2S)$, and K includes $K^{\pm}$, K^0_S and $K^{*(\pm,0)}(892)$, with an emphasis on a search for the radiative decays $X(3872) \to J/\psi\,\gamma$ and $X(3872) \to \psi(2S)\gamma$. This analysis is also sensitive to the well-known radiative charmonium decays $B \to \chi_{c1}(1P)K$ and $B \to \chi_{c2}(1P)K$, which can be used as benchmark modes to confirm the analysis technique, as well as to make improved measurements of their respective branching fractions in their own right. It aims to determine the internal structure of the $X(3872)$ and improve the understanding of the known charmonium system, contributing to the wider base of knowledge describing the formation of quarks into matter.

Chapter 2 provides background information relevant to this analysis, including the theoretical description of the charmonium system, a review of the recent experimental results concerning the $X(3872)$, and a summary of the theoretical proposals to describe the nature of this newly discovered state. Chapter 3 gives a physical description of the PEP-II collider, the *BABAR* detector, and its hardware and software. Chapter 4 describes the data set, its properties and the selection criteria used in this analysis. Chapter 5 explains the signal extraction methodology and its verification on simulated datasets. Chapter 6 contains the analysis of the actual data and the branching fraction measurements. Chapter 7 summarizes this research and presents its larger implications.

Chapter 2

Background Information

This chapter outlines the theoretical and experimental background appropriate to this analysis. It specifically describes the charmonium system, including $c\overline{c}$ binding, production, and decay. The recent experimental results of several newly discovered charmonium-like phenomena are presented along with their likely theoretical interpretation. The potential contribution of this analysis to the further understanding of these new states is explained.

2.1 The Charmonium Model

The understanding of particle physics was revolutionized in 1974 with the discovery of the J/ψ [1] and $\psi(2S)$ [8], identified as $c\overline{c}$ mesons. These discoveries were the first evidence for the existence of the charm quark, and taken as confirmation of the quark model describing the underlying constituents of baryons and mesons. In its simplest terms, the quark model for mesons describes them as a combination of a spin-$\frac{1}{2}$ quark and antiquark. The combined total spin is $S = 0$ or 1, the orbital angular momentum can be $L = 0, 1, 2, ...$, and the principle quantum number is denoted by N. For charmonium, the parity[1] of these states is $P = (-1)^{L+1}$, and the charge conjugation[2] C-parity is defined as $C = (-1)^{L+S}$. In standard spectro-

[1]The parity transformation is a spatial inversion operator, i.e.: $P|\Psi(x, y, z) > \rightarrow |\Psi(-x, -y, -z) >$. (Anti)quarks have (negative)positive parity. Bound states with wavefunctions described by spherical harmonics have the property $P = (-1)^L$. The total parity is multiplicative.

[2]The charge conjugation operator transforms a particle into its antiparticle. The total charge conjugation eigenvalue is multiplicative. Similar to parity, $C = (-1)^L$ for the spatial part of the wavefunction. Conjugation of the spin part is antisymmetric for $S = 0$ and symmetric for $S = 1$, thus $C = (-1)^{S+1}$. A factor is introduced for the charge part of the wavefunction, its value defined by $C = -1$ for the photon.

scopic notation, a state is referred to as $N^{2S+1}L_J$ (where $L = 0, 1, 2, ...$ is represented by letter notation $S, P, D, ...$), with quantum numbers J^{PC}.

The earliest theoretical models describing the $c\overline{c}$ system are purely phenomenological. Their assumption is that the bound charm and anticharm quarks are non-relativistic, and interact via a simple mechanism of one gluon exchange. This interaction reduces to the same form as the electromagnetic interaction and can be represented in a form similar to the Coulomb potential with $1/r$ dependence (where r is the distance between quarks). One of the tenets of the quark model, known as quark confinement, stipulates that quarks are restricted to bound states and cannot be free. A term proportional to r was added to the potential to model this behaviour. The $c\overline{c}$ interaction in this "Cornell model" [2] of charmonium was thus described by the potential

$$V(r) = -\frac{\kappa}{r} + \frac{r}{a^2} \tag{2.1}$$

where κ and a are parameters determined by fitting to experimental data. This basic description serves as the foundation of the charmonium model, upon which all subsequent developments were based. Necessary corrections can be made by including spin-spin and chromodynamic couplings, such that the potential is described as

$$V(r) = -\frac{4}{3}\frac{\alpha_s}{r} + br + \frac{32\pi\alpha_s}{9m_c^2}\tilde{\delta}_\sigma(r)\,\overrightarrow{S}_c \cdot \overrightarrow{S}_{\overline{c}} \tag{2.2}$$

where $\tilde{\delta}_\sigma(r) = (\sigma/\sqrt{\pi})^3 e^{-\sigma^2 r^2}$, is a Gaussian-smeared contact hyperfine interaction, and the standard $\propto 1/r$ colour-Coloumb and $\propto r$ confinement terms are retained. The parameters α_s, b, m_c, and σ are determined from a fit to the experimental spectrum. Perturbation theory can be used to include the spin-orbit interaction, Thomas precession, and the tensor interaction, resulting in an additional term for the potential

$$V_{spin}(r) = \frac{1}{m_c^2}\left[\left(\frac{2\alpha_s}{r^3} - \frac{b}{2r}\right)\overrightarrow{L} \cdot \overrightarrow{S} + \frac{4\alpha_s}{r^3}T\right] \tag{2.3}$$

where $\overrightarrow{L}$ and $\overrightarrow{S}$ are the orbital and spin angular momentum operators with

$< \overrightarrow{L} \cdot \overrightarrow{S} >= [J(J+1) - L(L+1) - S(S+1)]/2$, and the tensor T has non-zero entries between $L > 0$ spin-triplet states,

$$\langle {}^3L_J|T|{}^3L_J\rangle = \begin{cases} -\frac{L}{6(2L+3)}, & J = L+1 \\ +\frac{1}{6}, & J = L \\ -\frac{(L+1)}{6(2L-1)}, & J = L-1 \end{cases} \tag{2.4}$$

These perturbations are applied to solutions of Schrödinger equation for the basic central potential. Values for the unknown parameters, α_s, b, m_c, and σ, are determined by fitting the predicted spectrum to the data. This model is generally known as the "non-relativistic" model.

One of the most important theoretical developments is the so-called "Godfrey-Isgur model" [9], which extended the basic model to include relativistic corrections and a variable ("running") strong force coupling constant, and applied it to u, d, s, c and b quark systems. The power of this model is that it is valid for describing all quarkonia flavours, heavy and light, yet it reduces to the usual non-relativistic approximations of the original charmonium model (to first order).

These two theoretical descriptions are the most widely accepted basis for a complete description of the charmonium system. The charmonium spectrum predicted by the most up-to-date calculations [10] is presented in Figure 2.1.

It is worth mentioning in passing that lattice QCD, a numerical method for calculating the strong force interaction between quarks and gluons on a tiny, discrete scale, can also be employed to study the charmonium system [11]. Unfortunately the accuracy and predictive power of these calculations does not yet approach that of the phenomenological models presented here; therefore they will not figure substantively into this discussion.

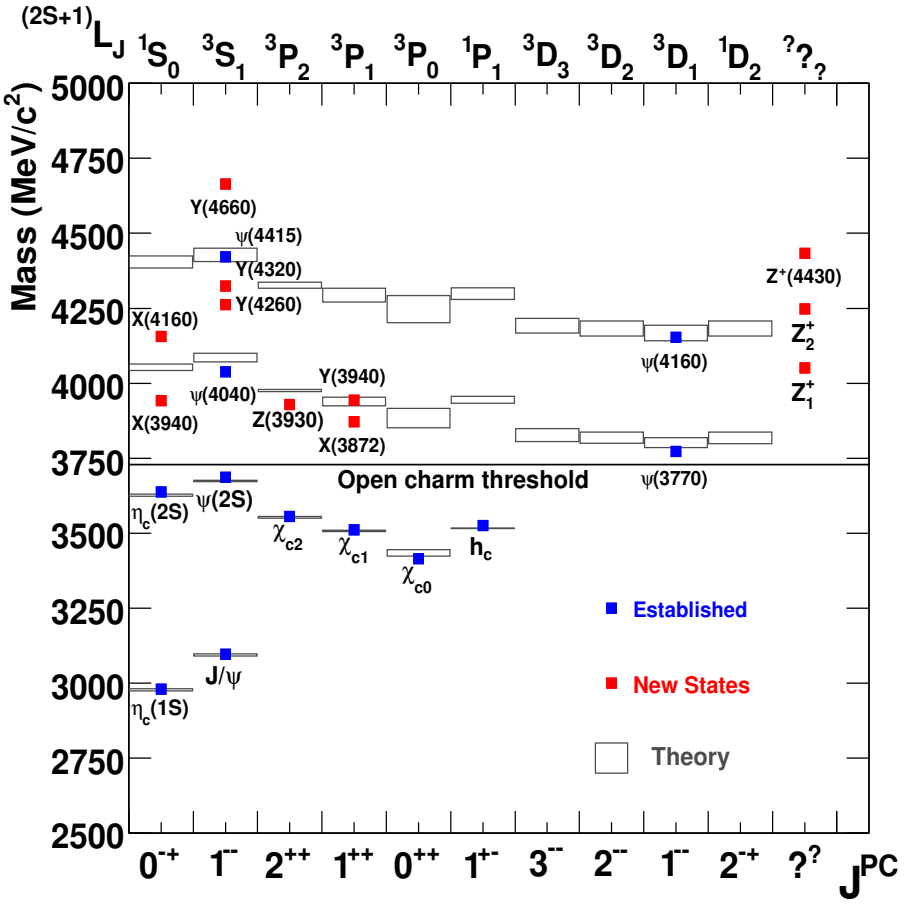

Figure 2.1: Predicted and observed spectrum of the charmonium model. The blue points indicate the experimental results for well-established charmonium states, the red points indicate newly discovered states and their likely J^{PC} assignments, and the gray boxes indicate the range of theoretical predictions from the non-relativistic model and the Godfrey-Isgur model [10]. The $D\overline{D}$ threshold is also shown.

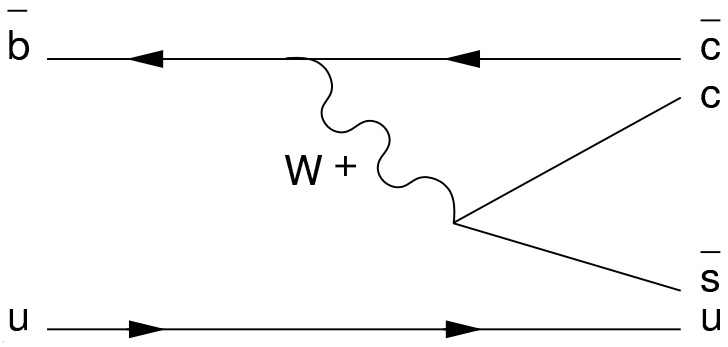

Figure 2.2: Feynman diagram of $B \to c\overline{c}K$.

2.2 Charmonium Production

There are four main production mechanisms for $c\overline{c}$ states in *BABAR*. The colour-suppressed[3] $b \to c$ decay of B mesons ($B \to c\overline{c}K$, for example) is the dominant method of production, and the most important in this analysis. Charmonium states of any quantum numbers J^{PC} are accessible from this decay. Charmonium can also be produced via an initial-state-radiation (ISR) process, i.e. $e^+e^- \to \gamma c\overline{c}$, where the incoming $e^\pm$ has lost some energy via photon emission. The third charmonium production method accessible in e^+e^- collisions is the two-photon process $e^+e^- \to e^+e^- c\overline{c}$. Finally, *double charmonium* production, $e^+e^- \to c\overline{c}+c\overline{c}$, was stumbled upon experimentally at the B Factories only recently.

The decay of the B meson to $c\overline{c}K$, shown in Figure 2.2, is a hadronic decay. While it is a flavour-changing weak decay, it is greatly complicated by additional gluonic strong interactions between the particles. These interactions are typically described by a phenomenological approach known as *factorization* [12]. When the $c\overline{c}$ pair is produced, it is susceptible to additional interactions with gluons and light quark-antiquark pairs. However, because it is a colour-singlet[4] bound state, the $c\overline{c}$ will both move away from

[3] In Figure 2.2, the $\overline{s}$ quark must be produced with the correct colour to match that of the "spectator" quark, u. This results is a suppression factor for the decay rate.

[4] For simplification, the colour-octet contribution is ignored and colour-singlet is considered to dominate.

the production vertex and interact as a single bound state rather than as individual quarks. As a result, the $c\overline{c}$ pair hadronizes as a single meson. The benefit of the factorization assumption is that the decay amplitude can be broken down into the multiplication of two currents, for example, $\langle Kc\overline{c}|\mathcal{H}_{eff}|B\rangle$ is evaluated as the product of the matrix elements between the B and K, and between $c\overline{c}$ and the vacuum.

The matrix element for the $B \to c\overline{c}K$ decay can be expressed as [13]:

$$\langle Kc\overline{c}|(\overline{s}c)_{V-A}(\overline{c}b)_{V-A}|B\rangle \propto \langle K|(\overline{s}b)_{V-A}|B\rangle\langle c\overline{c}|(c\overline{c})_{V-A}|0\rangle \tag{2.5}$$

where the notation $(\overline{q}q)_{V-A}$ represents $\overline{q}\gamma^{\mu}(1-\gamma^{\mu})q$. Thus the amplitude for the decay is proportional to the matrix element $\langle c\overline{c}|(\overline{c}c)_{V-A}|0\rangle$. This analysis is particularly interested in the case $c\overline{c}$ includes the χ_{c1} and χ_{c2} charmonium states. The axial-vector 1^+ χ_{c1} couples to the $V-A$ operator, resulting in a non-zero matrix element and a decay amplitude that can be predicted theoretically using further numerical inputs. Because χ_{c2} is a tensor (2^+) particle, it does not couple to vector or axial-vector operators, hence the matrix element $\langle\chi_{c2}|(\overline{c}c)_{V-A}|0\rangle = 0$. Similarly, $\langle\chi_{c0}|(\overline{c}c)_{V-A}|0\rangle = 0$ because $\langle 0^{++}|(\overline{c}c)_{V-A}|0^{++}\rangle = 0$ due to charge conjugation invariance. Thus according to this naïve factorization approach, decays of the type $B \to \chi_{c0,2}K$ are forbidden while decays to $\chi_{c1}K$ decays are allowed [14].

Experimental data from both *BABAR* [15, 16, 17] and Belle [18, 19] somewhat contradict these predictions. Decays $B \to \chi_{c0}K$ have been observed with branching fractions $\mathcal{O}(10^{-4})$, while $B \to \chi_{c2}K$ only has upper limits nearly an order of magnitude lower. Extensions to the factorization model (for example, rescattering effects [20], next-to-leading order corrections [21], etc.) allow for $B \to \chi_{c0,2}K$ decays with branching fractions similar to what has been observed for $\mathcal{B}(B \to \chi_{c1}K) \approx 4\times10^{-4}$. Measurement and discovery of B decays to $\chi_{c2}K$ are a crucial test for these theories.

2.3 Charmonium Decay

The decays of charmonium states can be broadly classified into three types: annihilation, radiative, and via the strong interaction. Annihilation decays (i.e. $J/\psi \to \ell^+\ell^-$) are generally suppressed for bound states, but the final state of two leptons is an experimentally clean signal that is easily identified. Common radiative decays include electromagnetic radiative transitions of an excited $c\overline{c}$ state to a lower energy charmonium state by emitting a photon, or by the emission of gluons creating light quarks (i.e. $\psi(2S) \to J/\psi\pi^+\pi^-$). Above the threshold for the production of a pair of D mesons, ≈ 3.72 GeV, decays via the strong interaction are entirely dominant. Below this energy, strong decays are OZI-suppressed[5] [22], leading to (relatively) long lifetimes and narrow widths. Radiative decays are often the most accessible transitions.

The principle charmonium decay modes of interest in this analysis are radiative decays of the form $c\overline{c}' \to c\overline{c}\gamma$. The electromagnetic transition between two states is expected to be dominated by the electric dipole (E1) transition[6], for which the decay width can be calculated from [23]:

$$\Gamma_{E1}(n^{2S+1}L_J \to n'^{2S'+1}L'_{J'} + \gamma) = \frac{4}{3} C_{fi}\delta_{SS'}e_c^2\alpha|\langle\psi_f|r|\psi_i\rangle|^2 E_\gamma^3 \qquad (2.6)$$

where $e_c = 2/3$ is the charge of the c quark, α is the fine structure constant, E_γ is the photon energy, $\langle\psi_f|r|\psi_i\rangle$ is the matrix element between the initial and final radial wavefunctions describing the charmonium states in question, and the angular matrix element C_{fi} is defined as:

$$C_{fi} = max(L, L')(2J' + 1) \begin{Bmatrix} L' & J' & S \\ J & L & 1 \end{Bmatrix}^2 \qquad (2.7)$$

[5] The "OZI rule" identifies the suppression of strong decays that occur between disjoint Feynman diagrams via multiple gluon exchange. In these decays, gluons must carry enough energy to hadronize into the final state products. As a result, they have a high energy and hence a smaller value for the strong coupling constant α_s.

[6] Higher order multipole (so-called "forbidden") transitions such as M1 are not considered here as their rates are expected to be relatively suppressed by orders of magnitude.

where the curly brackets indicate a $6-j$ symbol, which are a generalization of Clebsch-Gordon coefficients for the coupling of three angular momenta (in this case, the initial and final $c\overline{c}$ states and photon).

Equation 2.6 can be evaluated for any charmonium state given the expected masses and an expression for the wavefunctions ψ_i and ψ_f. These inputs can be provided from the phenomenological models described in Section 2.1 to produce estimates for the radiative transition widths. Of particular interest are the yet to be discovered charmonium modes for which decays to J/ψ and $\psi(2S)$ are expected or favoured, namely the $\chi_{cJ}(2P)$ states. Although the predictions are highly model-dependent for these states, they generally predict decay widths ranging $\sim 10-100\,\text{keV}$, with decays to $\psi(2S)\gamma$ tending to be favoured over decays to $J/\psi\,\gamma$ by a factor of $\sim 1-10$. Thus a measurement of the relative branching fraction of a newly discovered state to these final states could help to identify it, given certain assumptions regarding the choice of model.

Although they are not the subject of this study, it is important to mention the role of open-flavour strong decays of charmonium. The general description is the creation of a light $q\overline{q}$ pair from the vacuum, with the $c\overline{c}$ splitting to form separate $c\overline{q}$ and $\overline{c}q$ mesons. The $q\overline{q}$ pair is assumed to be produced with quantum numbers 0^{++}, hence the model describing these decays is called the "$^3P_0$ model" [24]. This model has been successfully applied to most meson and baryon systems. In terms of charmonium, it is used to describe the expected decays for $c\overline{c}$ states above the $D\overline{D}$ threshold. In general, calculations of the decay widths above this "open charm threshold" demonstrate that decays $c\overline{c} \to D^{(*)}_{(S)}\overline{D}^{(*)}_{(S)}$ are expected to entirely dominate [10].

2.4 Exotic Quarkonia

In addition to the well-known charmonium model, there have been other proposals describing the formation of exotic QCD states expected above the $D\overline{D}$ threshold. Three particular classes of models, *diquark molecules*, *tetraquarks*, and *charmonium hybrids*, illustrated in Figure 2.3, are poten-

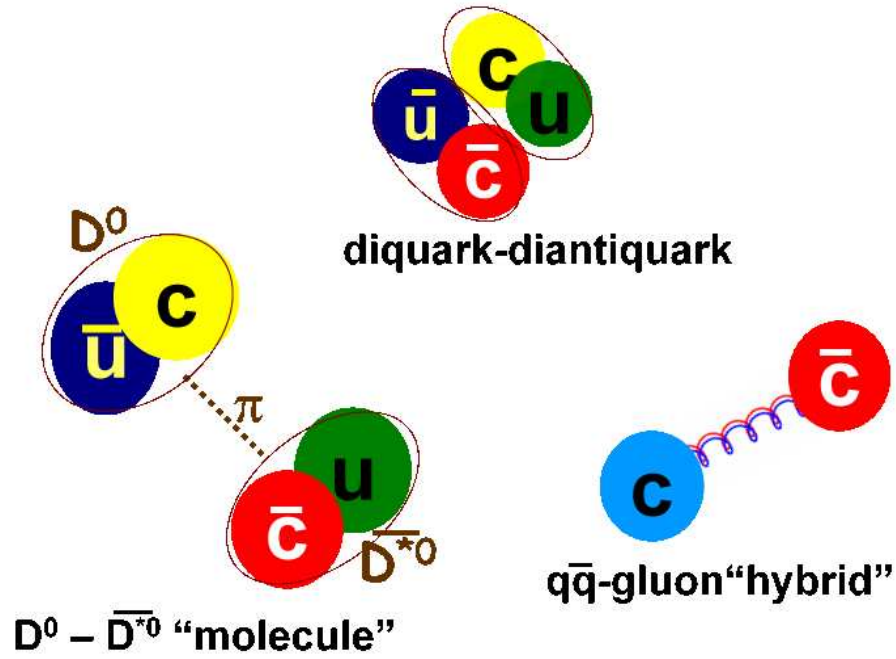

Figure 2.3: Cartoon depiction of plausible exotic QCD states: diquark molecules, tetraquarks, and $c\bar{c}g$ hybrids. Figure from [25].

tially relevant to this analysis.

Diquark molecules, also called *deusons*, are a pair of loosely bound charmed mesons [26]. While predictions for states of this sort have existed for some time, it is only in light of recent evidence from the B Factory experiments(described in Section 2.5) that they have been closely re-evaluated. The binding of these states is described as dominantly via pion exchange at large distance, with short-range contributions from quark interactions. Because of their weak binding and separation distance, the mesons are expected to decay as though they are free. Detailed theoretical treatments of a bound $D^0\overline{D}^{*0}$ state [27] have produced specific and testable quantum number and decay branching fraction predictions, the implications of which will be discussed in detail in Section 2.6. In brief, a $D^0\overline{D}^{*0}$ molecular bound state is expected to violate isospin, decay dominantly to $D^0\overline{D}^0\pi^0$ and $D^0\overline{D}^0\gamma$, and

have quantum numbers of 1^{++}.

The tetraquark model [28] describes a closely bound four-quark state, $[cq][\overline{cq}]$ in which scalar and vector triplets are formed and attract via spin-spin interactions. Decays are expected to occur by internal rearrangement of the tetraquark followed by dissociation into component mesons. This theory predicts a rather ambitious multitude of states in the region above the open-charm threshold. Should they exist, tetraquark states are expected to exhibit a range of quantum numbers ($0^{++}, 1^{++}, 1^{+-}$, and 2^{++}, with degeneracies), and include states with non-zero strangeness and non-zero charge.

The final set of states worth considering in this analysis are charmonium-gluon hybrids. These are $c\overline{c}$ states with an excited gluonic degree of freedom. There are several models describing quarkonium-gluon hybrids [29]. As a general remark, these models predict many states with distinct and exotic quantum numbers (e.g. a doubly-degenerate octet [30]), and could possibly decay to $c\overline{c}gg$ and $D^{(*,**)}\overline{D}^{(*,**)}$. For charmonium-gluon hybrids, the lowest mass predictions are expected to be at least $4.2\,\mathrm{GeV}/c^2$, well above the open-charm threshold.

2.5 Recent Experimental Results

The past few years have seen a flurry of activity in the charmonium sector. The B Factories, *BABAR* and Belle, have thoroughly explored the charmonium system below the $D\overline{D}$ threshold. In addition to measuring the well known $\eta_c(1S)$, J/ψ, $\chi_{cJ}(1P)$, and $\psi(2S)$ states, they have also observed the $\eta_c(2S)$ [31][7]. Perhaps the most interesting of these results have been the discovery of many new charmonium-like states above the $D\overline{D}$ threshold that do not fit into the standard charmonium model and possibly point to more exotic QCD discoveries. A concise review of these surprising new findings is given here.

[7] The only remaining below-threshold charmonium state yet to be observed in the B Factories, h_c, was discovered at CLEO [32]

2.5.1 $X(3872)$

In 2003, Belle discovered a narrow peak in the invariant mass distribution of $X \to J/\psi\pi^+\pi^-$ in the exclusive decay $B \to J/\psi\pi^+\pi^- K$ [3]. Until its nature is fully understood, the placeholder name assigned to this particle is $X(3872)$. This discovery was subsequently confirmed by the CDF [6] and DØ [5] experiments, as well as in *BABAR* [4]. The current world average mass of this new resonance is $m(X) = 3872.2 \pm 0.8\,\mathrm{MeV}/c^2$ with a width of $\Gamma = 3.0^{+1.9}_{-1.4} \pm 0.9\,\mathrm{MeV}/c^2$ [33]. The decay has been seen in both neutral and charged B decays, although the latest updates from *BABAR* [34] and Belle [35] in the high-statistics $X(3872) \to J/\psi\pi^+\pi^-$ mode agree only marginally regarding the ratio of $X(3872)$ decays from charged and neutral B mesons.

Both Belle (in an unpublished conference presentation [36]) and *BABAR* (as a precursor to this thesis, published by the author [37]) have found evidence for the decay $X(3872) \to J/\psi\gamma$. These results are shown in Figure 2.4. Because the charge conjugation (C) parity of the J/ψ and γ are both negative, this implies $C = +$ for the $X(3872)$. Combining charged and neutral B decays, the Belle measurement found $\mathcal{B}(B \to X(3872)K) \cdot \mathcal{B}(X(3872) \to J/\psi\gamma = (1.8 \pm 0.6 \pm 0.1) \times 10^{-6}$ with a significance of 4.0σ, while *BABAR* measured $\mathcal{B}(B \to X(3872)K^+) \cdot \mathcal{B}(X(3872) \to J/\psi\gamma = (3.3 \pm 1.0 \pm 0.3) \times 10^{-6}$ with a statistical significance of 3.4σ.

CDF [38] and Belle [39] analysed the dipion mass distribution from $X(3872) \to J/\psi\pi^+\pi^-$ decays and found them to favour a "ρ-like" shape, suggesting $X(3872) \to J/\psi\rho^0$. Belle also found evidence for the decay $X(3872) \to \pi^+\pi^-\pi^0$ in B decays, where the $X(3872)$ decay is thought to proceed via $X(3872) \to J/\psi\omega$ [36]. However, this claim has been disputed by *BABAR* [40]. CDF performed an analysis of the angular distributions of the daughters in the $X(3872) \to J/\psi\pi^+\pi^-$ decay, ruling out all J^{PC} assignments except for 1^{++} and 2^{-+} [7].

In studies of the decay $B \to D^0\overline{D}^0\pi^0 K$, both Belle [41] and *BABAR* [42] find a significant narrow enhancement slightly above threshold. Belle's initial measurement of the mass was $m(X) = 3875.2 \pm 1.9\,\mathrm{MeV}/c^2$, while *BABAR* found $m(X) = 3875.1 \pm 1.2\,\mathrm{MeV}/c^2$, with a width of $\Gamma(X) = 3.0^{+1.9}_{-1.4} \pm$

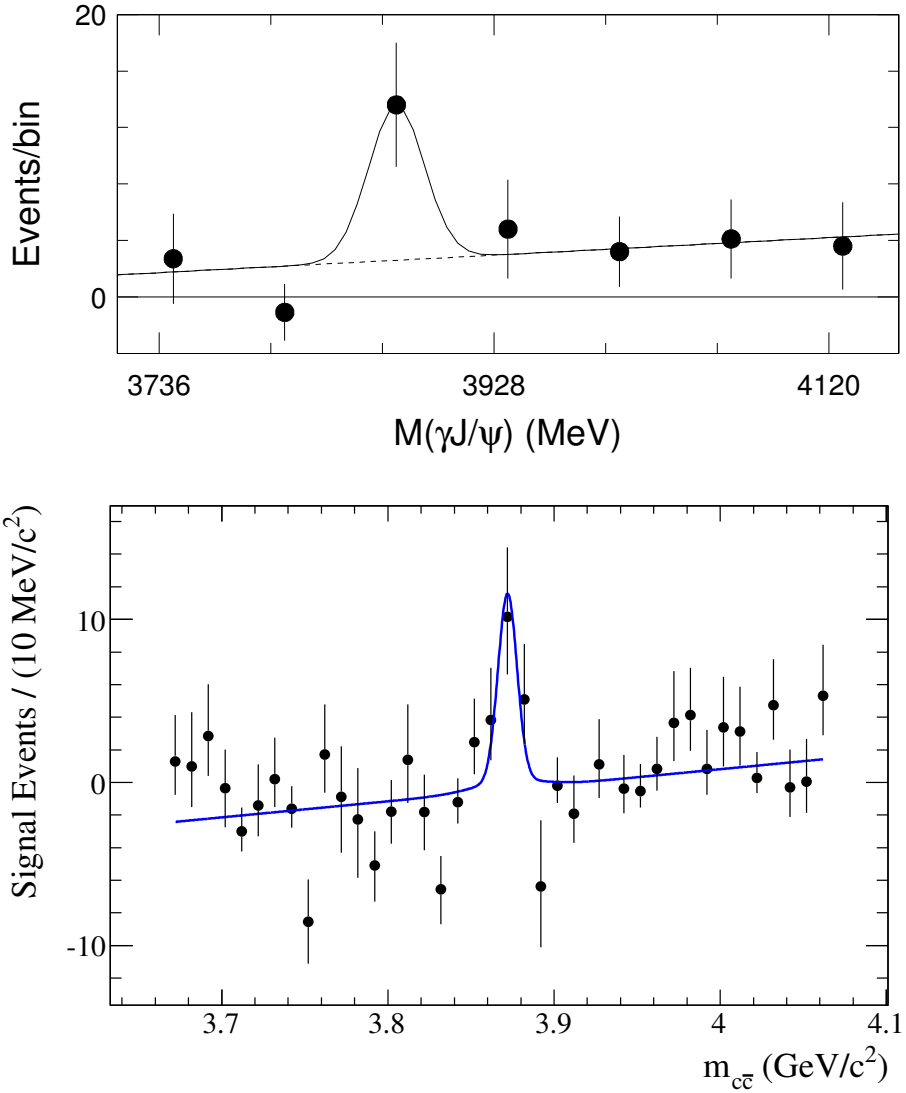

Figure 2.4: Previous results of $X(3872) \to J/\psi\gamma$ from Belle [36] (top) and *BABAR* [37] (bottom).

$0.9\,\mathrm{MeV}/c^2$ and confirmation that the decay proceeds via $X \to D^0\overline{D}^{*0}$. This mass value is roughly 4.5σ above the mass of the $X(3872)$ as measured in $X(3872) \to J/\psi\,\pi^+\pi^-$. A recent higher statistics update from Belle presented at conference [43] also favours the decay $X \to D^0\overline{D}^{*0}$, although the mass value of $3872.6^{+0.5}_{-0.4} \pm 0.4\,\mathrm{MeV}/c^2$ is much closer to that of the $X(3872)$. It is generally agreed [44, 45] that a mass shift at this level is still consistent with a single $X(3872)$ state.

The B Factories have conducted several other searches for the $X(3872)$ decays, though all have returned null results and upper limits only. These include $X(3872) \to J/\psi\,\eta$ [46], $X(3872) \to D\overline{D}$ [47], $X(3872) \to \chi_{c1,2}\gamma$ [3], and $X(3872) \to J/\psi\,\pi^-\pi^0$ [48].

Most of the experimental evidence at this time suggests that the $X(3872)$ state is a $D^0\overline{D}^{*0}$ molecule, but the results are not entirely conclusive. Full details of the theoretical interpretations of the $X(3872)$ are discussed in Section 2.6.

2.5.2 The $X/Y/Z$ Family

Following the discovery the $X(3872)$, three more charmonium-like states were discovered by Belle in a similar mass region but via distinct production methods and decay modes. All three states have possible conventional charmonium model interpretations.

A resonance with a mass of $m(X) = 3942 \pm 8\,\mathrm{MeV}/c^2$, called the $X(3940)$, was discovered by the recoil of the J/ψ in the double-charmonium production of $e^+e^- \to J/\psi X(3940)$ and confirmed in decays to $D^0\overline{D}^{*0}$ (but not $D\overline{D}$) [49]. Observation of an additional state with a mass of $m(X) = 4156 \pm 29\,\mathrm{MeV}/c^2$ was also claimed by Belle [50]. Given the production mechanism and the decays to $D^0\overline{D}^{*0}$, the most obvious quantum number assignment is $J^{PC} = 0^{-+}$, implying $^1S_0$ charmonium. However, the masses of both observations are inconsistent with charmonium model predictions. The $X(3940)$ is at least $100\,\mathrm{MeV}/c^2$ below the $\eta_c(3S)$ expectation, while the $X(4160)$ is similarly above this value yet $\sim 300\,\mathrm{MeV}/c^2$ below the predicted mass for the next excited state, $\eta_c(4S)$.

The $Y(3940)$ was first seen by Belle in the decay $B \to KY(3940)$, $Y(3940) \to J/\psi\omega$. Belle measured a mass and width of $m(Y) = 3943 \pm 11 \pm 13$ MeV/c^2 and $\Gamma(Y) = 87 \pm 22 \pm 26$ MeV/c^2 [51]. This state was recently confirmed by *BABAR*, measuring a mass and width of $m(Y) = 3914.3^{+3.8}_{-3.4} \pm 1.6$ MeV/c^2 and $\Gamma(Y) = 33^{+12}_{-8} \pm 1$ MeV/c^2 [40]. While the mass and width are generally consistent with predictions for the $\chi_{c0}(2P)$ or $\chi_{c1}(2P)$, the branching fraction to the observed decay mode is orders of magnitude higher than what would be expected for a charmonium state above the $D\overline{D}$ threshold. It is also still unclear if the $X(3940)$ and $Y(3940)$ are separate states.

Finally, the $Z(3930)$ was found by Belle in the two-photon process $\gamma\gamma \to Z(3930)$ decaying to $D\overline{D}$ [52]. They measured a mass and width of $m(Z) = 3929 \pm 6\,\text{MeV}/c^2$ and $\Gamma(Z) = 29 \pm 10\,\text{MeV}/c^2$, respectively. Belle also performed an angular analysis of the D decay daughters that favours $J^{PC} = 2^{++}$. Given charmonium model predictions of $m(\chi_{c2}(2P)) \approx 3970\,\text{MeV}/c^2$ and $\Gamma_{total}(\chi_{c2}(2P)) \approx 30\,\text{MeV}/c^2$, the combined experimental information strongly implies that the $Z(3930)$ is the $\chi_{c2}(2P)$ charmonium state.

2.5.3 States Produced in ISR

Several new states have been discovered via initial-state-radiation production. The first of these was *BABAR*'s discovery [53] of a broad structure in the decay $e^+e^- \to Y(4260)$, $Y(4260) \to J/\psi\pi^+\pi^-$ with a mass and width of $m(Y) = 4259 \pm 8^{+2}_{-6}$ MeV/c^2 and $\Gamma(Y) = 88 \pm 23^{+6}_{-4}\,\text{MeV}/c^2$. Following this discovery, CLEO performed a centre-of-mass energy scan and also collected data directly at the $Y(4260)$ resonance, confirming *BABAR*'s discovery as well as finding evidence for the decay $Y(4260) \to J/\psi\,\pi^0\pi^0$ [54]. Belle has recently also confirmed this state, and claims a second, much broader resonance at $m = 4008 \pm 40^{+72}_{-28}\,\text{MeV}/c^2$ with a width of $\Gamma = 226 \pm 44^{+87}_{-79}\,\text{MeV}/c^2$ [55].

BABAR's search for an accompanying $Y(4260) \to \psi(2S)\pi^+\pi^-$ decay turned up a structure at a higher mass incompatible with the $Y(4260)$ [56]. This new state was found to have a mass of $m(Y) = 4324 \pm 24$ MeV/c^2 and a width of $\Gamma(Y) = 172 \pm 33\,\text{MeV}/c^2$. Belle confirmed this discovery, while finding ev-

idence for a higher resonance with a mass of $m(Y) = 4664 \pm 11 \pm 5\,\mathrm{MeV}/c^2$ and width of $\Gamma(Y) = 48 \pm 15 \pm 3$ MeV/c^2 [57].

Because these states are produced in the annihilation of e^+e^-, they necessarily have $J^{PC} = 1^{--}$. However, all of the 1^{--} charmonium states have already been accounted for. This makes it difficult to accommodate even one, let alone all, of these new resonances within the charmonium model. Based on the masses ($m(Y) > 4200\,\mathrm{GeV}/c^2$) and lattice QCD predictions, charmonium hybrid assignments appear to be an attractive explanation, although tetraquark predictions, DD molecules, and threshold effects remain possibilities. At this time there are no definite conclusions.

2.5.4 Charged Multiquark States

Belle recently announced the observation of a state in the decay $B \to \psi(2S)\pi^+K$ [58]. Based on a Dalitz-plot analysis, they claim evidence for a charged state, Z^+, decaying via $Z^+ \to \psi(2S)\pi^+$ with a mass of $m(Z) = 4433 \pm 4 \pm 1\,\mathrm{MeV}/c^2$ and a width of $\Gamma(Z) = 44^{+17+30}_{-13-11}\,\mathrm{MeV}/c^2$. In response, *BABAR* performed a search for the same state and found no significant evidence to confirm Belle's claim [59]. Provided this state actually exists, its non-zero charge implies that it could be the first evidence for a charged tetraquark.

Belle also claims evidence for two additional features in the decay of $B \to \chi_{c1}\pi K$ that could be identified as charged tetraquarks decaying via $Z^+ \to \chi_{c1}\pi^+$ [60]. These results need further confirmation.

2.6 $X(3872)$ Phenomenology

From the results presented in Section 2.5, it is known that the $X(3872)$ has a mass of $3872.2 \pm 0.8\,\mathrm{MeV}/c^2$ and a width of $3.0^{+2.1}_{-1.7}\,\mathrm{MeV}/c^2$. Both *BABAR* and Belle have seen evidence for it decaying to the final states $J/\psi\,\pi^+\pi^-$, $D^0\overline{D}^{*0}$, and $J/\psi\,\gamma$. Belle also claims to have observed $X(3872) \to J/\psi\,\omega$, although this is not confirmed by *BABAR*. The decay to $J/\psi\,\gamma$ determines $C = +$, and the ρ-like shape of the dipion distribution in $X(3872) \to J/\psi\,\pi^+\pi^-$ is

consistent with this finding. Based on the angular analysis from CDF, the J^{PC} quantum numbers have been narrowed down to either 1^{++} or 2^{-+}.

If the $X(3872)$ is a conventional charmonium state, then according to the quantum number assignments from CDF's angular analysis, it could be either the $\chi_{c1}(2\,^3P_1)$ or the $\eta_{c2}(1\,^1D_2)$. In the case of the $\chi_{c1}(2P)$ assignment, the mass does not match predictions given the assumption that Belle's $Z(3930)$, discovered in two-photon production, is the $\chi_{c2}(2P)$. The charmonium model predicts a splitting of $< 50\,\mathrm{MeV}/c^2$ between the $\chi_c(2P)$ states, thus the mass of the $X(3872)$ is too low. Regarding the η_{c2} possibility, higher multipole (M1 and E2) radiative decays of the type $\eta_{c2} \to J/\psi\gamma$ should be strongly suppressed. The decay $c\overline{c} \to J/\psi\,\rho^0$ violates isospin and is unexpected for either charmonium assignment (i.e.: $I_{c\overline{c}} = 0 \to I_{J/\psi} = 0 + I_{\rho^0} = 1$).

Of the exotic QCD models, the tetraquark explanation predicts the presence of a second neutral $X(3872)$ with a mass splitting of $8\,\mathrm{MeV}/c^2$, and allows for charged partners. Both Belle and *BABAR*'s measurements of the $X(3872)$ in neutral and charged B decays find an $X(3872)$ mass consistent with one another. The *BABAR* search for a charged partner to the $X(3872)$ found no result. Furthermore, no indications for the predicted rich spectrum of charged and neutral accompanying states has been found. Given the experimental evidence to date, the tetraquark explanation is highly disfavoured.

Regarding charmonium-gluon hybrids, the experimental results seemingly do not match any predictions. The lightest charmonium-gluon hybrids have predicted masses more than 300 MeV/c^2 above the current $X(3872)$ mass. The expected dominant decay is to DD_2^* (no results to date) over $D\overline{D}$ (ruled out by *BABAR*), with little expected contribution to $D\overline{D}^*$ (the opposite has been observed by both *BABAR* and Belle).

The mass of the $X(3872)$ is very nearly equal to the mass of the D^0 and $\overline{D}^{*0}$ mesons, $m_{D^0} + m_{\overline{D}^{*0}} = 3871.81 \pm 0.36\,\mathrm{MeV}/c^2$ [33], leading many to believe that the $X(3872)$ may be a $D^0\overline{D}^{*0}$ diquark molecular state. Molecular models predict the decay of the $X(3872)$ to $D^0\overline{D}^0\pi^0$ and $D^0\overline{D}^0\gamma$ as the constituent D mesons decay separately. These models can accommodate mixing

of the $D^0\overline{D}^{*0}$ wavefunction with $J/\psi\,\omega$ and $J/\psi\,\rho$, which may explain the apparent isospin violating decays observed in experiment. The 1^{++} quantum number assignment is also consistent with the molecular model picture.

It is worth noting that not all of the molecular model predictions have been confirmed by experiment. The large decay rate of $X(3872) \to D^0\overline{D}^{*0}$ seen in *BABAR* and Belle is inconsistent with the molecular model, as is the relatively large $B \to X(3872)K$ production rate. The radiative $X(3872) \to J/\psi\,\gamma$ decay is allowed by the molecular model, but the predicted rate is again, smaller than experimentally observed. Finally, the production rate of the $X(3872)$ in $p\overline{p}$ and B decays is strikingly similar to that of $\psi(2S)$ charmonium. A possible simple interpretation is that the $X(3872)$ contains some $c\overline{c}$ component, and is thus an admixture of a weakly-bound $D^0\overline{D}^{*0}$ state and $\chi_{c1}(2P)$ charmonium.

The current status of the $X(3872)$ remains an open question requiring further theoretical and experimental input.

2.7 Analysis Outlook

The goal of this analysis is to use the full *BABAR* dataset to search for radiative decays of the $X(3872)$, namely $X(3872) \to J/\psi\gamma$ and $X(3872) \to \psi(2S)\gamma$, produced in the decays $B \to X(3872)K$. This search includes both charged and neutral B meson decays to excited kaon and charmonium states. Because the general form of the decay is $B \to (J/\psi\,\gamma)K$, a measurement of $B \to \chi_{c1,2}(J/\psi\,\gamma)K$ can be performed in conjunction with the $X(3872)$ search. The $B \to \chi_{c1}K$ modes are well-established and can be used to validate the signal extraction method, while the factorization-suppressed $B \to \chi_{c2}K$ decay modes have never been observed. This analysis uses the largest data sample to date for such a search.

To preserve signal efficiency, only charged final states of the kaons are reconstructed, and the $c\overline{c}$ candidates are reconstructed decaying to lepton pairs. The $\psi(2S) \to J/\psi\,\pi^+\pi^-$ decay mode is also included to increase statistics. Based on the $B^\pm \to X(3872)K^\pm, X(3872) \to J/\psi\,\gamma$ branching fraction measured by *BABAR* [37], this analysis could expect in the range of $20 - 35$

events with $\sim 4\sigma$ statistical significance, given a similar analysis efficiency. The decay process to K^* should follow the same Feynman diagram, and if the standard charmonium system is any guide, the branching fraction for decays of this type could be of similar order (with some reduction due to kaon daughter branching fractions).

The expected number of $\psi(2S)\gamma$ events is completely unknown. Within the framework of the charmonium model, Barnes and Godfrey [61] calculated that the branching fraction for the decay of $\chi_{c1}(2P) \to \psi(2S)\gamma$ could be several factors higher than $\chi_{c1}(2P) \to J/\psi\gamma$. Radiative decays of a 2^{-+} charmonium state to $J/\psi\,\gamma$ and $\psi(2S)\gamma$ should be highly suppressed. Regarding the molecular model for the $X(3872)$, radiative decays to $J/\psi\,\gamma$ are allowed in a vector-meson dominance scenario (where the ρ^0 or ω in the $J/\psi\,\rho^0$ and $J/\psi\,\omega$ components of the $X(3872)$ couple to a photon), whereas decays to $\psi(2S)\gamma$ proceed via annihilation of $u\overline{u}$ quarks (from the $D^0\overline{D}^{*0}$ components of the $X(3872)$) and the branching fraction is expected to be very small [62]. If the $X(3872)$ is the $\chi_{c1}(2P)$ charmonium state, the decay $X(3872) \to \psi(2S)\gamma$ may be observed. If $X(3872)$ is a molecular or tetraquark state, decays to $\psi(2S)\gamma$ are unexpected. As stated in [27], "Perhaps the most robust diagnostic is the $\gamma\psi(2S)$ decay mode...Clearly a measurement of the $\gamma J/\psi$ and $\gamma\psi(2S)$ decay modes of the $X(3872)$ will provide compelling clues to its internal structure."

Chapter 3

The *BABAR* Experiment

This chapter summarizes the detector hardware components and operation of the *BABAR* Experiment, including the design specifications, and the reconstruction and simulation software. A full description of the technical aspects of the detector can be found in [63] and [64].

3.1 The Linear Accelerator and PEP-II Storage Rings

The PEP-II B-Factory is an asymmetric e^+e^- collider located at the Stanford Linear Accelerator (SLAC) in Menlo Park, California. The electrons and positrons are first generated and accelerated in the 2-mile long linear accelerator (linac), and then circulated in opposite directions and focussed to collide by the PEP-II storage rings. A diagram illustrating the layout of the linac and PEP-II is shown in Figure 3.1.

Electrons are first produced by an "electron gun", where a filament is heated by an electrical current within a strong applied electric field. This generates free electrons which are accelerated away by the field toward the linear accelerator structure. The electrons are injected into the linac and accelerated to an energy of approximately 1 GeV, where they are then channeled into damping rings. These are circular storage rings where the electrons are maintained at a constant energy by accelerating them only to compensate for synchrotron radiation losses. This has the effect of "damping" the electrons, that is, tuning the spread and energy of the electrons in the beam to a desired constant. The damped electrons are then returned to the linac where they are accelerated to 9 GeV. Half of these electrons are

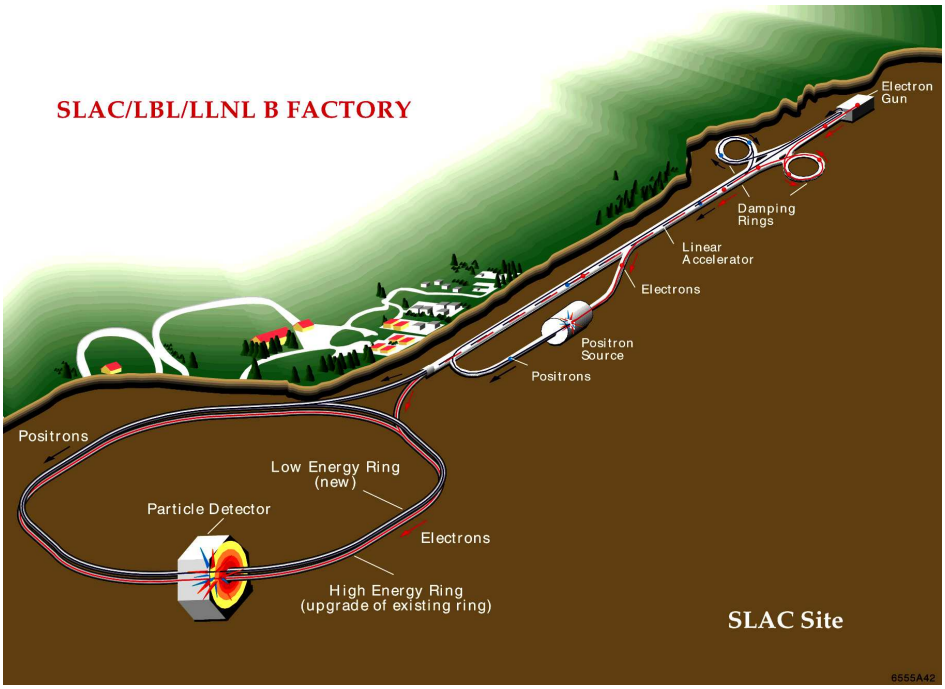

Figure 3.1: Illustration of the linear accelerator and PEP-II collider.

diverted from the linac and accelerated onto a tungsten target to produce electron-positron pairs. The positrons are collected and returned back to the start of the linac by a separate beam line, then redirected, damped, and accelerated to an energy of 3.1 GeV.

The acceleration in the injector, damping rings, and the linac is produced by microwave pulses generated by klystrons adjacent to the beam line. Klystrons consist of an electron gun whose electrons are accelerated into a resonant cavity to produce microwaves, which are transmitted to the linac cavities via a waveguide. The microwave pulses from the klystrons create electromagnetic fields in the copper linac cavities. The pulses are timed to provide the maximum acceleration to the particle bunches, and the field varies for electrons and positrons.

Once accelerated to the desired energies, the electrons and positrons are split off from the end of the linac into the High Energy Ring (HER) and Low Energy Ring (LER), respectively. They travel around the rings in opposite directions, receiving additional acceleration to match synchrotron radiation losses. The beams are steered and focused using a series of magnets to collide at an interaction point (IP) located at the centre of the *BABAR* detector.

The initial PEP-II collider design aimed to deliver an instantaneous luminosity of 3×10^{33} cm^{-2} s^{-1}. Upgrades during the *BABAR* running period allowed the collider to reach up to a peak luminosity of of $\sim 12 \times 10^{33}$ cm^{-2} s^{-1}. The machine operated from 1999 through 2008, delivering a total luminosity of ~ 553 fb^{-1} of which more than $\sim 95\%$ was recorded by *BABAR*. This included ~ 433 fb^{-1} taken at the $\Upsilon(4S)$ resonance resulting in approximately 476 million $B\overline{B}$ pairs. The integrated luminosity over the course of the *BABAR* experiment is shown in Figure 3.2.

3.2 Detector Overview

The *BABAR* detector is located at the collision point of the PEP-II B Factory. It is designed primarily for the study of CP violation in the B meson sector, but also supports a robust secondary physics program for the study of bottom and charm mesons and τ leptons. To meet these goals, it requires

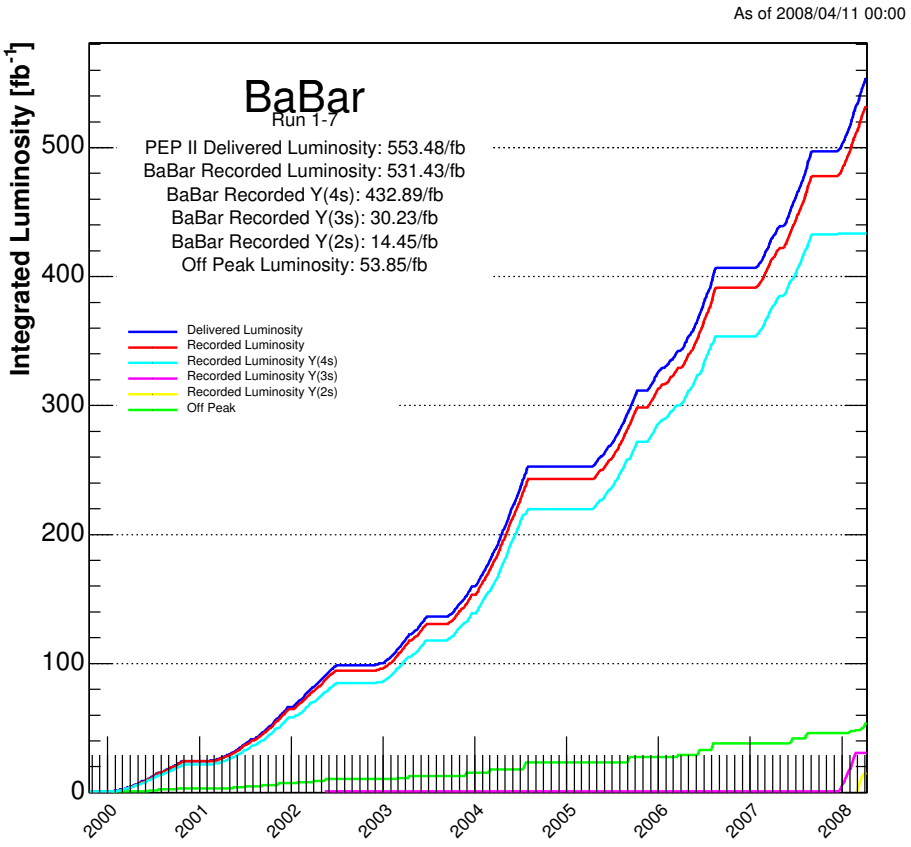

Figure 3.2: Integrated luminosity delivered by PEP-II to the *BABAR* experiment.

a large acceptance, good vertexing, reconstruction, energy and momentum resolution, high lepton (particularly e and μ) and hadron particle identification efficiency, and radiation hardness.

Moving outwards from the centre, the detector consists of a silicon vertex tracker (SVT) responsible for measuring the decay vertices close to the interaction point (IP), a drift chamber (DCH) for charged particle tracking and momentum measurement, a ring-imaging Cherenkov detector for particle identification, and an electromagnetic calorimeter (EMC) for measuring electromagnetic showers from electrons and photons. These detector subsystems are contained within a large solenoidal magnet capable of generating a 1.5 T magnetic field, and for which the steel flux return is instrumented with a muon detection system. The *BABAR* detector is illustrated in Figures 3.3 and 3.4.

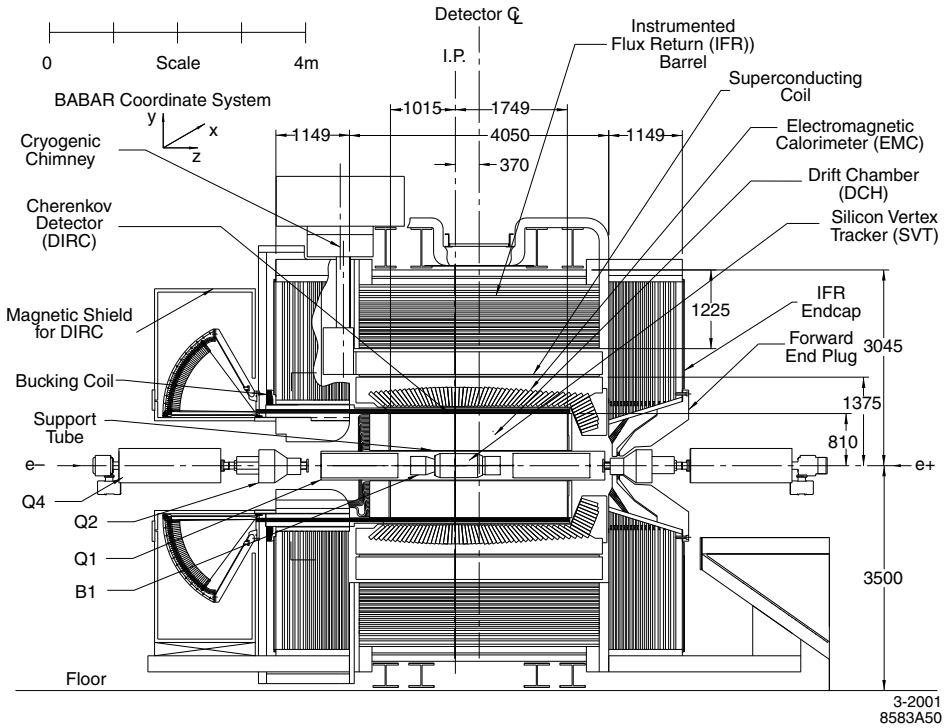

Figure 3.3: Longitudinal view of the *BABAR* detector.

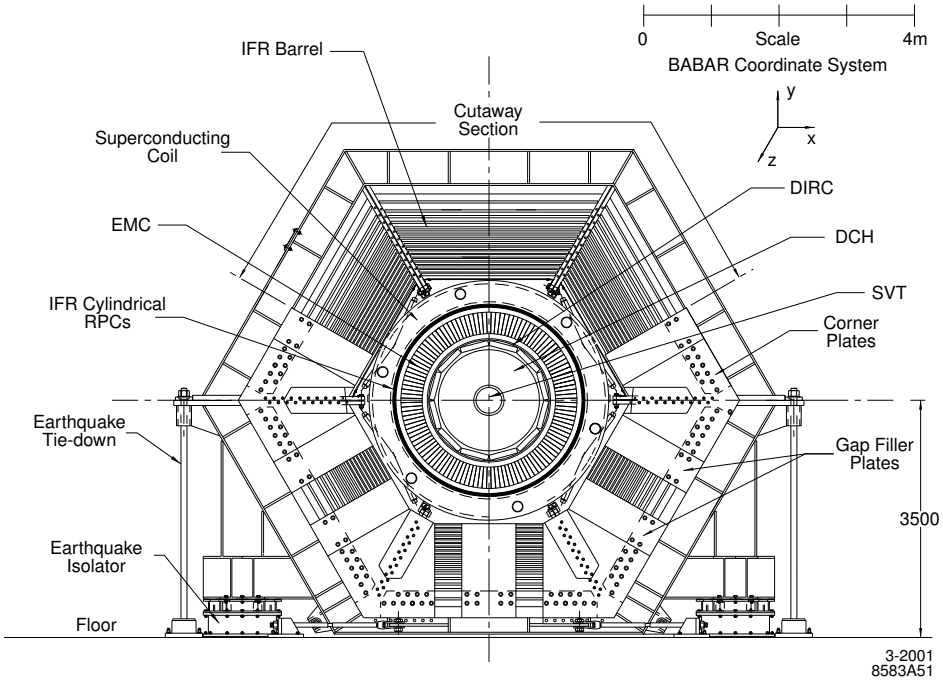

Figure 3.4: End view of the *BABAR* detector.

3.3 The Silicon Vertex Tracker (SVT)

The purpose of the SVT is to provide precise tracking and reconstruction of charged particles close to the interaction point. The design specifications aim for a resolution of better than 80μm and $\sim 100\mu$m in the x and yz planes, respectively, driven by the requirements for time-dependent $CP-$violation in B meson decays. As well, the SVT is responsible for providing tracking information for low momentum particles ($p_t < 120\,\mathrm{MeV}/c$) that may not reach the DCH. To accomplish these goals, the SVT is made of five layers of double-sided silicon strip sensors, with the inner three layers responsible for accurate vertex resolution, and the outer two for low p_t tracking. The strips on opposite sides of the silicon sensors run orthogonal to one another, and the layers are arranged to cover the largest angular coverage possible. Figures 3.5 and 3.6 show transverse and longitudinal cross-sectional views of the SVT, respectively.

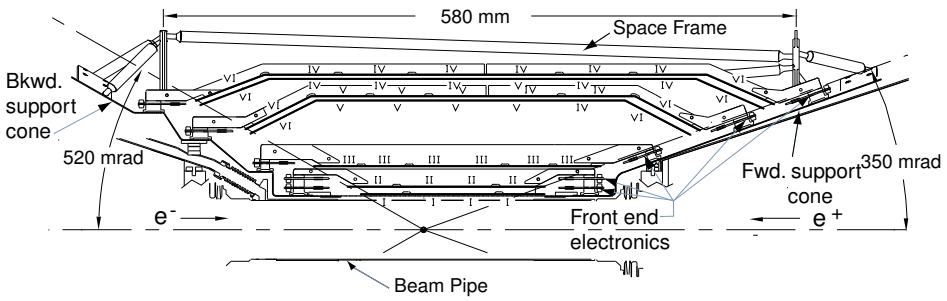

Figure 3.5: Transverse cross-sectional view of the SVT.

The silicon sensors in the SVT are 300μm thick, composed of high-resistivity n-type bulk silicon with n+ and p+ strips on either side. When a charged particle passes through the silicon, it ionizes the material, producing electron-hole pairs. Under an applied depletion voltage of $\sim 25-35$ V, the electrons drift to the n+ strips, and the "holes" to the p+ strips.

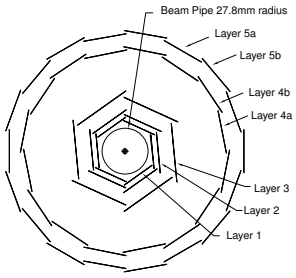

Figure 3.6: Longitudinal cross-sectional view of the SVT.

This results in an electrical signal that is read-out via capacitative coupling between the strips and the electronics.

Due to its proximity to the interaction point, one of the primary concerns for SVT operation is radiation hardness. The lifetime radiation budget for the SVT is an integrated dose of 2 Mrad. To limit the exposure, the SVT includes a radiation protection system consisting of PIN[8] and diamond diode sensors located in close proximity to the beam. These monitors can abort the colliding beams in the event of sudden high instantaneous or prolonged background levels that could be damaging to the hardware components. To ensure continued successful SVT operation, other operating conditions including temperature, humidity, and alignment are closely monitored, and the SVT system undergoes frequent electronics calibration.

3.4 The Drift Chamber (DCH)

The DCH is used for charged particle tracking and momentum measurement. It provides particle identification information based on the measurement of the ionization energy loss (dE/dx) for low momentum ($< 700\,\mathrm{MeV}/c$) particles, and those in the extreme forward and backward directions. It is also necessary to reconstruct longer-lived particles (such as K^0_S) that decay away from the interaction region outside of the SVT. It was designed to

[8]PIN diodes consist of doped p-type and n-type semiconductor regions separated by an intrinsic semiconducting region, hence the name "p-i-n".

provide a position resolution of 140μm and a dE/dx resolution of $\sim$ 7%. The DCH was constructed at TRIUMF on the UBC campus.

The DCH is a cylindrical gaseous multi-wire chamber detector; its dimensions are illustrated in Figure 3.7. It is approximately 3m in length, and consists of over 7000 hexagonally-shaped drift cells arranged in 40 cylindrical layers. Each cell consists of a tungsten-rhenium sense wire surrounded by six aluminum field wires. In 24 of the layers, the sense wire (or "stereo wire" in this instance) is strung at a slight angle with respect to the z direction to provide longitudinal position information (i.e.: for a given sense wire detection of a track, which adjacent stereo wire that detects the same track will depend on the track's z co-ordinate position). A schematic of the typical cell layout is shown in Figure 3.8. The sense wire is operated at a potential difference of $\sim 1900V$ compared to the grounded field wires, and the chamber is filled with a mixture of 80% helium and 20% isobutane. The gas is continually flushed and the system closely monitored to control temperature, pressure, mixture proportion, and to maintain a relatively high level of water vapour to prevent electrical discharge.

Charged particles ionize the gas, producing free electrons that are accelerated towards the sense wires by the applied electromagnetic field. This results in further ionization, resulting in an avalanche of electric charge close to the wire. The avalanche accumulates at the sense wire producing a measurable electrical signal that is amplified and read-out to the electronics. The integrated charge and drift time (time required for the ionized electrons to arrive at the wire) provide ionization energy-loss and position information of the particle track, respectively.

3.5 The Detector of Internally-Reflected Cherenkov Light (DIRC)

The DIRC is primarily responsible for the particle identification (PID) in *BABAR*. It is a novel device that uses internally-reflected Cherenkov light ring images to provide better than 4σ separation of π and K for the momentum

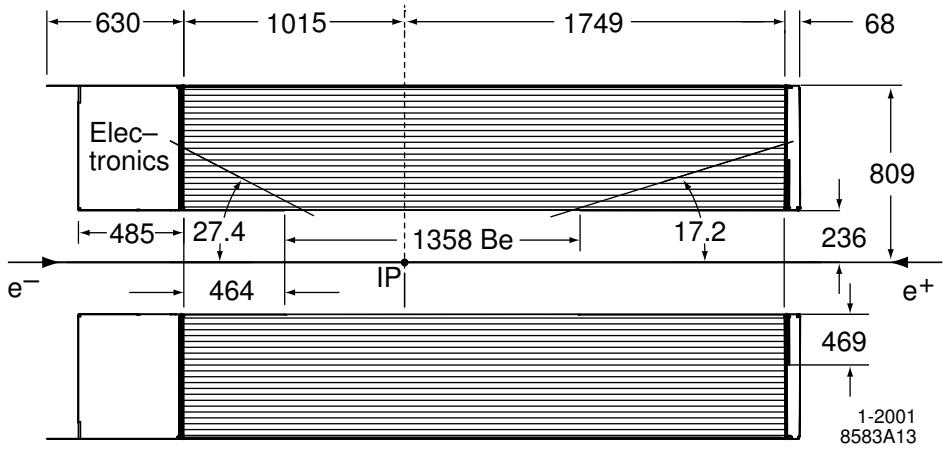

Figure 3.7: Longitudinal diagram of the DCH. Units in mm.

range from 700 MeV/c up to 4.2 GeV/c. It was designed to minimize its size and therefore the amount of material in front of the electromagnetic calorimeter.

When particles pass through a medium moving at a speed greater than that of light in that medium, they emit photons known as Cherenkov radiation. These photons are emitted at an angle relative to the particle's path, given by the Cherenkov angle:

$$\cos\theta_{\check{c}} = \frac{c}{nv} \tag{3.1}$$

where n is index of refraction of the medium and v is the speed of the particle. Particles of different mass have different Cherenkov angles for a given momentum. Cherenkov angle information taken together with the measured momentum can be used to separate one particle identification hypothesis from another.

A diagram of the DIRC can be found in Figure 3.9. The Cherenkov light radiator of the DIRC is composed of 144 radiation-hard fused silica bars with an index of refraction of $n = 1.473$. This high index of refraction leads to a smaller critical angle for the total internal reflection of the

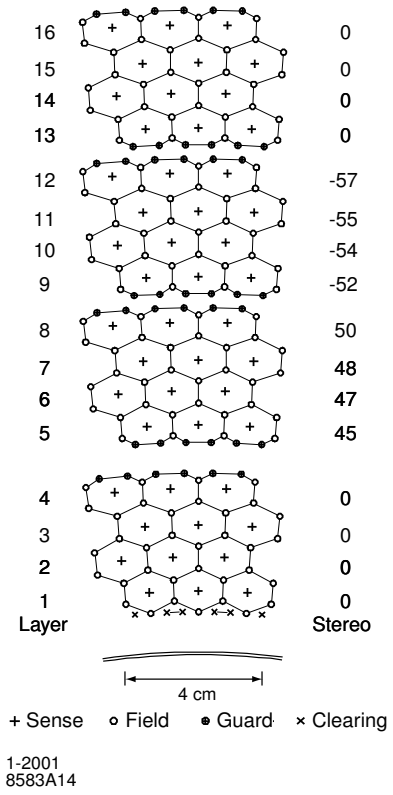

Figure 3.8: Layout of the DCH drift cells, with lines illustrating the cell boundaries, and the sense wire stereo angle (in mrad) for each layer.

Cherenkov light, and as such, can trap the Cherenkov light within the bar. The light propagates the length of the bar, reflecting at the boundaries and off a mirror at the forward end, to be emitted at the backward end. At the backward end, they pass into the "standoff box", a water-filled expansion region[9]. The standoff box contains approximately 6000 litres of ultra-pure, de-ionized water, and houses 12 sectors of 896 photomultiplier tubes (PMTs) located $\sim$ 1.2m from the end of the DIRC bar. The PMTs are outfitted with light-catcher cones to increase their effectiveness and, since they are located outside of the magnetic field region, the "traditional" photomultiplication method of photon-electron conversion and multiplication using photocathodes and dynodes is employed.

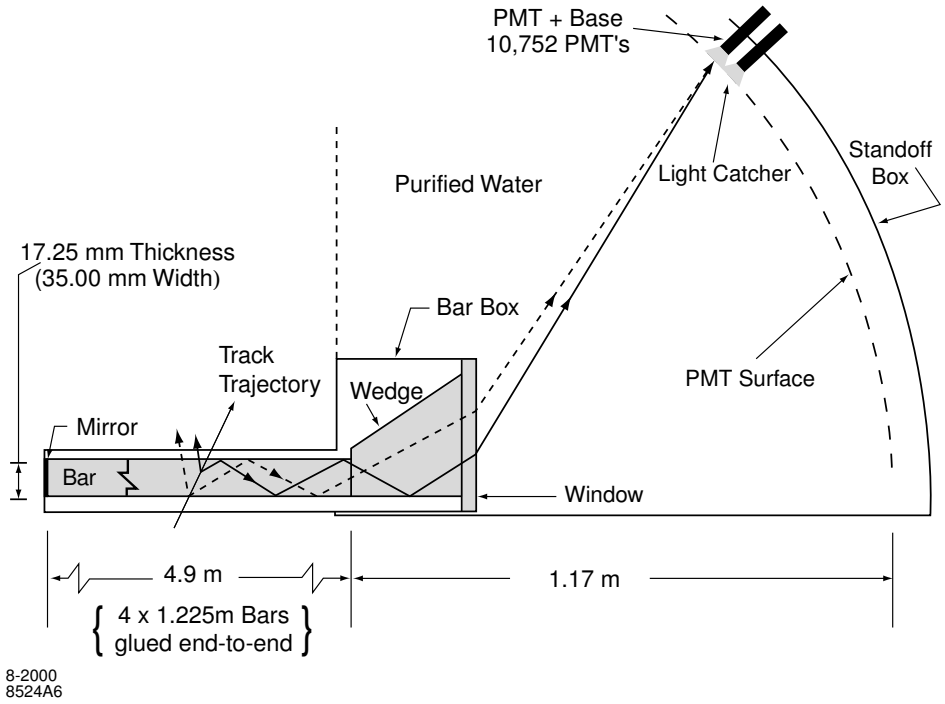

Figure 3.9: Diagram of the DIRC system.

[9]The index of refraction for water is $n = 1.346$, chosen in an attempt to match that of fused silica in order to minimize the amount of reflection and dispersion at the backward end of the bar.

Based on the position and timing of the PMT signals from the DIRC, coupled with the particle position and angle from the tracking system, the Cherenkov angle can be over-constrained and measured with a resolution of ~ 3 mrad.

3.6 The Electromagnetic Calorimeter (EMC)

The EMC is used to measure electromagnetic showers produced by electrons and photons. It is designed to be a hermetic total-absorption calorimeter, capable of measuring the position and energy of showers ranging from 20 MeV up to 9 GeV. For the *BABAR* experiment at large, the EMC is crucial for reconstructing $\pi^0 \to \gamma\gamma$ and $\eta \to \gamma\gamma$ decays. In this analysis, it is used for measuring the photon in $X(3872) \to c\bar{c}\gamma$, and identifying the electrons in $J/\psi \to e^+e^-$.

The absorptive material of the EMC consists of thallium-doped cesium iodide (CsI(Tl)) crystals, chosen for their high scintillation light yield, small Molière radius[10] (to minimize transverse shower size), and short radiation length. Photons and electrons interact with the crystal to produce electromagnetic showers that result in scintillation light. This light is captured and used to measure the shower properties.

The EMC consists of a cylindrical barrel with a conical forward endcap, each containing 5760 and 820 crystals, respectively. Figure 3.10 illustrates the this layout. Each crystal has typical dimensions of 4.7×4.7 cm^2 at the front face, a size on the order of the Molière radius of the material, increasing to approximately 6.1×6.0 cm^2 at the rear. The scintillation light is contained in each crystal by internal reflection at the polished surface and by white reflective wrapping. The accumulated light is read out by silicon PIN diodes (suitable for operation within a magnetic field) glued to the rear face of the crystal. The crystals are held into place by a large carbon-fibre support structure. A schematic of the crystal structure is found in Figure 3.11. The temperature of the system is closely monitored and controlled by

[10]The Molière radius for a material is the radius of a cylinder in which, on average, 90% of the energy of an electromagnetic shower is deposited.

water and Fluorinert cooling to prevent leakage currents in the photodiodes, and to protect the diode-crystal epoxy interface from temperature variation.

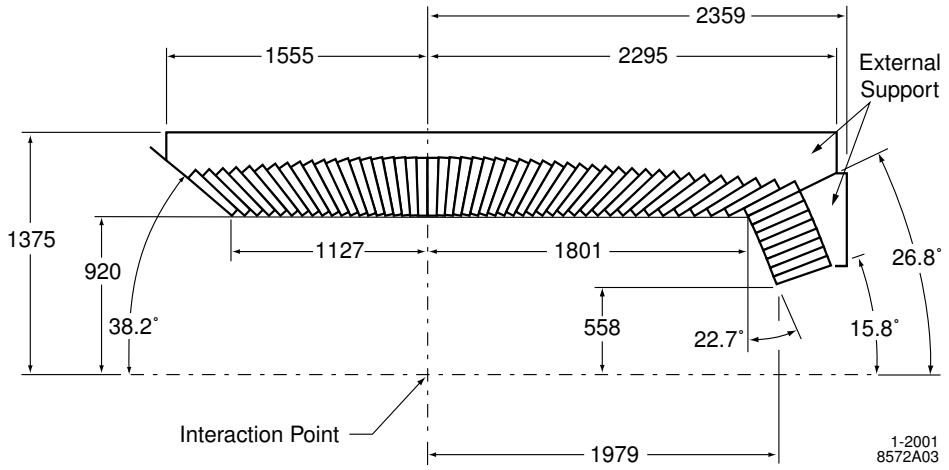

Figure 3.10: Layout of the EMC barrel and forward endcap. Units in mm.

The EMC crystals are calibrated individually to ensure reliable energy response. The low energy threshold is calibrated by irradiating the Fluorinert coolant with neutrons to produce radioactive ^{16}F, which emits a 6.13 MeV gamma ray. At high energy, the calibration is performed using Bhabha scattering events ($e^+e^- \to e^+e^-$) from the colliding beams, and by comparing the energy response of the detector with that from Monte Carlo (MC) simulation. The light response of the crystals is also tested using a light-pulser system that can transmit light from a xenon-flash lamp via fibre optics to each crystal. The radiation dosage and its effect on crystal light yield is also monitored over time.

Typical electromagnetic showers tend to spread over more than one crystal, forming a cluster of adjacent energy deposits. A reconstruction algorithm analyzes the shower shape and projects tracks from the inner detectors to the EMC to determine if a cluster can be associated with a charged particle. Otherwise, the EMC cluster is assumed to originate from a neutral particle. The energy resolution, based on the calibrations described as well

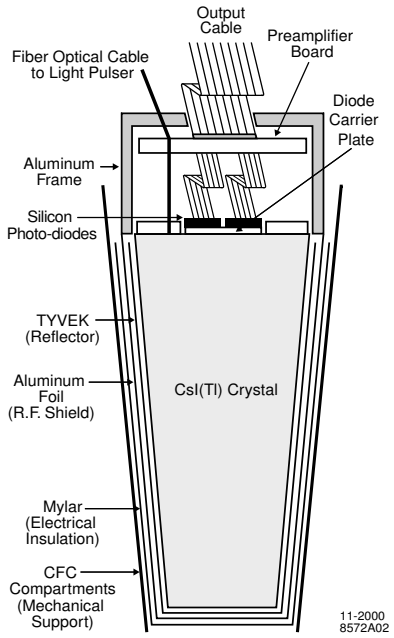

Figure 3.11: Diagram of a typical CsI(Tl) crystal in the EMC.

as other well known decays, is measured to be:

$$\frac{\sigma_E}{E} = \frac{(2.32 \pm 0.30)\%}{\sqrt[4]{E(\,\mathrm{GeV})}} \oplus (1.85 \pm 0.12)\% \tag{3.2}$$

where $\oplus$ signifies addition in quadrature. Analyzing decays of π^0 and η to two photons of equal energy produces an angular resolution parametrization of:

$$\sigma_\theta = \sigma_\phi = \frac{(3.87 \pm 0.07)}{\sqrt{E(\,\mathrm{GeV})}} \oplus (0.00 \pm 0.04)\mathrm{mrad} \tag{3.3}$$

The first (energy-dependent) term is due to statistical fluctuation in the number of photons and noise, while the second term arises due to non-uniformity in light collection and light absorption in the detector materials. Both results are close to design specification.

3.7 The Instrumented Flux Return (IFR)

The purpose of the IFR is twofold: it directs the field lines for the return of the solenoidal magnetic field, and acts as a particle identification system for muons and neutral hadrons (primarily K_L^0s and neutrons). It consists of alternating layers of steel plates and particle detection instrumentation, arranged into a hexagonal barrel region, and a forward and backward endcap.

Figure 3.12 illustrates the layout of the IFR. The IFR was originally equipped with 19 layers of resistive plate chambers (RPCs) between the 18 layers of steel, in addition to two layers of cylindrical RPCs close to the EMC. Resistive plate chambers are two highly-resistive planes closely separated by a gap filled with a gas mixture, held at a large potential voltage. Particles passing through the chamber ionize the gas, and the applied high voltage accelerates the resulting electrons into a controlled gas-discharge avalanche called a "streamer". The streamer signal is collected by inducing a charge in capacitatively-coupled read-out strips outside of the RPC. The gas gain in streamer mode is sufficient to produce a large signal independent of initial ionization, greatly simplifying the electronics read-out. The advantage of using RPCs lies in their relative simplicity, and ability to achieve a large

active area at a financially reasonable cost.

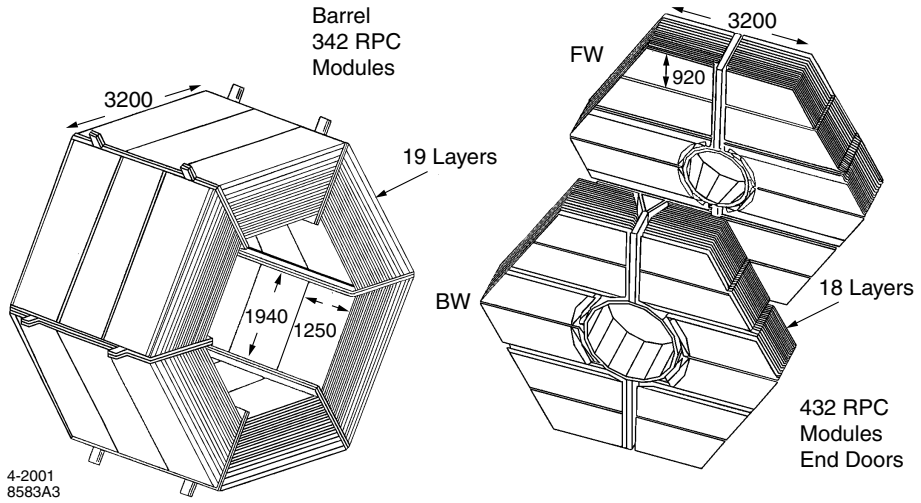

Figure 3.12: Layout of the IFR barrel and endcaps. Units in mm.

The *BABAR* RPCs were constructed of bakelite sheets coated with linseed oil (to provide a uniformly smooth surface) separated by a 2mm gap containing 56.7% argon, 38.8% Freon 134a, and 4.5% isobutane. The RPCs were operated at approximately 8000V, and the streamer signals read-out by aluminum strips on the exterior of the plates. A cross-sectional diagram of a planar RPC is shown in Figure 3.13.

Unfortunately, the RPCs did not perform well in *BABAR*. During the first summer of operation, many of the chambers began drawing very high dark currents and their efficiency dropped severely. It is suspected that high operating temperatures ($> 37^{o}$C) coupled with insufficient care and curing in the application of the linseed oil coating led to localized accumulation of the oil. These accumulating droplets, under the high electric field, could "bridge the gap" between plates, leading to discharge and large detector dead areas. As a result, the muon identification performance suffered. Extrapolation of the RPC failure rate indicated that *BABAR* would be without muon identification capability unless efforts were made to repair the system.

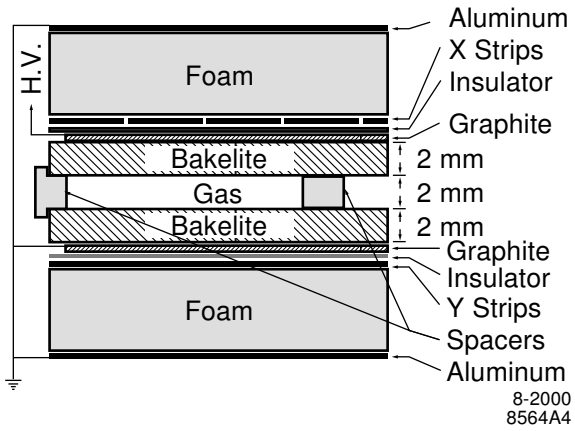

Figure 3.13: Cross section of Resistive Plate Chamber construction.

In 2002, new RPCs constructed under much stricter tolerances were installed into the forward endcap, and although their performance met expectations, it was decided to replace the entirety of the IFR barrel RPCs with Limited Streamer Tubes (LSTs)[11] [65]. LSTs consist of a gas-filled cell with grounded walls and a central wire at high voltage. Similar to RPCs, the gas operates in streamer mode when ionized, with the charge collected on the high voltage wire while simultaneously inducing a charge in the external read-out strips.

Figure 3.14 illustrates the *BABAR* limited streamer tubes. The LSTs consist of groupings of seven or eight 15×17mm graphite-coated PVC-walled cells approximately 3m in length. Each cell consists of a gold-plated beryllium-copper wire running its entire length, and is filled with a non-flammable mixture of 3.5% argon, 8% isobutane, and 88.5% carbon dioxide. The LSTs are operated at a voltage of $\sim$ 5500V. In order to avoid a repeat of the RPC debacle, the LSTs were subjected to a battery of strict quality assurance tests, which included high voltage conditioning, gas leak testing, examining sense wire quality with a radioactive source scan, and characteri-

[11] No action was taken to repair the deteriorating cylindrical and backward endcap RPCs, as their impact on muon identification is limited.

zation of tube performance by measuring the counting rate "plateau" versus applied voltage[12].

The phi-direction signals are read off of the high voltage wire using AC-coupled electronics. The z-signal is picked up by capacitatively-coupled read-out strips oriented in a plane orthogonal to the LSTs [66]. These "z-strips" were constructed[13] out of 35mm-wide conducting copper tape, grouped in a large Mylar-laminated sheet approximately 3×3.5m in size (dependent on the size of IFR layer). Figure 3.15 demonstrates the composition of the "z-planes", the accumulation of all of the z-strips of a single layer.

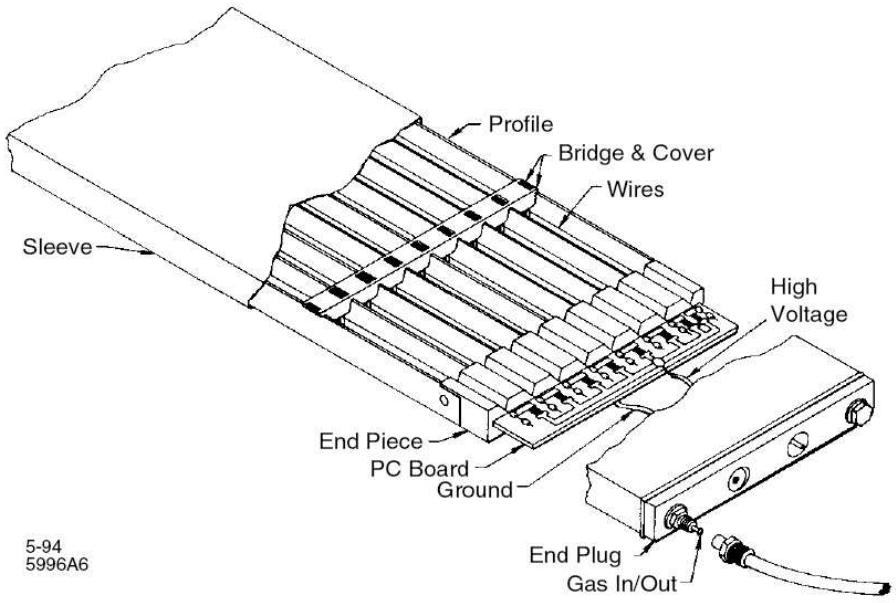

Figure 3.14: Diagram of a prototypical limited streamer tube.

Twelve layers of LSTs and six layers of brass (to preserve absorption length) were installed in the place of 18 layers of RPCs[14]. The first phase

[12]The author was personally involved in all of these tests for the IFR upgrade, and provided an important contribution to this effort with the authorship of software for the performance and automation of the rate plateau versus voltage scan

[13]The "z-planes" were built at SLAC, also with contribution from the author.

[14]The outermost layer of RPCs was inaccessible in the upgrade, but was disconnected

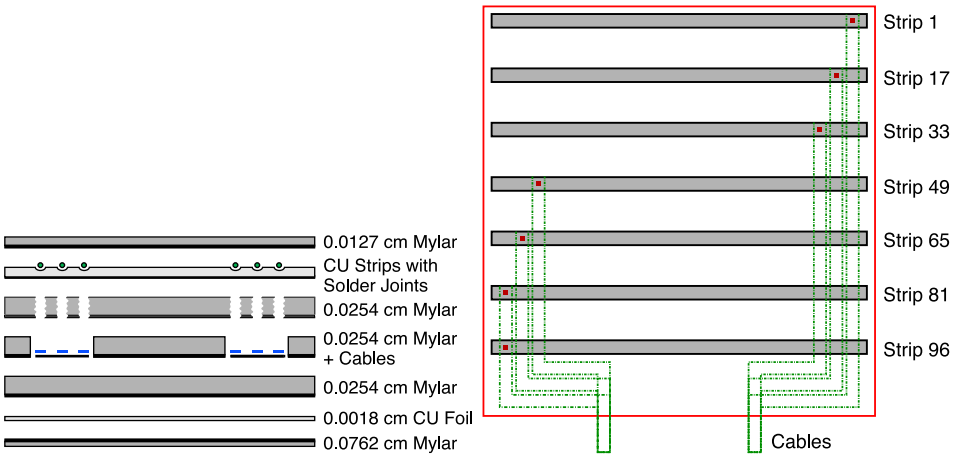

Figure 3.15: Diagram of the z-plane read-out strips constructed for the IFR LST upgrade. The figure on the left illustrates a cross-sectional view of a single z-strip. The figure on the right is shows a top-down view of a plane (not all strips shown).

of the installation replaced the top and bottom sextants of the barrel in the Summer of 2004. Replacement of the remaining four side sextants was completed in the Fall of 2006. In total, 1200 LSTs were installed in the detector. Their performance through the end of operations was exemplary, with an operating efficiency approaching the geometric limit of 90%. The total failure rate of LSTs and z-strips is less than 0.5%. Figure 3.16 demonstrates the improvement in muon detection efficiency in *BABAR*. The LST upgrade restored the muon detection efficiency to a level greater than that achieved from the RPCs even at the outset of the operations.

3.8 Triggering and Software

To select events of physical interest with high efficiency and adequate background rejection, *BABAR* relies on a two-tier trigger system. The Level 1 (L1) trigger is a hardware-based trigger that uses the raw information di-

nonetheless.

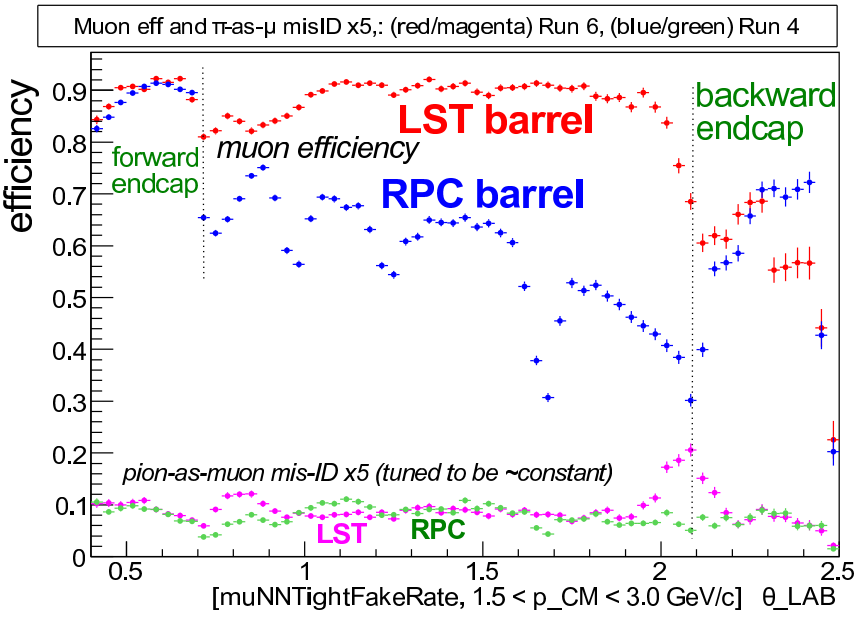

Figure 3.16: Comparison of the muon identification efficiency for various regions of the IFR. [67] The red and blue points represent a comparison of the LST and RPC muon identification efficiencies, while the magenta and green points represent a comparison of the pion-as-muon misidentification rate for the two subsystems scaled up by 5 times.

rectly from the DCH, EMC, and IFR[15] electronics, while the Level 3 (L3) trigger uses software to analyze data from the event to further refine the selection. The L1 trigger decision is based on tracks in the DCH exceeding a given transverse momentum, and showers in the EMC. It has a selection efficiency for $B\overline{B}$ events of greater than 99.9%, and a total rate of $\sim$ 1kHz under normal beam operation and background conditions. The L3 trigger rapidly identifies DCH tracks and EMC clusters, and makes a decision based on reconstructed DCH track momentum and distance of closest approach to the interaction point, and the EMC cluster multiplicity and deposited energy. The combined L1 and L3 triggers maintain a $B\overline{B}$ selection efficiency $> 99.9\%$ and reduce the rate to $100 - 200$ Hz for all event types.

Once an event passes the L1 and L3 triggers, it is processed by the reconstruction software to form charged tracks using the SVT and DCH information. Particle identification hypotheses are generated with this information combined with the information from the DIRC, EMC and IFR. These fundamental particles are formed into composite particle candidates, such as $J/\psi \to e^+e^-$ or $K^0_S \to \pi^+\pi^-$, and this information as well as the other event properties (e.g. vertexing, track momenta, cluster energy) is stored to disk for more detailed analysis.

Offline analysis is performed using a variety of software simulation tools and packages. Simulated events, known as Monte Carlo (MC), are produced using the EvtGen [68] generator for user-defined physics events, with the detector response modeled in GEANT4 [69], a toolkit for the simulation of the passage of particles through matter. User-defined programs for the analysis of data and MC events are based in C++ using the ROOT [70] software package, an object-oriented data analysis framework.

[15]The IFR trigger information consists of tracks detected from cosmic rays and $\mu^+\mu^-$ events, and is only used for diagnostic purposes.

Chapter 4

Analysis Preliminaries

This chapter describes the data sets used in this analysis, and the reconstruction of B-meson candidates. It defines the variables used to describe each event, and the procedure used to optimally define the event selection criteria and the results.

4.1 Data Set

This analysis uses the full *BABAR* dataset collected from the start of operations in 1999 to the conclusion of $\Upsilon(4S)$ running in 2007, for a total of 424.4 fb^{-1} or 465 ± 5M $B\overline{B}$ decays. *BABAR* defines data collection periods as "Runs", with the full $B\overline{B}$ data set referred to as Run 1–6.

Separate signal Monte Carlo modes have been generated for each of the $X(3872)$ decays to be studied in this analysis. The $X(3872)$ is generated as a zero-width particle, decaying by two-body phase space. Monte Carlo for modeling the background is taken from generic B^+B^-, $B^0\overline{B}^0$, $c\overline{c}$, $u\overline{u}, d\overline{d}, s\overline{s}$ and $\tau^+\tau^-$ samples, as defined with EvtGen. Inclusive J/ψ, $\chi_{c1,2}$, and, $\psi(2S)$ samples (i.e. generic $B\overline{B}$ decays filtered to include a J/ψ, $\chi_{c1,2}$ or $\psi(2S)$ in their decay chain) are also used to supplement the background sample and to provide $B \to \chi_{c1,2}K$ events.

A summary of the number of events generated for each mode and the appropriate cross-sections and weighting is given in Table 4.1. The integrated luminosity is calculated from $L = N/\sigma$, where σ is the cross-section for a given decay mode in units of nb. The Weight column of the Table is the fraction by which this mode's events were weighted in order for the MC sample to be equivalent to the Run 1-6 dataset size. For the signal MC modes, the weighting was based upon the branching fraction ($\mathcal{BF}$) values

for $B^{\pm} \to X(3872)K^{+}$ from [37].

4.2 B Candidate Reconstruction

The B-meson candidates are reconstructed using BABAR software packages designed to create composite particle candidates and store event information. To streamline this process, the data and MC are filtered or "skimmed" to reduce the number of events according to a set of well-defined criteria. Composite particles are constructed from daughters drawn from PID "lists" of particle candidates.

The B-meson candidates are built up from a final state of charged particles. A J/ψ or $\psi(2S)$ (hereafter referred to a "$c\overline{c}$") candidate is reconstructed from decays to two oppositely charged leptons (e^+e^- or $\mu^+\mu^-$) or the decay $\psi(2S) \to J/\psi\pi^+\pi^-$. This $c\overline{c}$ candidate is combined with a photon to make an "X" candidate, where X represents any possible physical combination, including the $X(3872)$ and the χ_{cJ}. K^0_S candidates are reconstructed from decays to two charged pions ($K^0_S \to \pi^+\pi^-$), while excited kaons are composed from the decays $K^{*\pm} \to K_S\pi^{\pm}$ and $K^{*0} \to K^{\pm}\pi^{\mp}$. Neutral final states are not considered to maintain a higher reconstruction efficiency. The B candidate is formed by pairing the X candidate with a kaon candidate.

This analysis considers 24 final states decaying to $B \to XK$ where: B includes charged and neutral B mesons; K represents kaons $K^{\pm}$, $K^0_S \to \pi^+\pi^-$, $K^{*\pm} \to K^0_S\pi^{\pm}$, and $K^{*0} \to K^{\pm}\pi^{\mp}$; and $X \to J/\psi\,\gamma$ and $X \to \psi(2S)\gamma$, where $J/\psi \to \ell^+\ell^-$, $\psi(2S) \to \ell^+\ell^-$, and $\psi(2S) \to J/\psi\,\pi^+\pi^-$ with $\ell = e$ and μ.

4.2.1 "JpsitollTight" Skim

The JpsitollTight skim used to restrict the dataset requires events to include decays identified as $J/\psi \to \ell^+\ell^-$ or $\psi(2S) \to \ell^+\ell^-$. The definition of these decays matches our J/ψ and $\psi(2S)$ reconstruction as defined in the following sections. The decay $\psi(2S) \to J/\psi(\ell^+\ell^-)\pi^+\pi^-$ is automatically included because of the decay of the daughter J/ψ into a lepton pair. The event must

Table 4.1: Number of events, equivalent luminosity, and weighting for the Run 1–6 MC modes and data sample.

Decay Mode	Total Events	Lumi (pb^{-1})	Weight
$q\overline{q}(q = u, d, s)$	$904,082,000$	$432,575$	0.967
$c\overline{c}$	$1,088,218,000$	$837,091$	0.500
B^+B^-	$702,558,000$	$1,277,378$	0.327
$B^0\overline{B}^0$	$702,788,000$	$1,277,796$	0.327
$\tau^+\tau^-$	$382,614,000$	$429,903$	0.973
J/ψ Inclusive	$15,307,903$	$5,358,275$	0.078
$\psi(2S)$ Inclusive	$2,393,121$	$6,762,395$	0.062
$\chi_{c1,2}$ Inclusive	$1,658,371$	$8,748,312$	0.048
$X(3872)$ Decay Modes			
$J/\psi \to \ell^+\ell^-$			
$K^\pm$	$195,000$		9.241×10^{-4}
$K^0_s(\pi^+\pi^-)$	$391,202$		3.187×10^{-4}
$K^{*\pm}(K^0_s\pi^\pm)$	$394,183$		2.109×10^{-4}
$K^{*0}(K^\pm\pi^\mp)$	$396,000$		3.029×10^{-4}
$\psi(2S) \to \ell^+\ell^-$			
$K^\pm$	$363,324$		0.612×10^{-4}
$K^0_s(\pi^+\pi^-)$	$378,160$		0.406×10^{-4}
$K^{*\pm}(K^0_s\pi^\pm)$	$379,050$		0.270×10^{-4}
$K^{*0}(K^\pm\pi^\mp)$	$406,486$		0.364×10^{-4}
$\psi(2S) \to J/\psi\pi^+\pi^-$			
$K^\pm$	$750,676$		0.763×10^{-4}
$K^0_s(\pi^+\pi^-)$	$780,317$		0.508×10^{-4}
$K^{*\pm}(K^0_s\pi^\pm)$	$782,425$		0.337×10^{-4}
$K^{*0}(K^\pm\pi^\mp)$	$838,514$		0.454×10^{-4}
Run 1–6 Data	$465,035,698$	$424,353$	1.000

also contain more than one particle identified as a hadron, or have $R2 < 0.5$ (this variable is described in Section 4.3.2). The skim selection rate from all events in the dataset is $\sim 1.1\%$. Skimming is not applied to signal MC modes as it is unnecessary.

4.2.2 $J/\psi \to \ell^+\ell^-$ Reconstruction

The J/ψ candidates are reconstructed in two decay modes. The e^+e^- decay uses a pair of bremsstrahlung-recovered[16] electron candidates reconstructed with a geometric constraint (i.e. both electrons are forced to originate from the same vertex) and requires $2.5 < m(e^+e^-) < 3.3$ GeV/c^2. The electron candidates are chosen from a standard *BABAR* list that calculates the likelihood of the electron particle ID hypothesis based on calorimeter, DIRC and energy loss information [73].

The $\mu^+\mu^-$ mode uses muon candidates with a geometric constraint applied and requires $2.8 < m(\mu^+\mu^-) < 3.3$ GeV/c^2. The muon candidates are chosen from a list defined using a neural net-based identification algorithm [74].

4.2.3 $\psi(2S)$ Reconstruction

The $\psi(2S)$ candidates are reconstructed in three decay modes: $\psi(2S) \to J/\psi\pi^+\pi^-$ and $\psi(2S) \to \ell^+\ell^-$, where $\ell = e$ or μ. For the former decay, J/ψ candidates use the same reconstruction as described in the previous section, and are constrained to the nominal J/ψ mass. The pion candidates are drawn from the list of all charged tracks identified in the event. The three decay particles are constrained to the same vertex and pass the requirements $3.586 < m(\psi(2S)) < 3.786$ GeV/c^2 and $0.4 < m(\pi^+\pi^-) < 0.6$ GeV/c^2. For the leptonic $\psi(2S)$ decays, the reconstruction uses electron and muon candidates selected in the exact same manner as for $J/\psi \to \ell^+\ell^-$ decays except that the invariant mass of the lepton pairs is restricted to $3.3 < m(\ell^+\ell^-) < 4.0$ GeV/c^2.

[16] Bremsstrahlung energy losses are recovered by an algorithm that associates low energy photons with the charged track and includes this into the electron candidate reconstruction.

4.2.4 $X \to c\bar{c}\gamma$ Reconstruction

The X candidates are reconstructed using J/ψ and $\psi(2S)$ candidates as defined above and refit with their masses constrained to the nominal value, combined with a photon candidate. The photon candidates are chosen from a list comprised of single EMC bumps unmatched with a track, requiring a minimum energy of 30 MeV and a maximum lateral moment of 0.8 (see Section 4.3.3 for a definition of this quantity). There are no restrictions on the X mass range to allow for the possibility of discovering new states up to the kinematic limit, and to include $\chi_{cJ} \to J/\psi\,\gamma$ decays as a benchmark mode.

4.2.5 Kaon Reconstruction

Four kaons are considered in this analysis: $K^{\pm}$, K^0_s, $K^{*\pm}$, and K^{*0}. Of these kaons, the $K^{\pm}$ are selected from a standard *BABAR* PID list, while the remainder are composite particles. The $K^{\pm}$ candidates require a likelihood of the kaon particle hypothesis versus pion to be > 0.5 and kaon versus proton > 0.018. The particle must have a momentum $p < 0.4$ GeV/c or else not be defined as an electron by other PID algorithms. The K^0_s candidates are reconstructed from the decay to oppositely charged pions drawn from the list of all charged tracks and are subject to a geometric constraint, and must be within ± 200 MeV/c^2 of the nominal K^0_s mass. The charged excited kaons, $K^{*\pm}$, are reconstructed from their decay to $K^0_s\pi^{\pm}$ using pion candidates that are charged tracks with a kaon and proton likelihood < 0.98, and K^0_s as defined here. The $K^{*\pm}$ mass is required to be within ± 200 MeV/c^2 of the nominal $K^*(892)$ mass. The neutral excited kaons are formed from the decay $K^{*0} \to K^{\pm}\pi^{\mp}$, drawing $K^{\pm}$ candidates as defined above and pions identified using the same definition for the $K^{*\pm}$ selection. For K^{*0}, a geometric constraint is applied and $0.7 < m_{K^{*0}} < 1.1$ GeV/c^2 required.

4.2.6 $B \to XK$ Reconstruction

The final B candidate is reconstructed from an X candidate and a kaon. The daughters are constrained to come from the same vertex, and loose

selection cuts of $5.0 < m_B < 5.5$ GeV/c^2, $5.2 < m_{miss} < 5.3$ GeV/c^2 (see Section 4.3.1 for a description of this variable), and the probability of the B vertex $\chi^2 > 0.001$ are applied. Once a B candidate has been established, it and its daughter decays are refit with the B mass constrained to the known value.

4.3 Event Variables

This section describes some of the variables used to characterize the reconstructed events used in this analysis. These variables are used for event selection and signal extraction. Final selection cuts and the optimization procedure for these variables is described in Section 4.4.

4.3.1 B Meson Variables

Kinematic Variables: m_{miss} and m_B

To select true B candidates from background events, two kinematic variables are used in this analysis: the mass of the reconstructed B candidate m_B, and the missing mass m_{miss}.

$$m_B = |p_B| \tag{4.1}$$

$$m_{miss} = |p_{e^+e^-} - \hat{p}_B| \tag{4.2}$$

where m_B is the unconstrained B-candidate mass from the four-momentum p_B of the reconstructed B meson, and the missing mass m_{miss} where $p_{e^+e^-}$ is the four-momentum of the e^+e^- system and $\hat{p}_B$ is the four-momentum of the B candidate after applying a B mass constraint. Correct values of m_B and m_{miss} for true B mesons should peak at the nominal B mass of 5.279 MeV/c^2 [33].

B Vertex χ^2 Probability

The probability χ^2 for the vertex reconstruction of the B meson is another variable to separate real B candidates from background events. It is a

measure of the probability that the decay daughters from the B candidate originated from the same initial vertex. This variable is used to remove very poorly reconstructed background events with low χ^2 values from the data sample.

4.3.2 Event Topology Variables

Fox-Wolfram Moment and $R2$

The Fox-Wolfram Moments are defined as [75]:

$$H_l = \sum_{i,j} \frac{|p_i||p_j|}{E_{tot}^2} P_l(\cos\theta_{ij}) \tag{4.3}$$

where p_i, p_j are the momenta of the particle candidates, θ_{ij} is the angle between them, E_{tot} is the total visible energy of the system, and P_l are the Legendre polynomials. The quantity $R2$ is defined as:

$$R2 = \frac{H2}{H0} \tag{4.4}$$

which can range from 0 to 1. This quantity is a measure of the isotropy of an event. Highly directional continuum events have higher $R2$ values, whereas B events tend to be more isotropic and have lower $R2$ values.

B Thrust and Sphericity Angles

The thrust angle, θ_{thrust}, and sphericity angle, θ_{sphere}, are a measure of the correlation between the direction of the B candidate compared to the other particles in the event. The thrust axis ($\overrightarrow{T}$) is the direction which maximizes the sum of the longitudinal momenta of the particles (also called thrust, T), while the sphericity axis is the direction maximizing the sum of the transverse momenta (called sphericity, S).

The thrust is defined as [76]:

$$T = \sum_i \frac{|\hat{T} \cdot p_i|}{\sum_i |p_i|} \tag{4.5}$$

The sphericity tensor is:

$$S^{ab} = \sum_i \frac{p_i^a p_i^b}{\sum_i |p_i|^2} \quad a, b = x, y, z \tag{4.6}$$

and the sphericity is defined as the 3/2 times the sum of the largest two eigenvalues of this tensor [77]:

$$S = \frac{3}{2}(\lambda_2 + \lambda_3) \tag{4.7}$$

The thrust and sphericity angle is the angle between the thrust or sphericity axis of the reconstructed B meson (based on its decay particles), and the equivalent axis for the rest of the event (all other particles).

For highly directional continuum events, the absolute value of the cosine of these angles peaks at 1 (i.e. the axes for the B candidate and all other particles point in the same or opposite direction). True B decays tend to be isotropic, hence $\cos\theta_{thrust}$ and $\cos\theta_{sphere}$ tend to be uniformly distributed.

4.3.3 Photon Variables

Photon LAT

The lateral energy distribution [78] of a photon candidate in the electromagnetic calorimeter (LAT) is defined as:

$$LAT = \frac{\sum_{i=3}^{N} E_i r_i^2}{\sum_{i=3}^{N} E_i r_i^2 + E_1 r_0^2 + E_2 r_0^2} \tag{4.8}$$

where N is the number of crystals in the shower, E_i is the energy deposited in the ith crystal, r_i is the polar radius in the plane perpendicular to the line pointing from the interaction point to the shower centre, and $r_0 = 5$cm is the average distance between two crystals. The energies are ordered $E_1 > E_2 > ... > E_N$ so that the sum in the numerator excludes the contribution from the two highest-energy crystals.

The LAT quantity is used to differentiate electromagnetic showers from hadronic showers, where most of the energy from an electromagnetic shower

is typically deposited in the first few crystals. This leads to a lower value of LAT, which can be used to distinguish photons shower from fake showers produced by hadrons.

Photon A_{42}

The Zernike moment is defined as [79]:

$$A_{nm} = \sum_{i=1}^{n} (E_i/E) \cdot f_{nm}(\rho_i) e^{-im\phi_i} \tag{4.9}$$

where E_i is the energy and (ρ_i, ϕ_i) are the locations of the hit crystals in the EMC with respect to the centre of the shower. The location is defined in cylindrical coordinates with the z axis running from the beam spot to the centroid, with $\rho_i = r_i/R_0$ where $R_0 = 15$ cm. f_{nm} represents the Zernike functions,

$$f_{nm}(\rho) = \sum_{s=0}^{(n-m)/2} \frac{(-1)^s (n-s)! \rho^n - 2s}{s!((n+m)/2 - s)!((n-m)/2 - s)!} \tag{4.10}$$

with $m \leq n$ and $(n-m)$ even. The Zernike moment A_{42} is a measurement of the azimuthal asymmetry of a photon's EMC cluster about its peak, another variable that can be used to distinguish hadronic and electromagnetic showers.

π^0 Veto

A possible source of misreconstruction is photons originating from the decay of a neutral particle such as $\pi^0 \to \gamma\gamma$. To ensure that the photon selected in the reconstruction of $X \to c\bar{c}\gamma$ has not originated from a π^0 decay, it is combined iteratively with each other photon candidate and the invariant mass of the four-momentum of the pair,

$$m_{\gamma\gamma} = \sqrt{(p_{\gamma 1} + p_{\gamma i})^2} \tag{4.11}$$

is determined. If the invariant mass from the pair of photons falls within a specified range of the π^0 mass, the event is rejected.

4.3.4 Kaon Variables

K_s^0 Flight Significance

Because K_s^0 have a measurable lifetime, they travel a finite distance in the detector before decaying into charged pions. The distance from the interaction point to the reconstructed vertex of the charged pions is defined as the kaon flight length, and the flight significance is this length divided by its uncertainty.

$K_s^0, K^{*\pm}, K^{*0}$ Vertex

The term "K vertex" is a shorthand notion used to describe the probability χ^2 for the vertex reconstruction of the kaon in question. It is a measure of the probability that the charged-track decay daughters from the kaon candidate originated from the same initial vertex.

4.4 Event Selection

This section describes the method used to establish values for the "cuts" applied to select signal events. The goal is to maximize the number of signal events versus background. In order to avoid bias, this exercise is first conducted independently from the experimental data using the signal and background Monte Carlo samples described in Section 4.1.

4.4.1 Cut Optimization Procedure

To best separate the signal from the background, selection cuts were imposed on several discriminating event variables. The selection criteria were found by maximizing a figure of merit defined as:

$$\mathcal{F} = \frac{n_S}{\sqrt{n_S + n_B}} \tag{4.12}$$

where n_S and n_B are the number of signal and background events, respectively. The number of events are subject to the weighting described in Table 4.1. To avoid double-counting in cases with multiple B candidates passing the reconstruction and selection cuts, the candidate with the value of m_B closest to the true B mass is used.

The optimization begins with a reasonable[17] choice of values for the possible discriminating variables. For each variable, all cuts are applied except those on the variable in question. The cut range on this variable is then chosen to maximize Equation 4.12. This is repeated for every variable, determining each optimized values independently. These values are then used as the input for the next iteration of the optimization procedure. The process continues until the cuts for each variable converge to stable values.

The event selection cuts for all of the $X \to J/\psi\gamma$ modes were optimized simultaneously, and the $X \to \psi(2S)\gamma$ modes simultaneously as well, but separately from each other (i.e. a single cut on variable x is applied to all $J/\psi\gamma$ events, and a different cut on x is applied to all $\psi(2S)\gamma$ events). The B vertex χ^2 probability cuts were optimized individually for each decay channel. The final values for some of the selection criteria were rounded off to provide agreement between signal modes and for ease of description and use. Note that the exact optimized values are not so much the priority as is selecting them in a manner uninfluenced by knowledge of what is in the experimental dataset.

4.4.2 Optimization Results

The results of the optimization procedure are given in this section.

The final selection cuts for the $B \to X(c\overline{c}\gamma)K$ modes are listed in Table 4.2. "No optimal cut" signifies that the optimization procedure found that this variable offers no discriminating power between signal and background. Loose, non-optimized cuts of $m_{miss} = m_{B(PDG)} \pm 100\,\mathrm{MeV}/c^2$ and $m_X = m_{X(3872)} \pm 100\,\mathrm{MeV}/c^2$ were chosen to limit the size of the data sample to our

[17] The initial values were roughly estimated based on the previous analysis [37]. Other starting points were found to converge to similar optimal results.

region of interest. Because the photon energy for the $\psi(2S)$ decay modes is relatively low, a non-optimized cut of $E_\gamma > 100$ MeV was applied to reduce the large combinatoric background contribution from misreconstruction due to selecting a random low-energy photon. For the J/ψ modes, no cut on E_γ was required because the resulting m_X from low-energy photons is well below the $X(3872)$ region of interest. Cuts were applied to $m_{K^{*+}}$ and $m_{K_0^*}$ during the optimization procedure to better isolate signal events, but cuts on these variables were not applied in the final selection.

Figures 4.1 through 4.10 show the distributions of the event variables for the J/ψ decay modes. Figures 4.11 through 4.21 are the corresponding plots for the $\psi(2S)$ modes. For each plot, the optimized cut values have been applied to all other event variables except for the one being plotted. In all cases, the red line indicates the distribution for the signal MC, the blue line indicates background MC, and the two black arrows indicate the optimal cut range. Although the distributions have been normalized to have the same area in the plots for visualization purposes, the optimization was conducted using the proper weights as given in Table 4.1.

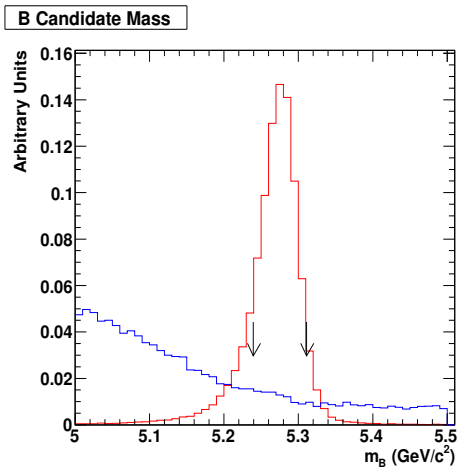

Figure 4.1: Optimized B mass for the $X(3872) \to J/\psi\,\gamma$ modes. Signal modes are represented in red; background modes are represented in blue. Arrows represent the optimized values of the selection cuts.

Table 4.2: Results of optimization of the selection criteria. The centre column lists the optimized values for the $c\overline{c} = J/\psi$ modes, and the right hand column gives the values for the $c\overline{c} = \psi(2S)$ modes.

Variable	J/ψ Range	$\psi(2S)$ Range
B $\chi^2(K^+)$	$P(\chi^2) > 0$	$P(\chi^2) > 0.01$
B $\chi^2(K_S)$	$P(\chi^2) > 0$	$P(\chi^2) > 0.002$
B $\chi^2(K^{*+})$	$P(\chi^2) > 0$	$P(\chi^2) > 0.05$
B $\chi^2(K^{*0})$	$P(\chi^2) > 0$	$P(\chi^2) > 0.05$
m_B (MeV/c^2)	$m_B(PDG)\ ^{+30}_{-36}$	$m_B(PDG) \pm 20$
m_{miss} (GeV/c^2)	$(5.2 < 5.3)$	
$m_{c\overline{c}}$ (MeV/c^2)	$m_{X(3872)} \pm 100$	
$m_{J/\psi \to e^+e^-}$ (GeV/c^2)	$(2.96, 3.15)$	$(3.01, 3.15)$
$m_{J/\psi \to \mu^+\mu^-}$ (GeV/c^2)	$(3.06, 3.13)$	
$m_{\psi(2S) \to e^+e^-}$ (GeV/c^2)	-	$(3.61, 3.73)$
$m_{\psi(2S) \to \mu^+\mu^-}$ (GeV/c^2)	-	$(3.65, 3.72)$
$m_{\psi(2S) \to J/\psi\,\pi^+\pi^-}$ (GeV/c^2)	-	$(3.68, 3.69)$
$R2$	$R2 < 0.45$	
$\cos\theta_{thrust}$	No optimal cut	
$\cos\theta_{sphere}$	No optimal cut	
E_γ (MeV)	No cut applied	$E_\gamma > 100$
γLAT	$0.001 < LAT < 0.5$	
$\gamma A42$	$A42 < 0.1$	
π^0 veto (MeV/c^2)	$124 < m_{\gamma\gamma} < 146$	No optimal cut
$m_{K^0_S}$ (MeV/c^2)	$m_{K^0_S}(PDG) \pm 17$	
K^0_S flight	K^0_S flight> 3.7	
K^0_S vertex	$P(\chi^2) > 0$	$P(\chi^2) > 0.001$
$m_{K^{*+}}$ (MeV/c^2)	$m_{K^{*+}}(PDG) \pm 50$	
K^{*+} vertex	$P(\chi^2) > 0$	$P(\chi^2) > 0.02$
$m_{K^*_0}$ (MeV/c^2)	$m_{K^*_0}(PDG) \pm 35$	
K^*_0 vertex	$P(\chi^2) > 0$	$P(\chi^2) > 0.002$

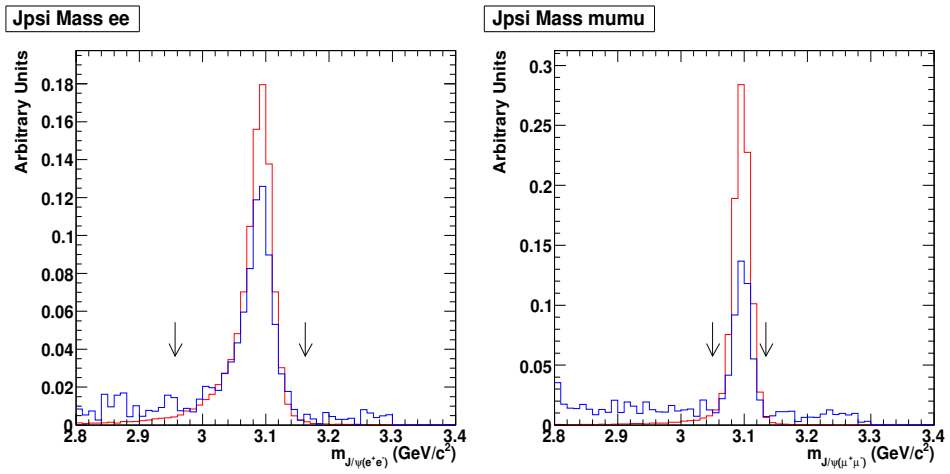

Figure 4.2: Optimized J/ψ mass for the $X(3872) \rightarrow J/\psi\gamma$ modes. Signal modes are represented in red; background modes are represented in blue. Arrows represent the optimized values of the selection cuts.

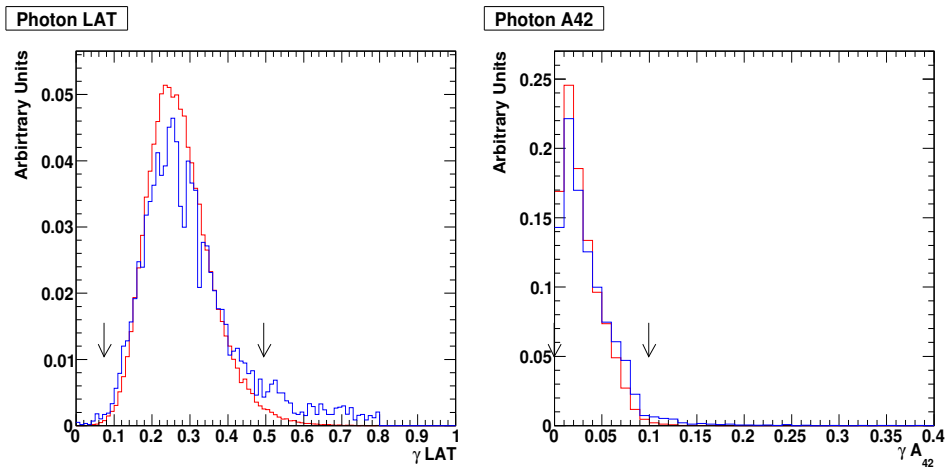

Figure 4.3: Optimized γ *LAT* and γA_{42} for the $X(3872) \rightarrow J/\psi\gamma$ modes. Signal modes are represented in red; background modes are represented in blue. Arrows represent the optimized values of the selection cuts.

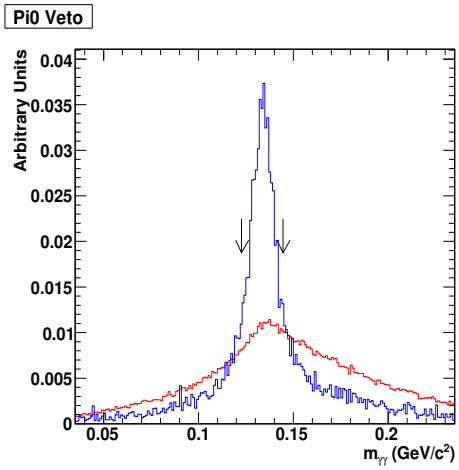

Figure 4.4: Optimized π^0 veto for the $X(3872) \to J/\psi\gamma$ modes. The invariant mass $m_{\gamma\gamma}$ closest to m_{π^0} is plotted. Signal modes are represented in red; background modes are represented in blue. Arrows represent the optimized values of the selection cuts.

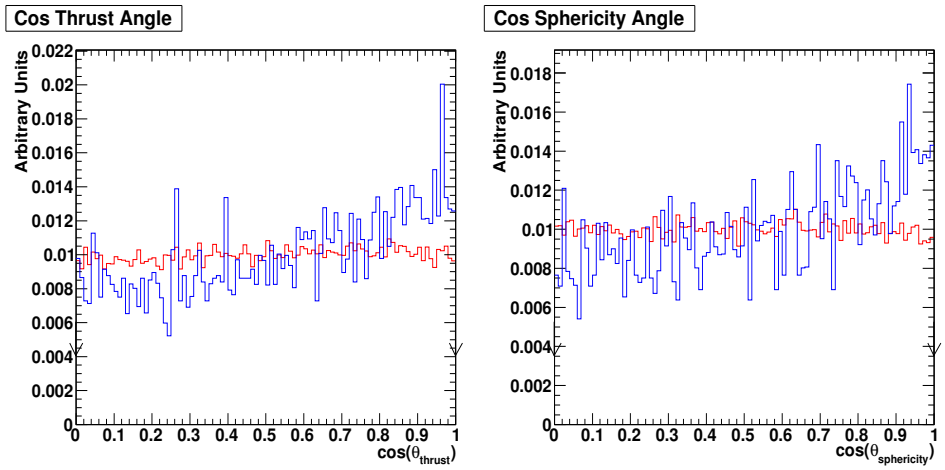

Figure 4.5: Optimized $\cos\theta_{thrust}$ and $\cos\theta_{sphericity}$ for the $X(3872) \to J/\psi\gamma$ modes. Signal modes are represented in red; background modes are represented in blue. Arrows represent the optimized values of the selection cuts.

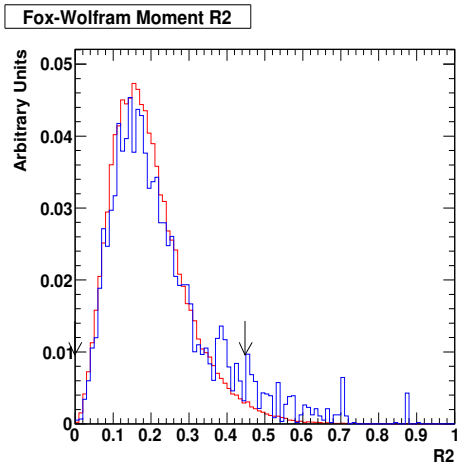

Figure 4.6: Optimized $R2$ for the $X(3872) \to J/\psi\,\gamma$ modes. Signal modes are represented in red; background modes are represented in blue. Arrows represent the optimized values of the selection cuts.

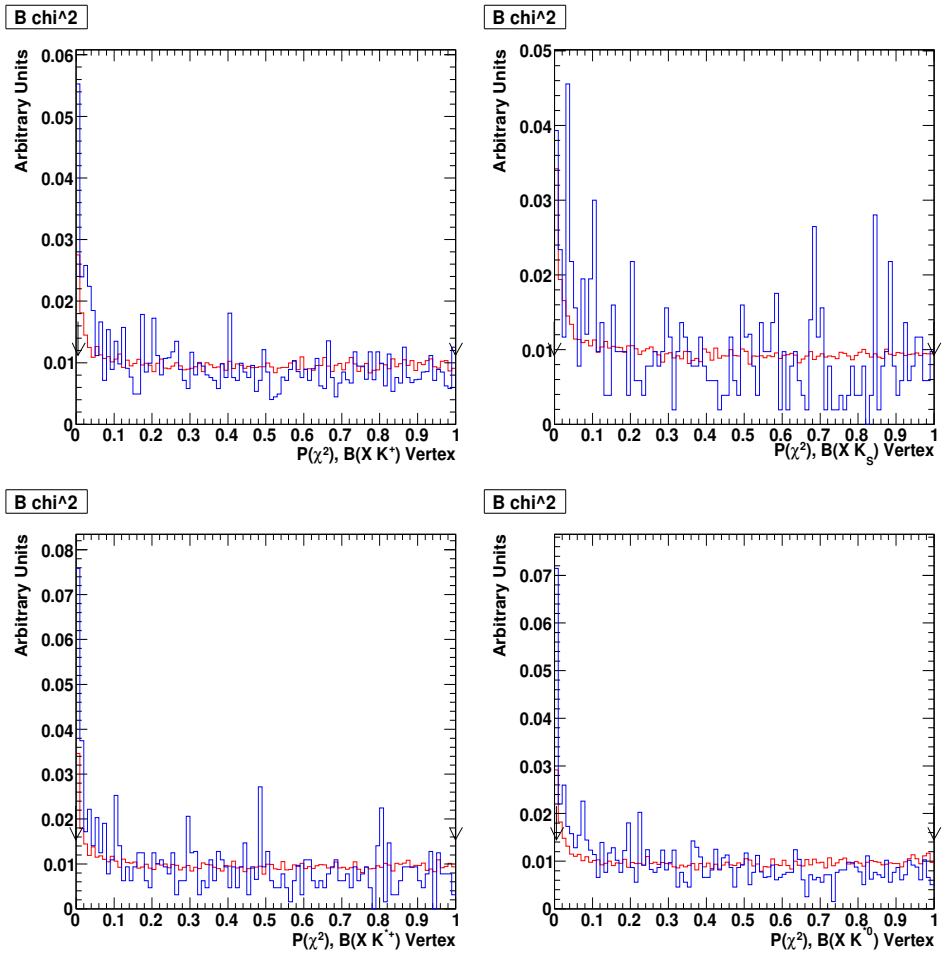

Figure 4.7: Optimized B vertex probability χ^2 values for the $X(3872) \rightarrow J/\psi\,\gamma$ modes. Signal modes are represented in red; background modes are represented in blue. Arrows represent the optimized values of the selection cuts.

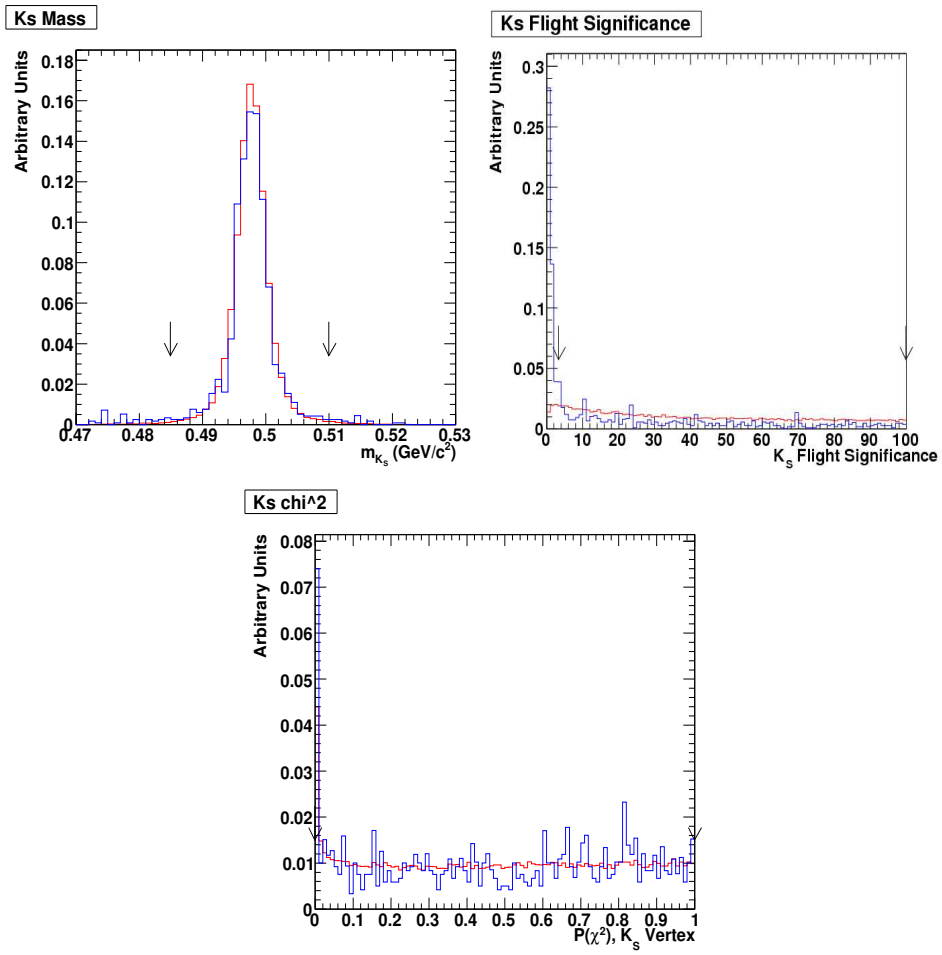

Figure 4.8: Optimized K_s cuts for the $X(3872) \rightarrow J/\psi\gamma$ modes. Signal modes are represented in red; background modes are represented in blue. Arrows represent the optimized values of the selection cuts.

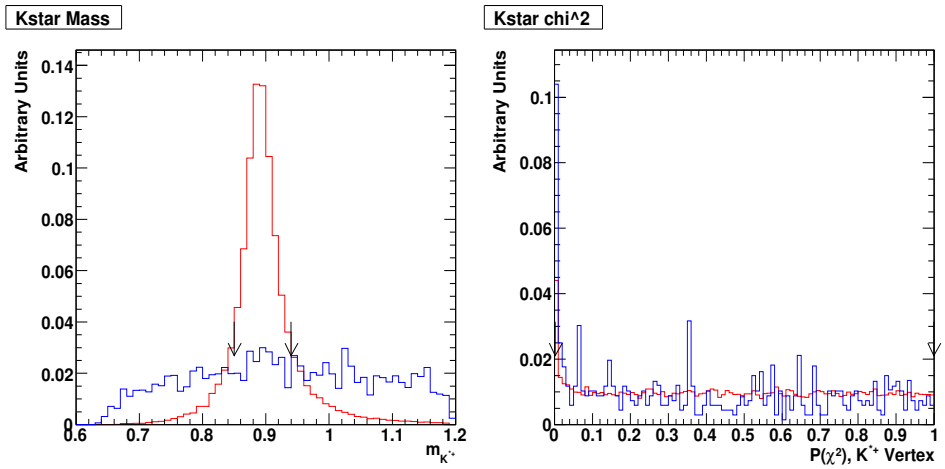

Figure 4.9: Optimized K^{*+} cuts for the $X(3872) \to J/\psi\gamma$ modes. Signal modes are represented in red; background modes are represented in blue. Arrows represent the optimized values of the selection cuts. In the final selection, the full $m_{K^{*+}}$ range shown here is used.

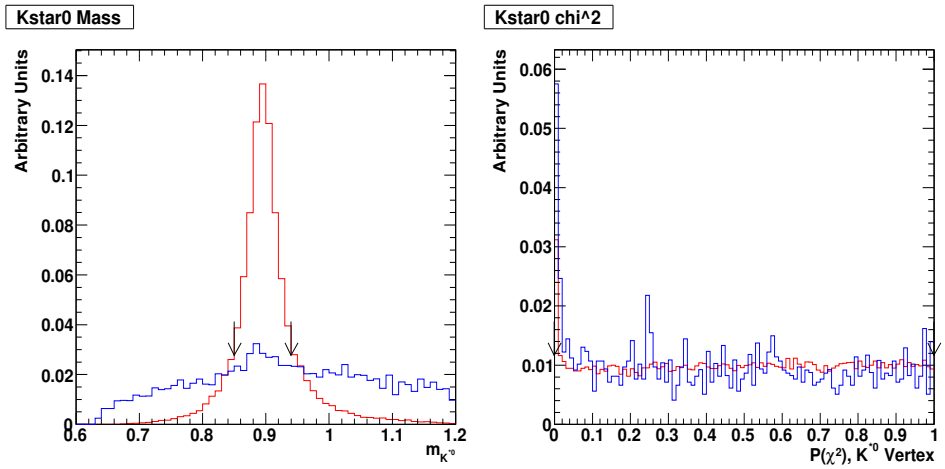

Figure 4.10: Optimized K^{*0} cuts for the $X(3872) \to J/\psi\gamma$ modes. Signal modes are represented in red; background modes are represented in blue. Arrows represent the optimized values of the selection cuts. In the final selection, the full $m_{K_0^*}$ range shown here is used.

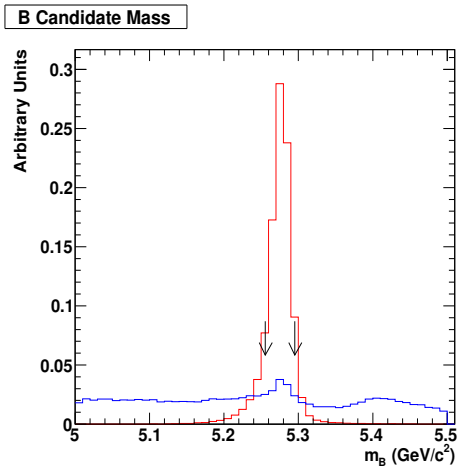

Figure 4.11: Optimized B mass for the $X(3872) \to \psi(2S)\gamma$ modes. Signal modes are represented in red; background modes are represented in blue. Arrows represent the optimized values of the selection cuts.

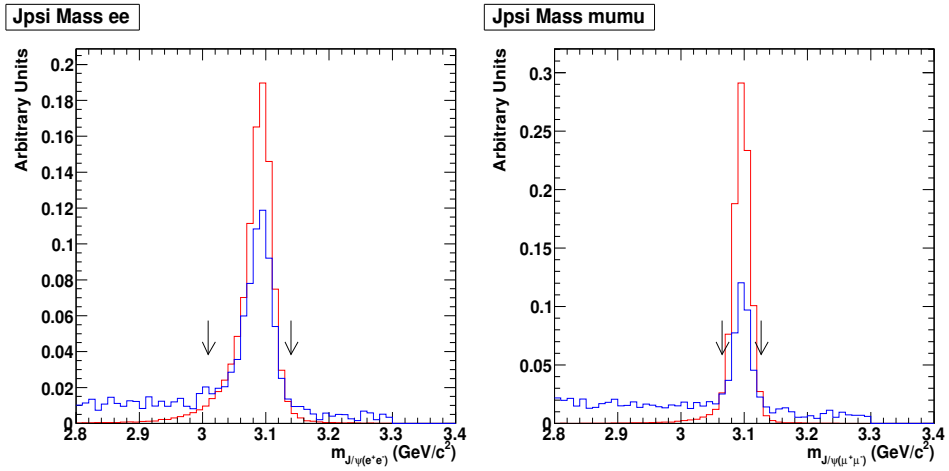

Figure 4.12: Optimized J/ψ mass for the $\psi(2S) \to J/\psi\pi^+\pi^-$ modes. Signal modes are represented in red; background modes are represented in blue. Arrows represent the optimized values of the selection cuts.

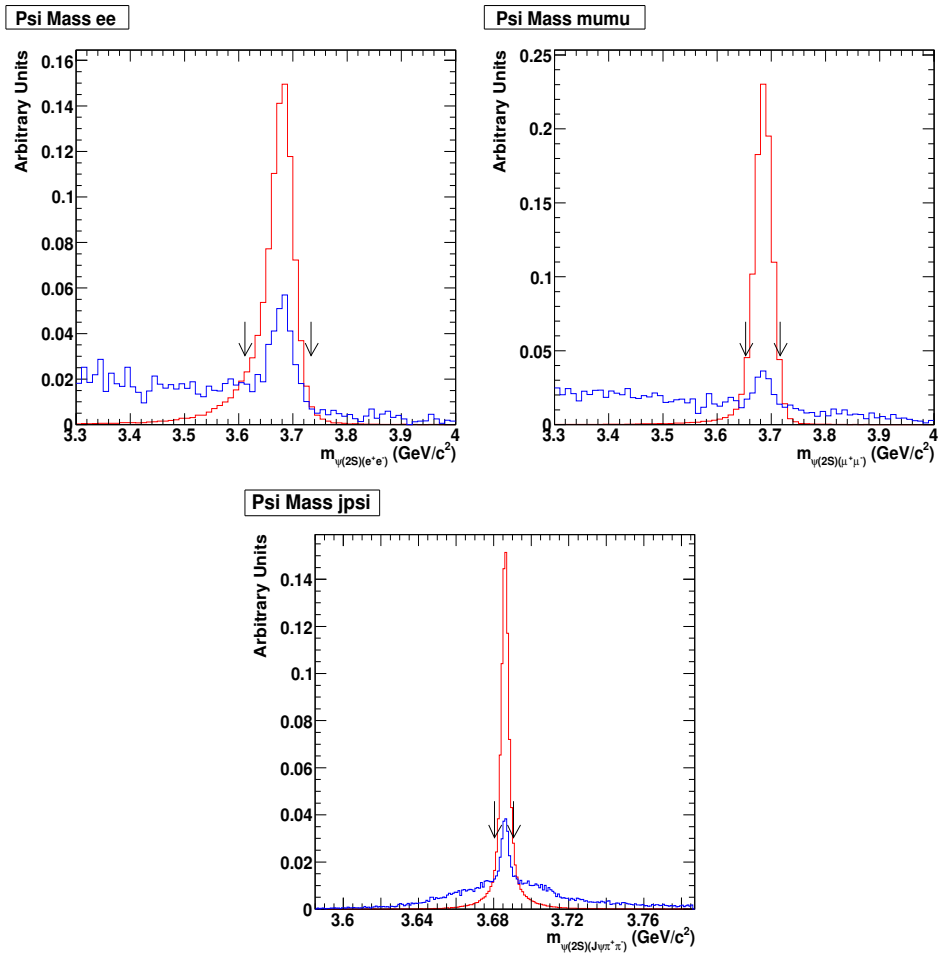

Figure 4.13: Optimized $\psi(2S)$ mass for the $X(3872) \rightarrow \psi(2S)\gamma$ modes. Signal modes are represented in red; background modes are represented in blue. Arrows represent the optimized values of the selection cuts.

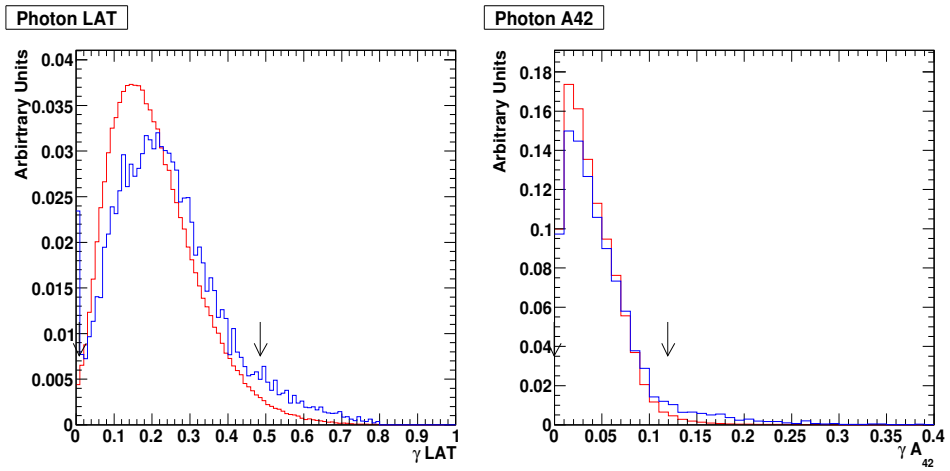

Figure 4.14: Optimized γ LAT and γA_{42} for the $X(3872) \rightarrow \psi(2S)\gamma$ modes. Signal modes are represented in red; background modes are represented in blue. Arrows represent the optimized values of the selection cuts.

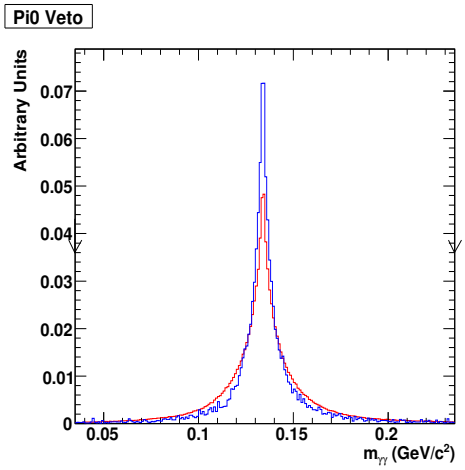

Figure 4.15: Optimized π^0 veto for the $X(3872) \rightarrow \psi(2S)\gamma$ modes. The invariant mass $m_{\gamma\gamma}$ closest to m_{π^0} is plotted. Signal modes are represented in red; background modes are represented in blue. Arrows represent the optimized values of the selection cuts.

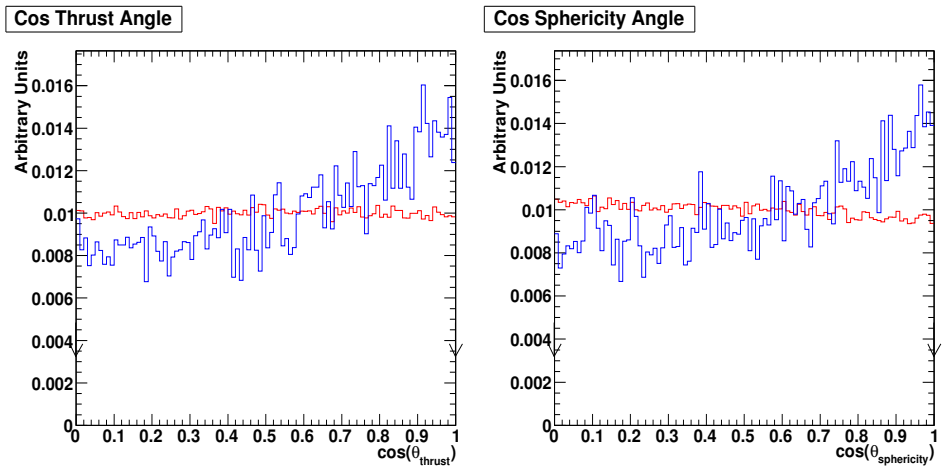

Figure 4.16: Optimized $\cos\theta_{thrust}$ and $\cos\theta_{sphericity}$ for the $X(3872) \rightarrow \psi(2S)\gamma$ modes. Signal modes are represented in red; background modes are represented in blue. Arrows represent the optimized values of the selection cuts.

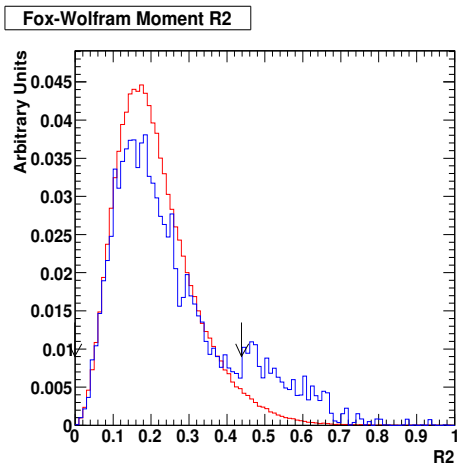

Figure 4.17: Optimized $R2$ for the $X(3872) \rightarrow \psi(2S)\gamma$ modes. Signal modes are represented in red; background modes are represented in blue. Arrows represent the optimized values of the selection cuts.

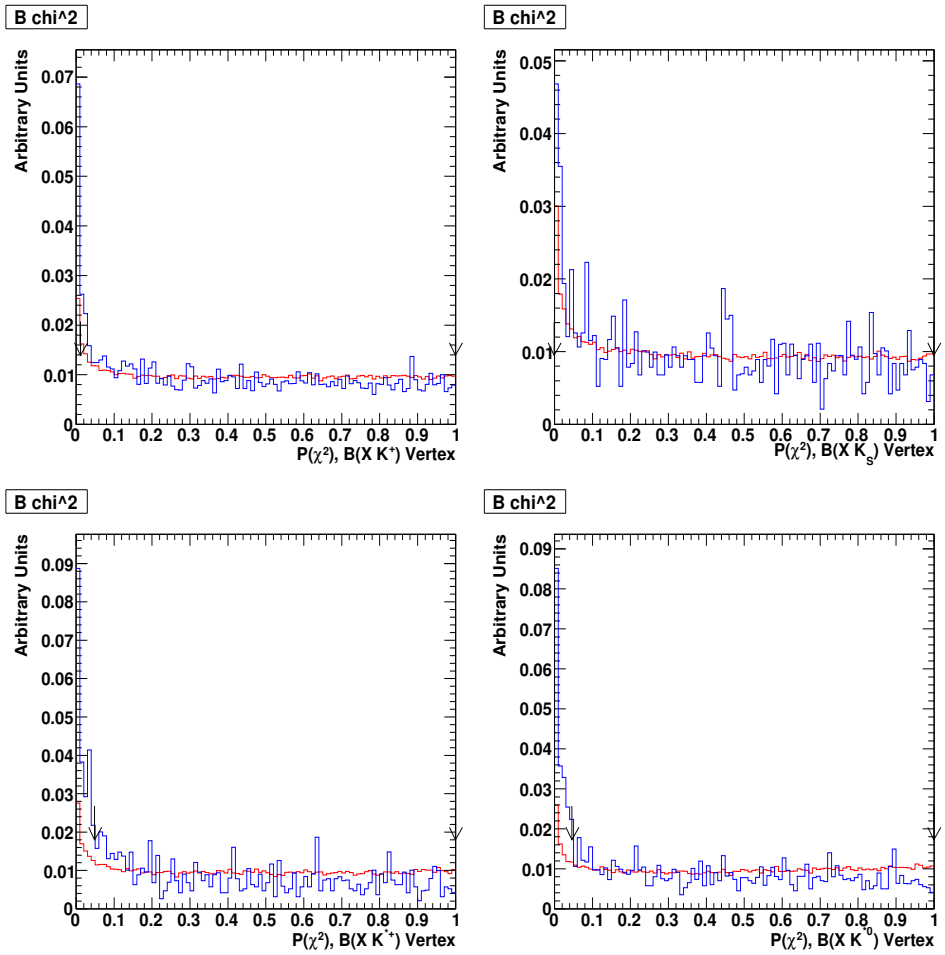

Figure 4.18: Optimized B vertex probability χ^2 values for the $X(3872) \rightarrow \psi(2S)\gamma$ modes. Signal modes are represented in red; background modes are represented in blue. Arrows represent the optimized values of the selection cuts.

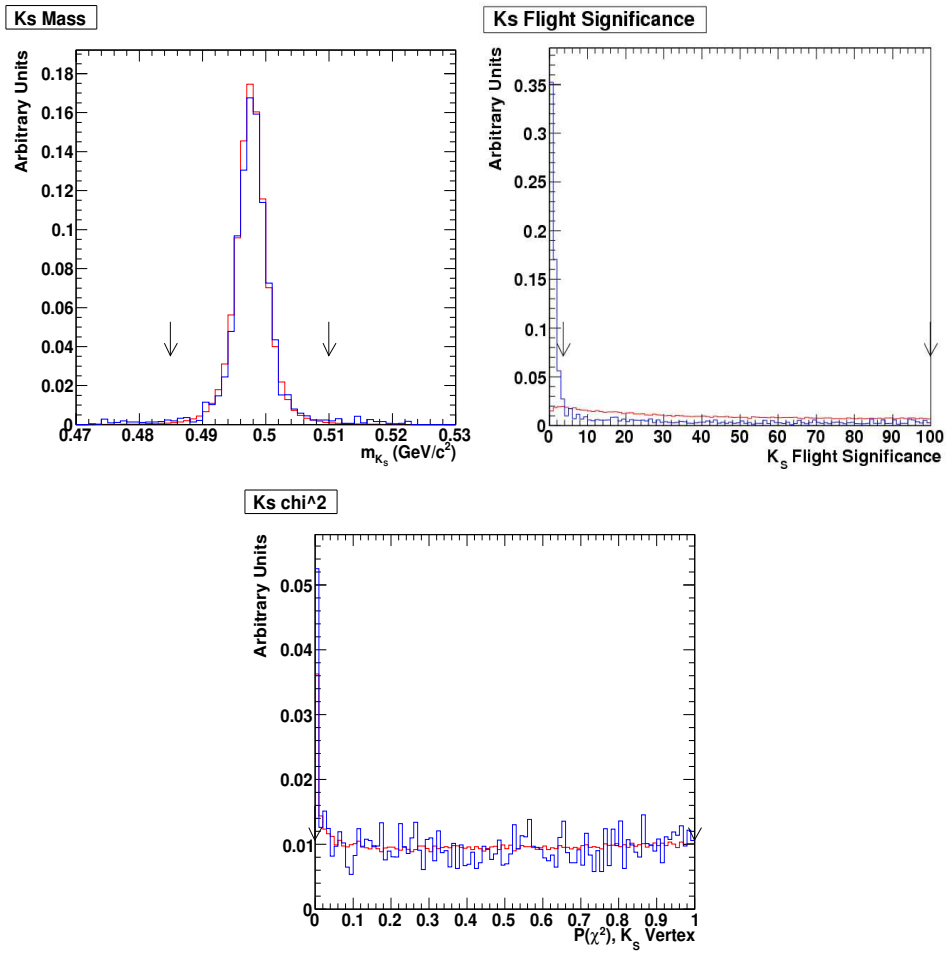

Figure 4.19: Optimized K_s cuts for the $X(3872) \rightarrow \psi(2S)\gamma$ modes. Signal modes are represented in red; background modes are represented in blue. Arrows represent the optimized values of the selection cuts.

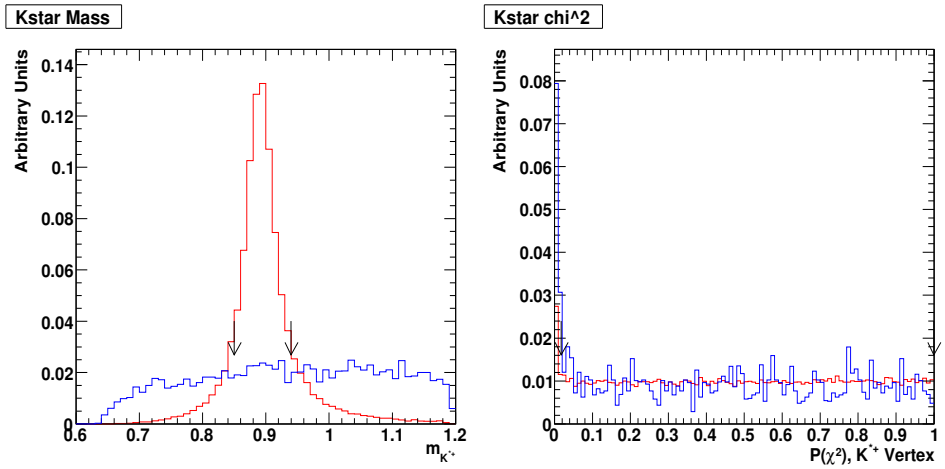

Figure 4.20: Optimized K^{*+} cuts for the $X(3872) \to \psi(2S)\gamma$ modes. Signal modes are represented in red; background modes are represented in blue. Arrows represent the optimized values of the selection cuts. In the final selection, the full $m_{K^{*+}}$ range shown here is used.

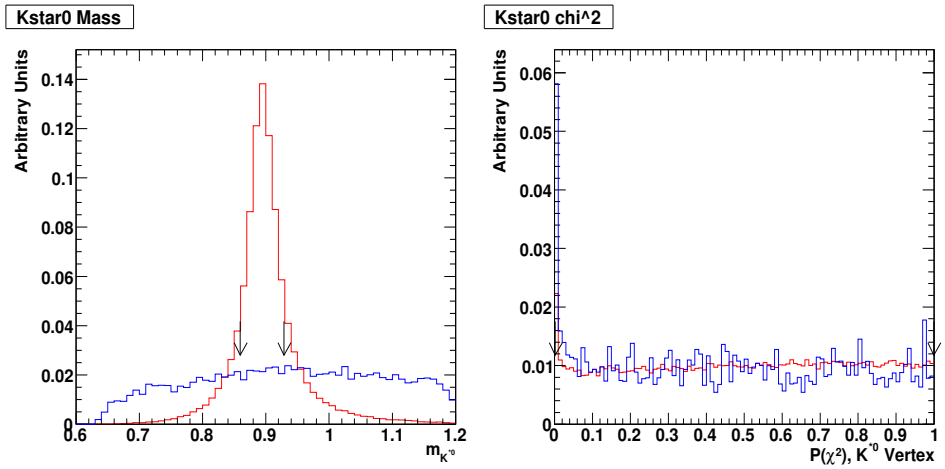

Figure 4.21: Optimized K^{*0} cuts for the $X(3872) \to \psi(2S)\gamma$ modes. Signal modes are represented in red; background modes are represented in blue. Arrows represent the optimized values of the selection cuts. In the final selection, the full $m_{K^{*0}}$ range shown here is used.

4.4.3 Multiple Candidate Selection

In some events there is more than one way to reconstruct the desired final state (due to reconstruction uncertainties and particle misidentification, for example). As in the optimization procedure, only the candidate with the value of m_B closest to the true B mass is retained. Table 4.3 lists the average number of B candidates per event versus decay mode, determined from signal Monte Carlo. This is the number of candidates per event that pass all of the optimized cuts described in Section 4.4.2.

Table 4.3: Average number of B candidates per event.

Decay Mode	Cand./Evt. (MC)
$X(J/\psi\gamma)K^{\pm}$	1.006
$X(J/\psi\gamma)K^0_S$	1.010
$X(J/\psi\gamma)K^{*\pm}$	1.170
$X(J/\psi\gamma)K^{*0}$	1.098
$X(\psi(2S)\gamma)K^{\pm}$	1.428
$X(\psi(2S)\gamma)K^0_S$	1.426
$X(\psi(2S)\gamma)K^{*\pm}$	1.781
$X(\psi(2S)\gamma)K^{*0}$	1.621
$\chi_{c1}(J/\psi\gamma)K^{\pm}$	1.023
$\chi_{c1}(J/\psi\gamma)K^0_S$	1.023
$\chi_{c1}(J/\psi\gamma)K^{*\pm}$	1.143
$\chi_{c1}(J/\psi\gamma)K^{*0}$	1.087

4.4.4 Event Selection Efficiency

The efficiency of event selection is the number of signal events reconstructed and passing the optimized cuts, divided by the total number of events generated in Monte Carlo. For the purposes of this analysis, two sets of Monte Carlo events are considered: those with truth-matching (i.e.: all reconstructed charged particles in the final state correspond to those generated in the MC), and those that do not require this condition. The efficiency for each signal mode based on the MC is summarized in Table 4.4. As

a general comment, the efficiency decreases as the number of final state particles increases. Furthermore, the noticeable drop in the efficiency for truth-matching seen for the $\psi(2S)\gamma$ signal modes is due to the fact that it is common to misidentify a pion in $\psi(2S) \to J/\psi\,\pi^+\pi^-$ decay or the low-energy photon or by selecting an incorrect π or γ from the rest of the event.

Table 4.4: Summary of the reconstruction and event selection efficiency (ϵ) for signal MC, without and with requirements on truth matching.

$X(3872)$ Decay	Events Generated	Pass cuts/reco	$\epsilon(\%)$	Pass cuts/ reco/truth	$\epsilon(\%)$
J/ψ					
$K^{\pm}$	195000	28469	14.6	24274	12.4
K^0_S	391202	43554	11.1	37051	9.5
$K^{*\pm}$	394183	31280	7.9	25118	6.4
K^{*0}	396000	45629	11.5	37541	9.5
$\psi(2S) \to \ell^+\ell^-$					
$K^{\pm}$	363324	83870	23.1	60194	16.6
K^0_S	378160	67303	17.8	49605	13.1
$K^{*\pm}$	379050	42277	11.2	29249	7.7
K^{*0}	406486	70216	17.3	50945	12.5
$\psi(2S) \to J/\psi\,\pi^+\pi^-$					
$K^{\pm}$	750676	87656	11.7	48019	6.4
K^0_S	780317	69471	8.9	42935	5.5
$K^{*\pm}$	782425	42508	5.4	25204	3.2
K^{*0}	838514	71874	8.6	44668	5.3
$\psi(2S) \to$all					
$K^{\pm}$	1114000	171526	15.4	108213	9.7
K^0_S	1158477	136774	11.8	92540	8.0
$K^{*\pm}$	1161475	84785	7.3	54453	4.7
K^{*0}	1245000	142090	11.4	95613	7.7

The expected number and composition of background events can be seen in Figure 4.22 and Figure 4.23 for $X(3872) \to J/\psi(2S)\gamma$ and $X(3872) \to \psi(2S)\gamma$ events, respectively, and for $\chi_{c1} \to J/\psi\gamma$ events in Figure 4.24. These plots represent the weighted MC background events remaining after the selection cuts have been applied. They are overwhelmingly from B^+B^-

and $B^0\overline{B}^0$ decays; there is little to no contribution from the $q\overline{q}$ and $\tau\tau$ MC modes.

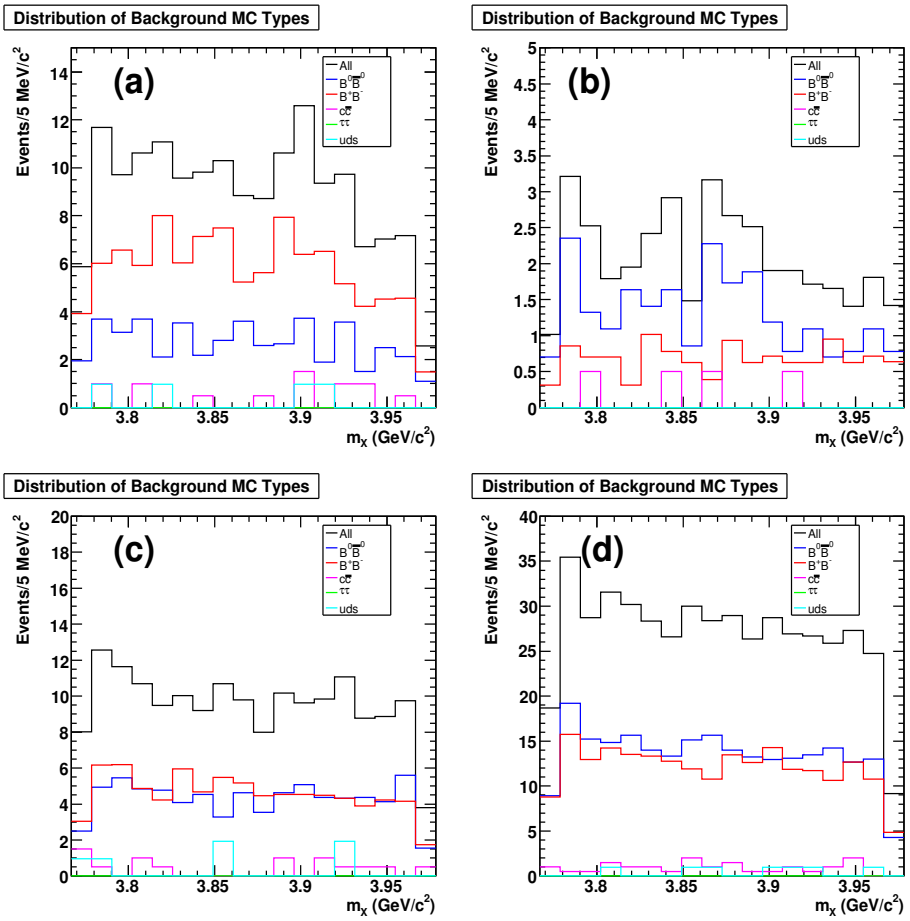

Figure 4.22: m_X distribution for MC background events passing all of the selection cuts for $X(3872) \to J/\psi\gamma$ decays for (a) $B^{\pm} \to X(3872)K^{\pm}$, (b) $B^0 \to X(3872)K^0_s$, (c) $B^{\pm} \to X(3872)K^{*\pm}$, and (d) $B^0 \to X(3872)K^{*0}$.

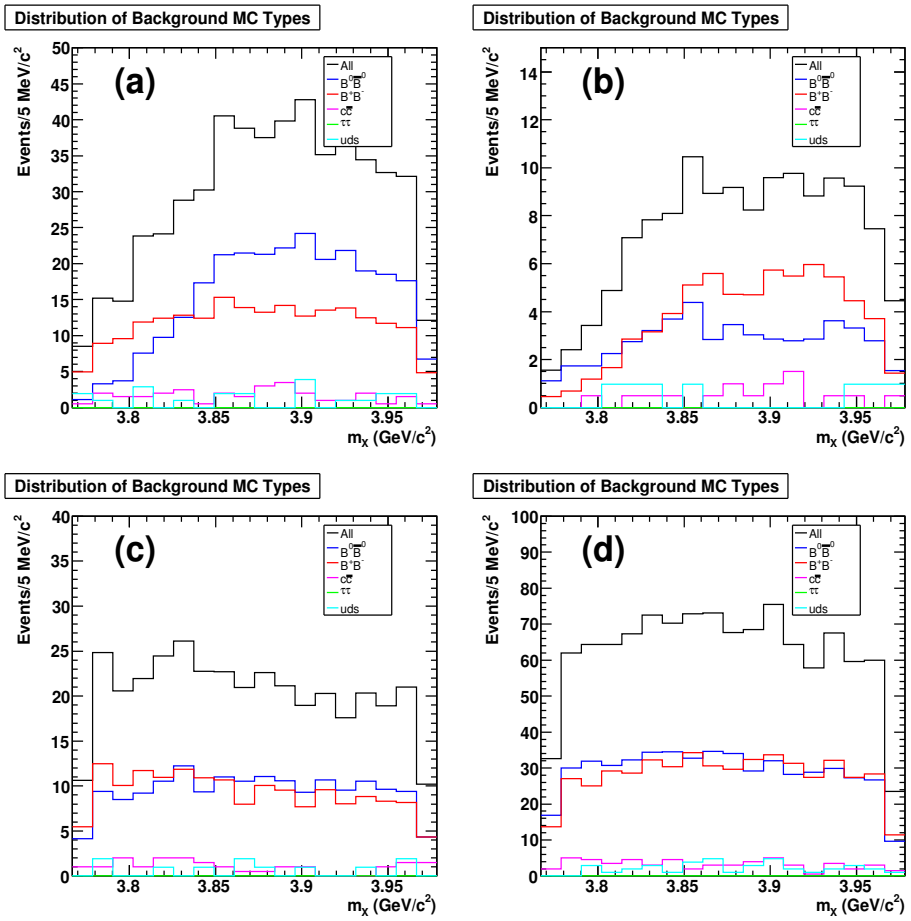

Figure 4.23: m_X distribution for MC background events passing all of the selection cuts for $X(3872) \to \psi(2S)\gamma$ decays for (a) $B^\pm \to X(3872)K^\pm$, (b) $B^0 \to X(3872)K^0_s$, (c) $B^\pm \to X(3872)K^{*\pm}$, and (d) $B^0 \to X(3872)K^{*0}$.

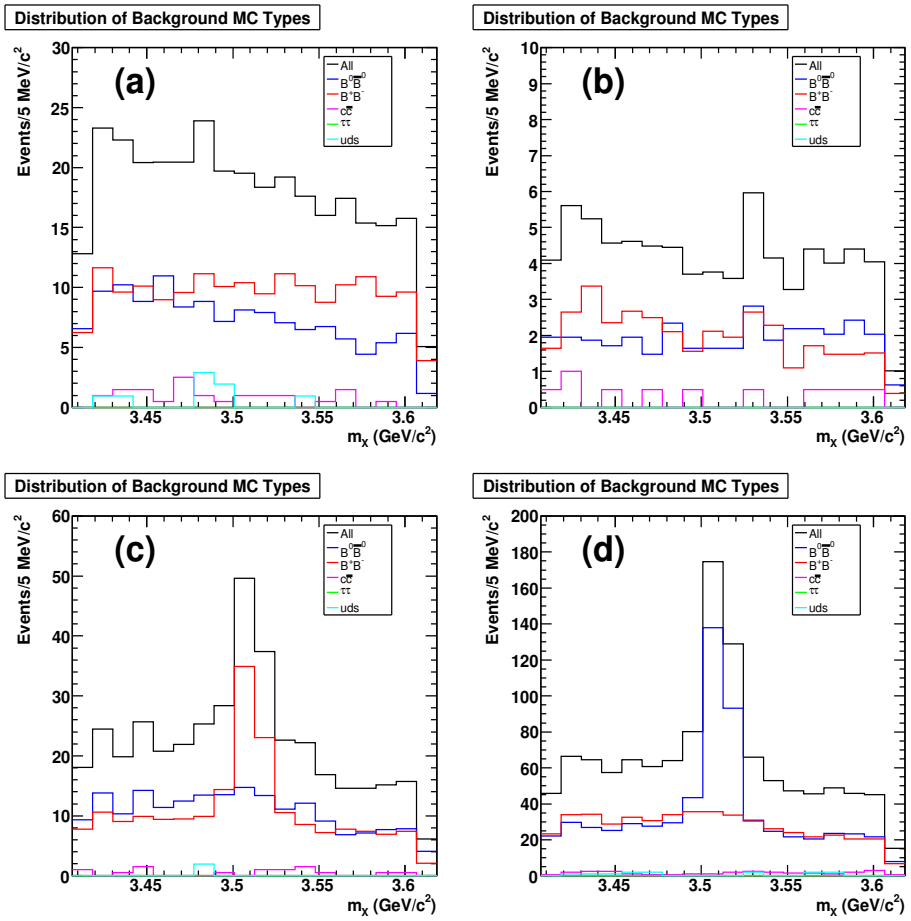

Figure 4.24: m_X distribution for MC background events passing all of the selection cuts for $\chi_{c1} \to J/\psi\gamma$ decays for (a) $B^\pm \to \chi_{c1}K^\pm$, (b) $B^0 \to \chi_{c1}K^0_s$, (c) $B^\pm \to \chi_{c1}K^{*\pm}$, and (d) $B^0 \to \chi_{c1}K^{*0}$. The peaks evident in (c) and (d) are from background events due to non-resonant $B \to \chi_{c1}K\pi$ decays (ie: events where the $K\pi$ final state does not come from a K^*).

Chapter 5

Analysis Methodology

This chapter contains a detailed description of the analysis technique. It includes tests of this procedure on simulated data sets for the extraction of $X(3872)$ events, as well as the method for extracting the $\chi_{c1,2}$ signal modes to be used as further verification of the signal extraction strategy.

5.1 Signal Extraction Procedure

This section describes how the analysis of $B \to c\bar{c}\gamma K^{(*)}$ will be performed. The signal extraction is based on an unbinned extended maximum likelihood (UML) fit to the kinematic variables m_{miss} and m_{K^*} (if applicable), followed by a fit to the ${}_s$Plot [80] projection of m_X. The ${}_s$Plot method, described in Section 5.1.7, is chosen over a conventional 2(3)-D UML fit to improve the visual presentation of the fit, and for the separation of signal types and the search for new bumps. The parametrization of the probability density functions (PDFs) of the relevant variables, m_{miss}, m_{K^*} and m_X, for each of the expected event types (signal, peaking background, non-peaking background) is performed by fitting the PDF shape to MC samples.

5.1.1 Probability Density Functions

From a signal extraction standpoint, each event is characterized by two important observables: m_{miss} and m_{K^*} (if applicable). For m_{miss} and m_{K^*}, the characteristic PDFs are derived for signal and background separately. The probability of observing a total of N events, some of which are signal

and the others background, is

$$\mathcal{L} = \prod_{i=1}^{N} \left[\alpha_{sig} \mathcal{F}_i^{sig}(m_{miss}, m_{K^*}) + \alpha_{bkd} \mathcal{F}_i^{bkd}(m_{miss}, m_{K^*}) \right] \tag{5.1}$$

where $\mathcal{F}$ represents the PDFs, and α_{sig} and α_{bkd} are the number of events for signal and background, respectively. For ease of computation, rather than maximizing Equation 5.1, it is customary to minimize the negative log likelihood:

$$\ln(\mathcal{L}) = -2 \sum_{i=1}^{N} \ln \left(\alpha_{sig} \mathcal{F}^{sig} + \alpha_{bkd} \mathcal{F}^{bkd} \right) \tag{5.2}$$

In practice, the minimization is performed on the extended likelihood function, defined as

$$\mathcal{L}_E = \frac{\exp^{-\phi} \phi^N}{N!} \mathcal{L} \tag{5.3}$$

which includes a Poisson statistics factor to account for the probability of measuring N events from a distribution of mean ϕ. This additional factor does not change the values of α, but it converts the uncertainty on the fit parameters to include an uncertainty from the Poisson distribution. The extended maximum likelihood equation is now

$$\ln(\mathcal{L}_E) = 2 \left[\alpha_{sig} + \alpha_{bkd} + \ln(N!) - \sum_{i=1}^{N} \ln \left(\alpha_{sig} \mathcal{F}^{sig} + \alpha_{bkd} \mathcal{F}^{bkd} \right) \right] \tag{5.4}$$

This is the equation which is minimized to determine the number of events of each type in the dataset.

5.1.2 Choice of PDF shapes

The PDFs were selected for a balance of ease of use and based on some physical relation to the variable being plotted[18]. To obtain a clean definition for the signal modes, truth-matching was required for all of the final state charged particles used to reconstruct the event, and the range of the fits

[18] This is a simplification from an initial attempt to determine the shape of the PDFs by comparing the χ^2 probabilities of fits to several different functional forms.

were truncated to $m_{miss} \pm 25\,\mathrm{MeV}/c^2$ and $m_X \pm 25\,\mathrm{MeV}/c^2$ to improve the χ^2 and the convergence of the fits. Note that the signal MC reconstruction is very clean, so that there are essentially no events falling outside of this range. For background shape PDFs, the cuts were applied as defined in Section 4.2.

5.1.3 PDF Parametrization, m_{miss}

For the signal modes, the m_{miss} PDF is described by the Crystal Ball function [81], defined as:

$$f(x;\alpha,n,m_0,\sigma) = N \cdot \begin{cases} e^{\frac{-(x-m_0)^2}{2\sigma^2}}, & \text{for } \frac{x-m_0}{\sigma} > -\alpha \\ A \cdot (B - \frac{x-m_0}{\sigma})^{-n}, & \text{for } \frac{x-m_0}{\sigma} \leq -\alpha \end{cases} \tag{5.5}$$

where

$$\begin{aligned} A &= \left(\frac{n}{|\alpha|}\right)^2 \cdot exp\left(-\frac{|\alpha|^2}{2}\right) \\ B &= \frac{n}{|\alpha|} - |\alpha| \end{aligned} \tag{5.6}$$

This function can be thought of as a Gaussian core with a power-law low-end tail. The parameters m_0 and σ can be thought of as the Gaussian mean and width, with n representing the power of the exponential tail, and α the number of Gaussian standard deviations from the mean where the low-side exponential tail begins. N is a normalization factor.

All of the parameters are determined by fitting to MC samples. In order for the fit to converge, an iterative approach was used by finding an initial value for n, fixing it while refitting the other parameters, then fixing all other parameters and refitting for n. The fits to signal MC for $X(3872) \to J/\psi\gamma$ and $X(3872) \to \psi(2S)\gamma$ are shown in Figures 5.1 and 5.2, respectively, with the numerical results summarized in Table 5.1.

For the background, the peaking component was represented by using the Crystal Ball shape with parameters fixed to values from the signal fit, plus an ARGUS function [82] used to model the non-peaking background component. The ARGUS function, used widely in $B\overline{B}$ physics analyses, is slightly curved over a large range of data points and terminates smoothly

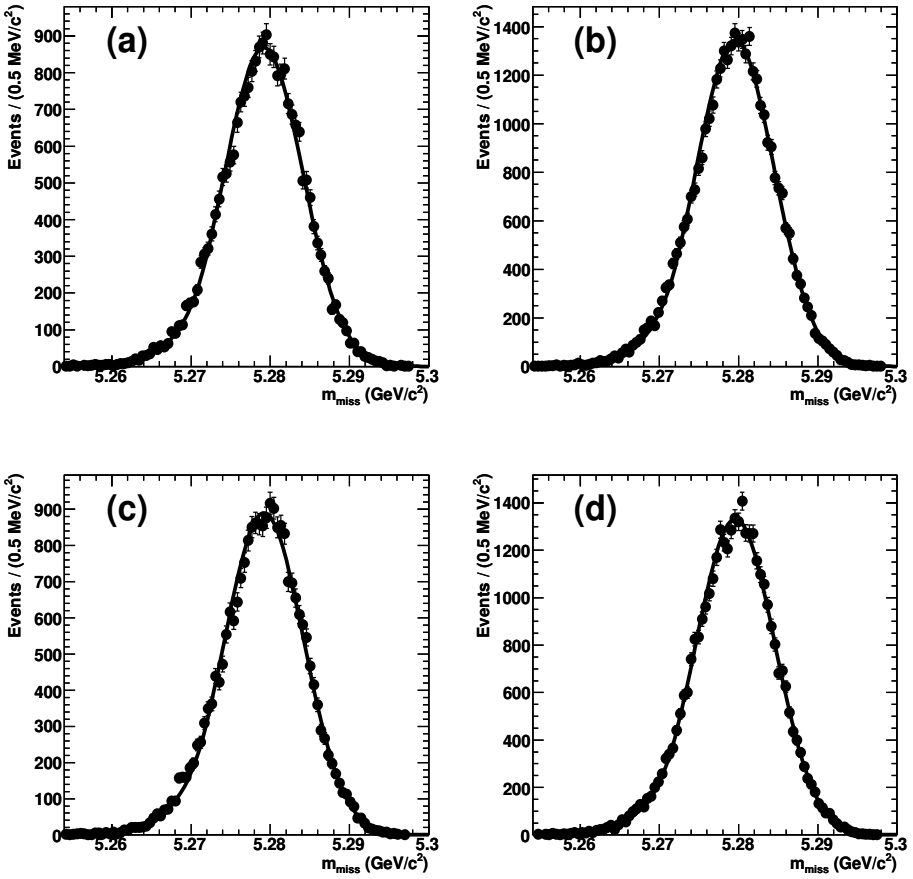

Figure 5.1: m_{miss} PDF fits for the J/ψ signal modes, (a) $B^{\pm} \to X(3872)K^{\pm}$, (b) $B^0 \to X(3872)K^0_s$, (c) $B^{\pm} \to X(3872)K^{*\pm}$, and (d) $B^0 \to X(3872)K^{*0}$.

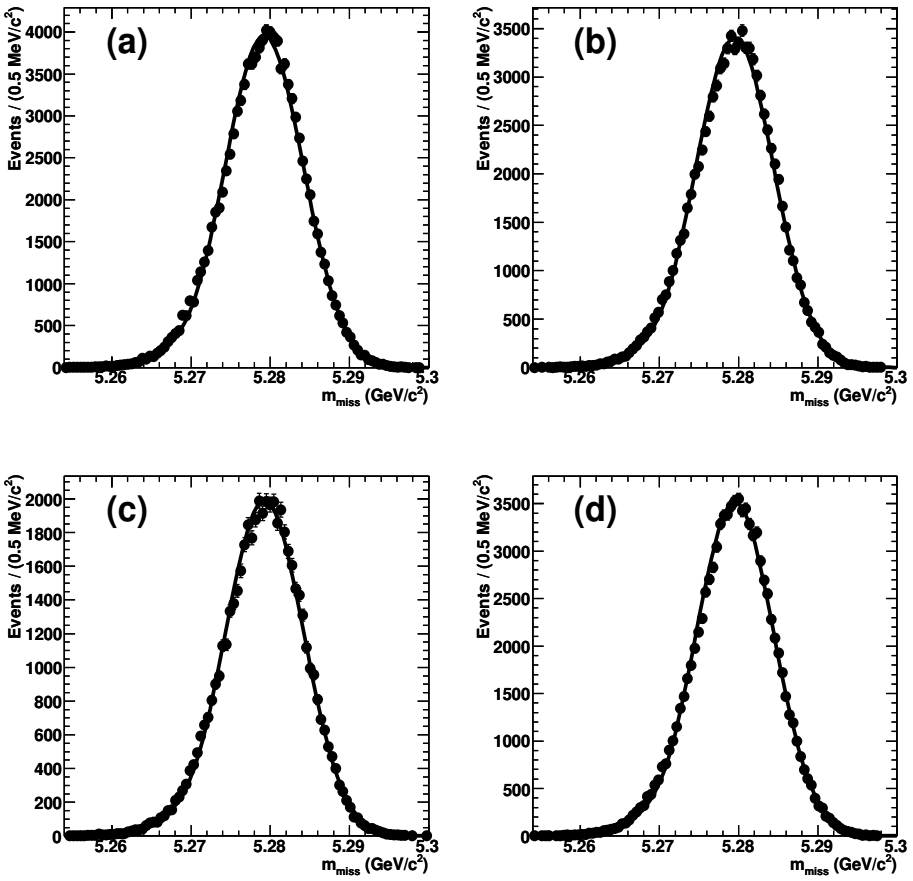

Figure 5.2: m_{miss} PDF fits for the $\psi(2S)$ signal modes, (a) $B^{\pm} \rightarrow X(3872)K^{\pm}$, (b) $B^0 \rightarrow X(3872)K^0_s$, (c) $B^{\pm} \rightarrow X(3872)K^{*\pm}$, and (d) $B^0 \rightarrow X(3872)K^{*0}$.

Table 5.1: Summary of the m_{miss} PDF parameter fit results for the signal modes.

	Crystal Ball Parameters			
Decay Mode	α	m_0 (GeV/c^2)	n	σ (MeV/c^2)
$J/\psi\gamma K^{\pm}$	1.54 ± 0.04	5.27919 ± 0.00004	145 ± 36	4.96 ± 0.03
$J/\psi\gamma K^0_S$	1.54 ± 0.03	5.27956 ± 0.00003	146 ± 29	4.92 ± 0.03
$J/\psi\gamma K^{*\pm}$	1.50 ± 0.04	5.27923 ± 0.00004	140 ± 29	4.99 ± 0.03
$J/\psi\gamma K^{*0}$	1.55 ± 0.03	5.27959 ± 0.00003	142 ± 38	4.98 ± 0.03
$\psi(2S)\gamma K^{\pm}$	1.68 ± 0.02	5.27925 ± 0.00001	155 ± 42	4.94 ± 0.01
$\psi(2S)\gamma K^0_S$	1.72 ± 0.03	5.27951 ± 0.00002	141 ± 46	4.93 ± 0.02
$\psi(2S)\gamma K^{*\pm}$	1.64 ± 0.03	5.27929 ± 0.00002	154 ± 19	4.94 ± 0.02
$\psi(2S)\gamma K^{*0}$	1.64 ± 0.02	5.27953 ± 0.00002	154 ± 21	4.91 ± 0.02

at an endpoint. It is defined as:

$$f(x;c,\chi) = x \cdot \sqrt{1-\left(\frac{x}{c}\right)^2} exp\left\{-\chi \cdot \left(1-\left(\frac{x}{c}\right)^2\right)\right\} \tag{5.7}$$

where χ represents the curvature of the function and c is the endpoint. The fraction of peaking to non-peaking events was fitted to the MC at this stage, but the value is allowed to float in the final fit to data. The results of the PDF fit for the background modes is shown in Figures 5.3 and 5.4, with a summary of the numerical results given in Table 5.2.

Based on the examination of $B\overline{B}$ generic MC events with $5.27 < m_{miss} < 5.29\,\mathrm{GeV}/c^2$, the peaking backgrounds for the $X(3872) \to J/\psi\gamma$ modes are predominantly of the type $B \to J/\psi K$, where the K is some excited kaon ($K^*(890)$, but also any higher resonance, $K_{1,2}$, $K^*(1430)$, etc.), as well as $B \to J/\psi K\pi$. Similarly for the $X(3872) \to \psi(2S)\gamma$ decays, the primary backgrounds come from $B \to \psi(2S)K^*$ and $B \to \psi(2S)K\pi$ non-resonant.

5.1.4 PDF Parametrization, m_X

To parametrize m_X for the signal modes, a double Gaussian shape was chosen for ease of use. The background parametrization for m_X uses a first-order polynomial for all modes except $B^{(+/0)} \to \psi(2S)\gamma K^{(+/0)}$. In

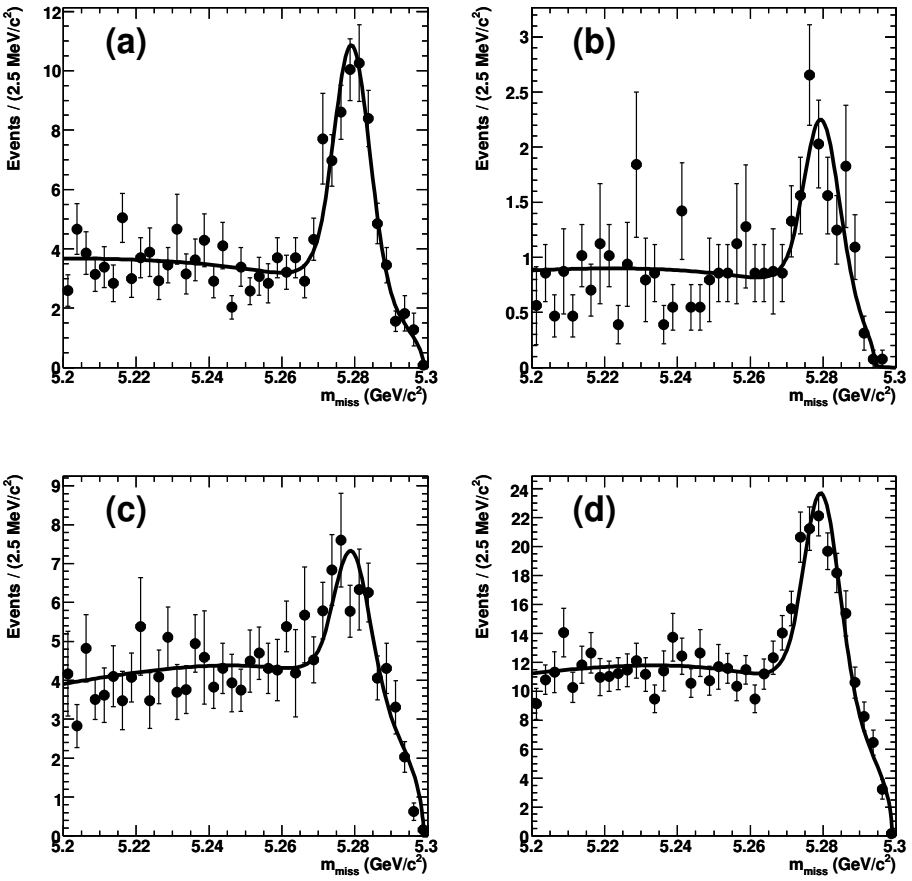

Figure 5.3: m_{miss} PDF fits for the J/ψ background modes, (a) $B^{\pm} \rightarrow X(3872)K^{\pm}$, (b) $B^0 \rightarrow X(3872)K^0_s$, (c) $B^{\pm} \rightarrow X(3872)K^{*\pm}$, and (d) $B^0 \rightarrow X(3872)K^{*0}$.

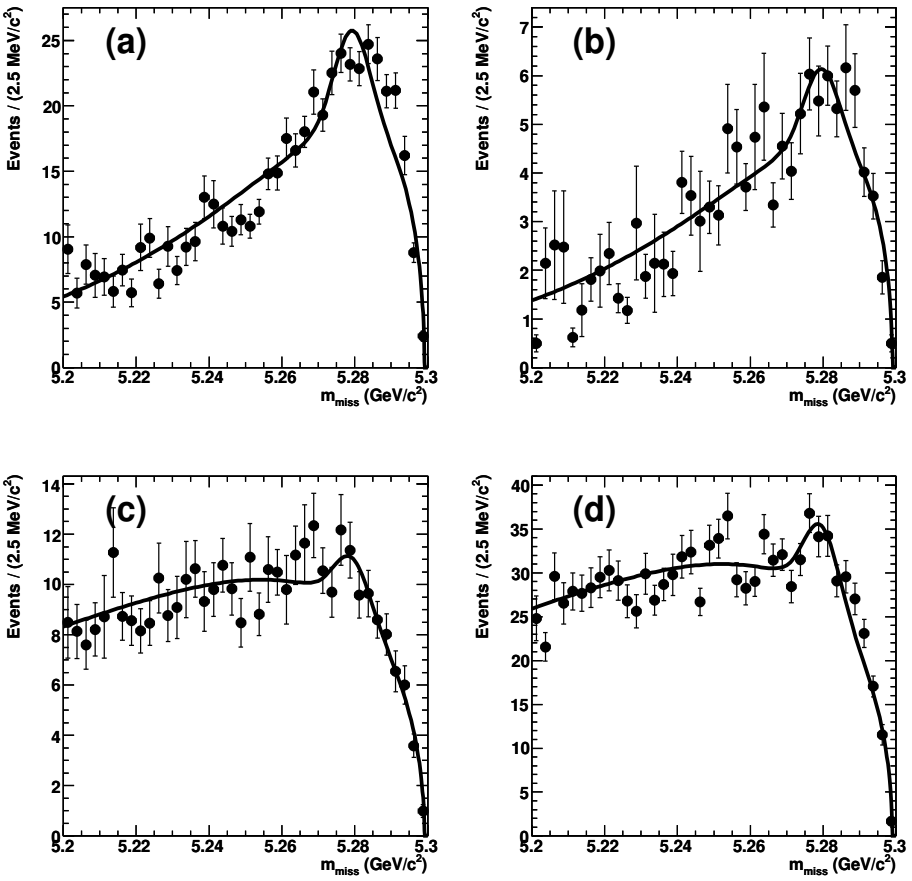

Figure 5.4: m_{miss} PDF fits for the $\psi(2S)$ background modes, (a) $B^{\pm} \to X(3872)K^{\pm}$, (b) $B^0 \to X(3872)K^0_s$, (c) $B^{\pm} \to X(3872)K^{*\pm}$, and (d) $B^0 \to X(3872)K^{*0}$.

Table 5.2: Summary of the m_{miss} PDF parameter fit results for the background modes.

	ARGUS Parameters		
Decay Mode	χ	c (GeV/c^2)	Peaking Fraction
$J/\psi\gamma K^{\pm}$	$-12.86^{+11.98}_{-11.60}$	5.299 ± 0.001	0.263 ± 0.057
$J/\psi\gamma K^0_S$	-17.98 ± 9.33	5.294 ± 0.003	$0.220^{+0.106}_{-0.112}$
$J/\psi\gamma K^{*\pm}$	$-24.36^{+10.13}_{-9.8}$	5.2989 ± 0.0005	0.109 ± 0.050
$J/\psi\gamma K^{*0}$	$-19.84^{+6.27}_{-6.20}$	5.2988 ± 0.0003	0.153 ± 0.030
$\psi(2S)\gamma K^{\pm}$	$-67.51^{+5.42}_{-5.45}$	5.2991 ± 0.0003	$0.071^{+0.033}_{-0.032}$
$\psi(2S)\gamma K^0_S$	$-66.92^{+10.97}_{-10.78}$	5.2990 ± 0.0005	0.061 ± 0.078
$\psi(2S)\gamma K^{*\pm}$	$-28.94^{+6.39}_{-6.25}$	5.2991 ± 0.0005	0.029 ± 0.038
$\psi(2S)\gamma K^{*0}$	$-27.83^{+3.67}_{-3.64}$	5.2990 ± 0.0003	$0.038^{+0.018}_{-0.017}$

these two decay channels, the m_X distribution for background events is not represented by a simple linear shape. There is a fall-off of the number of events for $m_X < 3.84$ MeV/c^2, related to the cut applied to E_γ.

To describe this background, a linear function multiplied by a Fermi-Dirac (F-D) function was used. The function is described by:

$$N(m_X) = \frac{m \cdot (m_X - 3.772) + 1}{1 + e^{-\frac{m_X - b}{c}}} \tag{5.8}$$

where m represents the slope of the linear part, b represents the point of inflection of the Fermi-Dirac function, and c represents the "steepness" of the Fermi-Dirac function.

The results of the fit for the signal modes are shown in Figures 5.5 and 5.6 for the J/ψ and $\psi(2S)$ signal modes, respectively, and summarized in Table 5.3. The results of the fits for the background modes are found in Figures 5.7 and 5.8 and Table 5.4.

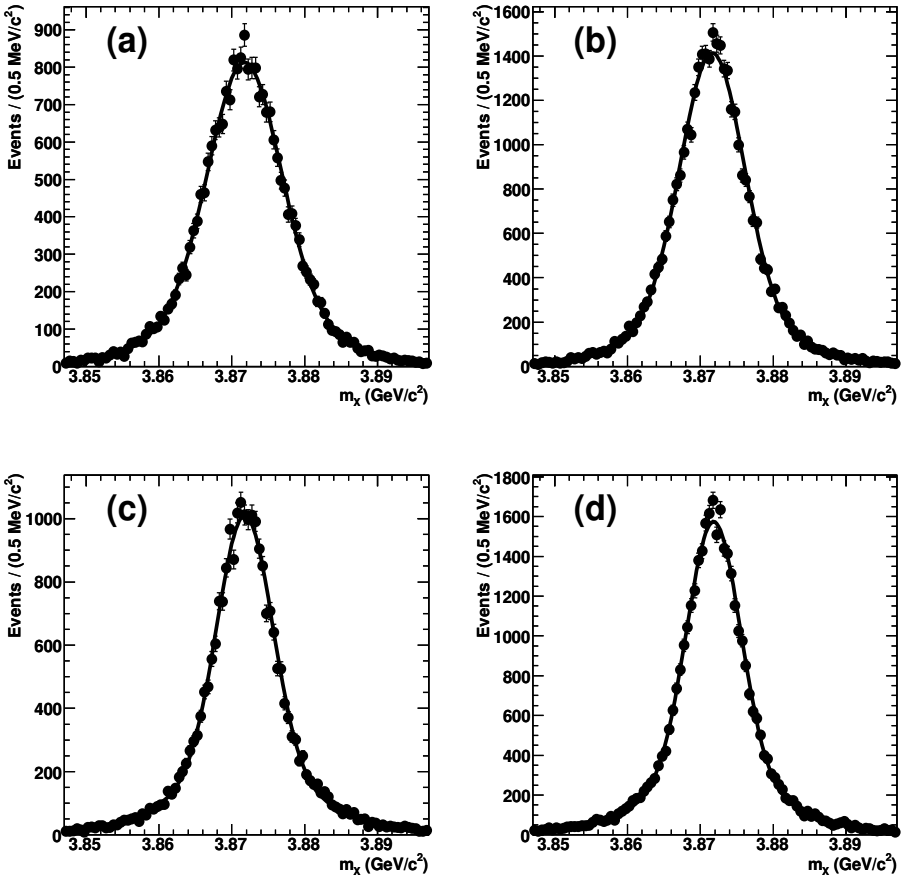

Figure 5.5: m_X PDF fits for the J/ψ signal modes, (a) $B^{\pm} \to X(3872)K^{\pm}$, (b) $B^0 \to X(3872)K^0_s$, (c) $B^{\pm} \to X(3872)K^{*\pm}$, and (d) $B^0 \to X(3872)K^{*0}$.

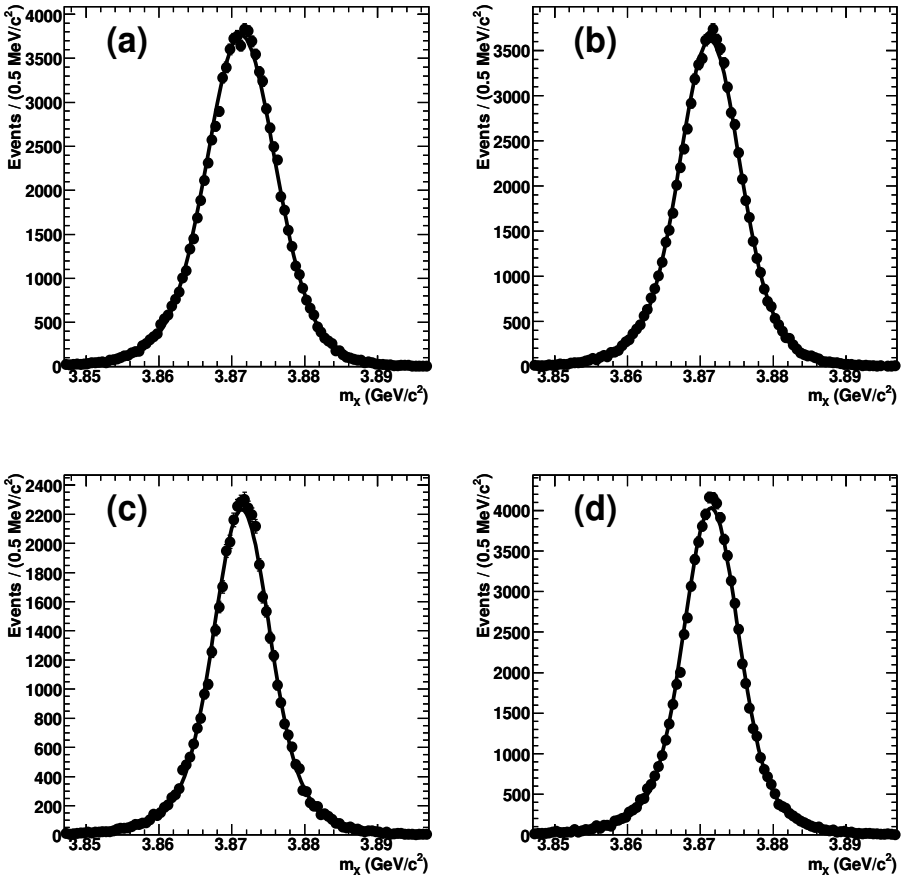

Figure 5.6: m_X PDF fits for the $\psi(2S)$ signal modes, (a) $B^{\pm} \to X(3872)K^{\pm}$, (b) $B^0 \to X(3872)K^0_s$, (c) $B^{\pm} \to X(3872)K^{*\pm}$, and (d) $B^0 \to X(3872)K^{*0}$.

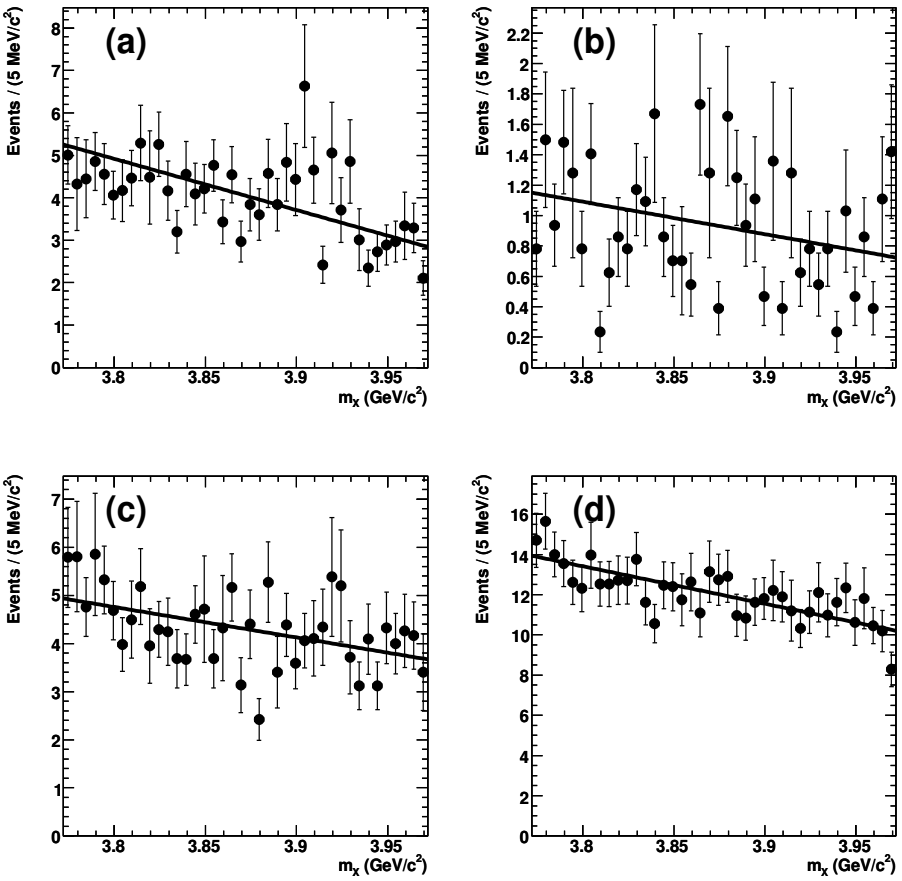

Figure 5.7: m_X PDF fits for the J/ψ background modes, (a) $B^{\pm} \rightarrow X(3872)K^{\pm}$, (b) $B^0 \rightarrow X(3872)K^0_s$, (c) $B^{\pm} \rightarrow X(3872)K^{*\pm}$, and (d) $B^0 \rightarrow X(3872)K^{*0}$.

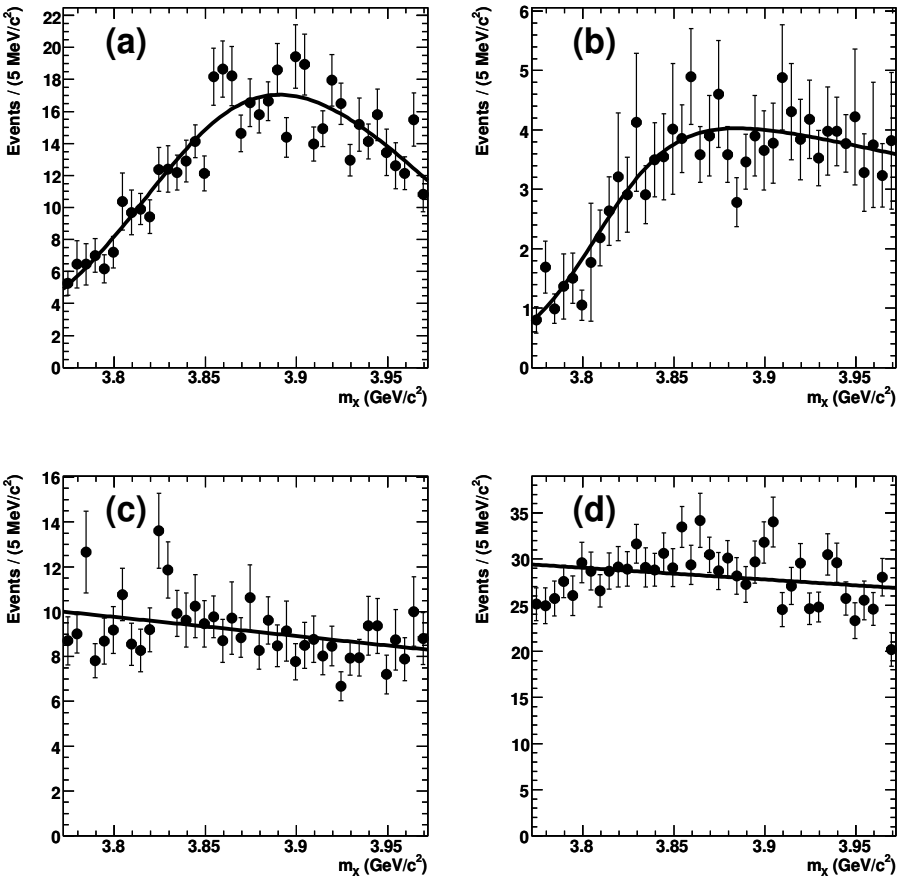

Figure 5.8: m_X PDF fits for the $\psi(2S)$ background modes, (a) $B^{\pm} \rightarrow X(3872)K^{\pm}$, (b) $B^0 \rightarrow X(3872)K^0_s$, (c) $B^{\pm} \rightarrow X(3872)K^{*\pm}$, and (d) $B^0 \rightarrow X(3872)K^{*0}$.

Table 5.3: Summary of the m_X PDF parameter fit results for the signal modes.

	Fit Parameter			
Decay Mode	μ (MeV/c^2)	σ_1 (MeV/c^2)	σ_2 (MeV/c^2)	Core Fraction
$J/\psi\gamma K^{\pm}$	3871.74 ± 0.04	4.93 ± 0.09	$10.48^{+0.37}_{-0.33}$	0.70 ± 0.03
$J/\psi\gamma K^0_S$	3871.63 ± 0.03	4.32 ± 0.06	$10.12^{+0.21}_{-0.23}$	0.71 ± 0.02
$J/\psi\gamma K^{*\pm}$	3871.78 ± 0.03	3.78 ± 0.06	$10.28^{+0.21}_{-0.19}$	0.64 ± 0.01
$J/\psi\gamma K^{*0}$	3871.82 ± 0.03	3.70 ± 0.04	$10.59^{+0.18}_{-0.17}$	0.68 ± 0.01
$\psi(2S)\gamma K^{\pm}$	3871.25 ± 0.02	4.44 ± 0.04	$8.10^{+0.12}_{-0.11}$	0.72 ± 0.02
$\psi(2S)\gamma K^0_S$	3871.30 ± 0.04	3.89 ± 0.04	7.56 ± 0.09	0.70 ± 0.01
$\psi(2S)\gamma K^{*\pm}$	3871.36 ± 0.02	3.66 ± 0.04	7.93 ± 0.11	0.71 ± 0.01
$\psi(2S)\gamma K^{*0}$	3871.47 ± 0.01	3.58 ± 0.03	$8.14^{+0.09}_{-0.08}$	0.73 ± 0.01

5.1.5 PDF Parametrization, m_{K^*}

For the signal modes, a Breit-Wigner function convoluted with a Gaussian[19] was chosen for the m_{K^*} PDF. For background, the same peaking shape was used with the addition of a first-order polynomial. This represents a peaking component (real K^* in the event) plus a combinatoric component. Like the m_{miss} case, the fraction of peaking background was fitted at this stage but allowed to float in the final signal extraction fit. The results of the fits for both the J/ψ signal and background modes are shown in Figure 5.9, and similarly for $\psi(2S)$ in Figure 5.10. The values for the parameters for all of the modes are summarized in Table 5.5.

5.1.6 PDF Correlations

The likelihood fit and PDFs defined in the previous sections rely on the assumption that the variables chosen for the fitting procedure are independent from one another. To investigate the presence of any dependencies, 2-D plots are produced between m_X, m_{miss}, and m_{K^*}, which are shown in Figures 5.11 – 5.14 for the $X(3872)$ signal modes, and Figures 5.15 – 5.18 for the

[19] This total convolved function is referred to here as a Voigtian function.

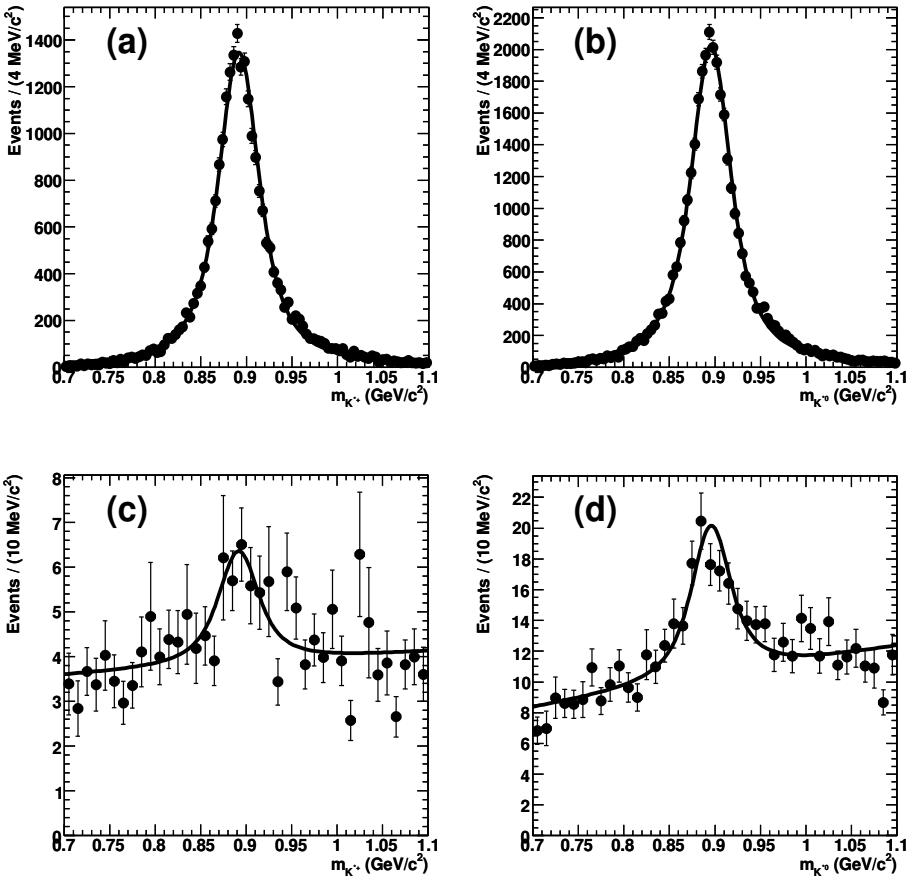

Figure 5.9: m_{K^*} PDF fits for the J/ψ signal and background modes, (a) $B^{\pm} \to X(3872)K^{*\pm}$ signal events, (b) $B^0 \to X(3872)K^{*0}$ signal events, (c) $B^{\pm} \to X(3872)K^{*\pm}$ background events, and (d) $B^0 \to X(3872)K^{*0}$ background events.

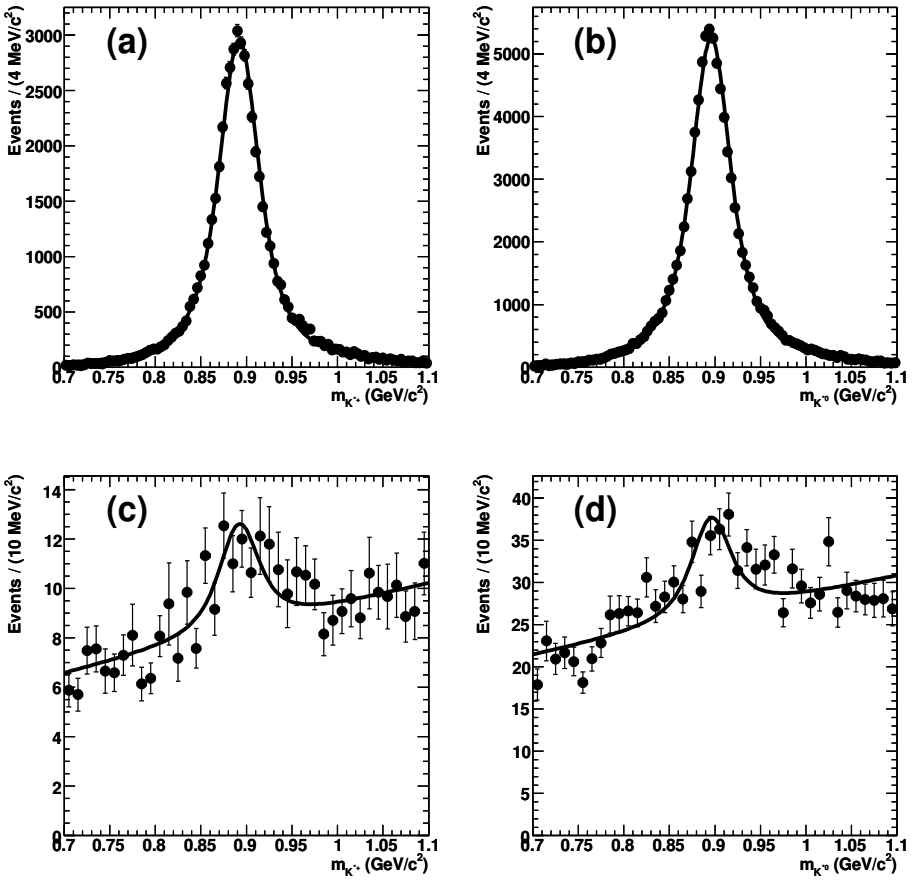

Figure 5.10: m_{K^*} PDF fits for the $\psi(2S)$ signal and background modes, (a) $B^{\pm} \to X(3872)K^{*\pm}$ signal events, (b) $B^0 \to X(3872)K^{*0}$ signal events, (c) $B^{\pm} \to X(3872)K^{*\pm}$ background events, and (d) $B^0 \to X(3872)K^{*0}$ background events.

Table 5.4: Summary of the m_X PDF parameter fit results for the background modes.

	Fit Parameter			
Decay Mode	y-intercept (GeV/c^2)	slope (GeV/c^2)$^{-1}$	F-D b (GeV/c^2)	F-D c (GeV/c^2)$^{-1}$
$J/\psi\gamma K^{\pm}$	47.1 ± 6.7	-11.2 ± 1.2	-	-
$J/\psi\gamma K^0_S$	6.9 ± 2.7	-1.6 ± 0.7	-	-
$J/\psi\gamma K^{*\pm}$	27.0 ± 7.6	-5.9 ± 2.0	-	-
$J/\psi\gamma K^{*0}$	82.1 ± 12.1	-18.2 ± 3.0	-	-
$\psi(2S)\gamma K^{\pm}$	-	-3.3 ± 1.0	3.8 ± 0.03	0.037 ± 0.016
$\psi(2S)\gamma K^0_S$	-	-1.4 ± 3.7	3.8 ± 0.06	0.023 ± 0.011
$\psi(2S)\gamma K^{*\pm}$	40.0 ± 10.8	-8.1 ± 2.8	-	-
$\psi(2S)\gamma K^{*0}$	76.1 ± 20.4	-12.5 ± 5.3	-	-

Table 5.5: Summary of the m_{K^*} PDF parameter fit results.

	Fit Parameter				
Decay Mode	μ (MeV/c^2)	σ (MeV/c^2)	width (GeV/c^2)	Slope (GeV/c^2)$^{-1}$	Peak (%)
$J/\psi\gamma K^{*\pm}$	891.8 ± 0.2	10.4 ± 0.7	42.3 ± 0.8	0.5 ± 1.5	11 ± 6
$J/\psi\gamma K^{*0}$	895.8 ± 0.2	9.5 ± 0.6	43.3 ± 0.6	8.2 ± 3.8	15 ± 4
$\psi(2S)\gamma K^{*\pm}$	891.9 ± 0.2	10.2 ± 0.5	42.9 ± 0.5	60 ± 20	9 ± 4
$\psi(2S)\gamma K^{*0}$	896.0 ± 0.1	9.1 ± 0.4	43.7 ± 0.4	4.9 ± 2.8	8 ± 2

background. For the signal modes, the absence of a linear relationship in the plots clearly demonstrates no correlation between the variables used in the fit. This statement applies equally to the background modes. This was also investigated numerically by calculating the correlation coefficient between each set of variables, which was found to be very small (generally $<< 0.1$). The lack of events in the low m_X region is due to the $E_\gamma > 100\,\mathrm{MeV}/c^2$ cut applied to reduce the level of background due to random low-energy photons, but this is an isolated effect that has a minor overall impact. The calculated correlation factor is found to be negligible (< 0.04) between all of the PDF fit variables.

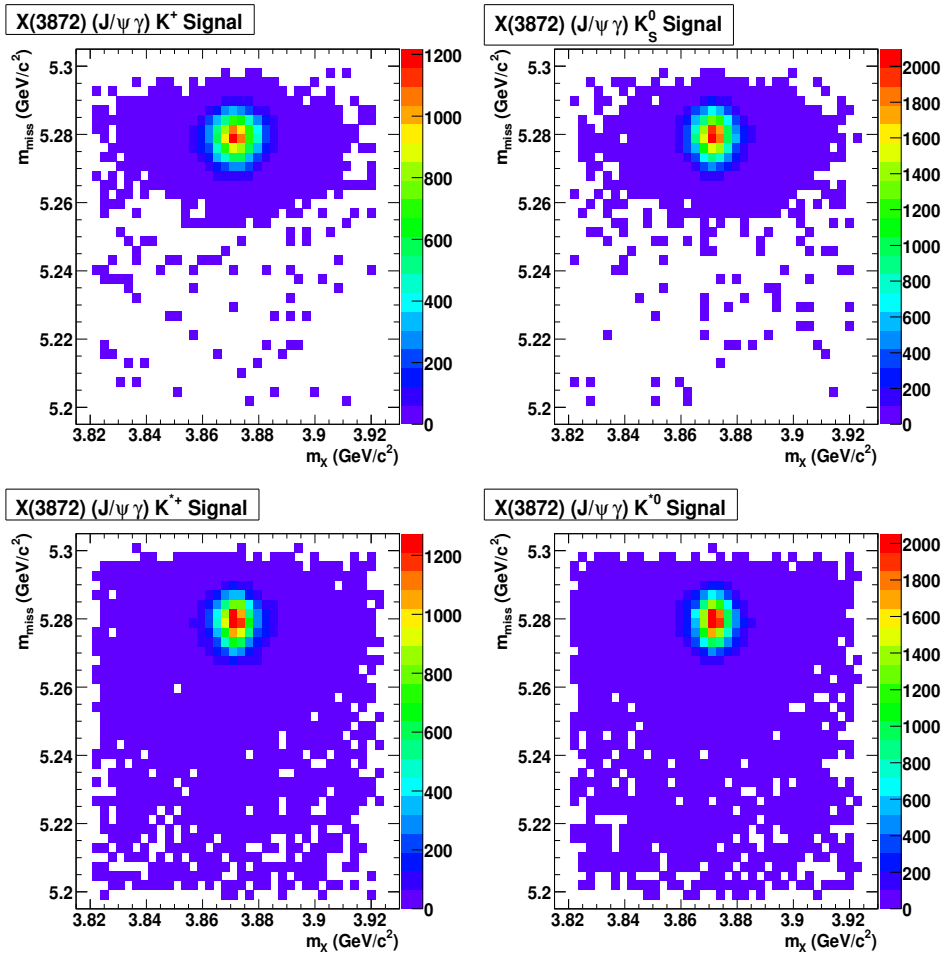

Figure 5.11: Plots of m_{miss} versus m_X for the $X(3872) \rightarrow J/\psi\gamma$ signal modes.

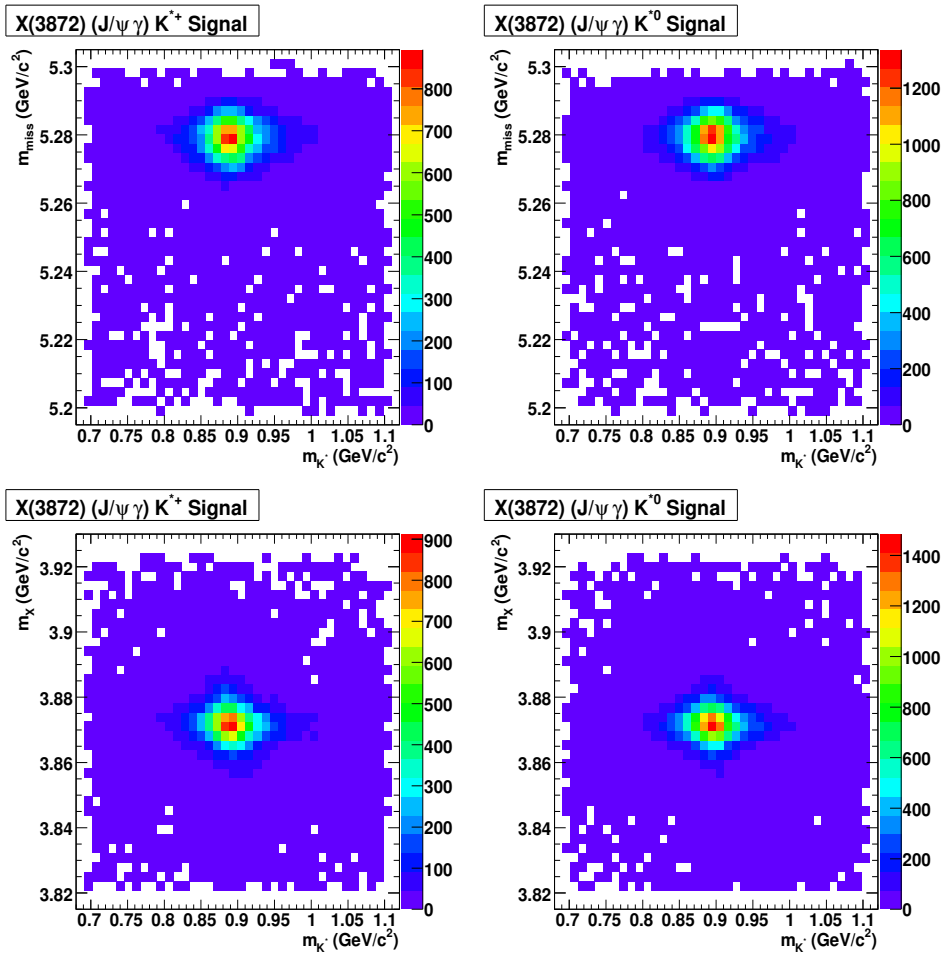

Figure 5.12: Plots of m_{miss} versus m_{K^*} and m_X versus m_{K^*} for the $X(3872) \to J/\psi\gamma$ signal modes.

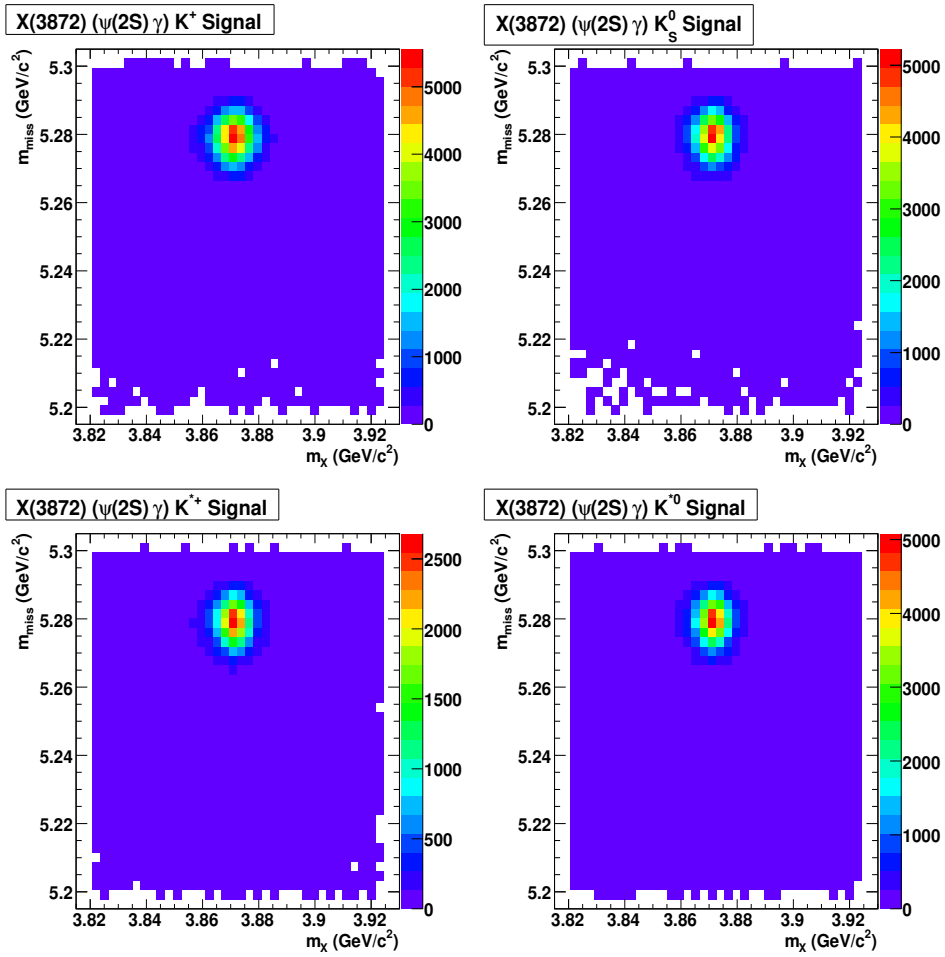

Figure 5.13: Plots of m_{miss} versus m_X for the $X(3872) \rightarrow \psi(2S)\gamma$ signal modes.

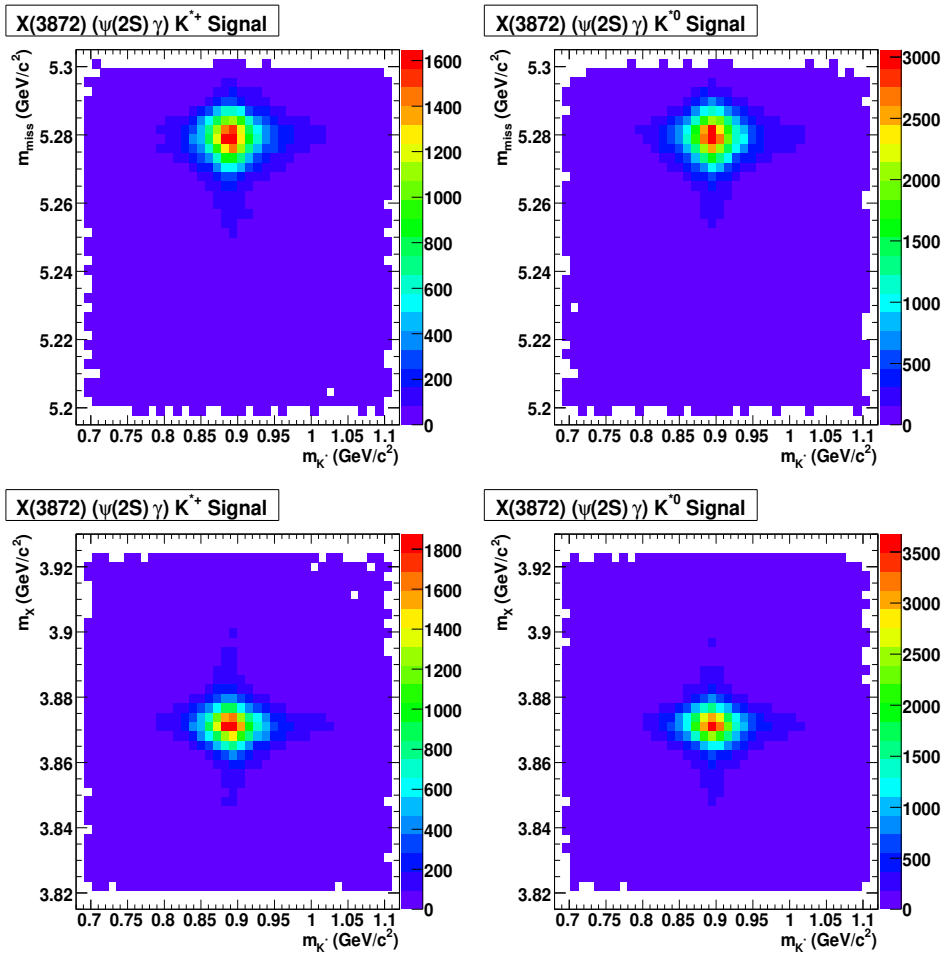

Figure 5.14: Plots of m_{miss} versus m_{K^*} and m_X versus m_{K^*} for the $X(3872) \to \psi(2S)\gamma$ signal modes.

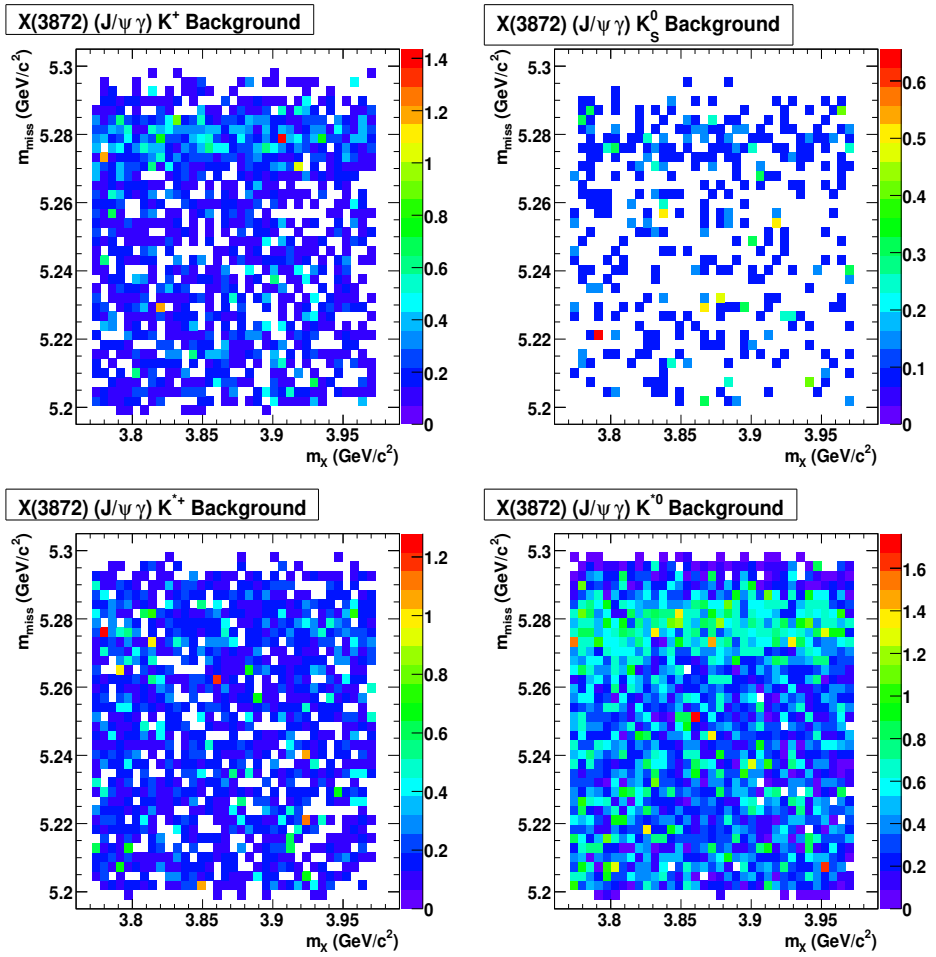

Figure 5.15: Plots of m_{miss} versus m_X for the $X(3872) \to J/\psi\,\gamma$ background modes.

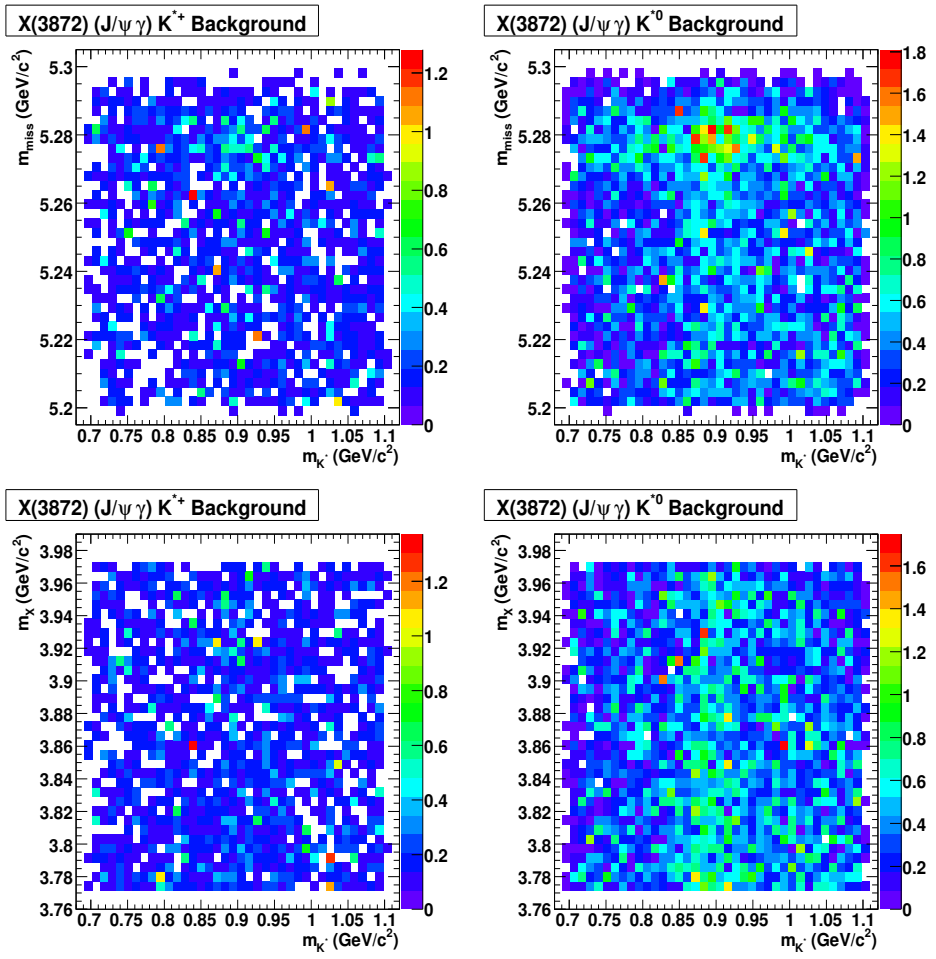

Figure 5.16: Plots of m_{miss} versus m_{K^*} and m_X versus m_{K^*} for the $X(3872) \to J/\psi\gamma$ background modes.

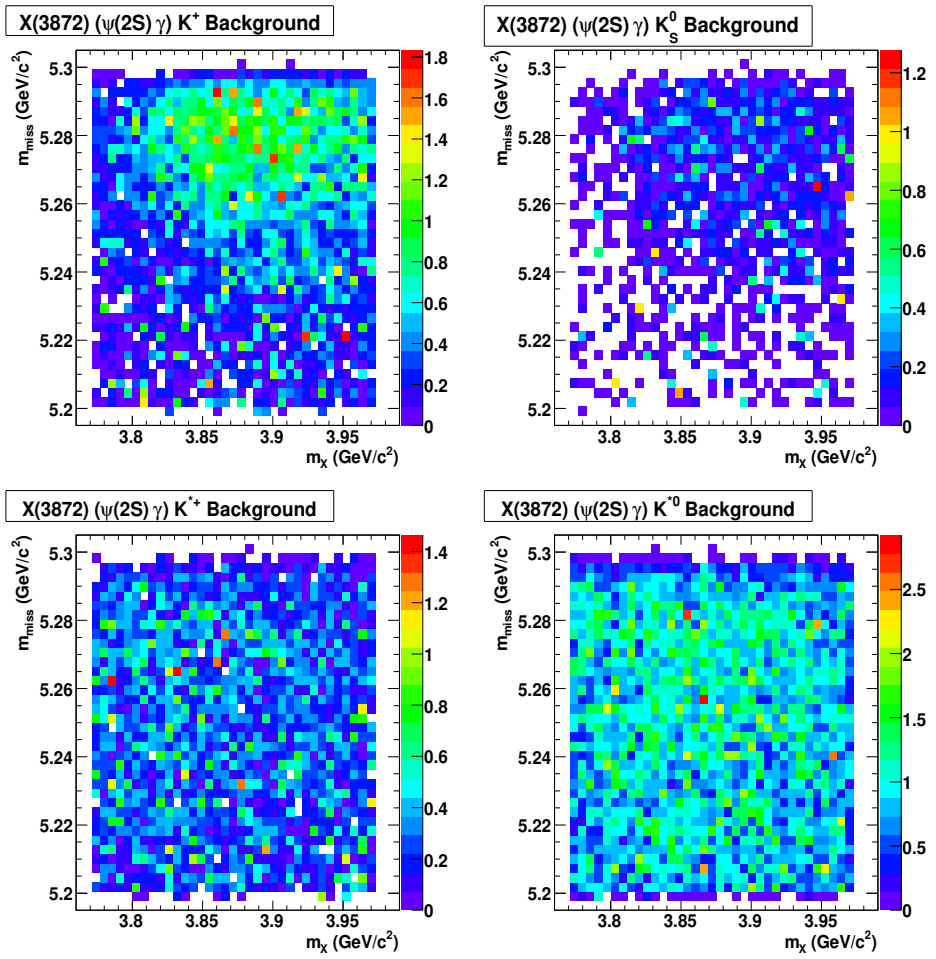

Figure 5.17: Plots of m_{miss} versus m_X for the $X(3872) \to \psi(2S)\gamma$ background modes.

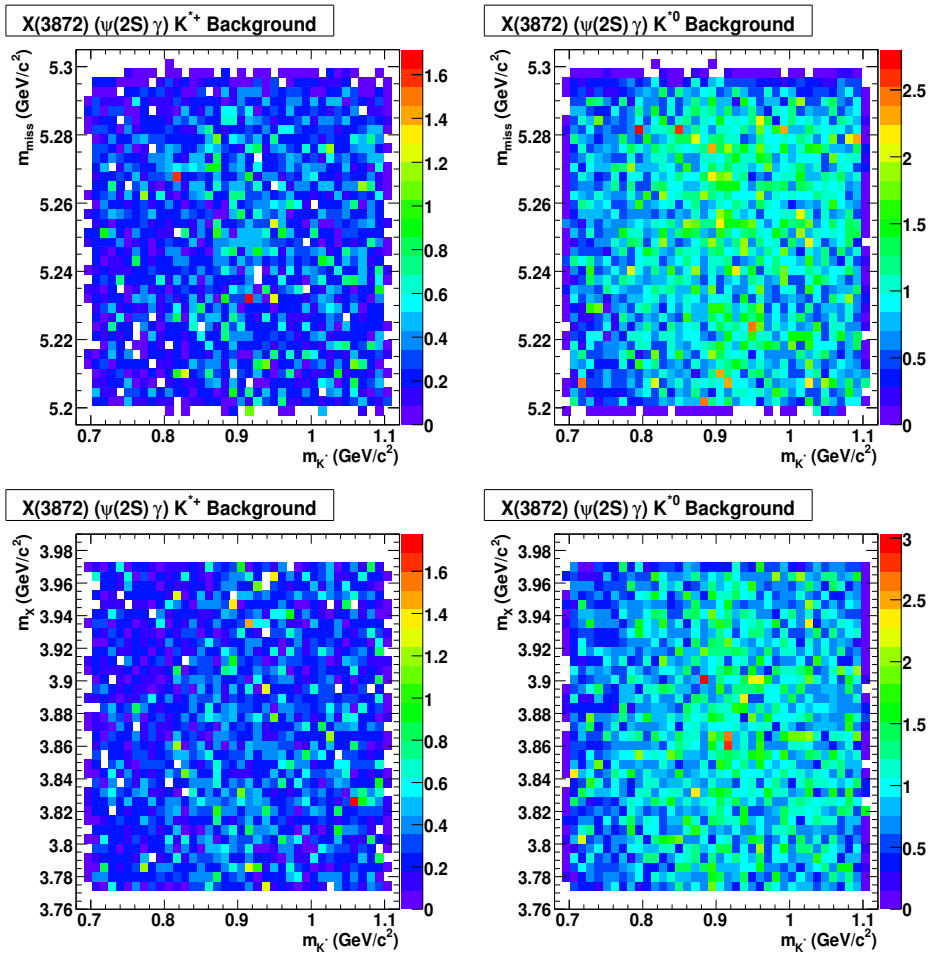

Figure 5.18: Plots of m_{miss} versus m_{K^*} and m_X versus m_{K^*} for the $X(3872) \to \psi(2S)\gamma$ background modes.

5.1.7 The $_s$Plot Technique

The $_s$Plot statistical technique [80] is used to display the results of the PDF fits to m_{miss} and m_{K^*}. This technique is effectively a sophisticated background-subtraction method that assigns weights to each event describing how "signal-like" the event is. These weights, represented here by the symbol ω, are calculated for each event i in the data sample according to:

$$\omega_{ai} = \frac{\Sigma_\alpha V_{a\alpha} \cdot \mathcal{F}_\alpha(\overrightarrow{y_i})}{(\Sigma_\beta N_\beta \cdot \mathcal{F}_\beta(\overrightarrow{y_i}))^2} \tag{5.9}$$

where a represents the event type or *species* (i.e.: signal, background, peaking background, etc.), $\overrightarrow{(y)}$ is the set of observables used in the fit (m_{miss} and m_{K^*}), $\mathcal{F}$ is the corresponding PDF as defined in Section 5.1.1, N_β is the total number of events of type β returned from a maximum likelihood fit to the data, and α and β are indices to indicate the summation over all possible event types. $V_{a\alpha}$ in this equation is the covariance matrix between a and α, defined as:

$$V^{-1}_{a\alpha} = \sum_i \frac{\mathcal{F}_a(\overrightarrow{y_i}) \cdot \mathcal{F}_\alpha(\overrightarrow{y_i})}{(\Sigma_\beta N_\beta \cdot \mathcal{F}_\beta(\overrightarrow{y_i}))^2}. \tag{5.10}$$

The sum of the weights over all species for a given event will be equal to 1 (i.e.: $\Sigma_a \omega_a = 1$).

The result is that each event in the dataset has a weight which describes how much like a given species that event is. This weight is based on the known PDFs and event yield from the fit to a given variable. In practice, the weight for signal events will typically be ~ 1 for true signal events, while background events will be weighted ~ 0. The power of this technique arises from the ability to examine the distribution of the data in another, uncorrelated variable, using the event-species categorization information given by ω. For example, in this analysis, one fits the data for $B^\pm \to XK^\pm$ decays using the m_{miss} variable and its associated PDFs for signal and background events. The resulting information is used to calculate ω for each event. When the m_X distribution of the data is then plotted using the signal-species weights,

it gives a clear picture of X invariant mass for the signal-like content of the data. This resulting distribution can subsequently be fit to get a signal-event yield versus m_X, possibly indicating the presence of new resonances.

5.2 $X(3872)$ Signal Extraction on Monte Carlo

To reiterate, the signal extraction is based on an unbinned extended maximum likelihood fit to the kinematic variables m_{miss} and m_{K^*} (if applicable), followed by a fit to the $_s$Plot projection of m_X for signal events.

For the simplest modes, $B \to XK^{\pm,0}$, there are three species of events: signal events that peak in both m_{miss} and m_X, combinatoric background events that are parameterized with an ARGUS function in m_{miss} and are linear in m_X, and peaking background events that peak in m_{miss} but have a linear m_X distribution. The first fit (defining two event types and using two PDFs in m_{miss}) separates out the combinatoric background, and the second fit (in m_X) separates out the peaking background events.

For the excited kaon modes, $B \to XK^*$, there are three relevant kinematic distributions: m_{miss}, m_{K^*}, and m_X. For these modes, four types of events are defined (hence four PDFs in the $m_{miss} \times m_{K^*}$ fit): signal events that peak in all three distributions; combinatoric background events that have an ARGUS shape in m_{miss} and are flat in the other variables; peaking background events that peak in m_{miss} but are flat in m_{K^*} (i.e.: $B \to XK\pi$ non-resonant events, which also peak in m_X), and combinatoric background events that have a real K^* (ie: $B \to J/\psi K^*$) that may peak in m_{K^*} but are flat in m_{miss}.

5.2.1 Monte Carlo Tests

The signal extraction was tested by inputting a given number of signal events drawn from the Monte Carlo sample while generating a specified number of background events based on the PDFs for the background shape. While the amount of generated signal MC is large, the available sample of background events passing all cuts is much lower, hence the choice to generate the back-

ground events from the PDF distribution. This allows many repeated trials of the signal extraction in order to test the robustness, define any biases, and calculate the expected efficiency for measuring our signal from the data.

In the case of the $X(3872) \to \psi(2S)\gamma$ decay modes, it was necessary to trim the number of $\psi(2S) \to \ell^+\ell^-$ events in the MC sample. The ratio of $\psi(2S)$ decays to $\ell^+\ell^-$ compared with $J\psi\pi^+\pi^-$ was incorrectly defined in the generation of the MC events and does not match the physical value reported by the PDG [33]. In order to compensate, $\sim 20\%$ of the $\psi(2S) \to \ell^+\ell^-$ events were removed at this stage of the analysis. This was done in a uniform fashion across lepton type and over the chronological running period to avoid introducing any further bias into the MC sample.

The expected number of signal events was estimated by multiplying the "Total Events" column by the "Weight" column in Table 4.1 and by the "Efficiency" column in Table 4.4 for truth-matched events. The expected number of background events was estimated by counting the total number passing the reconstruction and selection cuts, while applying the correct weighting based on the MC background type. These values were used as inputs for testing the signal extraction and are included in the "Signal Input" and "Background Input" columns of Table 5.6.

For the case of $X(3872) \to \psi(2S)\gamma$ decays, using the assumption that it has the same branching fraction as $B^\pm \to X(3872)K^\pm$ leads to a very small number of expected events in the data. In order to test the robustness of the signal extraction technique, the $X(3872) \to \psi(2S)\gamma$ trials were also run using 6 times the number of signal events (roughly following the branching fraction assumption for a $\chi_{c1}(2P)$ assignment for the $X(3872)$ from [61]).

5.2.2 Bias

To test for a possible bias, repeated signal extraction trials using truth-matched signal events were performed. The PDF parametrization was based on this sample of events, so one would expect the signal extraction procedure to correctly handle events of this type. The results of the trials can be found in Table 5.6.

Table 5.6: Test of signal extraction for truth-matched signal MC events with PDF-generated background events.

Decay Mode $X(3872)$	Trials	Signal Input	Background Input	Mean Signal Output	Standard Deviation
$J/\psi\gamma K^{\pm}$	900	27	164	27.8 ± 0.2	4.79 ± 0.12
$J/\psi\gamma K^0_S$	2500	7	38	6.6 ± 0.1	2.43 ± 0.04
$J/\psi\gamma K^{*\pm}$	2500	3	217	2.4 ± 0.1	3.02 ± 0.05
$J/\psi\gamma K^{*0}$	2500	14	599	15.5 ± 0.1	6.26 ± 0.10
$\psi(2S)\gamma K^{\pm}$	1000	12	501	13.4 ± 0.2	6.29 ± 0.14
$\psi(2S)\gamma K^0_S$	1000	3	123	2.7 ± 0.1	3.16 ± 0.07
$\psi(2S)\gamma K^{*\pm}$	1000	1	501	1.1 ± 0.1	2.93 ± 0.08
$\psi(2S)\gamma K^{*0}$	1000	6	1417	7.1 ± 0.2	6.43 ± 0.14
$\psi(2S)\gamma K^{\pm}$	1000	71	501	71.7 ± 0.3	8.68 ± 0.21
$\psi(2S)\gamma K^0_S$	1000	19	123	19.2 ± 0.1	3.98 ± 0.11
$\psi(2S)\gamma K^{*\pm}$	1000	8	501	8.0 ± 0.2	4.77 ± 0.10
$\psi(2S)\gamma K^{*0}$	1000	35	1417	38.8 ± 0.3	9.29 ± 0.24

While these results show the procedure to be robust, it also points to some small systematic bias present in nearly all of the modes, as indicated by the difference between the number of input signal events compared with the number extracted. This shift will be applied to the number of events found from the signal extraction to correct for these biases arising from possible correlations between the PDFs and mechanics of the fit. Note that these tests are the culmination of hundreds of independent trials using different input signal and background events, thus the error is essentially equal to $\frac{\sigma}{\sqrt{N}}$. In practice, it was found by fitting the results of the N trials with a Gaussian. Furthermore, in a small fraction (dependent on the signal mode but generally $< 0.2\%$ for $X(3872) \to \psi(2S)\gamma$ decays) of the trials, the fitting procedure failed to properly converge. These trials were eliminated from the study without any loss of generality.

5.2.3 Fit Efficiency

To calculate the signal extraction efficiency of the fit method, the same procedure as described in the previous section is adopted for non-truth-matched MC events. These events are most like those one expects when analyzing the data. After extracting the number of signal events, the result is shifted by the bias defined in Table 5.6 and divided by the number of input events to determine the fit efficiency. The results of this series of trials are summarized in Table 5.7.

Repeating the $X(3872) \to \psi(2S)\gamma$ signal extraction tests with a greater number of input events for the signal mode shows that the technique is consistent, producing a fit efficiency that matches the small number of events within uncertainty. Because the values for the efficiency were shown to be the same, the results using the greater number of signal events will be taken as the fit efficiency since they have a smaller uncertainty.

While the signal extraction efficiency for the $B \to X(3872)(J/\psi\,\gamma)K^{(+,0)}$ modes is very high, there is a noticeable drop from the $K^{(+,0)}$ modes to the $K^{*(+,0)}$ modes. There is an even greater difference seen when comparing the J/ψ and $\psi(2S)$ modes. This is due to much larger effects of misreconstruction in the latter case (for instance, incorrect pions in the decay to $J/\psi\pi^+\pi^-$, or the greater probability of substituting a random low energy photon in place of the correct signal photon). Indeed, if one compares the cut and reconstruction efficiency between truth-matched and non-truth-matched events in Table 4.4, there is a notable difference in the case of the $\psi(2S)$ decay channels. This can also be seen by comparing the shapes of the distributions between truth-matched and non-truth-matched events (Figures 5.19 - 5.22). The PDFs for the fit are defined using truth-matched events, but the reconstructed events in data should look more like non-truth-matched events. In the latter case, there are tails in both m_{miss} and m_X which lead to the drop in efficiency. For the $X(3872) \to J\psi\gamma$ modes, there is a much closer agreement between truth- and non-truth-matched events, as shown in Figures 5.23 - 5.26, hence a better fit efficiency.

Table 5.7: Test of signal extraction for all signal MC events with PDF-generatedbackground events.

Decay Mode $X(3872)$	Trials	Sig. In	Bkgd. In	Mean Sig. Out	Standard Deviation	Bias Correction	Corrected Output	Fit Eff. (%)
$J/\psi\gamma K^{\pm}$	1000	27	164	27.8 ± 0.2	5.01 ± 0.13	-0.8 ± 0.2	27.0 ± 0.2	100.1 ± 0.8
$J/\psi\gamma K^{0}_{S}$	3000	7	38	6.6 ± 0.1	2.50 ± 0.04	$+0.4 \pm 0.1$	6.9 ± 0.1	99.3 ± 1.0
$J/\psi\gamma K^{*\pm}$	2500	3	217	2.0 ± 0.1	2.83 ± 0.05	$+0.6 \pm 0.1$	2.6 ± 0.1	87.4 ± 3.6
$J/\psi\gamma K^{*0}$	3000	14	599	14.0 ± 0.1	6.38 ± 0.08	-1.5 ± 0.1	12.6 ± 0.2	89.9 ± 1.3
$\psi(2S)\gamma K^{\pm}$	1000	12	501	9.5 ± 0.2	6.40 ± 0.14	-1.4 ± 0.2	8.2 ± 0.3	68.0 ± 2.4
$\psi(2S)\gamma K^{0}_{S}$	1000	3	123	1.8 ± 0.1	3.15 ± 0.07	$+0.3 \pm 0.1$	2.1 ± 0.2	71.0 ± 5.0
$\psi(2S)\gamma K^{*\pm}$	1000	1	501	0.8 ± 0.1	2.75 ± 0.08	-0.1 ± 0.1	0.7 ± 0.2	69.1 ± 16.3
$\psi(2S)\gamma K^{*0}$	1000	6	1417	4.6 ± 0.2	6.29 ± 0.16	-1.1 ± 0.2	3.5 ± 0.3	58.4 ± 4.8
$\psi(2S)\gamma K^{\pm}$	1000	71	501	48.9 ± 0.3	9.22 ± 0.19	-0.7 ± 0.3	48.2 ± 0.4	67.8 ± 0.6
$\psi(2S)\gamma K^{0}_{S}$	1000	19	123	13.1 ± 0.2	4.58 ± 0.12	-0.2 ± 0.1	12.8 ± 0.2	67.5 ± 1.0
$\psi(2S)\gamma K^{*\pm}$	1000	8	501	4.7 ± 0.2	4.32 ± 0.09	-0.0 ± 0.1	4.7 ± 0.2	58.2 ± 2.7
$\psi(2S)\gamma K^{*0}$	1000	35	1417	23.7 ± 0.3	8.58 ± 0.19	-3.8 ± 0.3	19.9 ± 0.4	56.7 ± 1.2

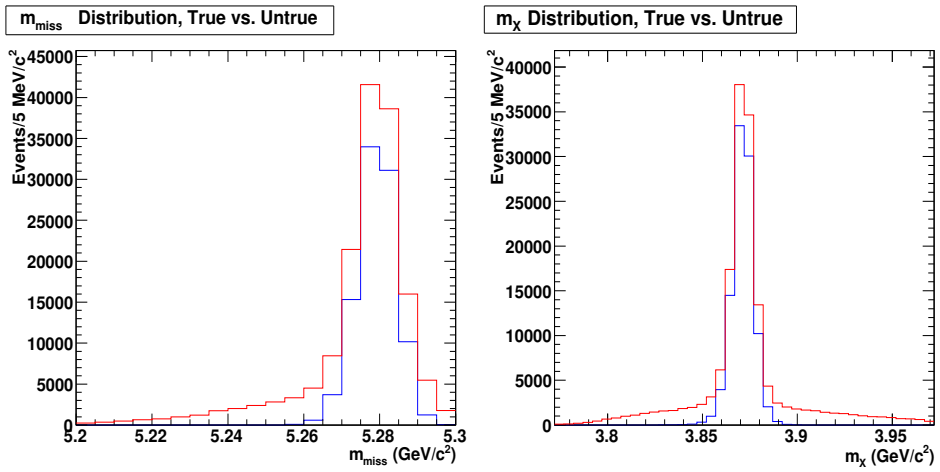

Figure 5.19: Comparison of truth-matched (blue) and non-truth-matched (red) MC for $B^{\pm} \to X(3872)(\psi(2S)\gamma)K^{\pm}$.

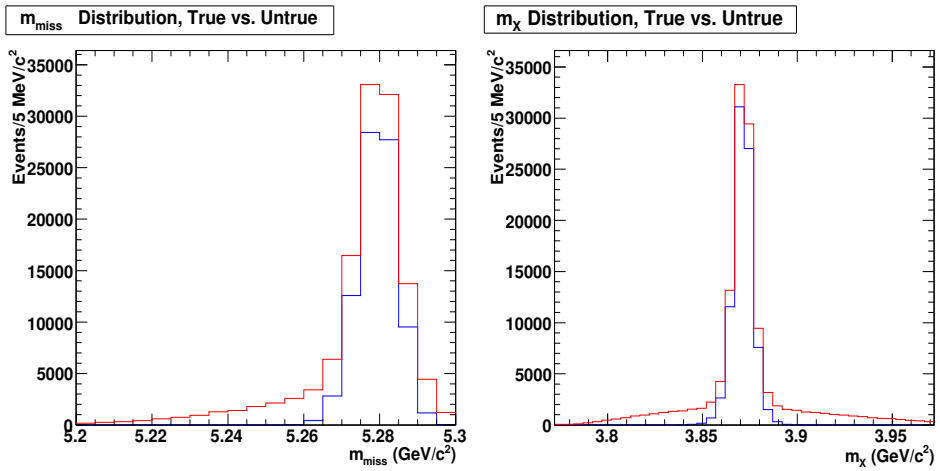

Figure 5.20: Comparison of truth-matched (blue) and non-truth-matched (red) MC for $B^0 \to X(3872)(\psi(2S)\gamma)K^0_S$.

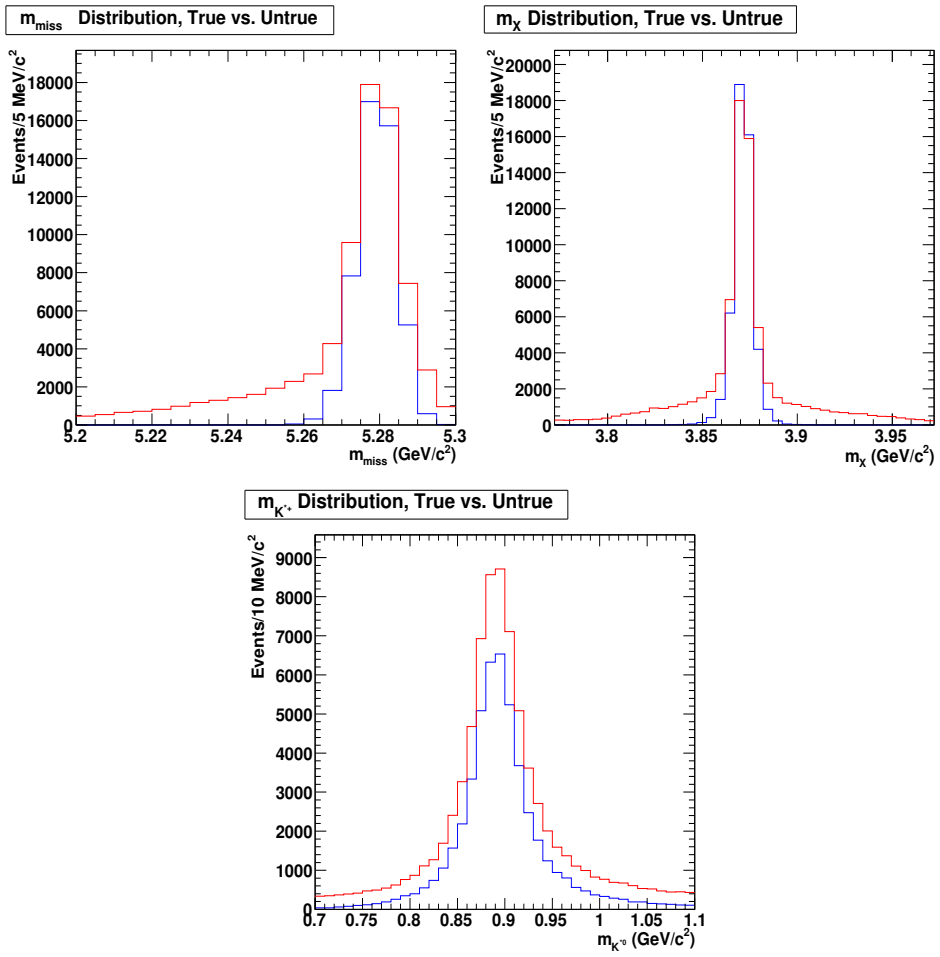

Figure 5.21: Comparison of truth-matched (blue) and non-truth-matched (red) and MC for m_X, m_{miss}, and $m_{K^{*\pm}}$ for $B^{\pm} \to X(3872)(\psi(2S)\gamma)K^{*\pm}$.

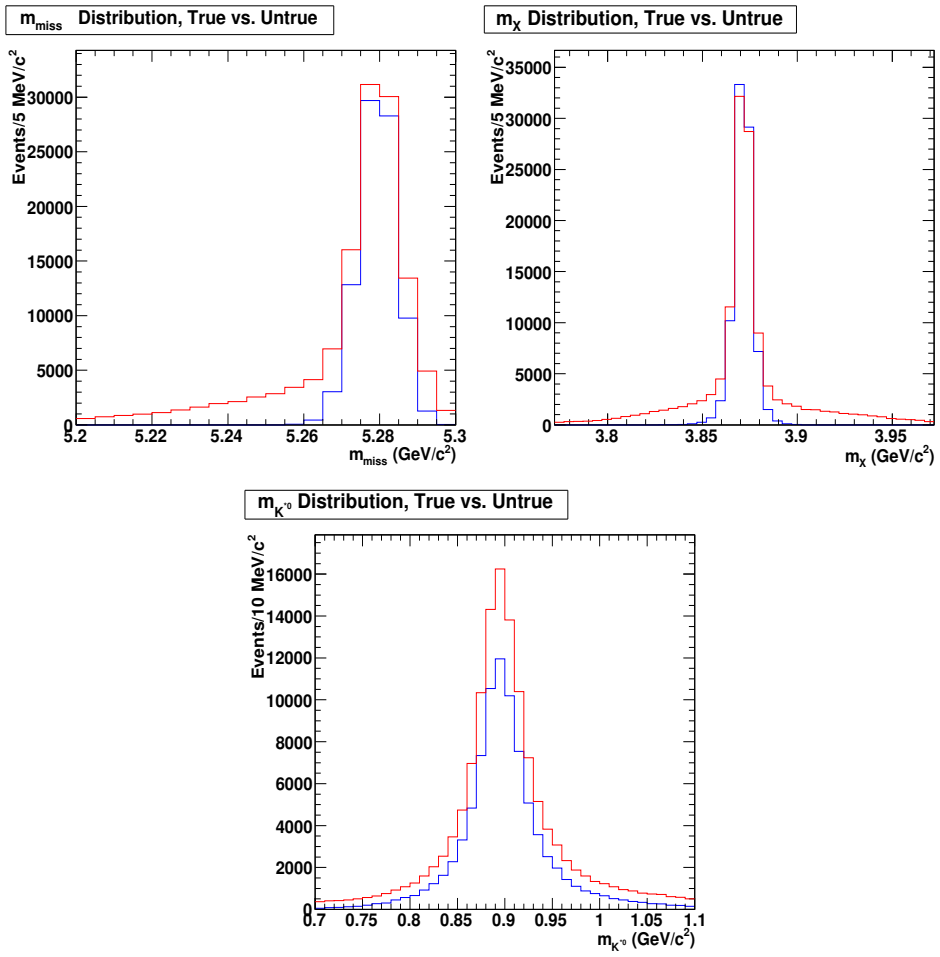

Figure 5.22: Comparison of truth-matched (blue) and non-truth-matched (red) and MC for m_X, m_{miss}, and $m_{K^{*0}}$ for $B^0 \to X(3872)(\psi(2S)\gamma)K^{*0}$.

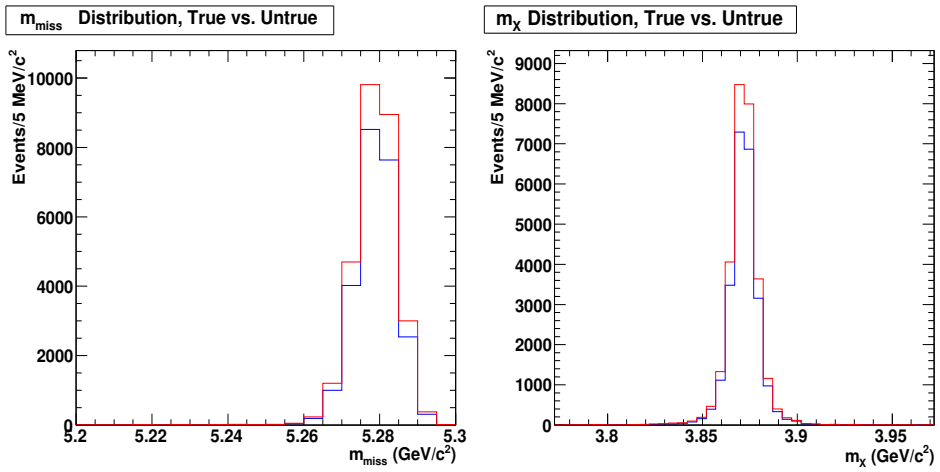

Figure 5.23: Comparison of truth-matched (blue) and non-truth-matched (red) MC for $B^{\pm} \to X(3872)(J/\psi\,\gamma)K^{\pm}$.

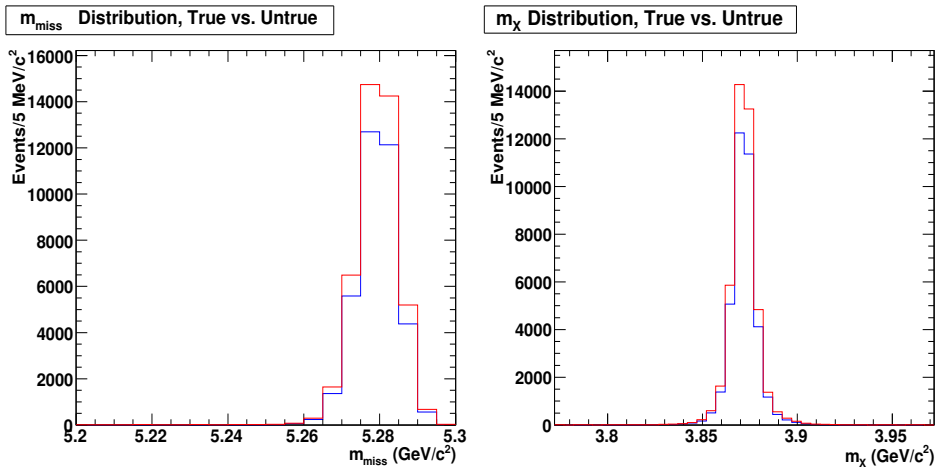

Figure 5.24: Comparison of truth-matched (blue) and non-truth-matched (red) MC for $B^{0} \to X(3872)(J/\psi\,\gamma)K^{0}_{S}$.

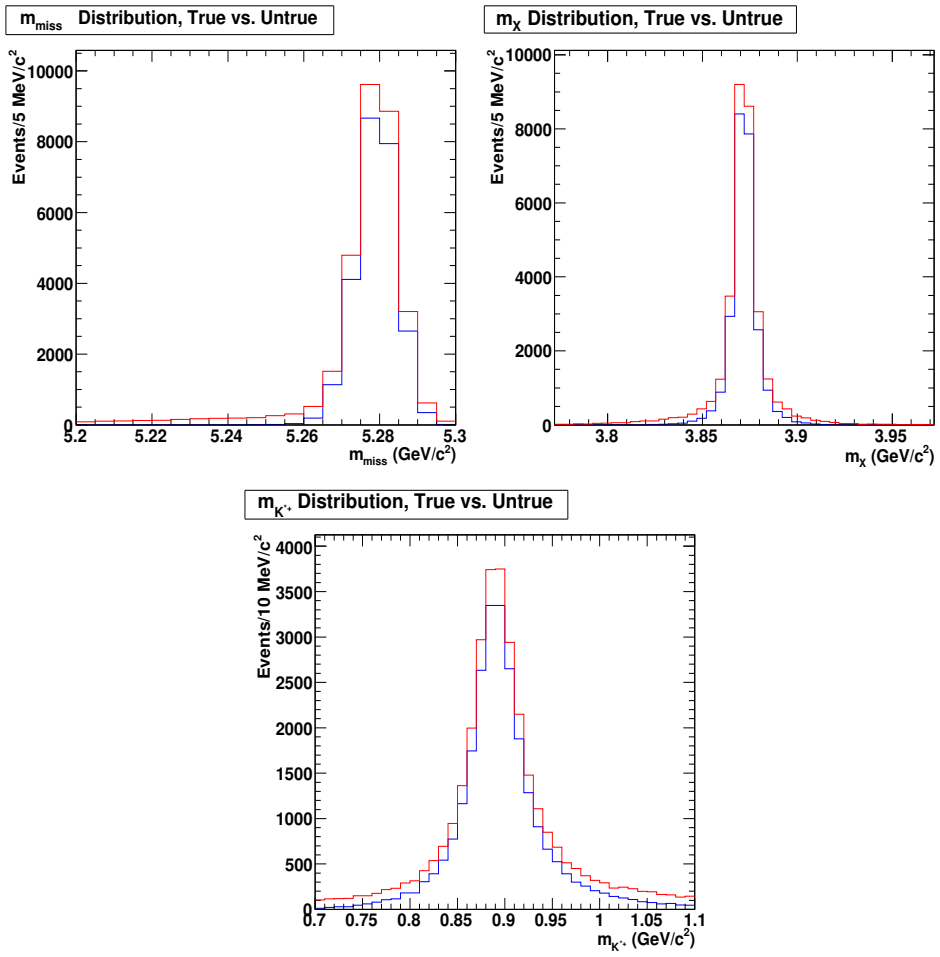

Figure 5.25: Comparison of truth-matched (blue) and non-truth-matched (red) MC for m_X, m_{miss}, and $m_{K^{*\pm}}$ for $B^{\pm} \to X(3872)(J/\psi\,\gamma)K^{*\pm}$.

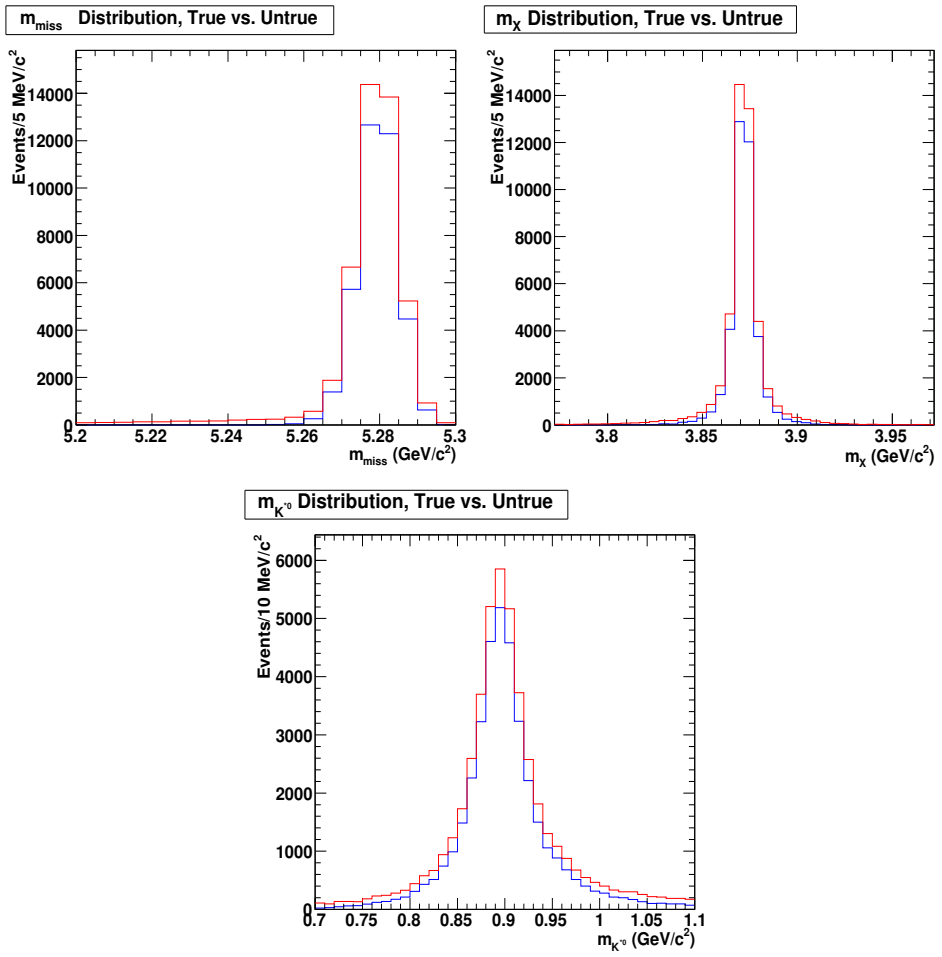

Figure 5.26: Comparison of truth-matched (blue) and non-truth-matched (red) MC for m_X, m_{miss}, and $m_{K^{*0}}$ for $B^0 \to X(3872)(J/\psi\,\gamma)K^{*0}$.

5.2.4 Total Efficiency

The total efficiency for each signal mode is found by multiplying the cut, reconstruction, and fit efficiencies together. These values are compiled in Table 5.8.

Table 5.8: Total signal extraction efficiency for each signal mode based on MC samples.

Decay Mode $X(3872)$	Cut/Reco Efficiency (%)	Fit Efficiency (%)	Total Efficiency (%)
$J/\psi\gamma K^{\pm}$	14.6	100.1 ± 0.8	14.6 ± 0.1
$J/\psi\gamma K^0_S$	11.1	99.3 ± 1.0	11.1 ± 0.1
$J/\psi\gamma K^{*\pm}$	7.9	87.4 ± 3.6	6.9 ± 0.3
$J/\psi\gamma K^{*0}$	11.5	89.9 ± 1.3	10.4 ± 0.1
$\psi(2S)\gamma K^{\pm}$	15.4	67.8 ± 0.6	10.4 ± 0.1
$\psi(2S)\gamma K^0_S$	11.8	67.5 ± 1.0	8.0 ± 0.1
$\psi(2S)\gamma K^{*\pm}$	7.3	58.2 ± 2.7	4.3 ± 0.2
$\psi(2S)\gamma K^{*0}$	11.4	56.7 ± 1.2	6.5 ± 0.1

5.2.5 Cross-feed and Other Backgrounds

Cross-feed is defined as one signal mode being misreconstructed as another. A priori, the main type of cross-feed that might be expected is the case of a K^* incorrectly being formed as a combination of a signal K plus a π, or vice versa with a π being missed in the reconstruction. This is tested by attempting to extract a number of events of type j from a MC sample of signal type i. This effect was found to be tiny. Based solely on the number of events passing reconstruction and cuts, the largest amount of cross-feed expected was in the case of $B^0 \to X(3872)K^{*0}$ events being misreconstructed as $B^{\pm} \to X(3872)K^{*\pm}$ events. The "efficiency" for this misreconstruction was measured to be $\sim 0.4\%$ of all $B^0 \to X(3872)K^{*0}$ events (for both $X(3872) \to J\psi\gamma$ and $X(3872) \to \psi(2S)\gamma$), and this is before even attempting to fit these events using our PDFs and discriminating variables (which look completely different for signal events). Thus this background is ignored.

Another source of background could be from other known $X(3872)$ decays, in particular $B^{\pm} \to X(3872)(J/\psi\pi^+\pi^-)K^{\pm}$. This is not included in our background MC sample, so the signal MC for these types of events (and the neutral B decay) was used. In general, the number of events of this type passing our reconstruction and selection cuts is small. To determine the expected number of events before fitting, one divides the number of events passing the reconstruction and selection cuts by the total number generated in the MC, and multiply it by the branching fractions for $B \to X(3872)(J\psi\pi^+\pi^-)K$ and subsequent daughter decays from the recent *BABAR* result [34]. As shown in Table 5.9, very little contamination is expected from this decay mode for all of the event types except possibly $B^{\pm} \to X(3872)(\psi(2S)\gamma)K^{\pm}$. This background comes from picking up a low energy photon to create the same final state, ie: $J/\psi\pi^+\pi^-\gamma K^{\pm}$. Note that the same background exists for the K^0_S mode, and the raw number of events from the MC sample confirms this, but the small branching fraction measurement for $B^0 \to X(3872)K^0$ makes this background relatively negligible in this analysis.

It is important to note that even though these events may pass the selection cuts, it does not mean their distribution is signal-like. To test the effect of these events, signal extraction trials are conducted using the nominal number of signal events from MC, toy-generated background events, and inserting cross-feed events from the MC. Two hundred trials are performed for the $B^{\pm} \to X(3872)(J/\psi\pi^+\pi^-)K^{\pm}$ mode, where the largest effect potentially exists, and find that an addition of 4 cross-feed events causes an average of change in the number of signal events extracted of less than 0.002. This check makes it clear that these cross-feed events are correctly separated from signal events and that they are not a source of background.

5.2.6 Null Signal Tests

The signal extraction was also tested for the null signal case. For each mode, 1000 toy trials were conducted with zero signal events and the expected number of background events, to determine if a fluctuation from the background

Table 5.9: Number of MC background events from $B \to X(3872)(J\psi\pi^+\pi^-)K$ passing reconstruction and selection cuts and the resulting number expected in the data based on known branching fractions. The total number of events generated in each MC mode was 175000.

Decay Mode	$X(J/\psi\pi^+\pi^-)K^\pm$		$X(J/\psi\pi^+\pi^-)K^0$	
$X(3872)$	Pass Cuts	Expected	Pass Cuts	Expected
$J/\psi\gamma K^\pm$	133	0.4	1	0.0
$J/\psi\gamma K^0_S$	0	0	98	0.0
$J/\psi\gamma K^{*\pm}$	5	0.0	52	0.0
$J/\psi\gamma K^{*0}$	40	0.1	10	0.0
$\psi(2S)\gamma K^\pm$	1311	3.5	18	0.0
$\psi(2S)\gamma K^0_S$	4	0.0	1145	0.4
$\psi(2S)\gamma K^{*\pm}$	23	0.1	247	0.1
$\psi(2S)\gamma K^{*0}$	215	0.6	87	0.0

could produce a significant signal. The results are summarized in Table 5.10. For each trial, the significance of the result is defined as the number of events divided by the uncertainty. A histogram of the significances for each trial was fitted with a Gaussian and the probability of a trial having $> 3\sigma$ result was determined from the integral of the Gaussian. This shows that while a small bias may be present in the signal extraction, none of the modes are expected to have a particularly strong bias that would generate a significant signal.

5.3 The $\chi_{c1,2}$ Benchmark Modes

The decays $B \to \chi_{cJ=0,1,2}K, \chi_{cJ=0,1,2} \to J/\psi\gamma$ have the same form as the $X(3872)$ decay searched for in this analysis. Using the same method for extracting the $X(3872)$ signal, a measurement of the χ_{c1} mode can be attempted. The branching fractions for the $B \to \chi_{c1}K$ decay channels are approximately 30 times greater than those to χ_{c0} (which is also much wider), and decays to $\chi_{c2}K$ have never been observed. Thus a measurement for $B \to \chi_{c1}K$ will be used as a validation of our signal extraction method. The

Table 5.10: Number of events returned by the signal extraction from a background-only toy data sample.

Decay Mode $X(3872)$	Signal Input	Background Input	Mean Signal Output	$P(>3\sigma)$ Fluctuation
$J/\psi\gamma K^{\pm}$	0	164	1.6 ± 0.1	3.2%
$J/\psi\gamma K^0_S$	0	38	1.1 ± 0.1	0.5%
$J/\psi\gamma K^{*\pm}$	0	217	1.0 ± 0.1	2.4%
$J/\psi\gamma K^{*0}$	0	599	0.0 ± 0.0	0.9%
$\psi(2S)\gamma K^{\pm}$	0	501	1.4 ± 0.2	0.5%
$\psi(2S)\gamma K^0_S$	0	123	0.1 ± 0.1	1.3%
$\psi(2S)\gamma K^{*\pm}$	0	501	0.1 ± 0.1	0.8%
$\psi(2S)\gamma K^{*0}$	0	1417	0.9 ± 0.2	0.4%

χ_{c0} region is effectively removed by the cut of $m_X = m_{\chi_{c1}} \pm 100\,\mathrm{MeV}/c^2$, but any χ_{c2} signal should remain in our selection window.

5.3.1 χ_{c1} PDF Parametrization

For purposes of defining the PDFs, the χ_{c1} sample was drawn from the B^+B^- and $B^0\overline{B}^0$ generic and J/ψ Inclusive MC collections. A mass cut of $3.411 < m_X < 3.611\,\mathrm{GeV}/c^2$ was applied to restrict our range to the χ_{c1} region, and truth-matching was required. The PDF functional forms used were the same as those from the $X(3872)$ decay modes. Figures 5.29 – 5.31 show the results of the PDF fit for signal and background in m_X, m_{miss} and m_{K^*}, with the numerical results summarized in Tables 5.11 – 5.15. The fits to the m_X distribution for $\chi_{c1}K^*$ background events in Figure 5.30 show that there is a considerable $B \to \chi_{c1}K\pi$ non-resonant component.

Examining a sample of the Monte Carlo background events falling in a tight m_{miss}, m_X and m_{K^*} signal range shows that $B \to \chi_{c1}K\pi$ events comprise the majority ($\sim 65\%$) of the events. Other decay modes include $B \to J/\psi K^*$+something events (where the K^* is *any* excited kaon), $B \to \psi(2S)K$, and $B \to \chi_{c1}K^*$ events with the K^* decaying to a mode not considered in this analysis (e.g.: $K^0_L\pi$, $K^{\pm}\pi^0$). However, no other single decay mode was comparable to the $B \to \chi_{c1}K\pi$ decay. The handling of this

non-resonant background will be described separately in Section 5.3.4.

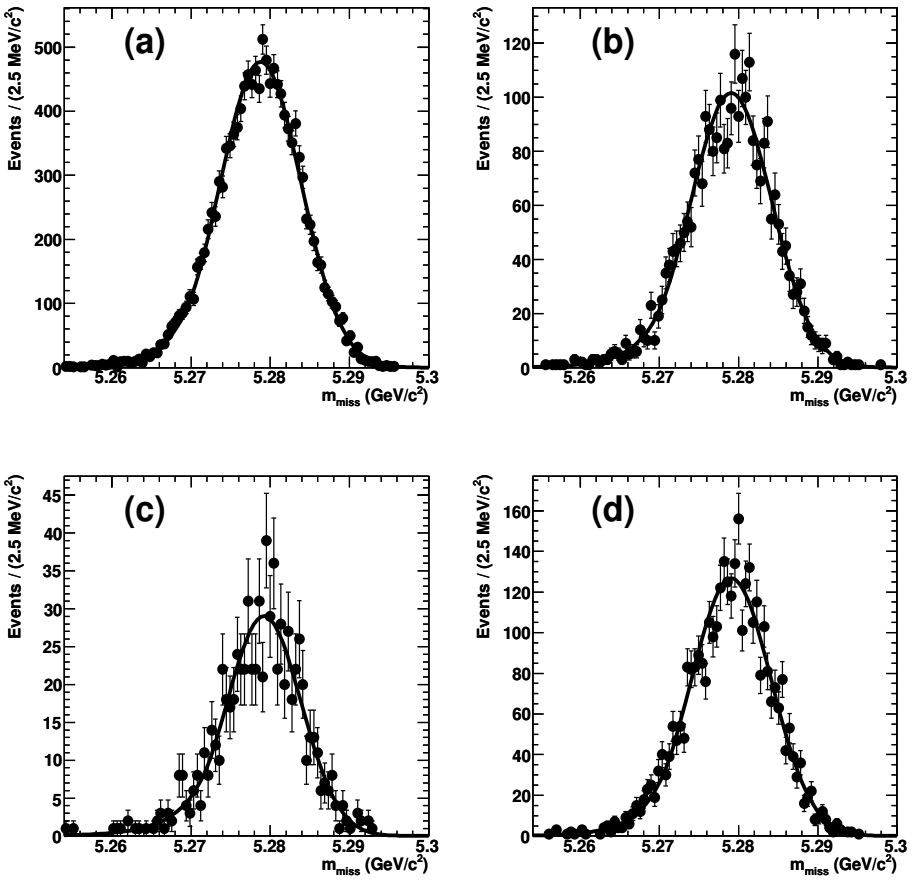

Figure 5.27: m_{miss} PDF fits for the χ_{c1} signal modes, (a) $B^{\pm} \to \chi_{c1}K^{\pm}$ events, (b) $B^0 \to \chi_{c1}K^0_s$ events, (c) $B^{\pm} \to \chi_{c1}K^{*\pm}$ events, and (d) $B^0 \to \chi_{c1}K^{*0}$ events.

5.3.2 χ_{c2} PDF Parametrization

For the χ_{c2} modes, the same m_{miss} and m_{K^*} parameters as derived for the χ_{c1} decays are used. The only difference comes in the m_X distribution, which is centred at approximately $m_{\chi_{c2}} = 3.55\,\mathrm{GeV}/c^2$. Due to the lack

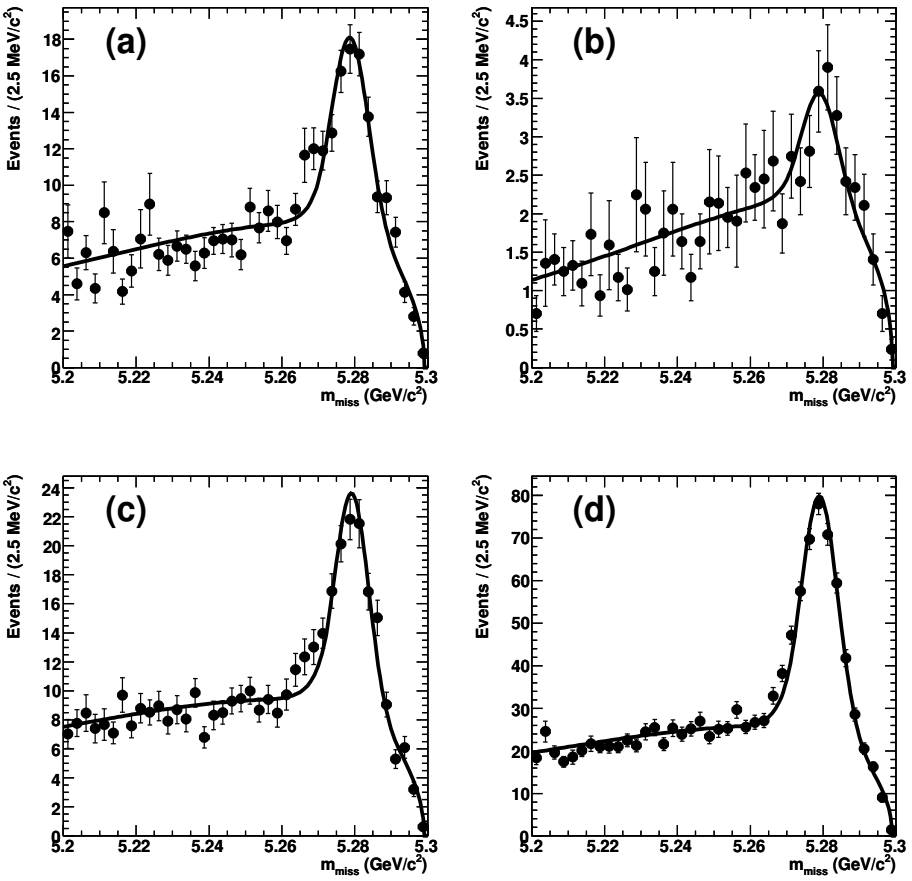

Figure 5.28: m_{miss} PDF fits for the backgrounds to the χ_{c1} modes, (a) $B^{\pm} \to \chi_{c1} K^{\pm}$ events, (b) $B^0 \to \chi_{c1} K^0_s$ events, (c) $B^{\pm} \to \chi_{c1} K^{*\pm}$ events, and (d) $B^0 \to \chi_{c1} K^{*0}$ events.

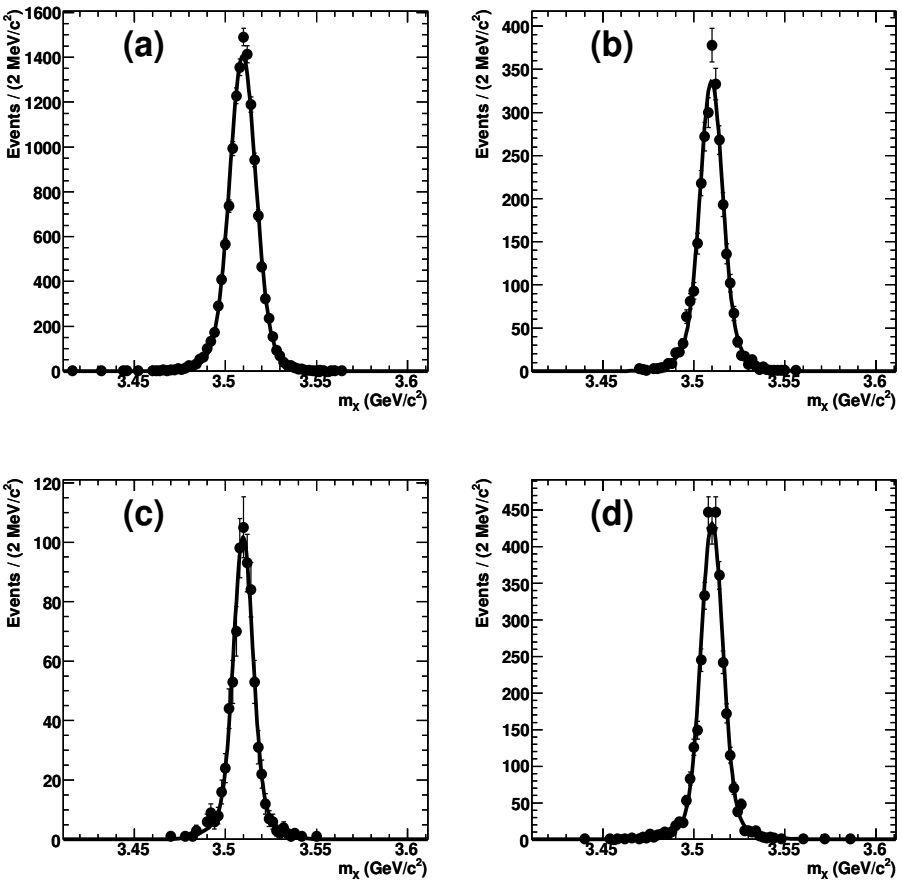

Figure 5.29: m_X PDF fits for the χ_{c1} signal modes, (a) $B^{\pm} \to \chi_{c1} K^{\pm}$ events, (b) $B^0 \to \chi_{c1} K^0_s$ events, (c) $B^{\pm} \to \chi_{c1} K^{*\pm}$ events, and (d) $B^0 \to \chi_{c1} K^{*0}$ events.

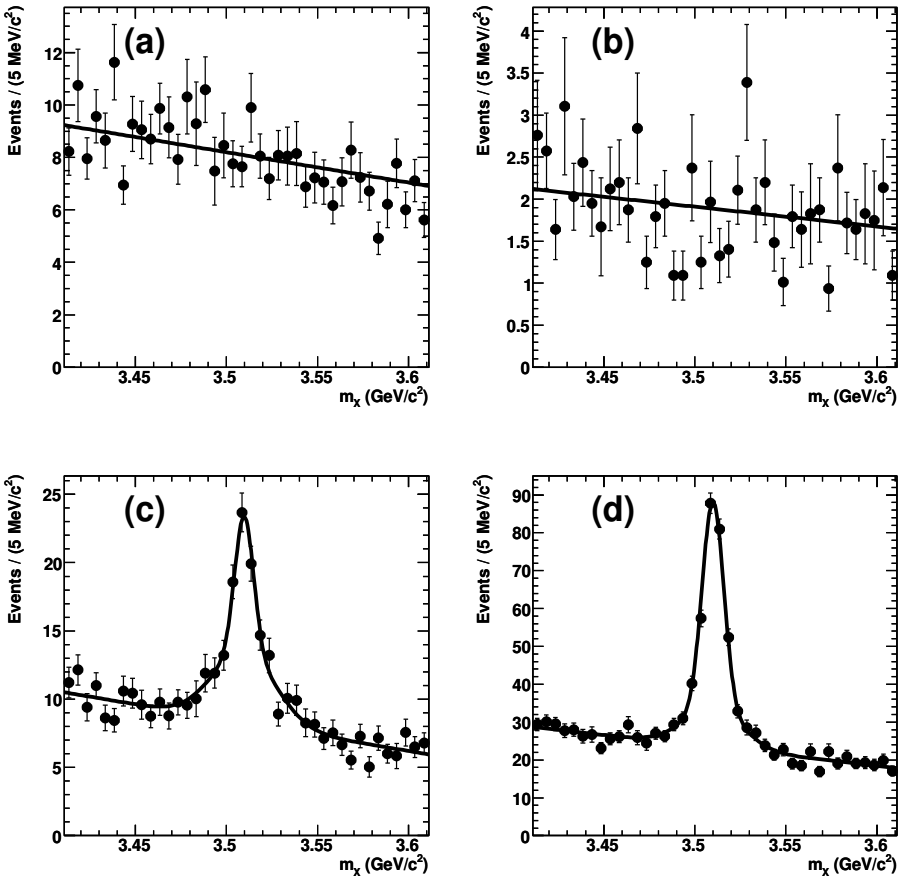

Figure 5.30: m_X PDF fits for the backgrounds to the χ_{c1} modes, (a) $B^{\pm} \to \chi_{c1}K^{\pm}$ events, (b) $B^0 \to \chi_{c1}K^0_s$ events, (c) $B^{\pm} \to \chi_{c1}K^{*\pm}$ events, and (d) $B^0 \to \chi_{c1}K^{*0}$ events. Figures (c) and (d) show clear evidence of $B \to \chi_{c1}K\pi$ non-resonant background events.

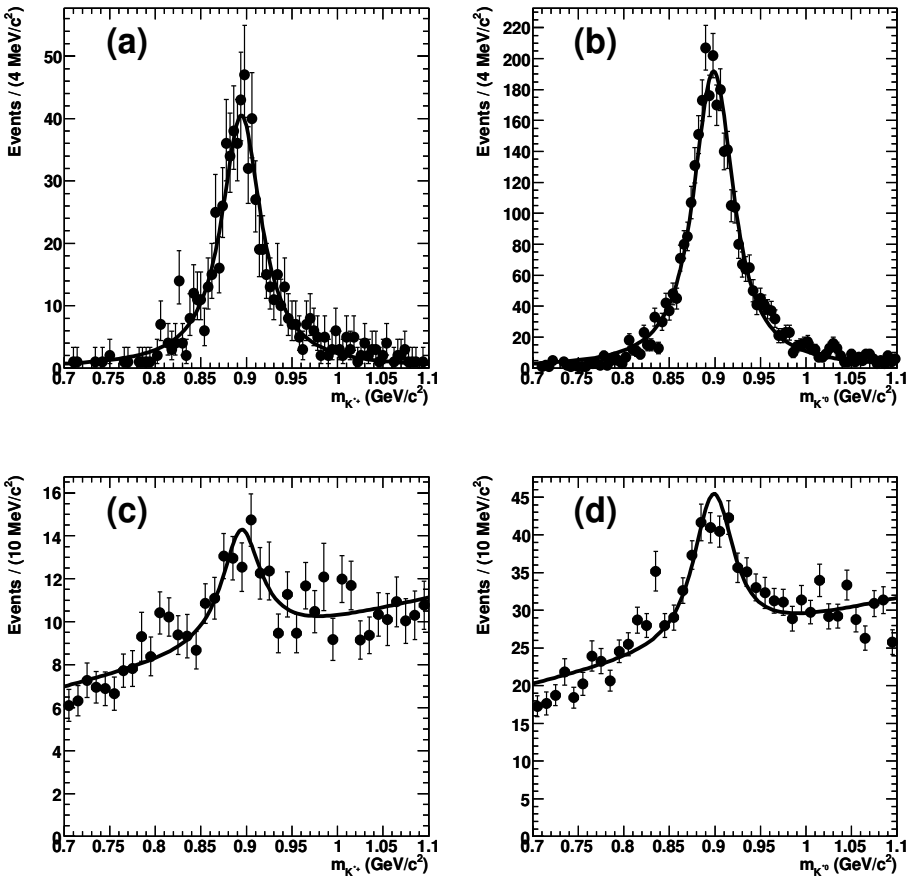

Figure 5.31: m_{K^*} PDF fits for the χ_{c1} signal and background modes, (a) $B^{\pm} \to \chi_{c1}K^{*\pm}$ signal events, (b) $B^0 \to \chi_{c1}K^{*0}$ signal events, (c) backgrounds to $B^{\pm} \to \chi_{c1}K^{*\pm}$ events, and (d) backgrounds to $B^0 \to \chi_{c1}K^{*0}$ events.

Table 5.11: Summary of the m_{miss} PDF parameter fit results for the χ_{c1} modes.

	Crystal Ball Parameter			
Decay Mode	α	m_0 (GeV/c^2)	n	σ (MeV/c^2)
$J/\psi\gamma K^{\pm}$	$1.57^{+0.05}_{-0.05}$	5.27880 ± 0.00005	144 ± 35	5.09 ± 0.04
$J/\psi\gamma K^0_S$	1.60 ± 0.10	5.27907 ± 0.00011	25 ± 12	5.11 ± 0.09
$J/\psi\gamma K^{*\pm}$	$1.34^{+0.16}_{-0.13}$	5.27923 ± 0.00022	18 ± 13	4.69 ± 0.18
$J/\psi\gamma K^{*0}$	$1.52^{+0.11}_{-0.10}$	5.27907 ± 0.00011	149 ± 35	5.04 ± 0.09

Table 5.12: Summary of the m_{miss} PDF parameter fit results for the χ_{c1} background modes.

	ARGUS Parameter		
Decay Mode	χ	c GeV/c^2	Peaking Fraction
$J/\psi\gamma K^{\pm}$	$-35.48^{+7.64}_{-7.49}$	5.299 ± 0.001	$0.174^{+0.041}_{-0.040}$
$J/\psi\gamma K^0_S$	$-46.82^{+15.02}_{-14.58}$	5.299 ± 0.001	$0.103^{+0.084}_{-0.081}$
$J/\psi\gamma K^{*\pm}$	$-29.67^{+6.92}_{-6.80}$	5.2990 ± 0.0005	0.188 ± 0.035
$J/\psi\gamma K^{*0}$	$-32.20^{+4.25}_{-4.20}$	5.2989 ± 0.0002	0.249 ± 0.022

of MC statistics for this mode, the m_X PDF could not be fit to the same precision as for the other modes (i.e. $X(3872)$ and χ_{c1}), so a single Gaussian is used rather than a double Gaussian. The results of the fit to m_X for truth-matched χ_{c2} MC are shown in Figure 5.32, with the numerical values summarized in Table 5.16.

5.3.3 PDF Correlations for χ_{cJ}

As in Section 5.1.6, the 2-D plots of m_X, m_{miss}, and m_{K^*} are useful for identifying correlation between fit variables. In the $X(3872)$ modes, no significant correlations were found. This process is repeated for the χ_{cJ} modes in Figures 5.33 – 5.36. As expected, no significant correlations are found.

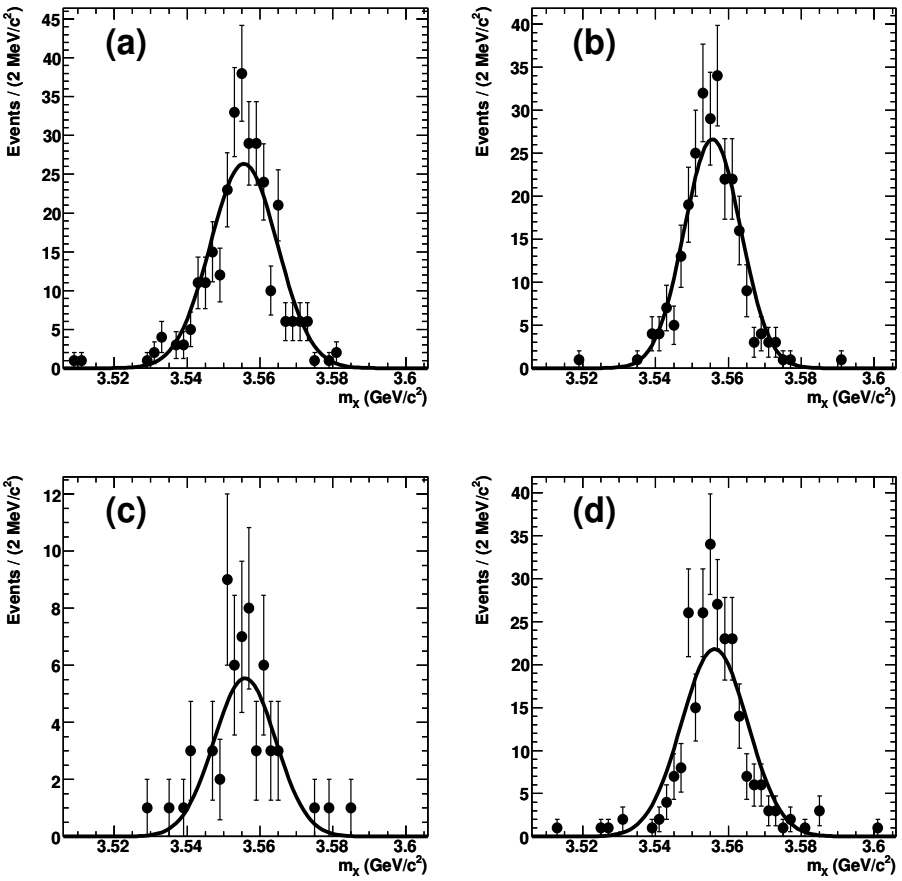

Figure 5.32: m_X PDF fits for the χ_{c2} background modes, (a) $B^{\pm} \to \chi_{c2} K^{\pm}$ events, (b) $B^0 \to \chi_{c2} K^0_s$ events, (c) $B^{\pm} \to \chi_{c2} K^{*\pm}$ events, and (d) $B^0 \to \chi_{c2} K^{*0}$ events.

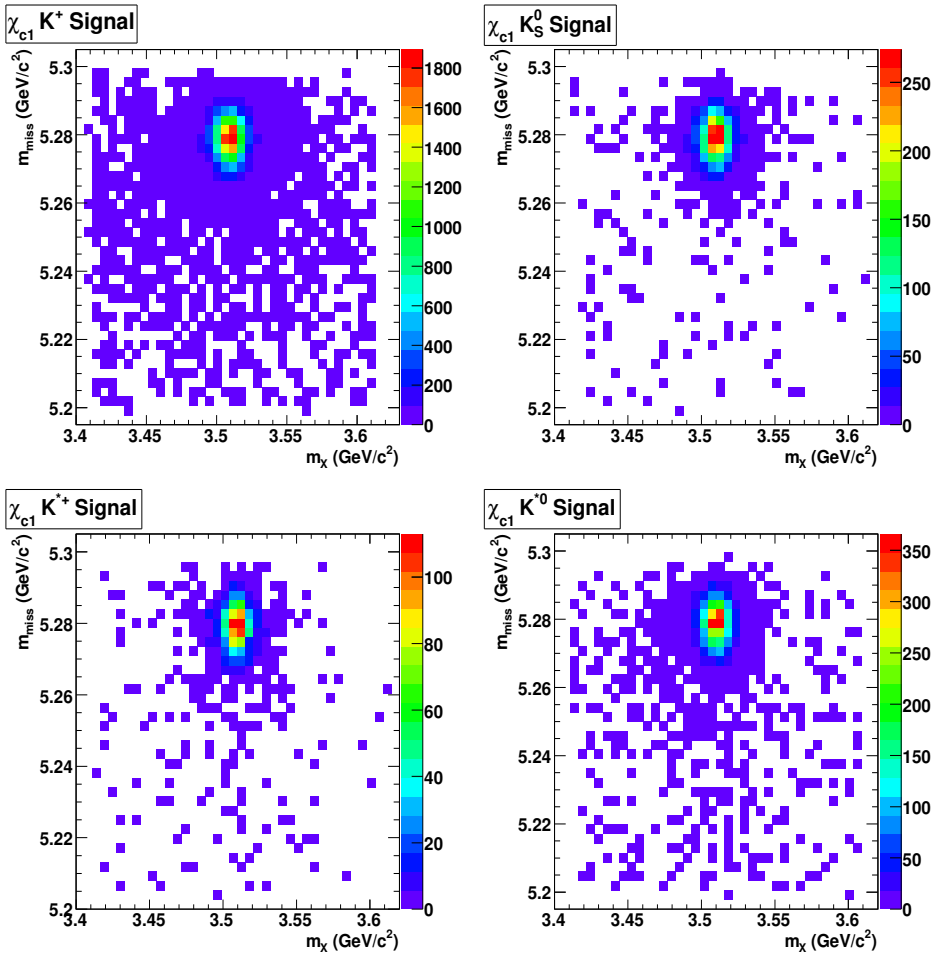

Figure 5.33: Plots of m_{miss} versus m_X for the χ_{cJ} signal modes.

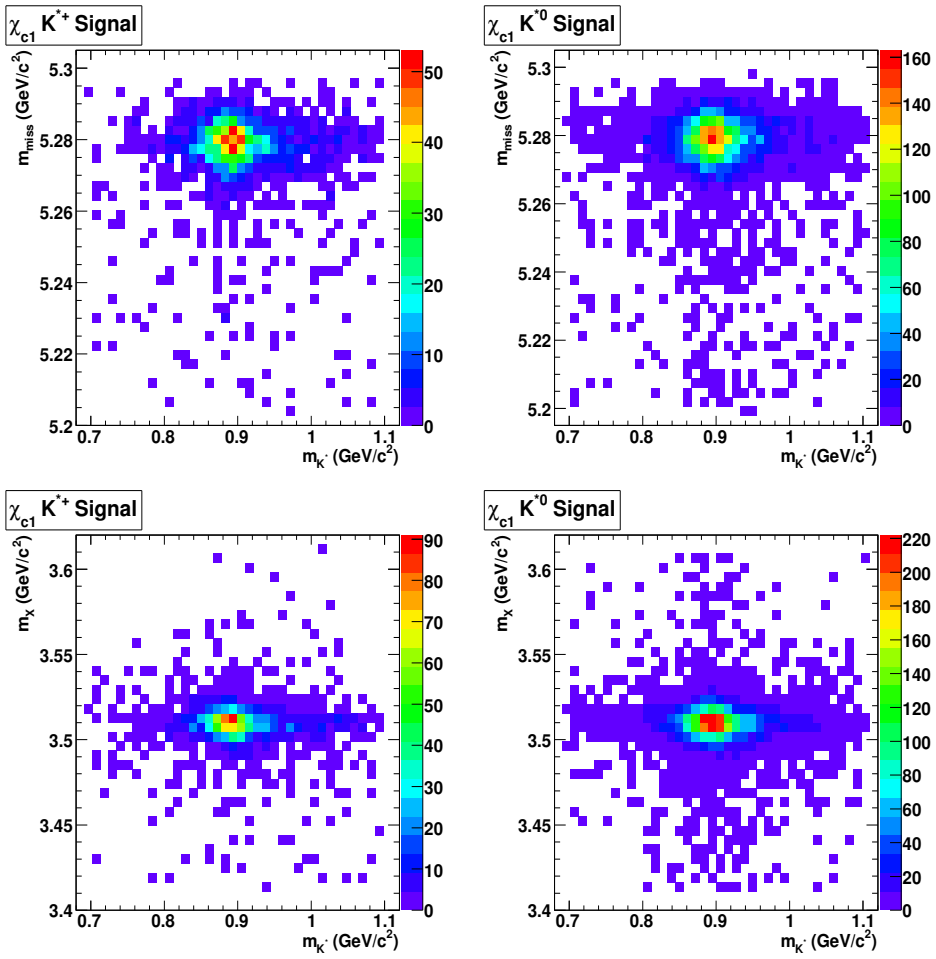

Figure 5.34: Plots of m_{miss} versus m_{K^*} and m_X versus m_{K^*} for the χ_{cJ} signal modes.

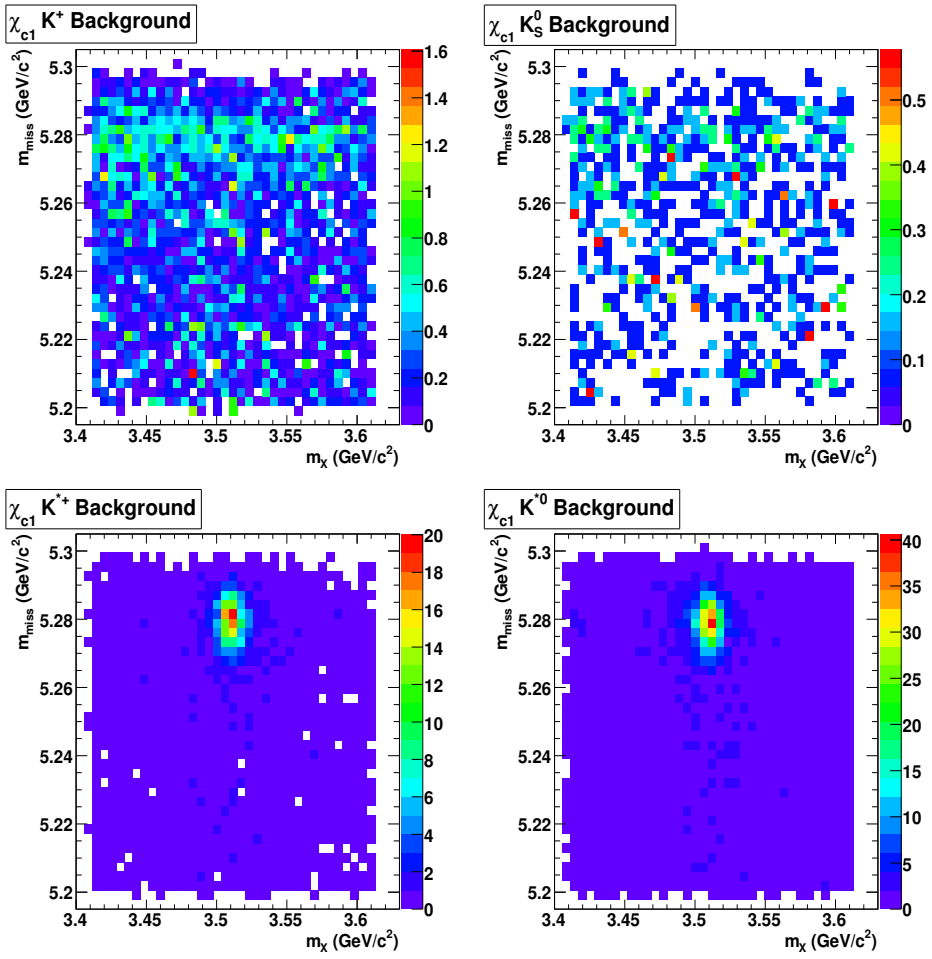

Figure 5.35: Plots of m_{miss} versus m_X for the χ_{cJ} background modes.

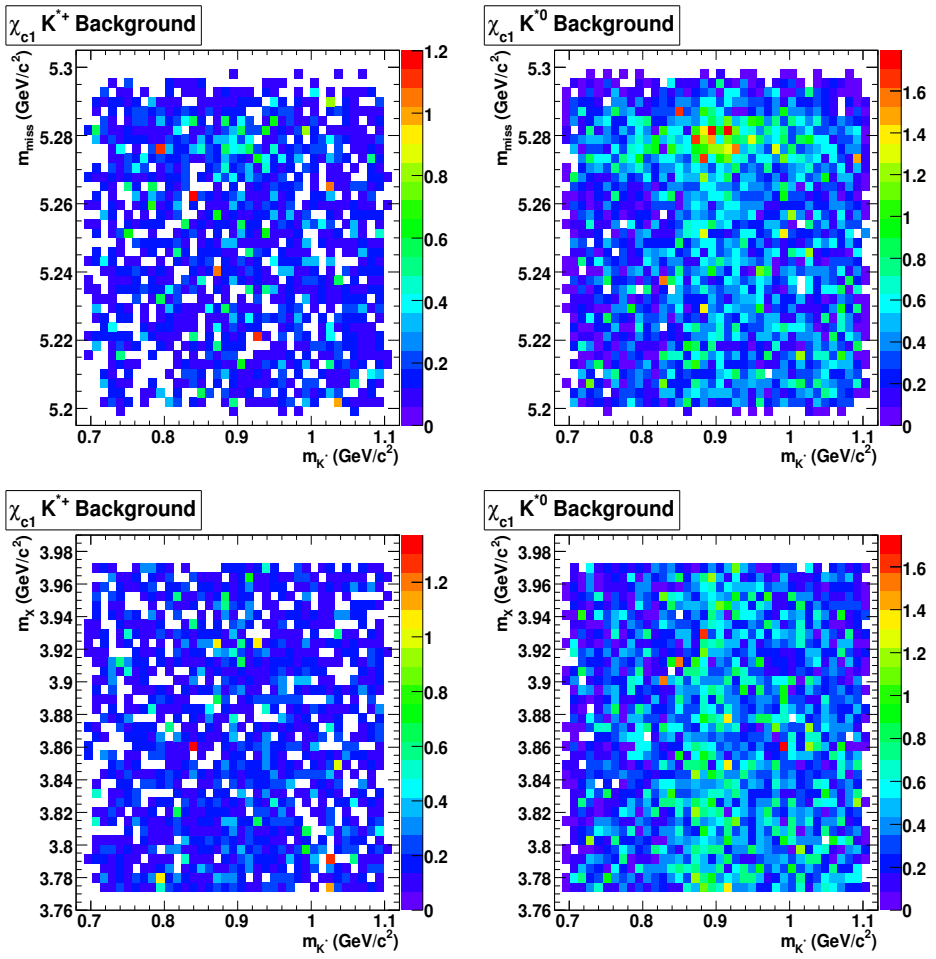

Figure 5.36: Plots of m_{miss} versus m_{K^*} and m_X versus m_{K^*} for the χ_{cJ} background modes.

Table 5.13: Summary of the m_X PDF parameter fit results for the χ_{c1} signal modes.

	Fit Parameter			
Decay	μ	σ_1	σ_2	Core
Mode	(MeV/c^2)	(MeV/c^2)	(MeV/c^2)	Fraction
$J/\psi\gamma K^{\pm}$	3509.53 ± 0.07	6.95 ± 0.11	$15.73^{+0.55}_{-0.50}$	0.84 ± 0.02
$J/\psi\gamma K^0_S$	3509.65 ± 0.14	$5.98^{+0.23}_{-0.24}$	$13.43^{+0.86}_{-0.75}$	$0.78^{+0.05}_{-0.04}$
$J/\psi\gamma K^{*\pm}$	3509.79 ± 0.24	5.17 ± 0.32	$13.08^{+1.33}_{-1.09}$	$0.76^{+0.05}_{-0.06}$
$J/\psi\gamma K^{*0}$	3509.97 ± 0.12	5.91 ± 0.15	$17.04^{+0.94}_{-0.85}$	$0.85^{+0.02}_{-0.02}$

Table 5.14: Summary of the m_X PDF parameter fit results for the χ_{c1} background modes.

	Fit Parameter	
Decay Mode	y-intercept	slope (GeV/c^2)
$J/\psi\gamma K^{\pm}$	47.13 ± 6.65	-11.20 ± 1.17
$J/\psi\gamma K^0_S$	6.94 ± 2.66	-1.61 ± 0.69
$J/\psi\gamma K^{*\pm}$	26.95 ± 7.59	-5.92 ± 1.96
$J/\psi\gamma K^{*0}$	82.11 ± 12.05	-18.17 ± 3.11

5.3.4 Treatment of $B \to \chi_{c1} K\pi$ Non-Resonant (NR) Backgrounds

Fits to two kinematics variables, m_{miss} and m_{K^*}, are used to produce the $_s$Plot versus m_X for signal extraction. Based on these two variables, four types of events are defined (with their names in parentheses): those that have a peaking distribution in both m_{miss} and m_{K^*} ("signal"), those that peak in only m_{miss} ("$K\pi$ non-resonant") or m_{K^*} ("K^* combinatoric"), and those that do not peak in either variable ("combinatoric"). Signal events were modeled with a Crystal Ball function in m_{miss} and Voigtian function in m_{K^*}. $K\pi$ non-resonant events use the same m_{miss} parametrization as signal events, but are linear in m_{K^*}. Combinatoric events of both types are modeled with the ARGUS background function in m_{miss}, and with the signal Voigtian or first-order polynomial in m_{K^*} for K^* and other combinatoric events, respectively. The parameters for the PDFs are fixed based on the

Table 5.15: Summary of the m_{K^*} PDF parameter fit results for the χ_{c1} modes.

	Decay Mode	
Parameter	$J/\psi\gamma K^{*\pm}$	$J/\psi\gamma K^{*0}$
Mean (GeV/c^2)	0.8945 ± 0.0013	0.8986 ± 0.0006
Sigma (GeV/c^2)	0.000 ± 0.005	$0.0066^{+0.0024}_{-0.0036}$
Width (GeV/c^2)	0.053 ± 0.003	0.048 ± 0.002
Bkgd Slope (GeV/c^2)	-28.1 ± 131.2	986 ± 818
Peaking Fraction	$0.102^{+0.042}_{-0.040}$	0.125 ± 0.029

Table 5.16: Summary of the m_X PDF parameter fit results for the χ_{c2} signal modes.

	Fit Parameter	
Decay Mode	μ (GeV/c^2)	σ (GeV/c^2)
$J/\psi\gamma K^{\pm}$	3.5556 ± 0.0004	0.0092 ± 0.0003
$J/\psi\gamma K^0_S$	3.5556 ± 0.0004	0.0078 ± 0.0003
$J/\psi\gamma K^{*\pm}$	3.5559 ± 0.0008	$0.0085^{+0.0006}_{-0.0005}$
$J/\psi\gamma K^{*0}$	3.5562 ± 0.0005	$0.0091^{+0.0004}_{-0.0003}$

fits to the Monte Carlo in the previous section, and allow the yield for each of these four event types to float in the final fit. Note that in m_X, both signal events and $K\pi$ non-resonant events peak at the χ_{c1} mass: this is because there is a real χ_{c1} properly reconstructed in the event, while for the combinatoric backgrounds of both types, the m_X distribution is predominantly flat.

One can get an indication of the distributions in the kinematic variables for the different background types by putting a cut requiring $m_{miss} < 5.26\,\mathrm{GeV}/c^2$. This roughly selects the combinatoric background events, whose distributions from Monte Carlo in m_X (linear) and m_{K^*} (linear plus a peaking part for events containing a real K^*) for events reconstructed as $B^{\pm} \to \chi_{c1}K^{*\pm}$ can be found in Figure 5.37. The $K\pi$ non-resonant events are sampled by requiring $5.27 < m_{miss} < 5.29\,\mathrm{GeV}/c^2$. The distribution of these events in m_X (peaking at $m_X = m_{\chi_{c1}}$ and including a flat component

from combinatoric events under the m_{miss} peak) and m_{K^*} (flat) are also found in Figure 5.37. The fits to the data shown in Figure 5.37 are used for the purpose of generating toy MC events to simulate the background in signal extraction tests. For the combinatoric events, the m_{K^*} distribution is fit with a linear plus Voigtian part, with the Voigtian parameters fixed to those determined from the signal MC, and only the relative fraction allowed to float. For the $K\pi$ non-resonant events, the m_X fit is modeled with a linear term plus a double Gaussian with the mean and core width fixed to the values determined from signal MC, and the secondary width and relative fractions allowed to float.

The same exercise can be performed for the background events for $B^0 \to \chi_{c1}K^{*0}$, shown in Figure 5.38. The combinatoric background events, selected using $m_{miss} < 5.26\,\mathrm{GeV}/c^2$, show a distribution similar to that seen for the K^{*+} mode. For the non-resonant events, the m_X distribution is fit in the same manner as for the K^* non-resonant case, but the $m_{K^{*0}}$ distribution includes some K^{*0} component, as fit with the Voigtian shape determined from signal MC. By plotting the m_X distribution versus $m_{K^{*0}}$ in Figure 5.39, one sees that the events peaking in $m_{K^{*0}}$ are due to events with a $\chi_{c0}K^{*0}$ part (based on the their collection at low m_X near $m_{\chi_{c0}}$). Indeed, this is also seen as a deviation from the fitted line at the low end of the m_X distribution for the m_{miss} peaking component in Figure 5.38. Figure 5.39 also shows there is no significant K^{*0} peak in the $m_X = m_{\chi_{c1,2}}$ regions. That is, there is no indication from the MC of any signal-like background that peaks in m_{miss}, $m_{K^{*0}}$ and $m_X = m_{\chi_{c1,2}}$.

5.3.5 χ_{c1} Cross-feed

Cross-feed for the χ_{c1} modes is slightly more substantial than for the $X(3872)$ modes. To estimate the contribution of each signal type i to each signal type j, dedicated $B \to \chi_{c1}K$ MC samples were used. To estimate the number of cross-feed events entering our samples, the number of events of type i passing the reconstruction and cuts as signal type j is divided by the total number of MC events generated, and multiplied by the expected BF for the

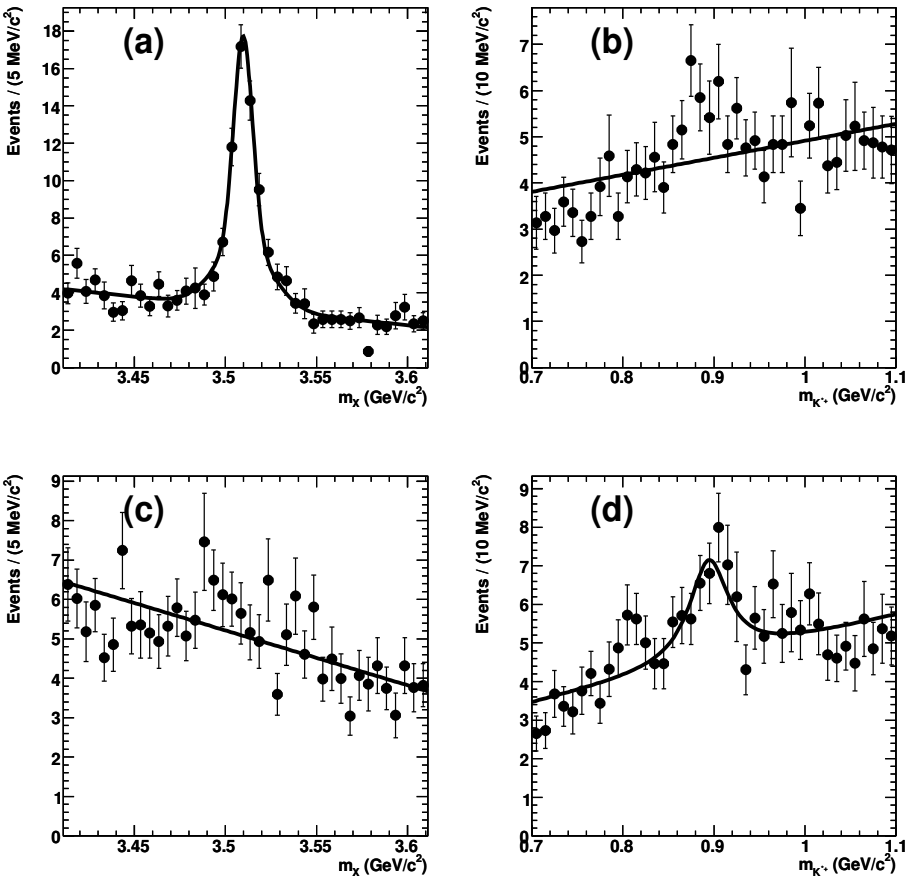

Figure 5.37: m_X and $m_{K^{*\pm}}$ distributions from MC for backgrounds to $\chi_{c1}K^{*\pm}$ events that are peaking ($K\pi$ non-resonant, a and b) or non-peaking (combinatoric, c and d) in m_{miss}.

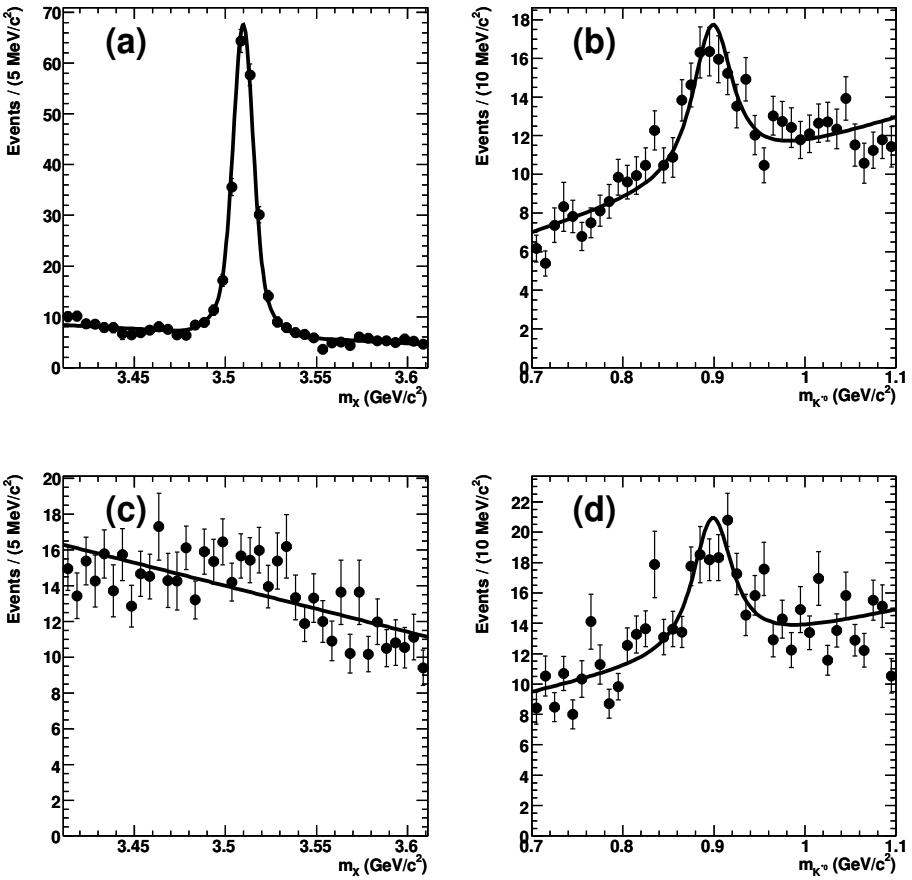

Figure 5.38: m_X and $m_{K^{*0}}$ distributions from MC for backgrounds to $\chi_{c1}K^{*0}$ events that are peaking ($K\pi$ non-resonant, a and b) or non-peaking (combinatoric, c and d) in m_{miss}.

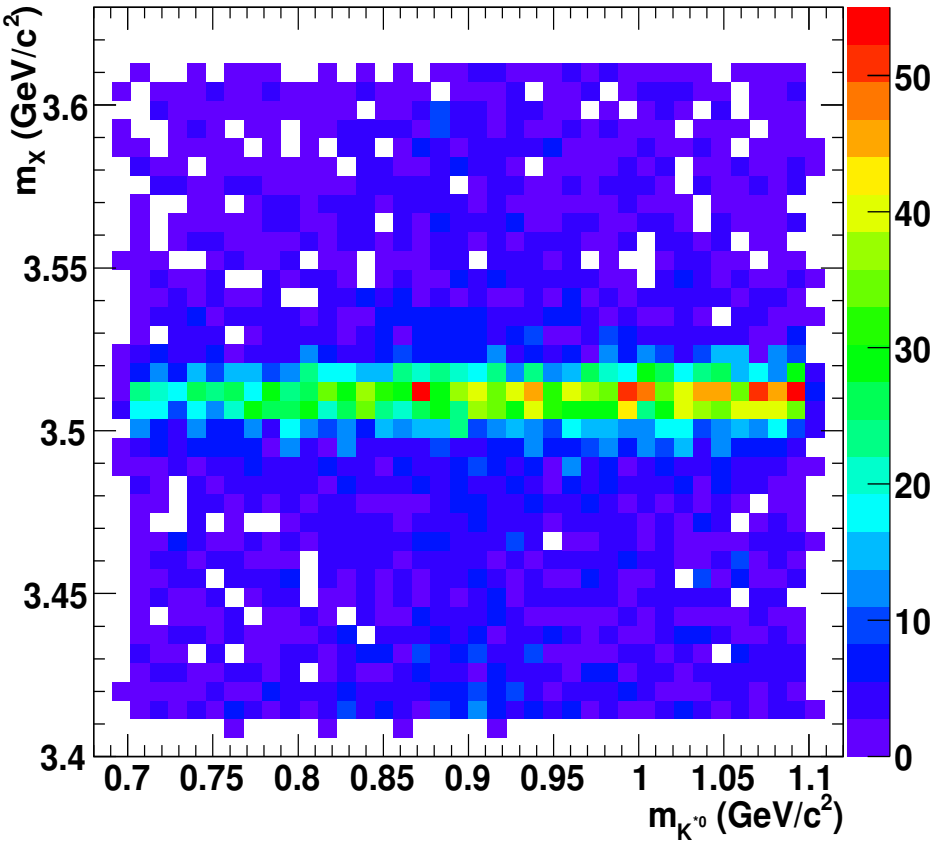

Figure 5.39: m_X versus $m_{K^{*0}}$ for $\chi_{c1}K^{*0}$ background MC events in the range $5.27 < m_{miss} < 5.29\,\mathrm{GeV}/c^2$. The small excess of events near $m_{K^{*0}} = m_{K^{*0}_{PDG}}$ in Figure 5.38 is from events in a low mass region near $m_X = m_{\chi c0}$ ($\sim 3.414\,\mathrm{GeV}/c^2$).

decay mode of type i. Although these events pass reconstruction and selection cuts, their distributions are not necessarily signal-like. For the cases where the number of cross-feed events of type i is greater than 1% of the total expected number of events of type j[20], the expected number of cross-feed events are passed into a fit with the expected number of signal and background MC events to determine by what amount the cross-feed affects the signal extraction. The results for this study are summarized in Table 5.17. The cross-feed from the K^* modes was not calculated due to lack of MC production. However, based on the results from the other event types, it is believed to be a tiny effect. The amount of cross-feed was simultaneously calculated for the χ_{c2} decay modes, and this was also found to be negligible.

Table 5.17: The number of cross-feed events and their expected fraction of the total signal for the $B \to \chi_{cJ}K$ modes. "N/A" modes cannot cross-feed to themselves. "($<<$ 1%)" indicates that the number of cross-feed events passing selection cuts is below 1%, and the resulting number of cross-feed events returned from a fit to the distribution is expected to essentially be zero. All results are negligible.

Decay Mode	Expected Contribution per Mode			
	$\chi_{c1}K^{\pm}$	$\chi_{c1}K^0_S$	$\chi_{c1}K^{*\pm}$	$\chi_{c1}K^{*0}$
$\chi_{c1}K^{\pm}$	N/A	($<<$ 1%)	($<<$ 1%)	0.27($<$ 0.1%)
$\chi_{c1}K^0_S$	($<<$ 1%)	N/A	0.06($<$ 0.1%)	0.01($\sim$ 0%)

5.3.6 χ_{c1} Signal Extraction Efficiency

The total signal extraction efficiency for the χ_{c1} decay modes was calculated using a similar procedure to that used for the $X(3872)$ modes. First, the efficiency of the reconstruction and applied cuts was found using only the $B\overline{B}$ generic MC sample. The total number of events generated in the MC was calculated from the branching fractions as defined in the MC generator decay file, which differ slightly from the most recent PDG values. The efficiency values are given in Table 5.18.

[20] Cases where the maximum amount of cross-feed is expected to be less than 1% of the total number of events are ignored.

Table 5.18: Summary of the reconstruction and event selection efficiency for $B \to \chi_{c1} K$ MC events.

Decay Mode	Events Generated	Pass cuts/reco	Efficiency (%)
$\chi_{c1} K^{\pm}$	29890 ± 173	3478	11.6 ± 0.1
$\chi_{c1} K^0_S$	8278 ± 91	753	9.1 ± 0.1
$\chi_{c1} K^{*\pm}$	3474 ± 59	219	6.3 ± 0.1
$\chi_{c1} K^{*0}$	10491 ± 102	908	8.7 ± 0.1

The fit bias and efficiency were estimated with $\chi_{c1} K$ events drawn from the $B\overline{B}$ generic and J/ψ Inclusive MC samples. Using the same procedure as defined for the $X(3872)$, a number of signal and background events roughly equal to that expected in data was input and then extracted using signal MC events and generated toy MC background events. At this stage, a χ_{c2} component is included in the m_X fit but zero χ_{c2} events were actually included in the test MC samples. For the K^* modes, an additional and separate non-resonant background component is generated and added to the signal extraction trials. The expected number of non-resonant-like events in data was estimated by imposing a cut of $5.27 < m_{miss} < 5.29\,\mathrm{GeV}/c^2$ and counting the number of surviving events in the MC background sample. While the non-resonant event PDF in the fit assumes a linear shape in m_{K^*}, in the tests of the signal extraction efficiency, the shapes of the m_{K^*} and m_X distributions were refit to the MC using the linear plus Voigtian parametrization discussed in Section 5.3.4 and generated with those distributions. The results are summarized in Table 5.19.

The total efficiency is a combination of the reconstruction and cut efficiency multiplied by the fit efficiency corrected for bias effects. The results for the χ_{c1} modes are given in Table 5.20. The efficiency of the $B^{\pm} \to \chi_{c1} K^{\pm}$ decay mode found here ($\sim 11\%$) is comparable to that from the previous version of this analysis ($\sim 13\%$) [37].

Table 5.19: Results of tests of signal extraction for $B \to \chi_{c1}K$ MC events with PDF-generated background events.

Decay Mode	Trials	Sig. In	Bkgd. In	NR In	Bias	Corrected Output	Fit Eff. (%)
$\chi_{c1}K^{\pm}$	24	1118	323	0	-2 ± 7	1072 ± 10	95.9 ± 0.9
$\chi_{c1}K^0_S$	16	241	75	0	$+7 \pm 4$	231 ± 6	95.9 ± 2.3
$\chi_{c1}K^{*\pm}$	15	103	270	130	$+10 \pm 5$	94 ± 6	91.1 ± 5.7
$\chi_{c1}K^{*0}$	12	362	749	435	-14 ± 8	332 ± 11	91.7 ± 3.1

Table 5.20: Total signal extraction efficiency for $B \to \chi_{c1}K$ signal modes based on MC samples.

Decay	Cut/Reco Efficiency (%)	Fit Efficiency (%)	Total Efficiency (%)
$\chi_{c1}K^{\pm}$	11.6 ± 0.1	95.9 ± 0.9	11.2 ± 0.1
$\chi_{c1}K^0_S$	9.1 ± 0.1	95.9 ± 2.3	8.7 ± 0.2
$\chi_{c1}K^{*\pm}$	6.3 ± 0.1	91.1 ± 5.7	5.7 ± 0.4
$\chi_{c1}K^{*0}$	8.7 ± 0.1	91.7 ± 3.1	7.9 ± 0.3

5.3.7 χ_{c2} Signal Extraction Efficiency

Although no signal is expected for χ_{c2}, the efficiency for its detection can be calculated based on our MC. The cut and reconstruction efficiency is defined identically to that used for the other decay modes. The number of events surviving the reconstruction and selection cuts is summarized in Table 5.21. The number of generated events is not an absolute value: it is calculated from the branching fractions as defined in the EvtGen decay definition file for $B\overline{B}$ generic events supplemented with events from the dedicated $\chi_{c1,2}$ Inclusive MC sample.

In the previous section, the χ_{c1} signal extraction was tested including a fit for a χ_{c2} component even though no events of that type were added to the MC sample. The results of the χ_{c2} portion of this fit are summarized in Table 5.22. These tests indicate that there is no significant interference or bias from the adjacent large χ_{c1} peak in m_X that would affect a χ_{c2} signal.

Table 5.21: Summary of the reconstruction and event selection efficiency for $B \to \chi_{c2}K$ MC events.

Decay Mode	Events Generated	Pass cuts/reco	Efficiency (%)
$\chi_{c2}K^{\pm}$	5481 ± 26	692	12.6 ± 0.1
$\chi_{c2}K^0_S$	2433 ± 26	266	10.9 ± 0.1
$\chi_{c2}K^{*\pm}$	1919 ± 18	125	6.5 ± 0.1
$\chi_{c2}K^{*0}$	2243 ± 26	201	9.0 ± 0.1

This is in contrast to the results obtained in the previous analysis [37].

Table 5.22: Test of signal extraction for χ_{c2} with zero χ_{c2} MC events included in the sample.

Decay Mode	Trials	χ_{c1} In	Bkgd. In	NR χ_{c1} In	χ_{c2} In	χ_{c2} Out
$\chi_{c2}K^{\pm}$	24	1118	323	0	0	-2.7 ± 1.1
$\chi_{c2}K^0_S$	16	241	75	0	0	1.2 ± 0.6
$\chi_{c2}K^{*\pm}$	15	103	270	130	0	-0.4 ± 0.9
$\chi_{c2}K^{*0}$	12	362	749	435	0	-2.2 ± 3.3

To estimate the efficiency of the fit for the χ_{c2} modes, the signal extraction trials are repeated while including a number of χ_{c2} MC events based upon the expected efficiency, the available number of events in MC, and branching fraction upper limit as given in the PDG [71]. The number of χ_{c1}, background, and $K\pi$ non-resonant events remains the same as given in Table 5.19. The number of $\chi_{c2}K\pi$ non-resonant events is assumed to be zero. The results and the total signal efficiency are summarized in Tables 5.23 and 5.24.

Table 5.23: Results of tests of signal extraction for $B \to \chi_{c2}K$ MC events with PDF-generated background events. The Total Efficiency is derived using the cut and reconstruction efficiency from Table 5.22.

Decay Mode	Trials	Sig. In	Bias	Corrected Output	Fit Eff. (%)
$\chi_{c2}K^{\pm}$	24	34	$+0.7 \pm 1.7$	33.6 ± 2.4	99 ± 7
$\chi_{c2}K^0_S$	16	17	$+4.3 \pm 1.1$	17.3 ± 1.6	102 ± 10
$\chi_{c2}K^{*\pm}$	15	9	$+0.5 \pm 1.5$	5.8 ± 2.0	65 ± 22
$\chi_{c2}K^{*0}$	12	30	$+1.2 \pm 0.3$	27.8 ± 0.5	93 ± 2

Table 5.24: Total signal extraction efficiency for $B \to \chi_{c2}K$ signal modes based on MC samples.

Decay	Cut/Reco Efficiency (%)	Fit Efficiency (%)	Total Efficiency (%)
$\chi_{c2}K^{\pm}$	12.6 ± 0.1	99 ± 7	12.5 ± 0.8
$\chi_{c2}K^0_S$	10.9 ± 0.1	102 ± 9	11.1 ± 1.0
$\chi_{c2}K^{*\pm}$	6.5 ± 0.1	65 ± 22	4.2 ± 1.4
$\chi_{c2}K^{*0}$	9.0 ± 0.1	93 ± 2	8.3 ± 0.2

Chapter 6

Signal Extraction from Data

This chapter presents the results of the signal extraction for $B \to \chi_{c1,2}K$, and $B \to X(3872)K$ for $X(3872) \to J/\psi\gamma$ and $X(3872) \to \psi(2S)\gamma$, from the full *BABAR* dataset. The final measurements of the branching fractions or their upper limits are calculated here. The results exploring the $c\bar{c}\gamma$ invariant mass range up to the kinematic limit are also shown.

6.1 $\chi_{c1,2}$ Signal Extraction from Data

A useful verification of the signal extraction method is to measure $\mathcal{B}(B \to \chi_{c1}K)$ from data, and to compare it with other previous experimental results. As a cross-check, the raw data distributions and their comparison with the generic MC sample (includes both signal and background) for the variables of interest are examined. The results for $\chi_{c1}K^{\pm}$, $\chi_{c1}K^0_S$, $\chi_{c1}K^{*\pm}$, and $\chi_{c1}K^{*0}$ are shown in Figures 6.1, 6.2, 6.3, and 6.4, respectively. There is fair agreement in the peaking regions. Note that the branching fractions for $B \to \chi_{c1}K$ in MC are only approximately equal to the current PDG values, so a difference in the peak height is expected. While the relative normalization between the peaking and the background events in MC does not exactly match the data (as evidenced by the lacking "sideband" regions), the features of the distributions are the same; hence the chosen parametrizations are good. These differences in the MC event yield are accounted for by allowing the event yields to vary in the final fit.

Using the PDFs defined from MC with the m_{miss} ARGUS parameters allowed to float (see Section 6.2.2), the number $B \to J/\psi\gamma K$ events in the χ_{c1} mass region is found by fitting the $_s$Plot result with the m_X double-Gaussian plus linear background shape, allowing the number of signal and

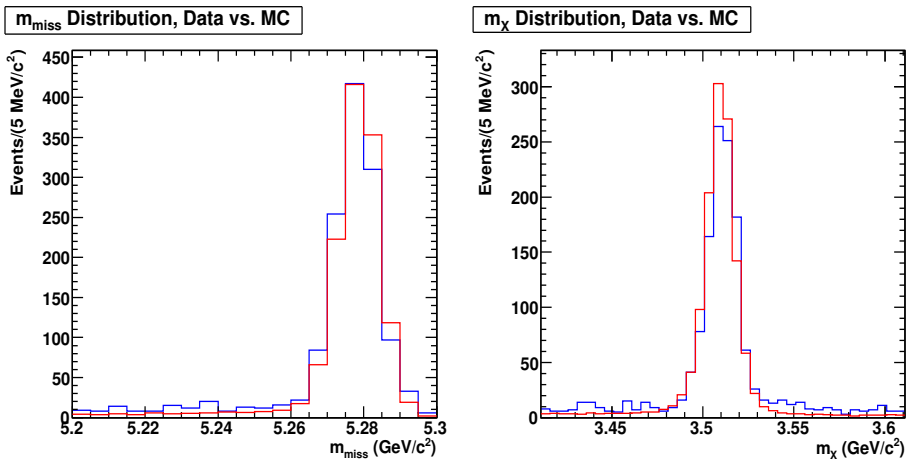

Figure 6.1: Comparison of data (blue) and MC (red) for m_X and m_{miss} for $B^{\pm} \to \chi_{c1} K^{\pm}$.

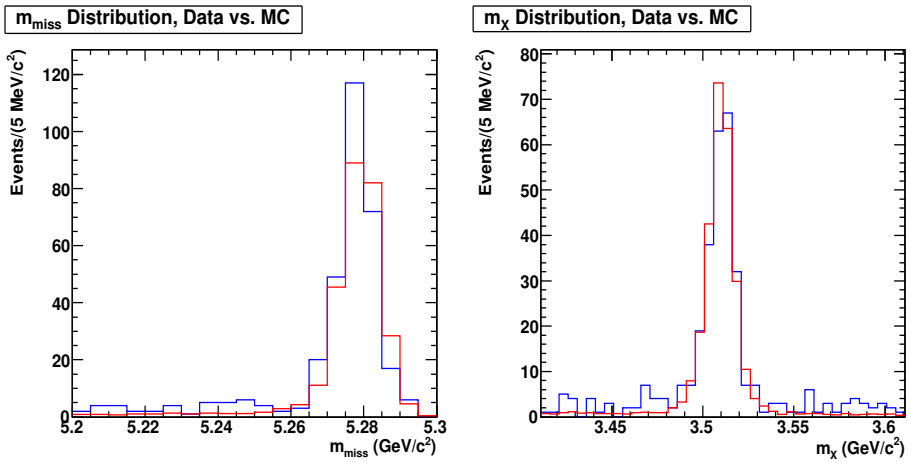

Figure 6.2: Comparison of data (blue) and MC (red) for m_X and m_{miss} for $B^0 \to \chi_{c1} K^0_S$.

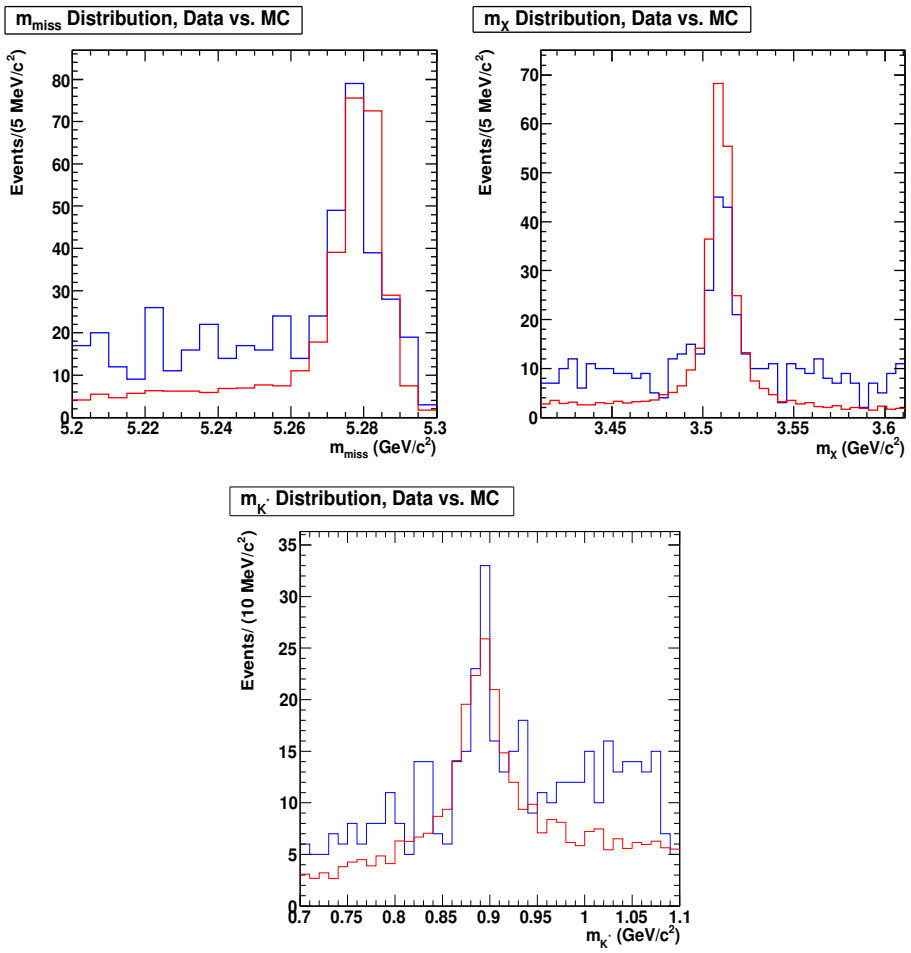

Figure 6.3: Comparison of data (blue) and MC (red) for m_X, m_{miss} and $m_{K^{*\pm}}$ for $B^{\pm} \to \chi_{c1} K^{*\pm}$.

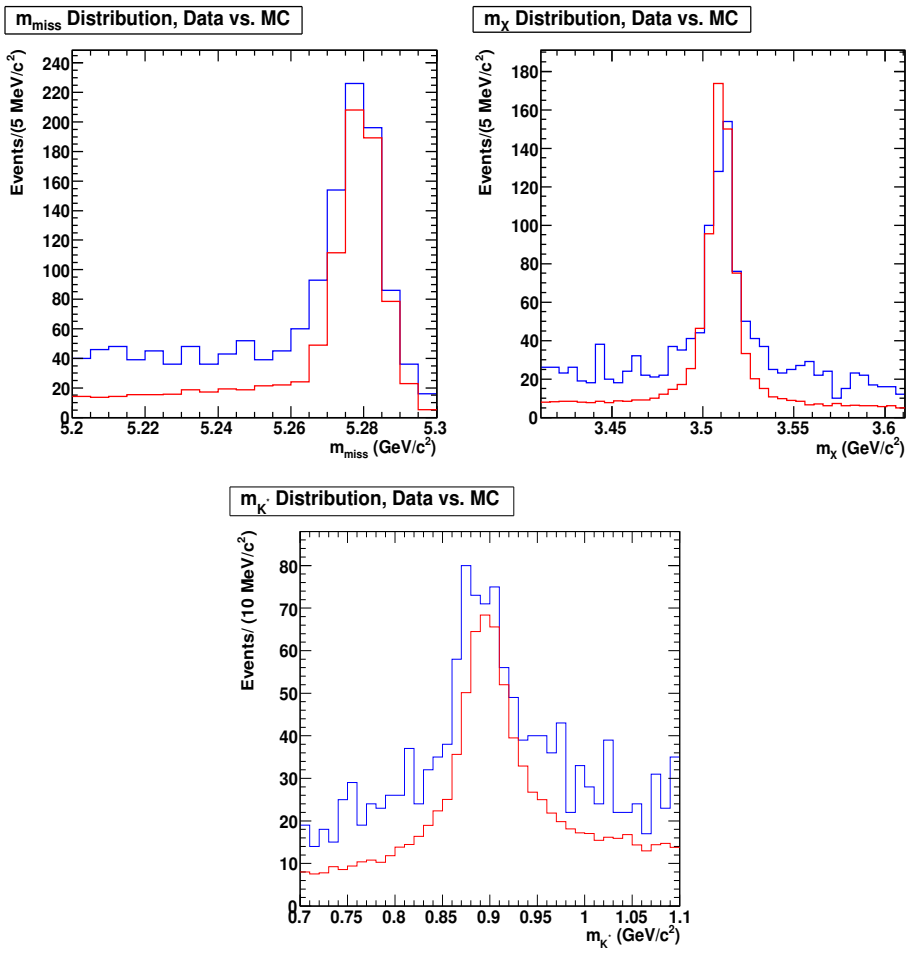

Figure 6.4: Comparison of data (blue) and MC (red) for m_X, m_{miss} and $m_{K^{*0}}$ for $B^0 \to \chi_{c1} K^{*0}$.

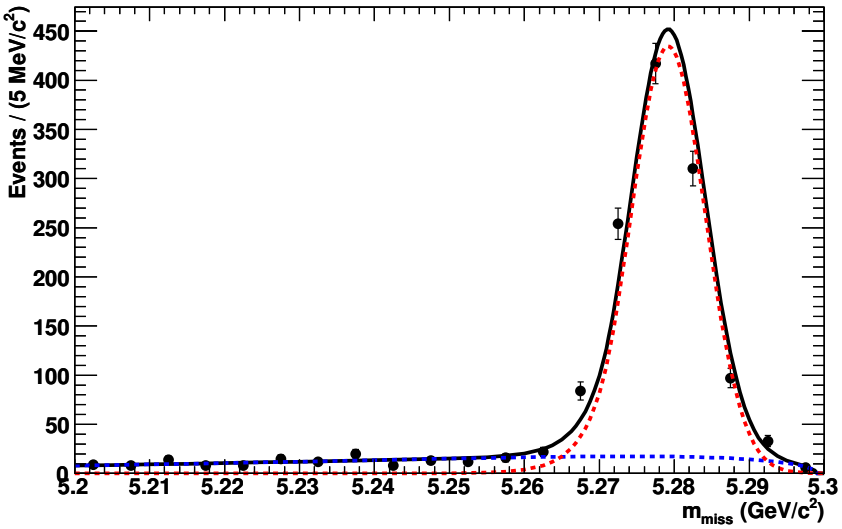

Figure 6.5: Projection of the peaking (dashed red) and background (dashed blue) event components for the fit to m_{miss} for $B^{\pm} \to \chi_{cJ} K^{\pm}$. The solid line represents the sum. The points are from data.

peaking background events and the linear background parameters to float. The number of signal events in the χ_{c2} region is found by adding a single Gaussian component to the fit, as determined in Section 5.3.2. The event yields are unrestricted in the fit, and are permitted to fluctuate statistically to negative values. The results of the UML fit to generate the ${}_sPlot$ weights, with projections of the various event type components, are shown in Figures 6.5 – 6.8. These plots demonstrate that the choice of parametrization was generally adequate, as described previously in this Section. The signal extraction results using this method and the corresponding ${}_sPlot$s for each event type are shown in Figures 6.9 – 6.11.

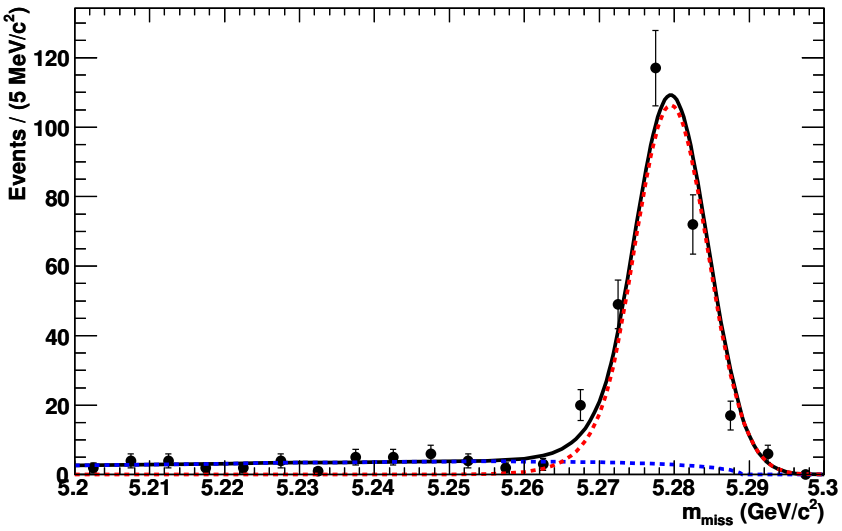

Figure 6.6: Projection of the peaking (dashed red) and background (dashed blue) event components for the fit to m_{miss} for $B^0 \to \chi_{cJ} K^0_S$. The solid line represents the sum. The points are from data.

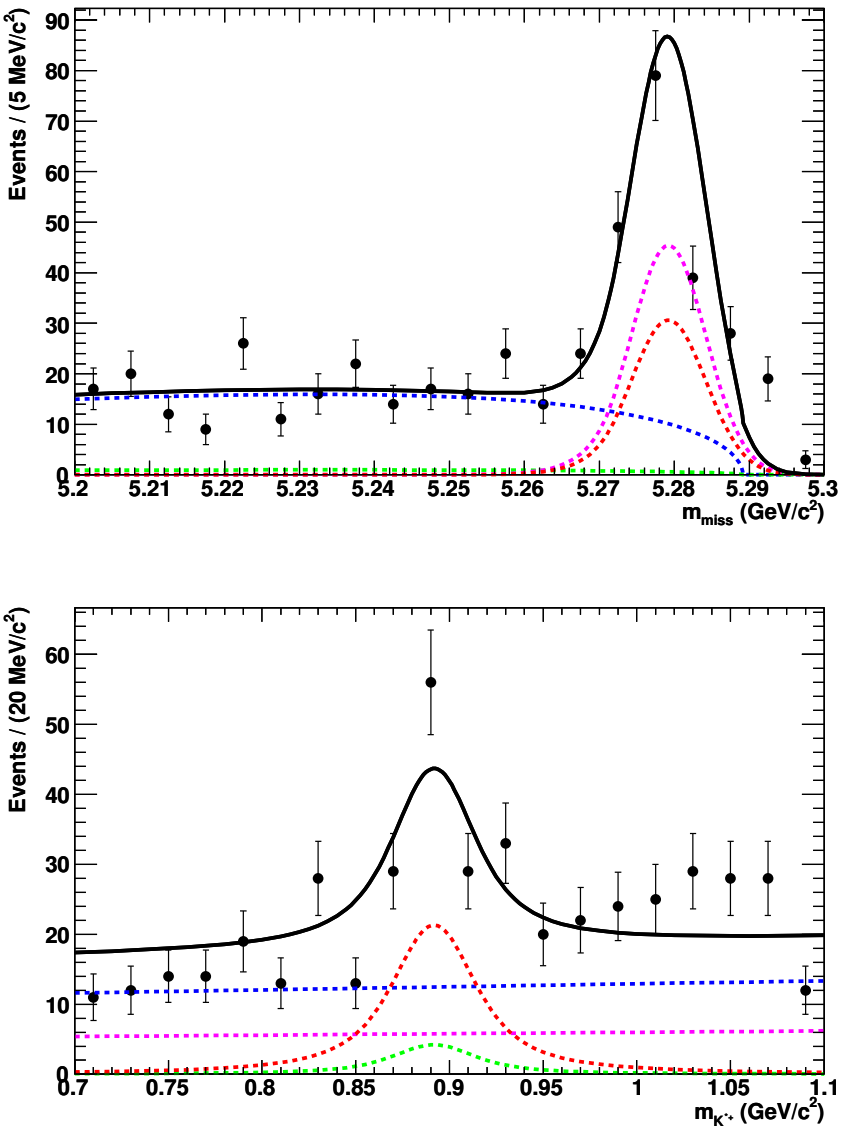

Figure 6.7: Projection of the signal (dashed red), combinatoric background with (dashed blue) and without (dashed green) a K^{*+}, and non-resonant background (dashed magenta) event components for the fit to m_{miss} and $m_{K^{*\pm}}$ for $B^{\pm} \to \chi_{cJ} K^{*\pm}$. The solid line represents the sum. The points are from data.

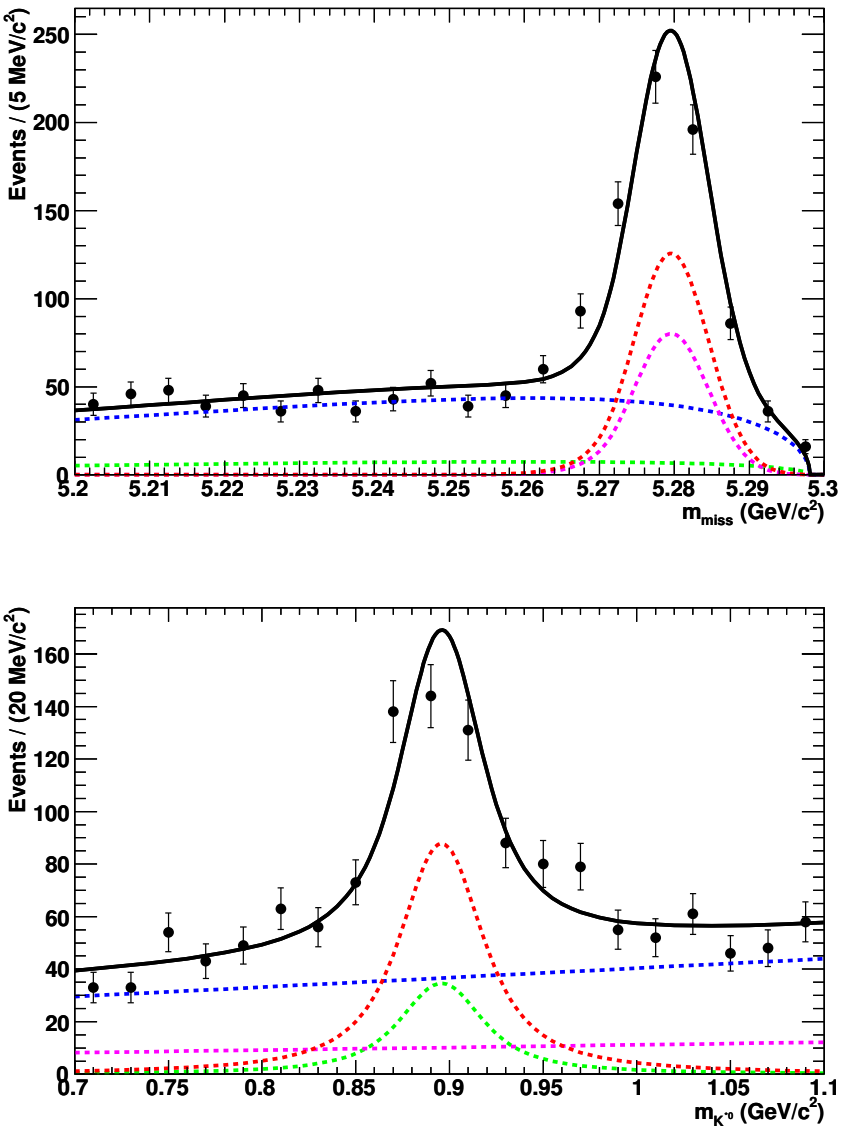

Figure 6.8: Projection of the signal (dashed red), combinatoric background with (dashed blue) and without (dashed green) a K^{*0}, and non-resonant background (dashed magenta) event components for the fit to m_{miss} and $m_{K^{*0}}$ for $B^0 \to \chi_{cJ} K^{*0}$. The solid line represents the sum. The points are from data.

The number of events measured in each mode can be related back to a branching fraction measurement of $B \to \chi_{c1,2}K$ via

$$\mathcal{B}(B \to \chi_{c1,2}K) = \frac{N_{fit} - N_{bias}}{N_B \cdot \epsilon_{tot} \cdot \mathcal{B}(\chi_{c1,2} \to J/\psi\gamma) \cdot \mathcal{B}(J/\psi \to \ell^+\ell^-) \cdot \mathcal{B}(K \to x)} \tag{6.1}$$

where N_{fit} is the number of extracted events, N_{bias} is the bias correction from Table 5.19, N_B is the number of B mesons in the data[21], ϵ_{tot} is the signal extraction efficiency (see Tables 5.20 and 5.23, and the PID correction factor given in Section 6.3.7), and the remaining terms represent branching fractions of particle decays (where the decay $K \to x$ represents the decay chain of a composite kaon to the daughters specified in this analysis). Using the PDG values for these branching fractions [33] and calculating N_B from the number of events in Run 1–6 data as given in Table 4.1, the branching fractions for $B \to \chi_{c1}K$ are derived and given in Table 6.1. The significance is defined as the square root of the difference in the χ^2 values of the fit with and without a signal component included. The uncertainty on these results is statistical only; systematic uncertainties are included in Section 6.3.

Table 6.1: Results of $B \to \chi_{c1,2}K$ signal extraction from data. Error is statistical only.

Decay	Events (Corrected)	σ	Total Eff.	Daughter BFs [33]	Derived $\mathcal{B}(B \to \chi_{c1,2}K)$
$\chi_{c1}K^{\pm}$	1018 ± 34	31σ	11.0%	2.21%	$(4.50 \pm 0.15)\times10^{-4}$
$\chi_{c1}K^0_S$	242 ± 16	14σ	8.7%	0.72%	$(4.18 \pm 0.28)\times10^{-4}$
$\chi_{c1}K^{*\pm}$	71 ± 13	4.9σ	5.7%	0.51%	$(2.63 \pm 0.47)\times10^{-4}$
$\chi_{c1}K^{*0}$	255 ± 25	11σ	8.0%	1.4%	$(2.50 \pm 0.24)\times10^{-4}$
$\chi_{c2}K^{\pm}$	14.0 ± 7.9	1.8σ	12.3%	1.22%	$(1.00 \pm 0.56)\times10^{-5}$
$\chi_{c2}K^0_S$	6.1 ± 3.9	0.6σ	11.1%	0.40%	$(1.48 \pm 0.95)\times10^{-5}$
$\chi_{c2}K^{*\pm}$	1.2 ± 4.7	0.2σ	4.2%	0.28%	$(1.09 \pm 4.27)\times10^{-5}$
$\chi_{c2}K^{*0}$	38.8 ± 10.5	3.7σ	8.3%	0.76%	$(6.60 \pm 1.78)\times10^{-5}$

[21] The ratio of $\Upsilon(4S)$ decays to B^+B^- and $B^0\overline{B}^0$ is not assumed to be equal to 1. N_B is derived from the total number of $B\overline{B}$ pairs multiplied by a factor of 2 and $\mathcal{BF}(\Upsilon \to B^+B^-)$ or $\mathcal{BF}(\Upsilon \to B^0\overline{B}^0)$, as appropriate.

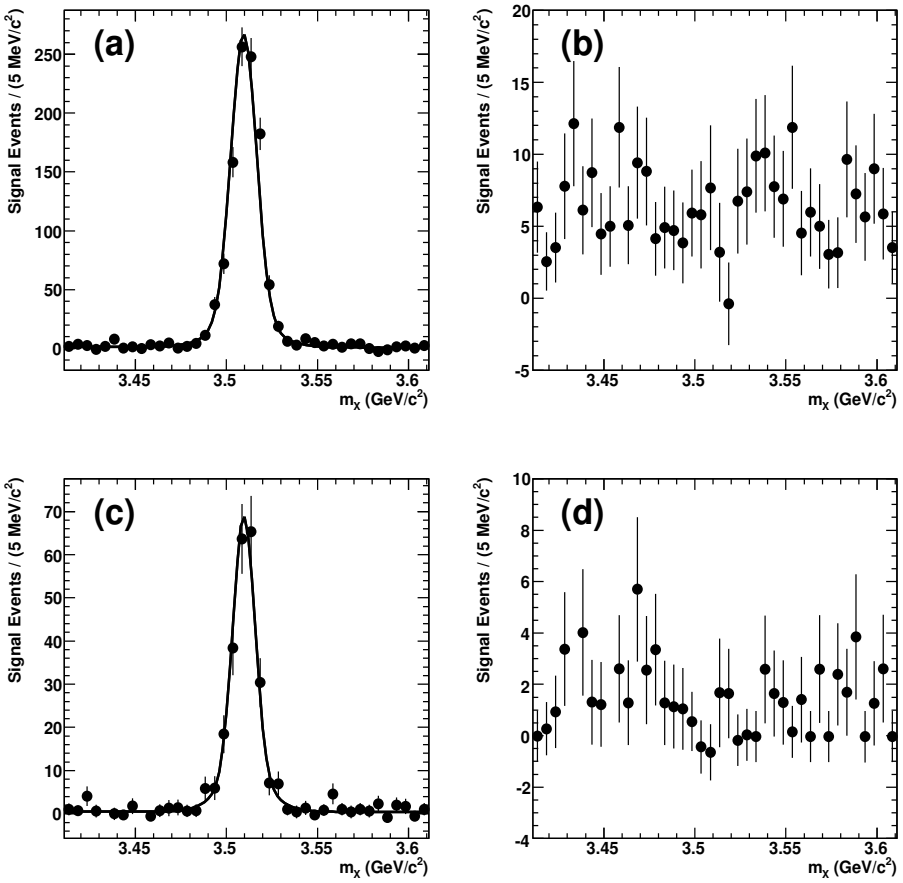

Figure 6.9: $_s$Plots for the number of events versus m_X for $B \to \chi_{c1,2}K$ from data: (a) $B^{\pm} \to \chi_{c1,2}K^{\pm}$ signal events, (b) $B^{\pm} \to \chi_{c1,2}K^{\pm}$ background events, (c) $B^0 \to \chi_{c1,2}K^0_S$ signal events, and (d) $B^0 \to \chi_{c1,2}K^0_S$ background events.

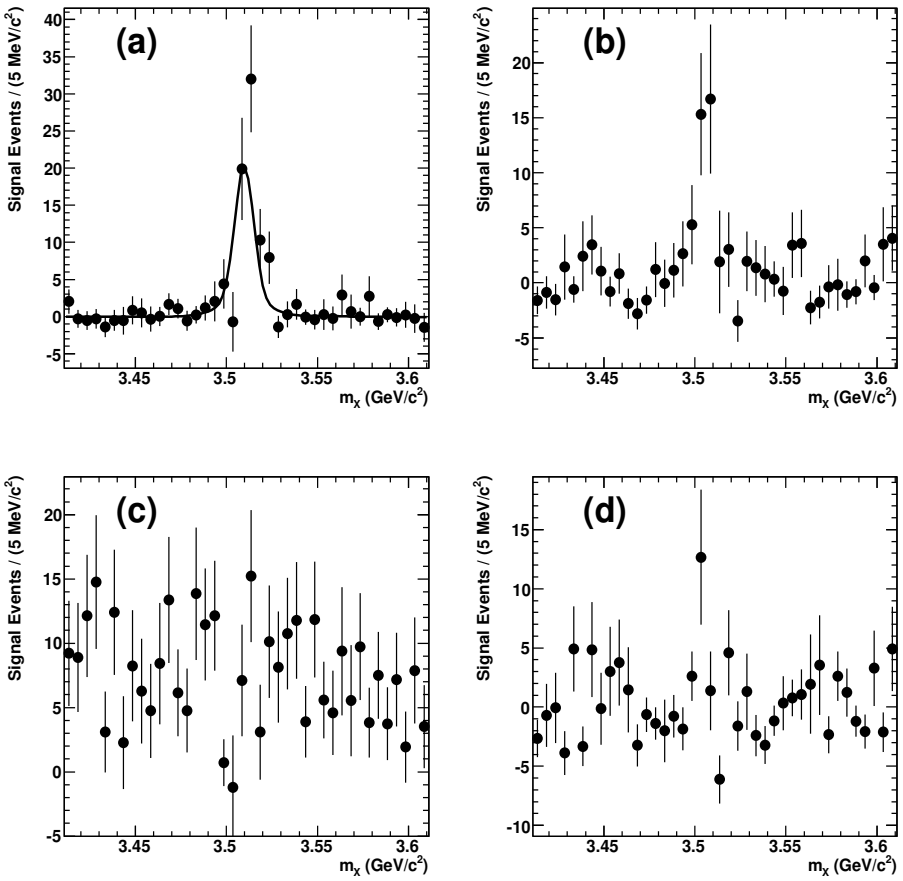

Figure 6.10: $_s$Plots for the number of events versus m_X for $B^{\pm} \to \chi_{c1,2} K^{*\pm}$ from data: (a) signal events, (b) $B^{\pm} \to \chi_{c1,2} K^0_S \pi^{\pm}$ non-resonant events, (c) combinatoric background events, and (d) $K^{*\pm}$ combinatoric background events.

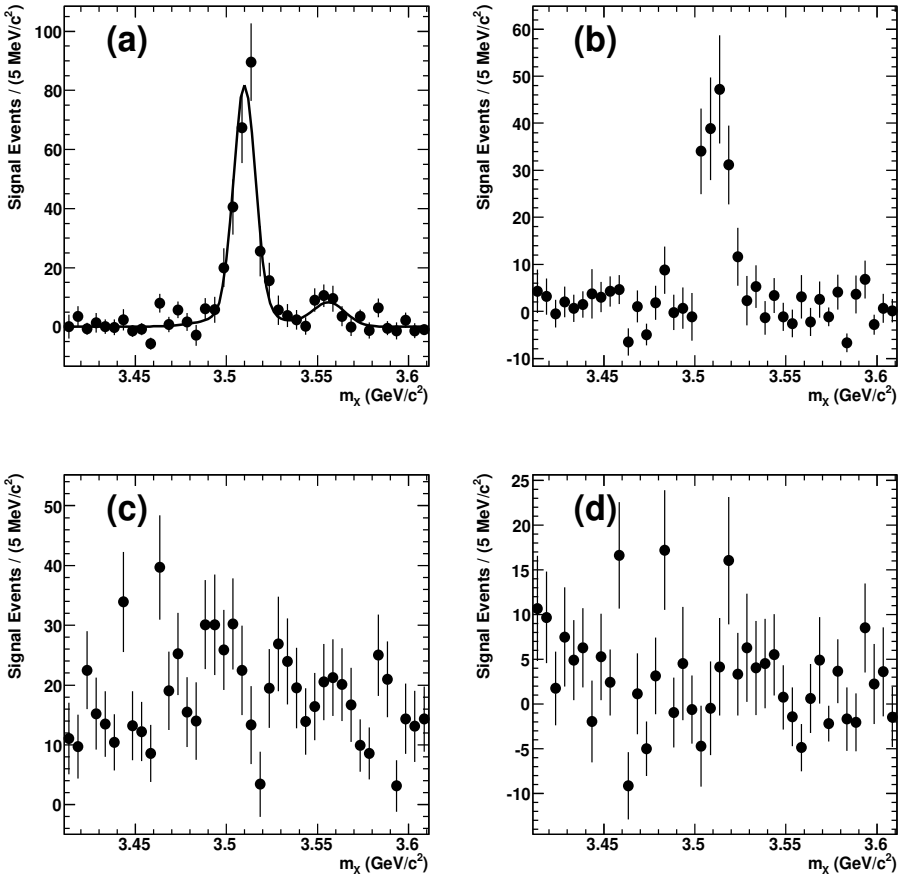

Figure 6.11: $_s$Plots for the number of events versus m_X for $B^0 \to \chi_{c1,2}K^{*0}$ from data: (a) signal events, (b) $B^0 \to \chi_{c1,2}K^{\pm}\pi^{\mp}$ non-resonant events, (c) combinatoric background events, and (d) K^{*0} combinatoric background events.

6.2 $X(3872)$ Signal Extraction from Data

6.2.1 $B \to X(3872)K$, $X(3872) \to J/\psi\gamma$

A comparison between MC and the raw distributions for our variables of interest is shown for each of our modes in Figures 6.12 – 6.15. In these plots, there is fairly good agreement between the MC and data. The MC consists entirely of background events; no signal events have been added to these samples. There are some hints of a signal based naively on the data/MC difference in some key regions (m_{miss} peak and $m_X = m_{X(3872)}$). To discriminate signal from background, the fits are performed as described and tested in Section 5.2, with the additional step of allowing the m_{miss} background ARGUS parameters to float (see Section 6.2.2). The resulting event type projections and $_s$Plots of these fits are shown in Figures 6.16 – 6.22.

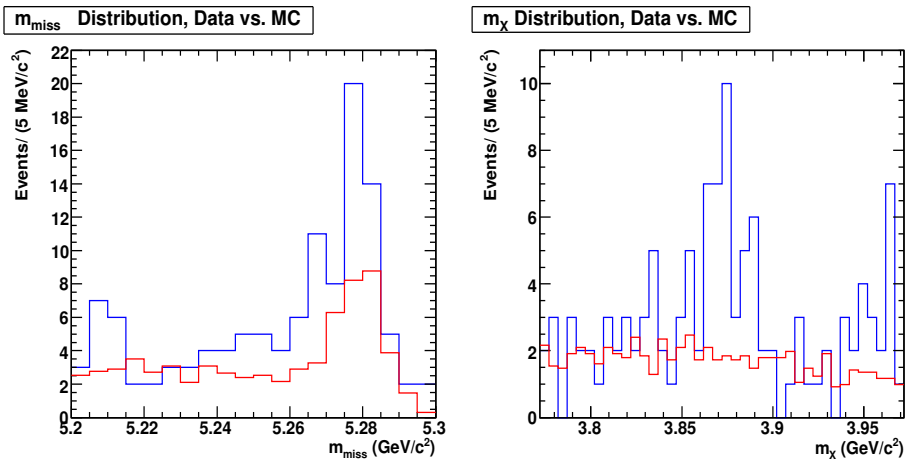

Figure 6.12: Comparison of data (blue) and MC (red) for m_X and m_{miss} for $B^{\pm} \to X(3872)K^{\pm}$, $X(3872) \to J/\psi\,\gamma$.

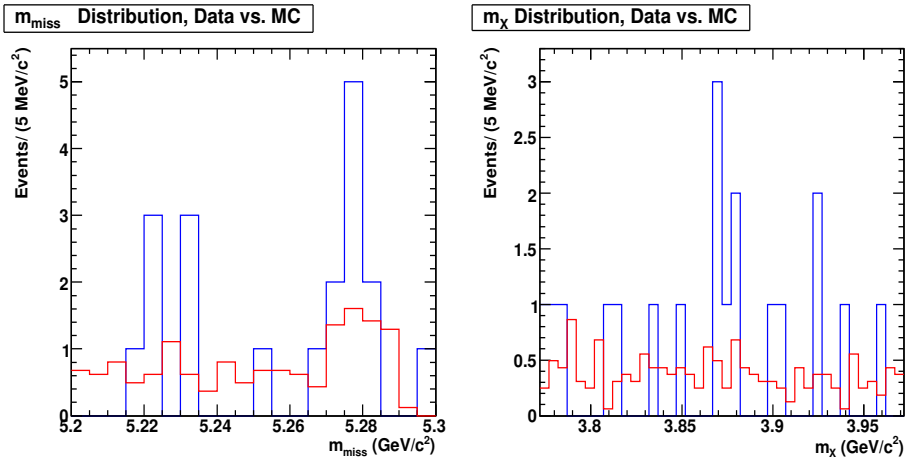

Figure 6.13: Comparison of data (blue) and MC (red) for m_X and m_{miss} for $B^{\pm} \to X(3872)K^0_S$, $X(3872) \to J/\psi\gamma$.

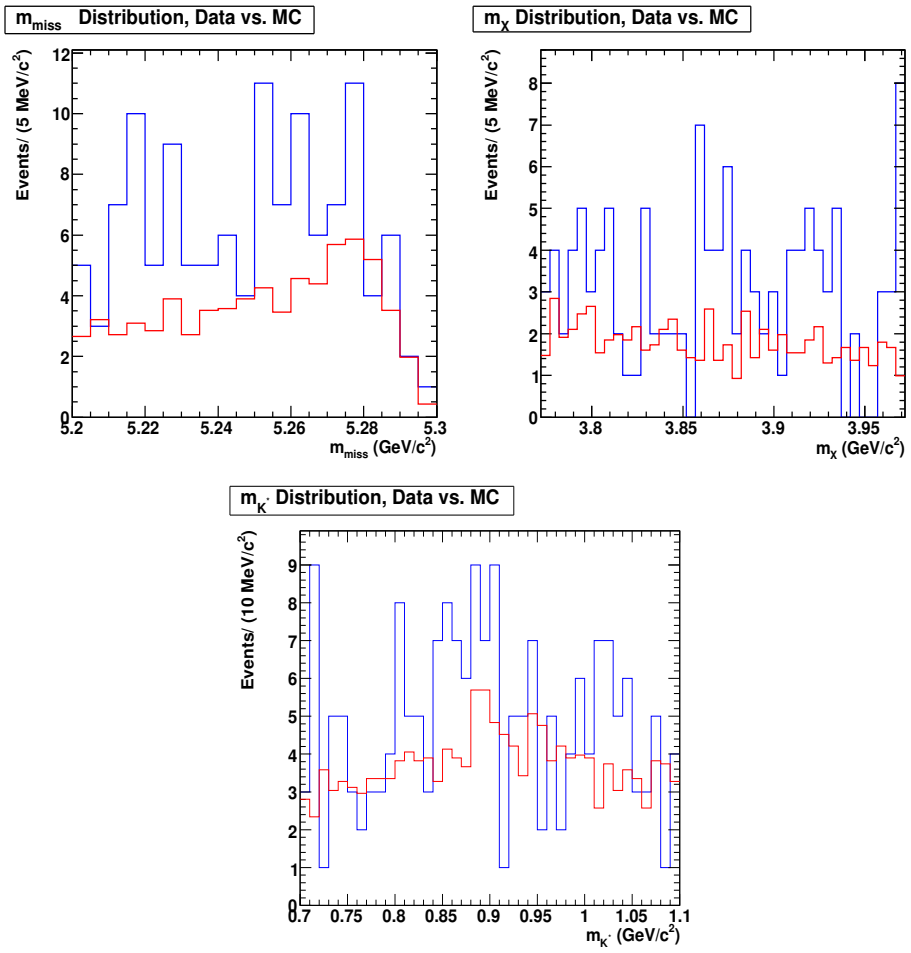

Figure 6.14: Comparison of data (blue) and MC (red) for m_X, m_{miss} and $m_{K^{*\pm}}$ for $B^{\pm} \to X(3872)K^{*\pm}$, $X(3872) \to J/\psi\gamma$.

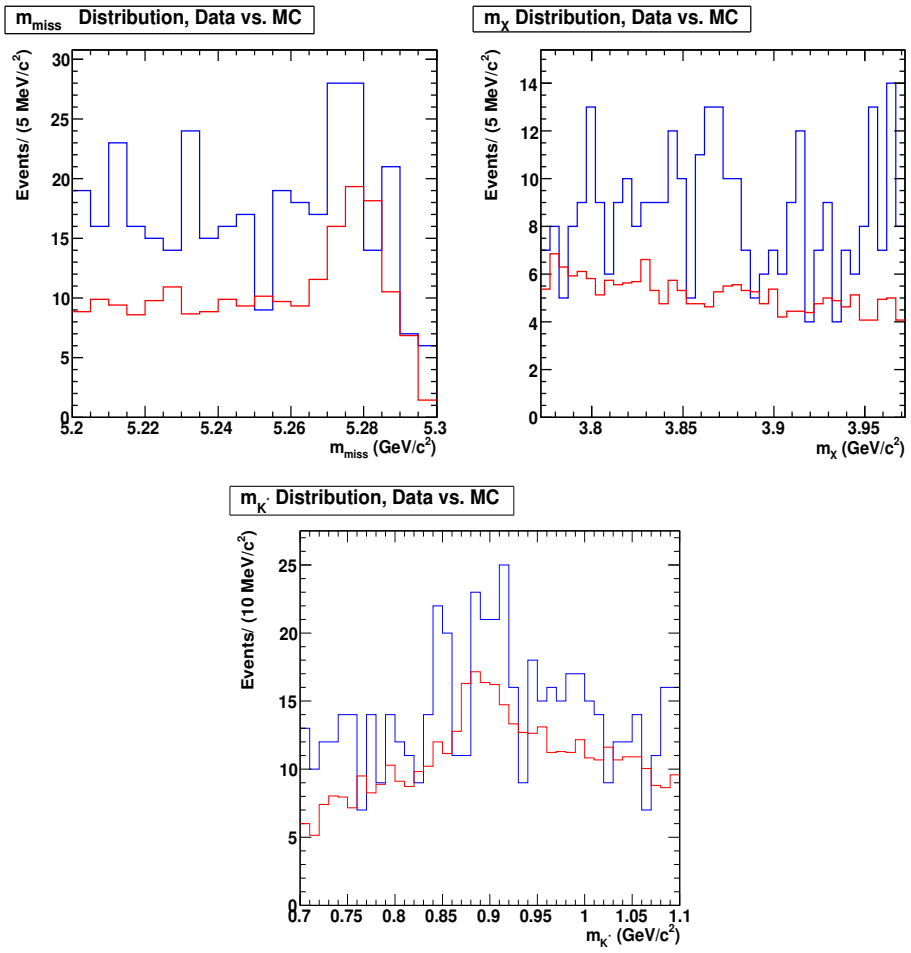

Figure 6.15: Comparison of data (blue) and MC (red) for m_X, m_{miss} and $m_{K^{*0}}$ for $B^{\pm} \to X(3872)K^{*0}$, $X(3872) \to J/\psi\gamma$.

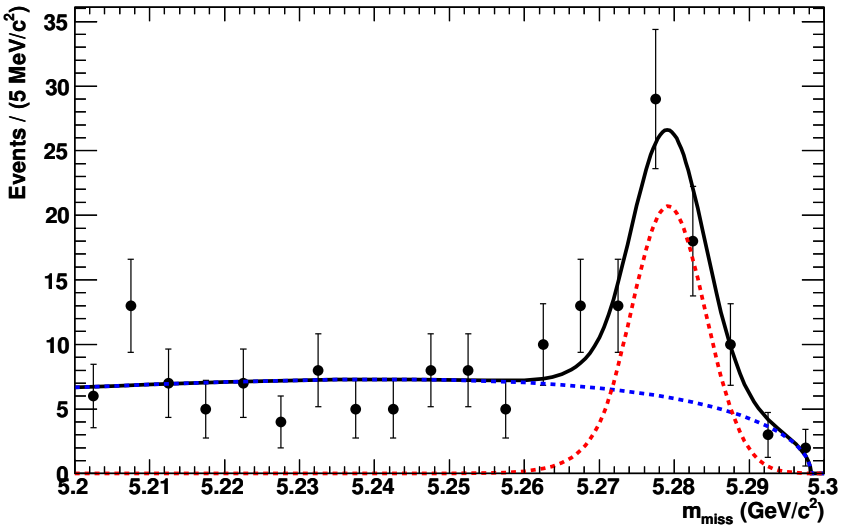

Figure 6.16: Projection of the peaking (dashed red) and background (dashed blue) event components for the fit to m_{miss} for $B^{\pm} \to X(3872)K^{\pm}$, $X(3872) \to J/\psi\,\gamma$. The solid line represents the sum. The points are from data.

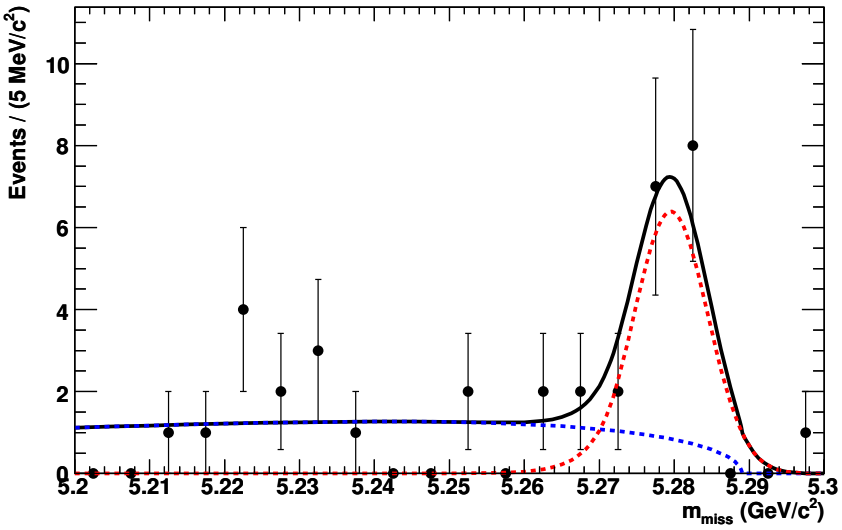

Figure 6.17: Projection of the peaking (dashed red) and background (dashed blue) event components for the fit to m_{miss} for $B^0 \to X(3872)K^0_S$, $X(3872) \to J/\psi\,\gamma$. The solid line represents the sum. The points are from data.

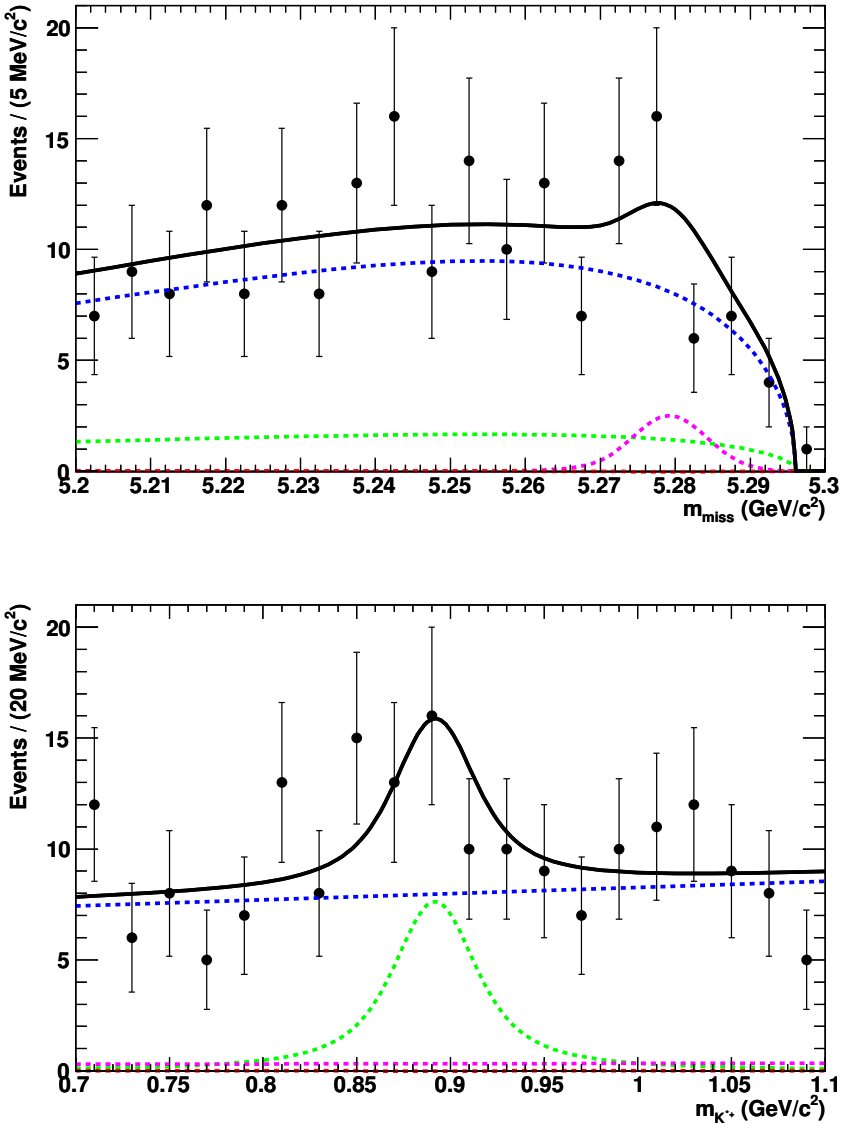

Figure 6.18: Projection of the signal (dashed red), combinatoric background with (dashed blue) and without (dashed green) a K^{*+}, and non-resonant background (dashed magenta) event components for the fit to m_{miss} and $m_{K^{*\pm}}$ for $B^{\pm} \to X(3872)K^{*\pm}$, $X(3872) \to J/\psi\gamma$. The solid line represents the sum. The points are from data.

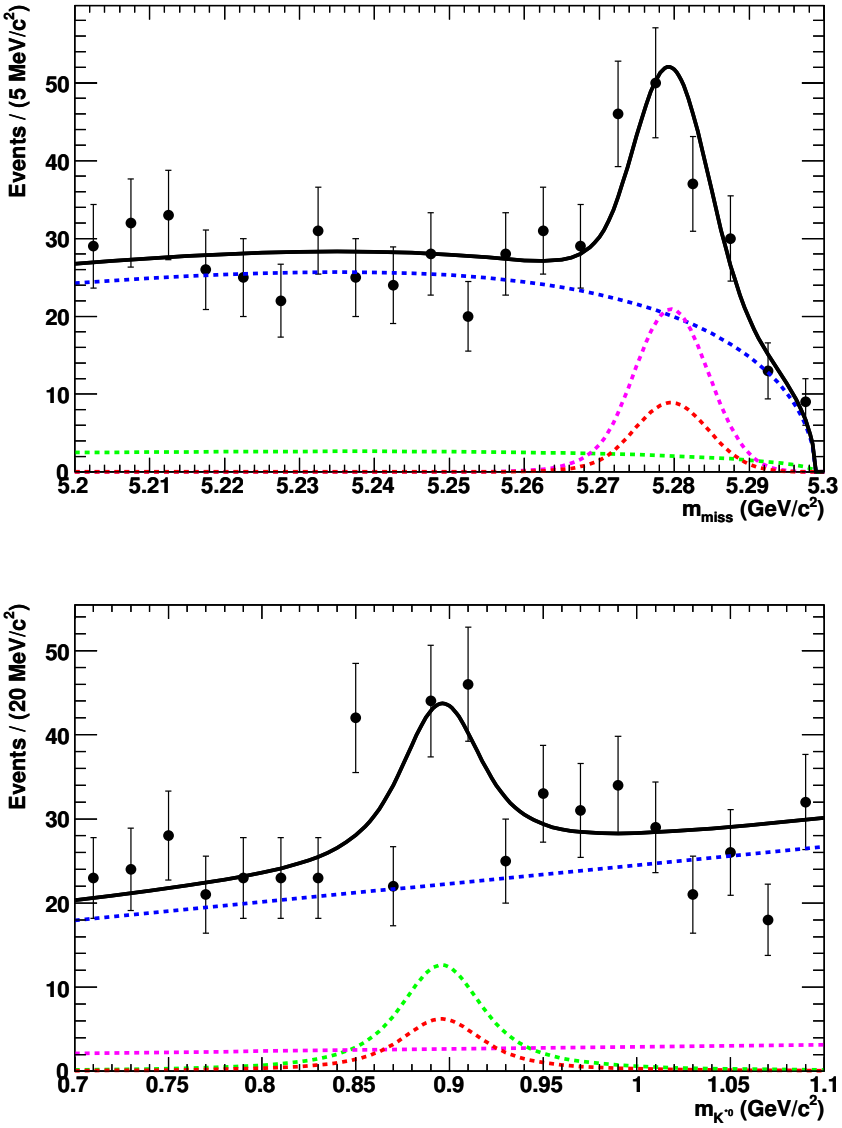

Figure 6.19: Projection of the signal (dashed red), combinatoric background with (dashed blue) and without (dashed green) a K^{*0}, and non-resonant background (dashed magenta) event components for the fit to m_{miss} and $m_{K^{*0}}$ for $B^0 \to X(3872)K^{*0}$, $X(3872) \to J/\psi\gamma$. The solid line represents the sum. The points are from data.

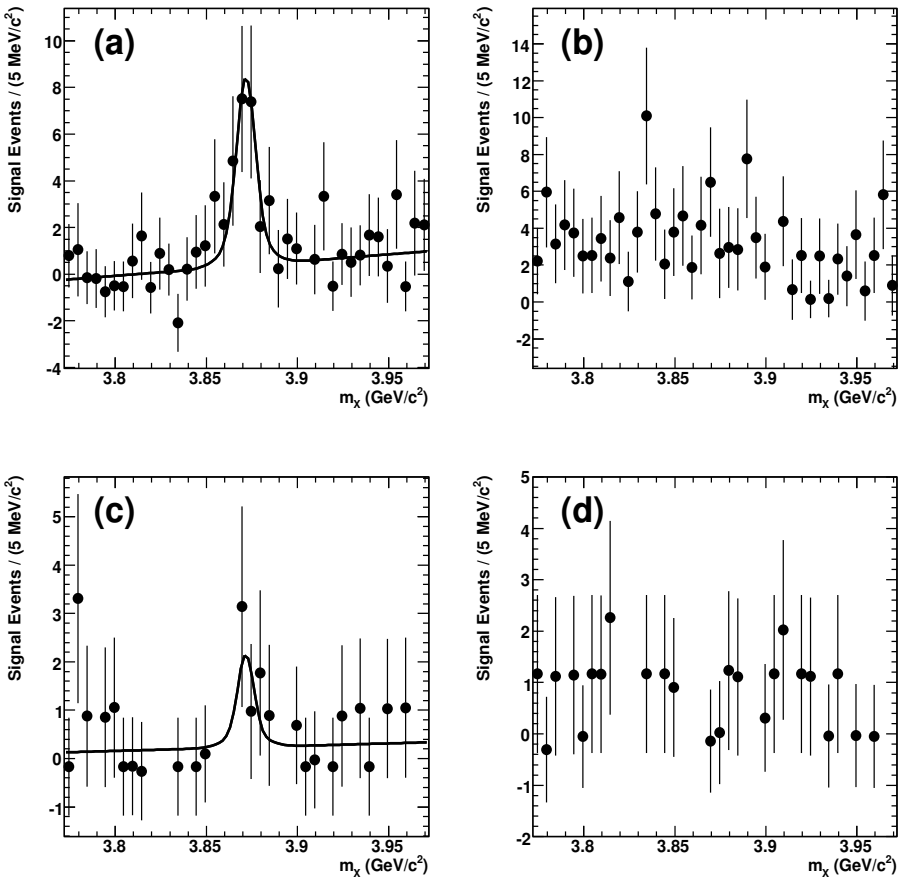

Figure 6.20: $_s$Plots for the number of events versus m_X for $B \to X(3872)K$ from data for $X(3872) \to J/\psi\gamma$: (a) $B^{\pm} \to X(3872)K^{\pm}$ signal events, (b) $B^{\pm} \to X(3872)K^{\pm}$ background events, (c) $B^0 \to X(3872)K^0_S$ signal events, and (d) $B^0 \to X(3872)K^0_S$ background events.

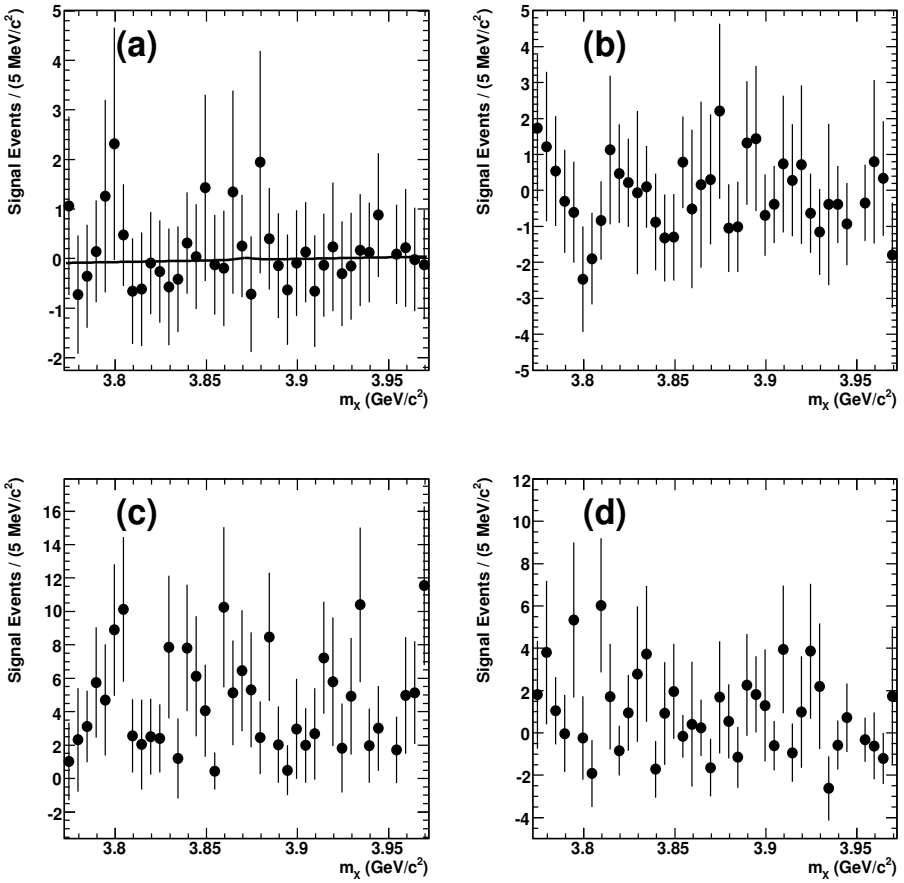

Figure 6.21: $_s$Plots for the number of events versus m_X for $B^{\pm} \to X(3872)K^{*\pm}$ from data for $X(3872) \to J/\psi\gamma$: (a) signal events, (b) $B^{\pm} \to X(3872)K^0_S\pi^{\pm}$ non-resonant events, (c) combinatoric background events, and (d) $K^{*\pm}$ combinatoric background events.

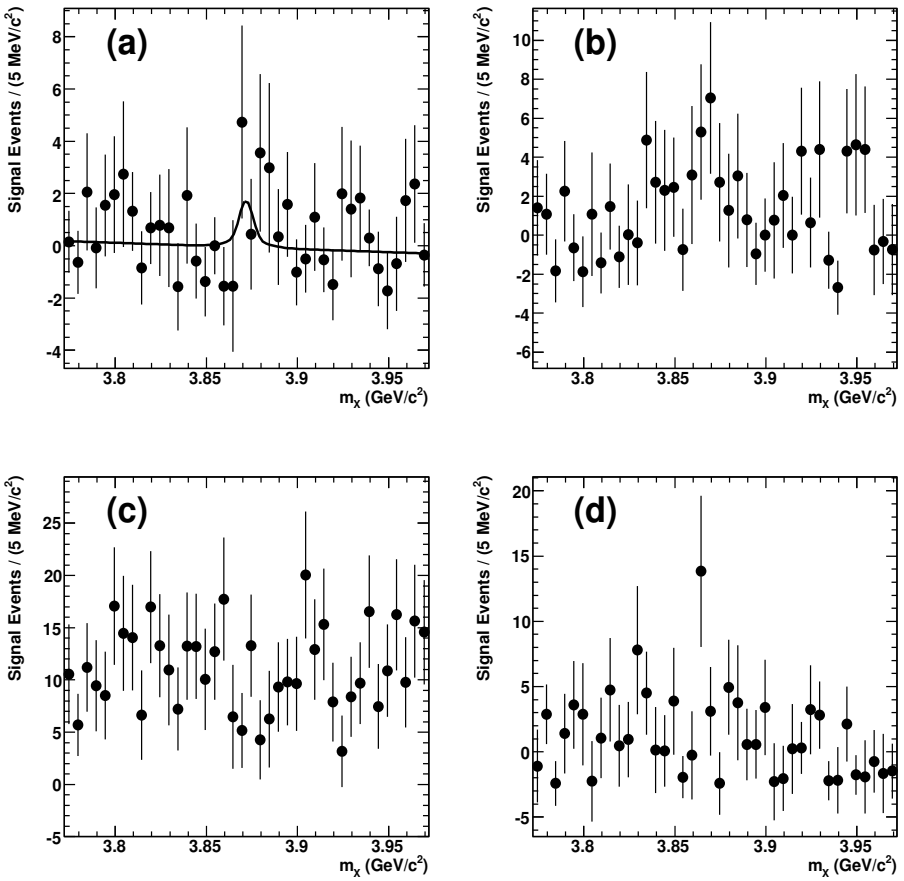

Figure 6.22: $_s$Plots for the number of events versus m_X for $B^0 \to X(3872)K^{*0}$ from data for $X(3872) \to J/\psi\gamma$: (a) signal events, (b) $B^0 \to X(3872)K^{\pm}\pi^{\mp}$ non-resonant events, (c) combinatoric background events, and (d) K^{*0} combinatoric background events.

Defining the significance as the square root of the difference in the χ^2 values of the fit with and without a signal component included, evidence of a signal for the decay mode $B^{\pm} \to X(3872)(J/\psi\gamma)K^{\pm}$ is found with a level of significance greater than 3 standard deviations. Nothing significant is found in the other decay modes. Using Equation 6.1, substituting $X(3872)$ for χ_{cJ}, one derives the product of branching fractions, $\mathcal{B}(B \to X(3872)K) \cdot (X(3872) \to J/\psi\gamma)$. The results for $X(3872) \to J/\psi\gamma$ signal extraction are summarized in Table 6.2.

Table 6.2: Results of $B \to X(3872)K$ signal extraction from data for $X(3872) \to J/\psi\gamma$. Error is statistical only.

Decay	Events (Corrected)	σ	Total Eff.	Daughter BFs [33]	Derived BF $\times 10^{-6}$
$X(3872)K^{\pm}$	23.0 ± 6.4	3.7σ	14.5%	6.12%	(2.78 ± 0.77)
$X(3872)K^{0}$	5.3 ± 3.6	1.4σ	11.0%	1.99%	(2.62 ± 1.76)
$X(3872)K^{*\pm}$	0.6 ± 2.3	0.0σ	6.9%	1.41%	(0.71 ± 2.56)
$X(3872)K^{*0}$	2.8 ± 5.2	0.8σ	10.4%	3.82%	(0.74 ± 1.41)

6.2.2 $B \to X(3872)K$, $X(3872) \to \psi(2S)\gamma$

The procedure of the previous Section is repeated for the $X(3872) \to \psi(2S)\gamma$ decay modes. A comparison between MC and the raw distributions for the variables of interest is shown for each of our modes in Figures 6.23 – 6.26. Again, in these plots, no signal MC has been added. The agreement between MC and data is somewhat adequate for the m_X and m_{K^*} distributions, though the m_{miss} distributions in MC show a clear difference from the data for $m_{miss} < 5.25\,\mathrm{GeV}/c^2$. In order to account for the inability of the MC to accurately model the m_{miss} background distribution, the parameters for the ARGUS function (endpoint and shape) are allowed to vary in the final fit. This improves the quality of the fit to the data and effectively removes a large systematic effect due to MC/data difference. The results of these fits for each $X(3872) \to \psi(2S)\gamma$ decay mode are shown in Figures 6.27 – 6.33.

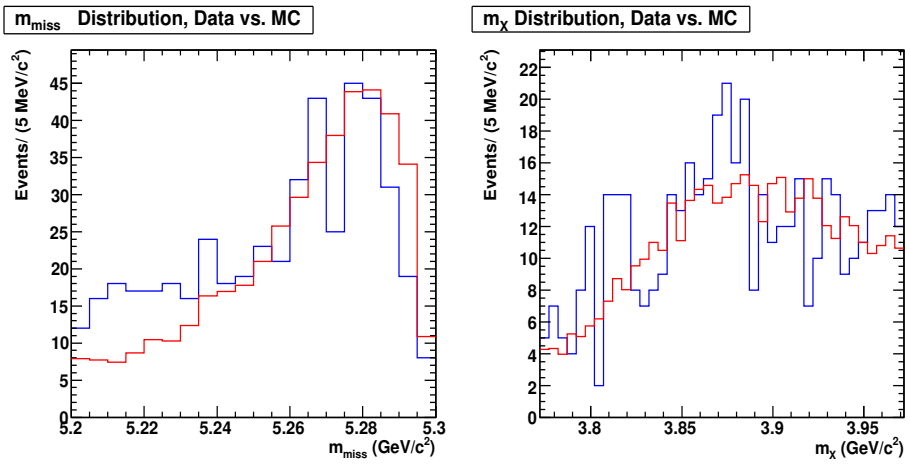

Figure 6.23: Comparison of data (blue) and MC (red) for m_X and m_{miss} for $B^{\pm} \to X(3872)K^{\pm}$, $X(3872) \to \psi(2S)\gamma$.

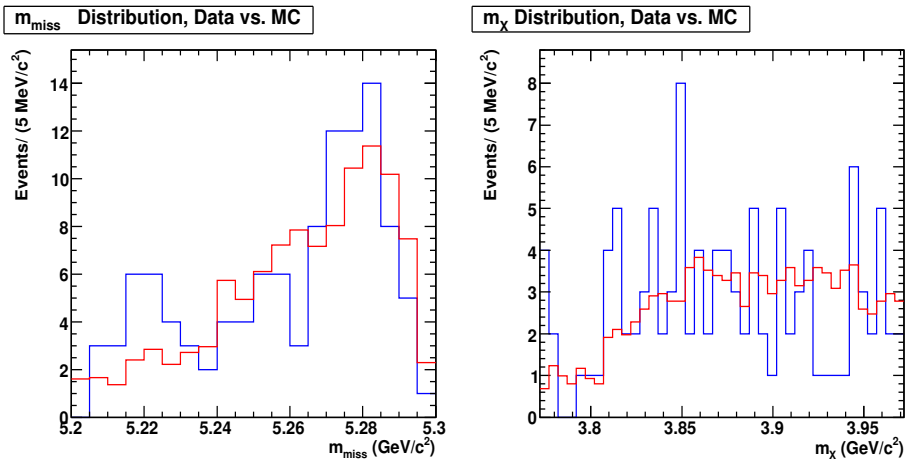

Figure 6.24: Comparison of data (blue) and MC (red) for m_X and m_{miss} for $B^{\pm} \to X(3872)K^0_S$, $X(3872) \to \psi(2S)\gamma$.

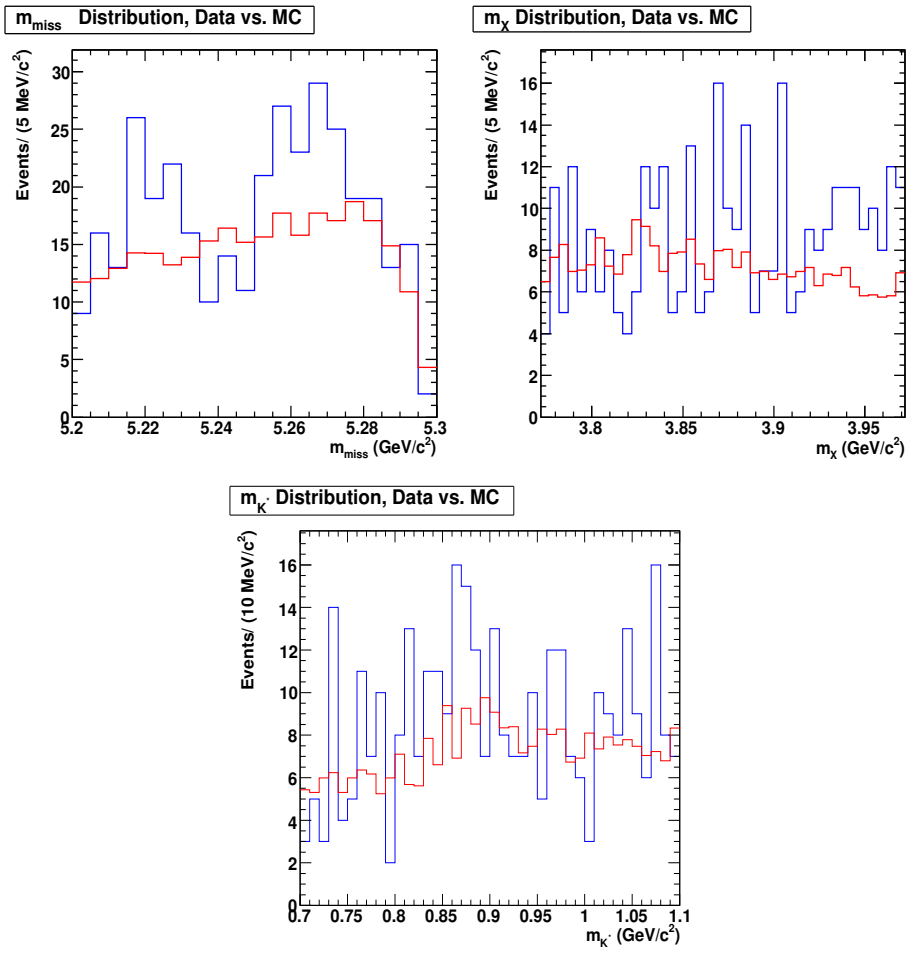

Figure 6.25: Comparison of data (blue) and MC (red) for m_X, m_{miss} and $m_{K^{*\pm}}$ for $B^{\pm} \to X(3872)K^{*\pm}$, $X(3872) \to \psi(2S)\gamma$.

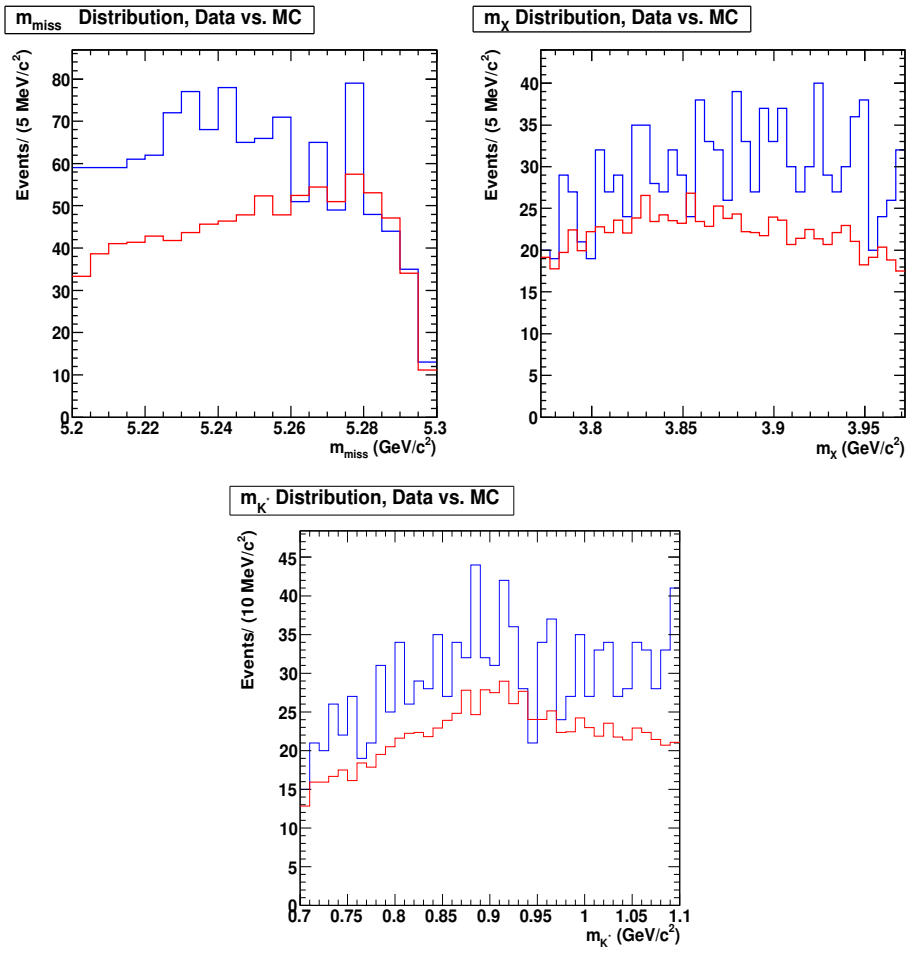

Figure 6.26: Comparison of data (blue) and MC (red) for m_X, m_{miss} and $m_{K^{*0}}$ for $B^{\pm} \to X(3872)K^{*0}$, $X(3872) \to \psi(2S)\gamma$.

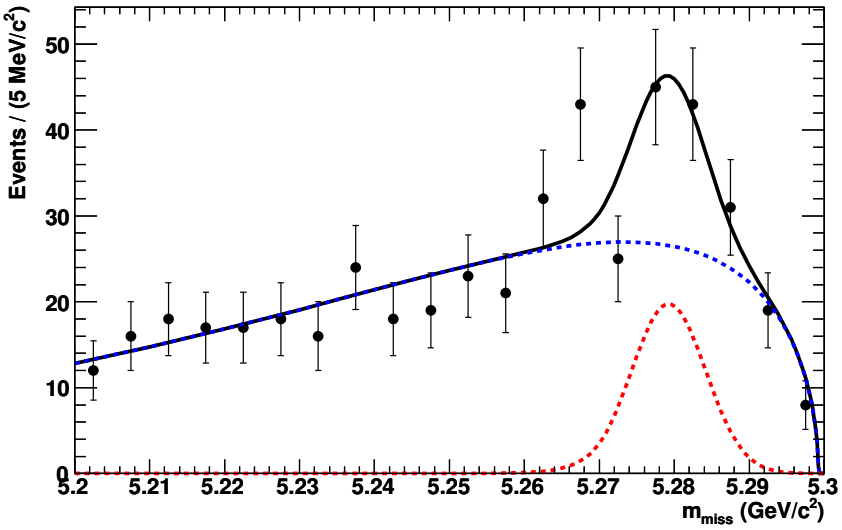

Figure 6.27: Projection of the peaking (dashed red) and background (dashed blue) event components for the fit to m_{miss} for $B^{\pm} \rightarrow X(3872)K^{\pm}$, $X(3872) \rightarrow \psi(2S)\gamma$. The solid line represents the sum. The points are from data.

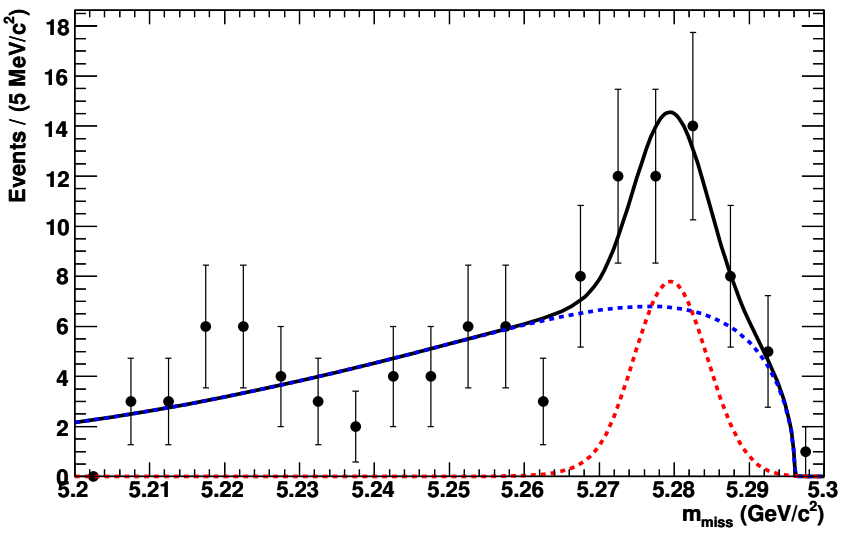

Figure 6.28: Projection of the peaking (dashed red) and background (dashed blue) event components for the fit to m_{miss} for $B^0 \to X(3872)K^0_S$, $X(3872) \to \psi(2S)\gamma$. The solid line represents the sum. The points are from data.

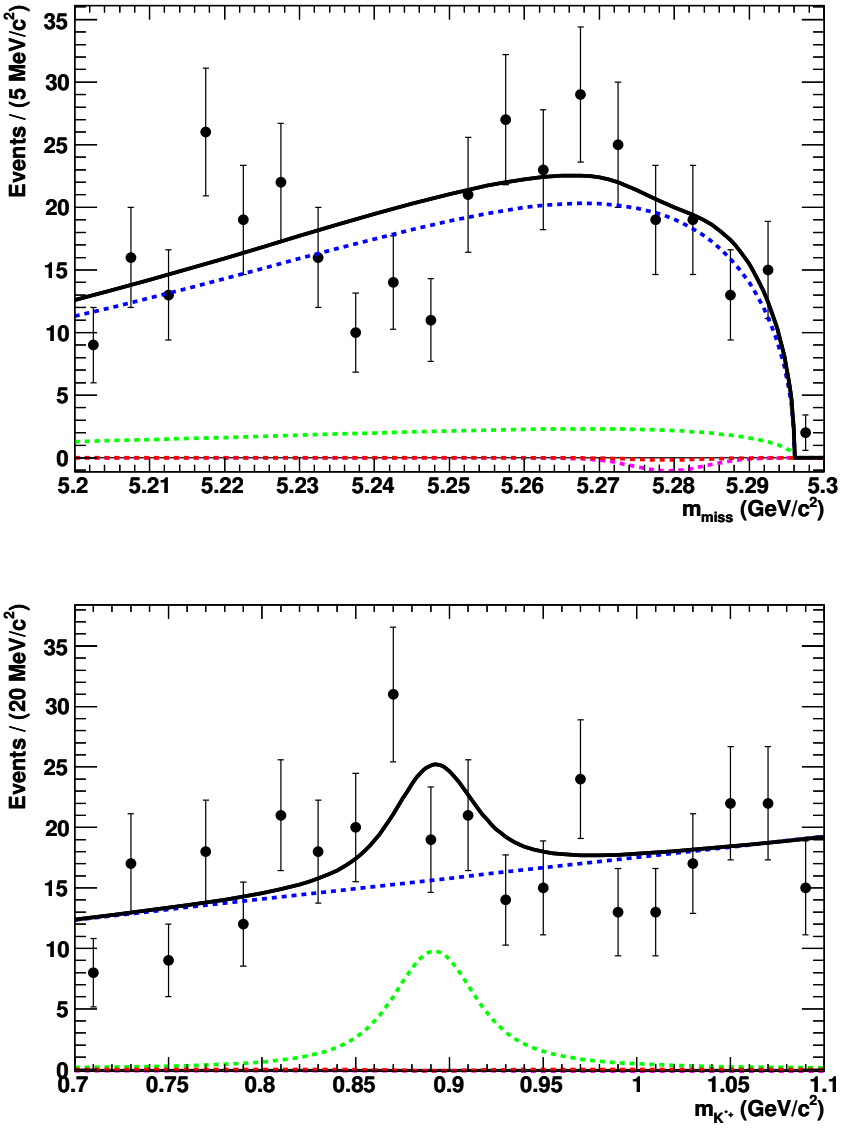

Figure 6.29: Projection of the signal (dashed red), combinatoric background with (dashed blue) and without (dashed green) a K^{*+}, and non-resonant background (dashed magenta) event components for the fit to m_{miss} and $m_{K^{*\pm}}$ for $B^{\pm} \to X(3872)K^{*\pm}$, $X(3872) \to \psi(2S)\gamma$. The solid line represents the sum. The points are from data.

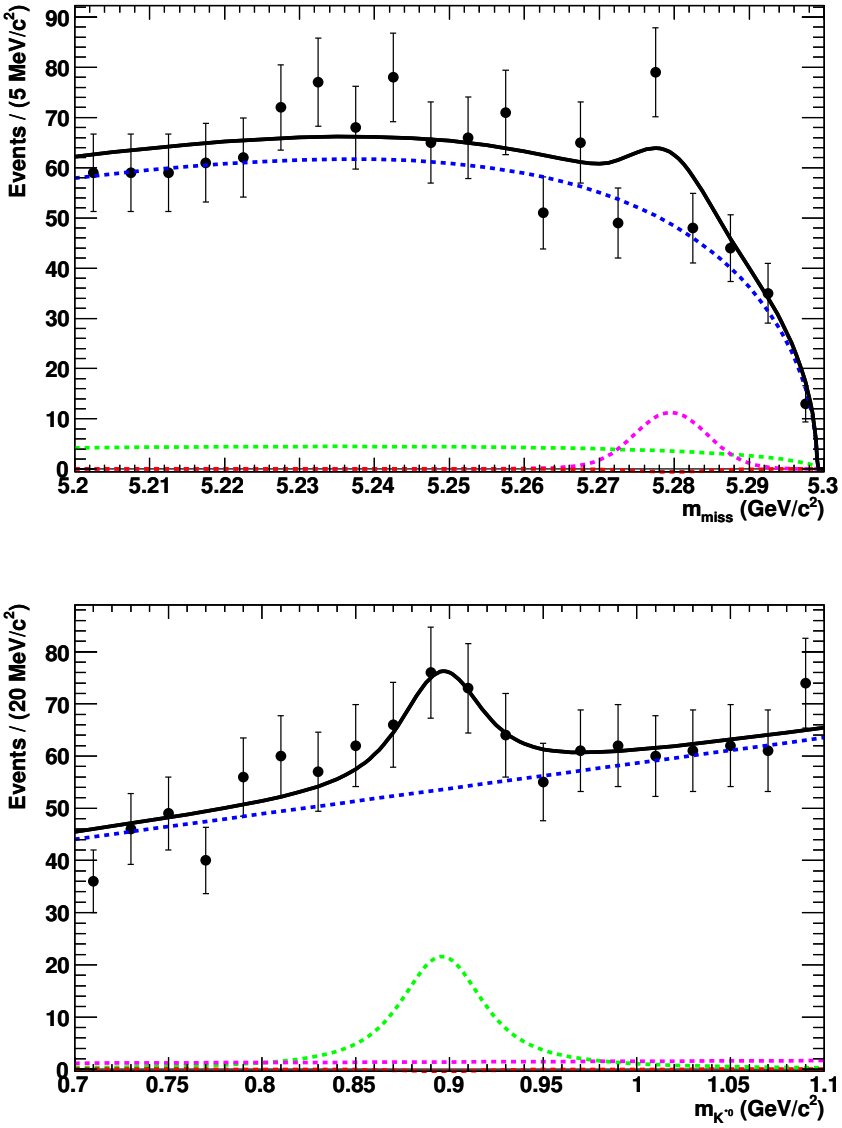

Figure 6.30: Projection of the signal (dashed red), combinatoric background with (dashed blue) and without (dashed green) a K^{*0}, and non-resonant background (dashed magenta) event components for the fit to m_{miss} and $m_{K^{*0}}$ for $B^0 \to X(3872)K^{*0}$, $X(3872) \to \psi(2S)\gamma$. The solid line represents the sum. The points are from data.

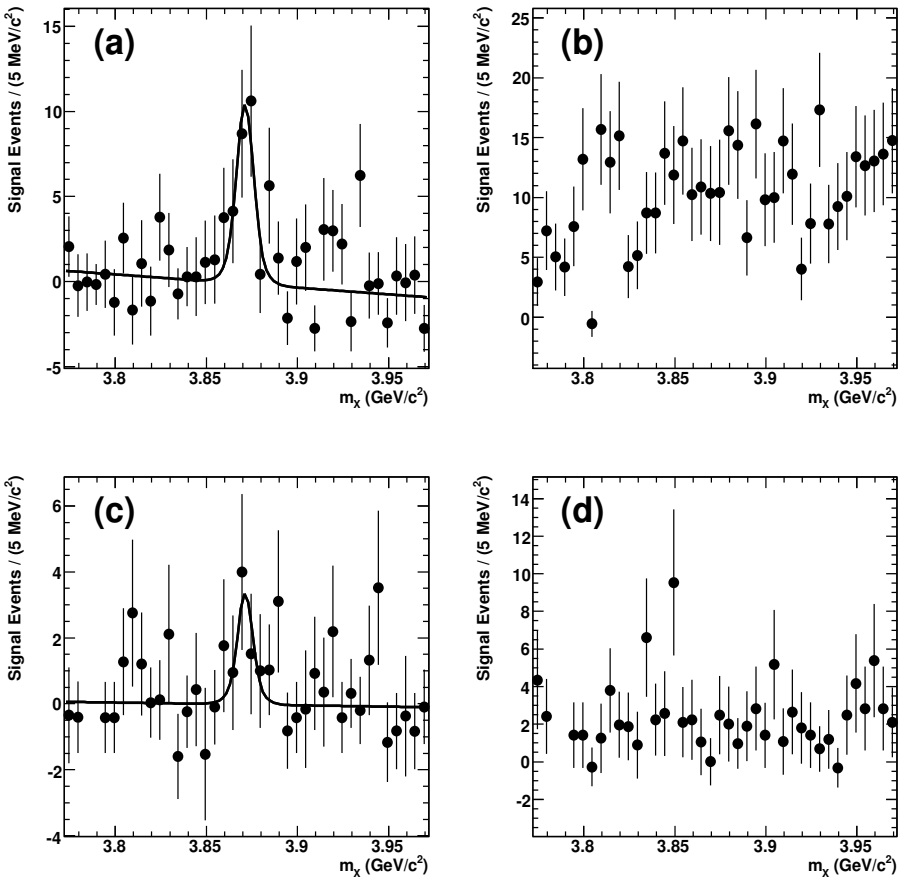

Figure 6.31: $_s$Plots for the number of events versus m_X for $B \to X(3872)K$ from data for $X(3872) \to \psi(2S)\gamma$: (a) $B^{\pm} \to X(3872)K^{\pm}$ signal events, (b) $B^{\pm} \to X(3872)K^{\pm}$ background events, (c) $B^0 \to X(3872)K^0_S$ signal events, and (d) $B^0 \to X(3872)K^0_S$ background events.

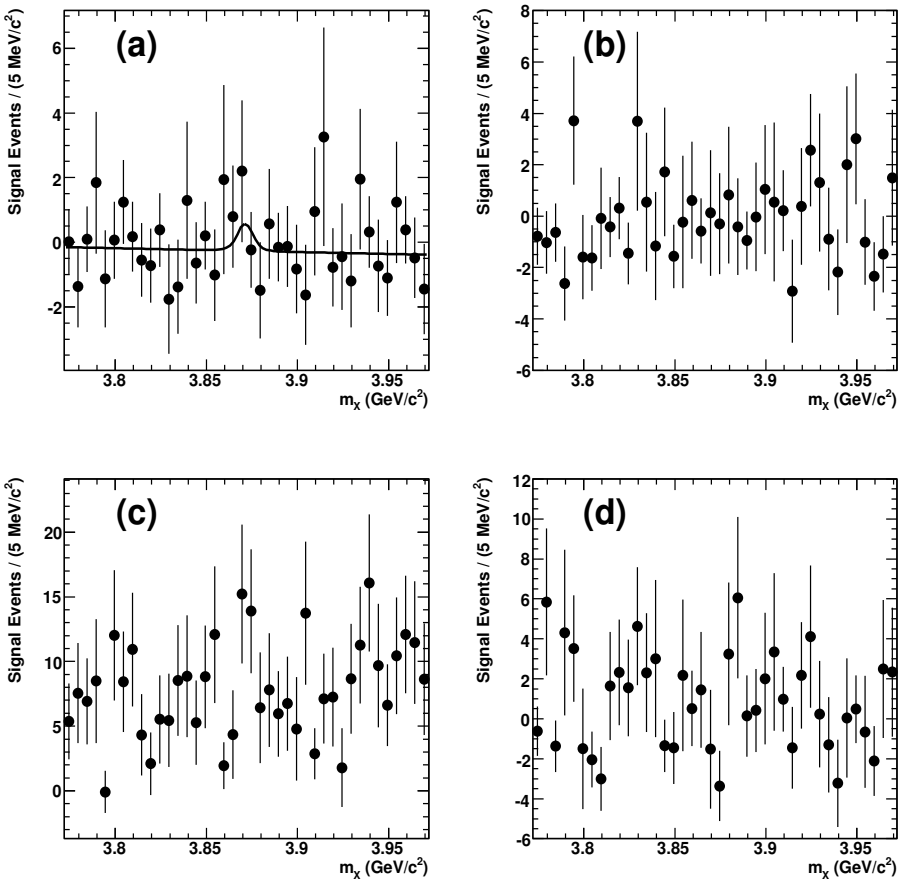

Figure 6.32: $_s$Plots for the number of events versus m_X for $B^{\pm} \to X(3872)K^{*\pm}$ from data for $X(3872) \to \psi(2S)\gamma$: (a) signal events, (b) $B^{\pm} \to X(3872)K^0_S\pi^{\pm}$ non-resonant events, (c) combinatoric background events, and (d) $K^{*\pm}$ combinatoric background events.

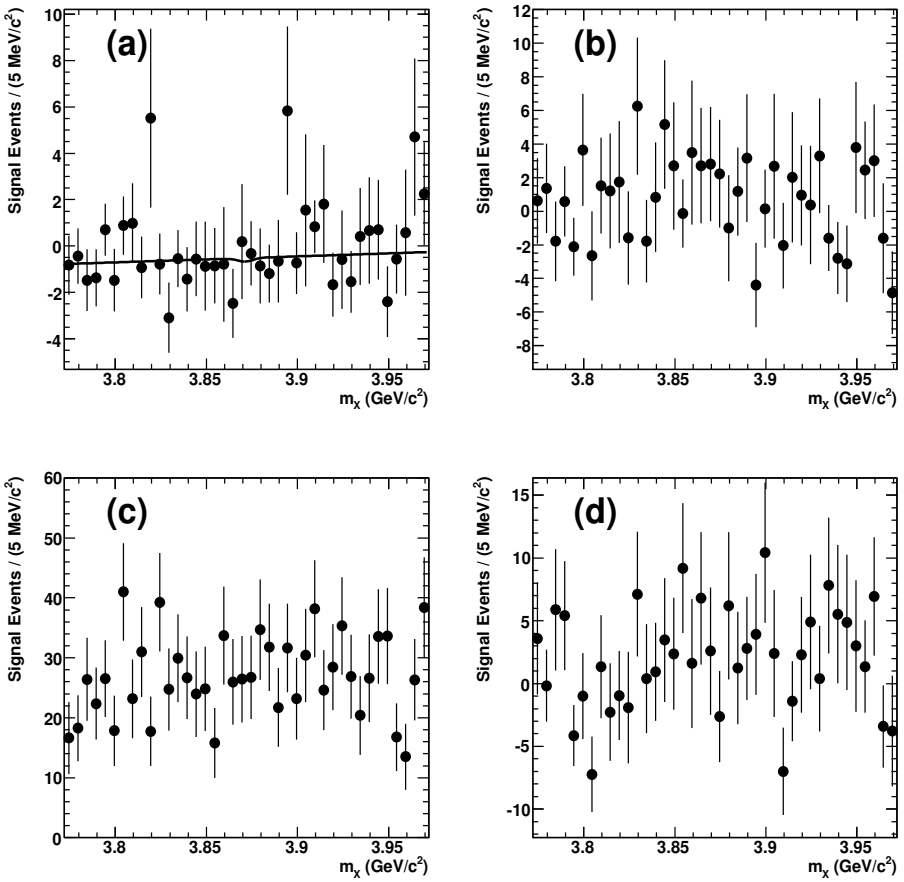

Figure 6.33: $_s$Plots for the number of events versus m_X for $B^0 \to X(3872)K^{*0}$ from data for $X(3872) \to \psi(2S)\gamma$: (a) signal events, (b) $B^0 \to X(3872)K^{\pm}\pi^{\mp}$ non-resonant events, (c) combinatoric background events, and (d) K^{*0} combinatoric background events.

Like the $X(3872) \to J/\psi\gamma$ mode, significant evidence ($> 3\sigma$) of a signal for the decay mode $B^{\pm} \to X(3872)(\psi\gamma)K^{\pm}$ is discovered, but nothing significant is seen in the remaining modes. The number of events extracted from the data and the corresponding product of branching fractions $\mathcal{BF}(B \to X(3872)K)(X(3872) \to \psi(2S)\gamma)$ are summarized for these decay modes in Table 6.3.

Table 6.3: Results of $B \to X(3872)K$ signal extraction from data for $X(3872) \to \psi(2S)\gamma$. Error is statistical only.

Decay	Events (Corrected)	σ	Total Eff.	Daughter BFs [33]	Derived BF $\times 10^{-6}$
$X(3872)K^{\pm}$	25.4 ± 7.3	3.7σ	11.0%	2.77%	(9.50 ± 2.74)
$X(3872)K^{0}$	8.0 ± 3.9	2.0σ	8.4%	0.90%	(11.36 ± 5.50)
$X(3872)K^{*\pm}$	1.9 ± 2.9	0.7σ	5.0%	0.64%	(6.38 ± 9.77)
$X(3872)K^{*0}$	-1.4 ± 3.3	-	6.7%	1.73%	(-1.31 ± 3.10)

As a crosscheck for $X(3872) \to \psi(2S)\gamma$ in the $K^{\pm}$ decay mode, the signal extraction was repeated treating the $\psi(2S) \to \ell^+\ell^-$ and $\psi(2S) \to J/\psi\,\pi^+\pi^-$ decay modes separately. The raw number of signal events measured is 12.4 ± 5.1 and 11.1 ± 5.4, respectively. To translate this into a rough branching fraction measurement, the total efficiency used in Table 6.3 is rescaled according to the cut and reconstruction efficiencies listed in Table 4.4, and the correct daughter branching fractions are applied. The resulting products of branching fractions are $9.7 \pm 4.0(stat.) \times 10^{-6}$ for the $\psi(2S) \to \ell^+\ell^-$ mode, and $8.7 \pm 4.2(stat.) \times 10^{-6}$ for the $\psi(2S) \to J/\psi\,\pi^+\pi^-$ mode, results that are consistent with one another (albeit with large statistical uncertainty).

6.2.3 $B \to X(any)K$, $X(any) \to c\bar{c}\gamma$

For the sake of interest, the range of the m_X invariant mass window can be opened beyond the $X(3872)$ region to search for other higher mass radiative decays to the $J/\psi\,\gamma$ and $\psi(2S)\gamma$ final states. Figures 6.34 and 6.35 span from $3.6\,\mathrm{GeV}/c^2$, just above $m_X = m_{\chi_{c2}}$, to $5.0\,\mathrm{GeV}/c^2$. While the $B^{\pm} \to X(3872)K^{\pm}$ signals are clearly visible in these plots, there are no other

significant features of interest.

6.3 Systematic Uncertainties and Corrections

6.3.1 B Counting

The number of $B\overline{B}$ events counted from the data sample is assigned a systematic error of 1.1%. This is based on a number of factors detailed in [72], with the largest contributions from uncertainty in the number of μ pairs in the on and off resonance data samples, and uncertainty in the efficiency of hadron selection for defining $B\overline{B}$ events.

6.3.2 Branching Fraction Uncertainties

To calculate the final branching fractions, the known values for the branching fractions of the daughter particles are required. The values and their uncertainties are taken from the PDG [33]. The branching fractions for the decays of interest are listed in Table 6.4.

Table 6.4: Values and uncertainties for the relevant daughter branching fractions.

Decay Mode	BF Value
$\mathcal{B}(\Upsilon(4S) \to B^+B^-)$	$(51.6 \pm 0.6)\%$
$\mathcal{B}(\Upsilon(4S) \to B^0\overline{B}^0)$	$(48.4 \pm 0.6)\%$
$\mathcal{B}(J/\psi \to e^+e^-)$	$(5.94 \pm 0.06)\%$
$\mathcal{B}(J/\psi \to \mu^+\mu^-)$	$(5.93 \pm 0.06)\%$
$\mathcal{B}(\chi_{c1} \to J/\psi\gamma)$	$(36.0 \pm 1.9)\%$
$\mathcal{B}(\chi_{c2} \to J/\psi\gamma)$	$(20.0 \pm 1.0)\%$
$\mathcal{B}(\psi(2S) \to J/\psi\pi^+\pi^-)$	$(32.6 \pm 0.5)\%$
$\mathcal{B}(\psi(2S) \to e^+e^-)$	$(0.752 \pm 0.017)\%$
$\mathcal{B}(\psi(2S) \to \mu^+\mu^-)$	$(0.75 \pm 0.08)\%$
$\mathcal{B}(K^0 \to K^0_s)$	50%
$\mathcal{B}(K^0_s \to \pi^+\pi^-)$	$(69.20 \pm 0.05)\%$
$\mathcal{B}(K^{*+} \to K^0\pi^\pm)$	$\frac{2}{3} \times (99.901 \pm 0.009)\%$
$\mathcal{B}(K^{*0} \to K^\pm\pi^\mp)$	$\frac{2}{3} \times (99.769 \pm 0.020)\%$

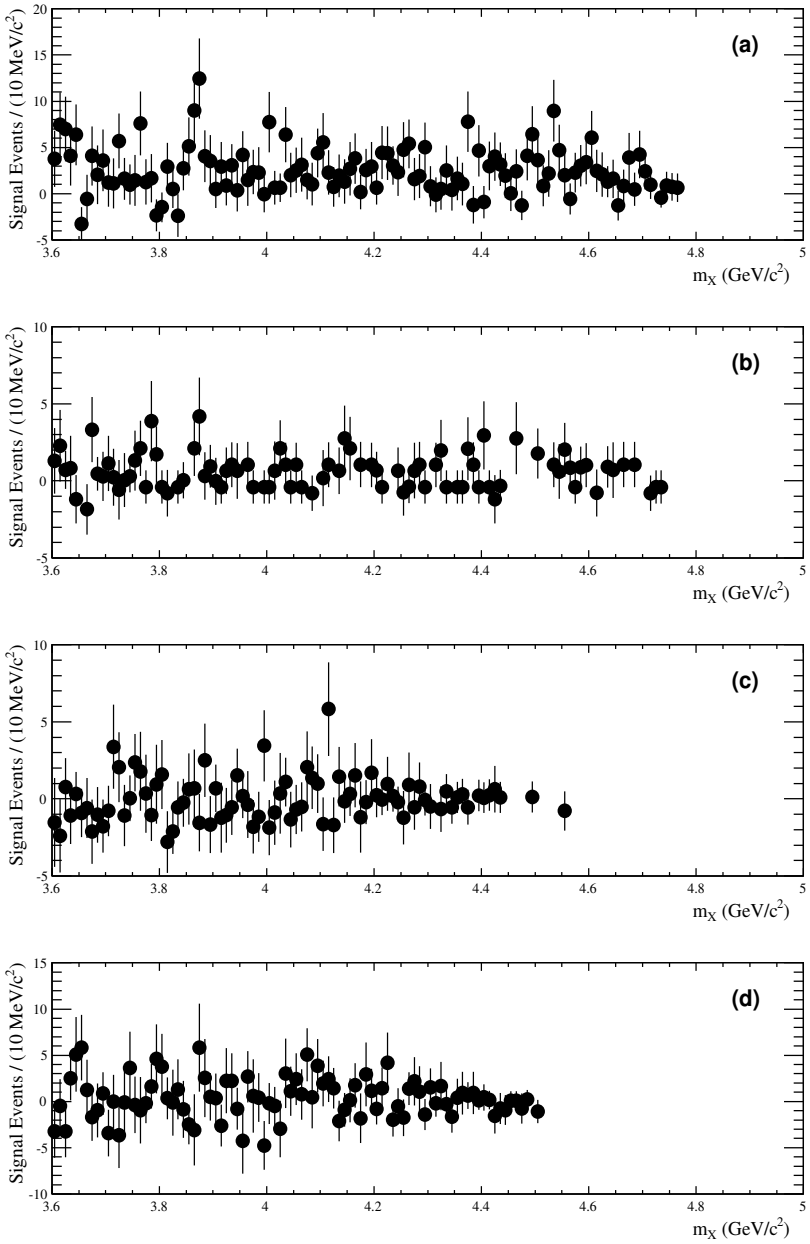

Figure 6.34: $_s$Plots for $X \to J/\psi\gamma$ signal-like events in the range $3.6 < m_X < 5.0\,\mathrm{GeV}/c^2$, (a) $B^\pm \to J/\psi\gamma K^\pm$, (b) $B^0 \to J/\psi\gamma K^0_S$, (c) $B^\pm \to J/\psi\gamma K^{*\pm}$, and (d) $B^0 \to J/\psi\gamma K^{*0}$.

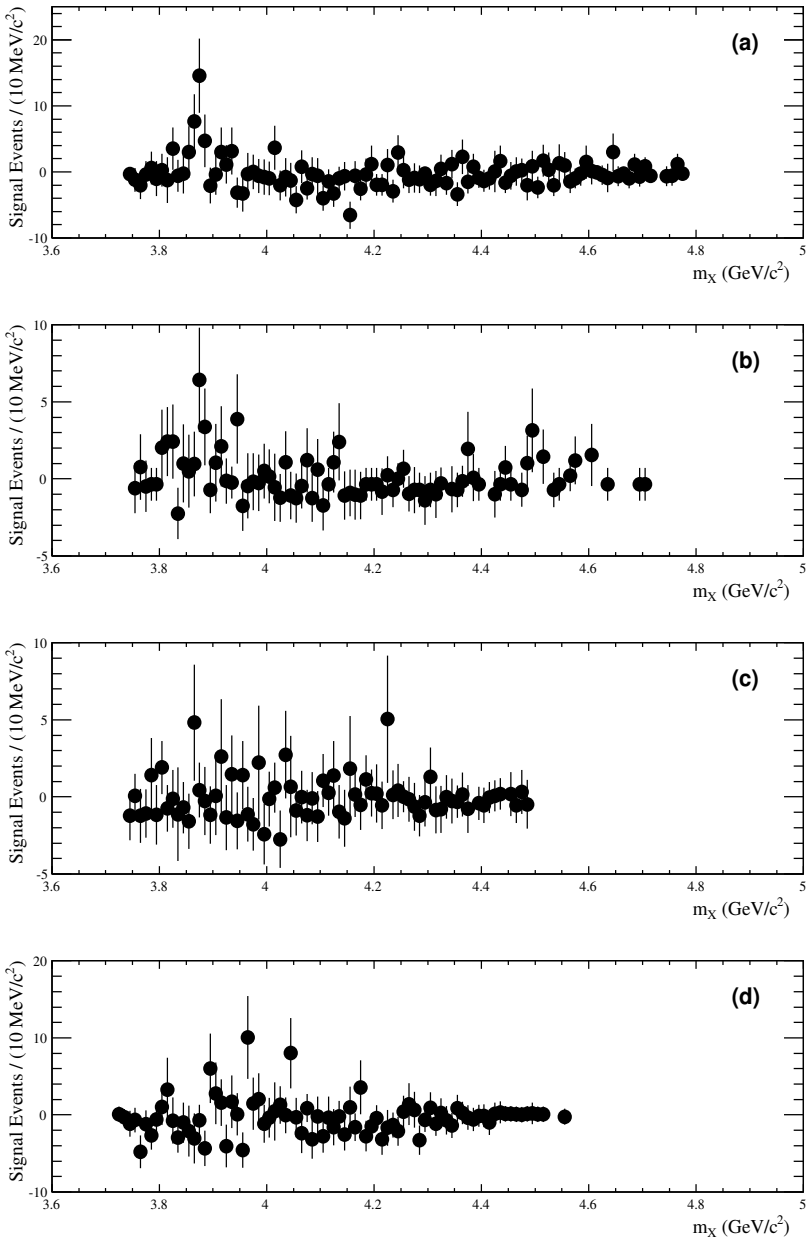

Figure 6.35: $_s$Plots for $X \to \psi(2S)\gamma$ signal-like events in the range $3.6 < m_X < 5.0\,\mathrm{GeV}/c^2$, (a) $B^\pm \to \psi(2S)\gamma K^\pm$, (b) $B^0 \to \psi(2S)\gamma K^0_S$, (c) $B^\pm \to \psi(2S)\gamma K^{*\pm}$, and (d) $B^0 \to \psi(2S)\gamma K^{*0}$.

6.3.3 MC/Data Differences

The signal extraction uses PDFs based on Monte Carlo. If the Monte Carlo distributions or the choice of parametrization do not match the data, it can lead to a systematic effect.

Due to a discrepancy in the MC description of m_{miss} for $X(3872) \to \psi(2S)\gamma$ decays from $B \to X(3872)K^{\pm/0}$ in the low m_{miss} region, the ARGUS parameters were allowed to float to eliminate these systematic effects. The m_{miss} mean was also allowed to float for the signal PDFs, and the difference in signal yield taken as a systematic uncertainty.

Uncertainty due to lack of knowledge regarding the shape of the m_X background for these modes was also evaluated. Fits were performed using the complicated m_X background model derived from MC and compared with similar fits performed with the seemingly more accurate (in data) and straightforward linear background model used for all other signal modes in this analysis. Because the correct background model is uncertain, the average number of events extracted by the two methods was taken for the signal yield and assigned a systematic uncertainty equal to half the difference between the two results. For other decay modes, the signal yield was recalculated fitting the m_X background with a second-order polynomial (in place of linear), with half the difference between the two results taken as the systematic uncertainty. For the m_X signal parametrization, the choice of peaking PDFs was robust and these uncertainties were considered to be negligible.

The value for these systematic uncertainties are included in Tables 6.10 – 6.13 under the heading "Signal m_{miss}" and "m_X Background", respectively.

6.3.4 PDF Fit Parameter Uncertainty

The uncertainties on the fit parameters determined from the Monte Carlo samples are translated into a systematic uncertainty on the signal extraction by repeating the signal extraction on data while varying the parameter values by $\pm 1\sigma$, as fitted in Chapter 5. The effect is quantified as the fractional change in the number of signal events, and the totals are added in

quadrature. Effects due to correlations between variables are assumed to be negligible, and in any case, the size of this systematic effect is relatively small. The results for each decay mode are summarized in Tables 6.5 – 6.7.

Table 6.5: Summary of the systematic uncertainties due to PDF parameter uncertainties for the $X(3872) \to J/\psi\gamma$ decay modes. Values are given in (%).

	$B \to X(3872)(J/\psi\,\gamma)K$ Decay			
	$K^{\pm}$	K^0_S	$K^{*\pm}$	K^{*0}
Signal m_{miss}				
α (tail transition)	0.17	0.02	0.15	0.07
m_0 (CB mean)	0.17	0.04	0.28	0.17
n (CB exponent)	0.02	0.00	0.04	0.02
σ (CB width)	0.09	0.00	0.12	0.09
m_{K^*} Parameters				
Mean	-	-	0.44	0.32
Gaussian Sigma	-	-	0.39	0.69
Breit-Wigner Width	-	-	1.11	0.12
Bkgd Slope	-	-	0.53	0.17
m_X Parameters				
μ (mean)	0.15	0.05	0.14	0.27
σ_1 (core width)	0.03	0.35	0.71	0.48
σ_2 (non-core width)	0.83	0.58	0.03	0.35
Core fraction	1.15	0.60	0.92	0.72
Total	1.45%	0.90%	1.60%	1.27%

6.3.5 True X Mass and Width Uncertainty

The m_X fit requires an assumption on the mass and width of the $X(3872)$ for the centre of the double-Gaussian peak. The data is refit using the PDG [71] value of $3871.4 \pm 0.6\,\mathrm{MeV}/c^2$ for the mass and the fit parameters are varied within these errors to assign a systematic error on the number of events extracted from the fit. The width was determined from MC, with the $X(3872)$ being generated as a zero-width particle.

The $X(3872)$ is known to be narrow, and the PDG limit is $\Gamma < 2.3$

Table 6.6: Summary of the systematic uncertainties due to PDF parameter uncertainties for the $X(3872) \to \psi(2S)\gamma$ decay modes. Values are given in (%).

	$B \to X(3872)(\psi(2S)\gamma)K$ Decay			
	$K^{\pm}$	K^0_S	$K^{*\pm}$	K^{*0}
Signal m_{miss}				
α (tail transition)	0.11	0.16	1.21	0.11
m_0 (CB mean)	0.08	0.19	0.21	0.00
n (CB exponent)	0.01	0.03	0.05	0.01
σ (CB width)	0.07	0.25	0.26	0.07
Background m_X				
F-D b (inflection point)	0.00	0.00	-	-
F-D c (slope)	0.00	0.00	-	-
m_{K^*} Parameters				
Mean	-	-	1.35	0.93
Gaussian Sigma	-	-	1.49	0.38
Breit-Wigner Width	-	-	0.41	0.03
Bkgd Slope	-	-	0.02	0.93
m_X Parameters				
μ (mean)	0.13	0.10	5.07	0.11
σ_1 (core width)	0.07	0.49	3.77	0.69
σ_2 (non-core width)	0.31	0.31	1.13	0.36
Core fraction	0.44	0.21	0.92	0.18
Total	0.58%	0.72%	6.92%	1.59%

MeV. This uncertainty is accounted for by increasing the width of the core Gaussian by adding this value in quadrature and repeating the fit. The values of these systematic uncertainties are given in Table 6.8.

To determine the systematic uncertainty due lack of knowledge of the true m_X mass distribution for the $\chi_{c1,2}$, the Gaussian peak position was allowed to float for the $\chi_{c1,2}$ modes and the difference in the event yield taken as the systematic uncertainty. The quantitative values for this uncertainty for $\chi_{c1,2}$ are listed in Tables 6.12 and 6.13, respectively.

Table 6.7: Summary of the systematic uncertainties due to PDF parameter uncertainties for the $\chi_{c1,2}$ decay modes. Values are given in (%).

	$\chi_{c1}K^{\pm}$	$\chi_{c2}K^{\pm}$	$\chi_{c1}K^{0}_{S}$	$\chi_{c2}K^{0}_{S}$	$\chi_{c1}K^{*\pm}$	$\chi_{c2}K^{*\pm}$	$\chi_{c1}K^{*0}$	$\chi_{c2}K^{*0}$
Signal m_{miss}								
α (tail transition)	0.08	0.69	0.06	0.55	0.56	114	0.32	1.03
m_0 (CB mean)	0.00	0.41	0.00	0.77	0.14	57	0.07	0.11
n (CB exponent)	0.01	0.03	0.13	0.08	1.66	94	0.01	0.04
σ (CB width)	0.07	0.05	0.08	0.08	0.30	61	0.18	0.89
m_{K^*} Parameters								
Mean	-	-	-	-	0.12	14	0.06	0.38
Gaussian Sigma	-	-	-	-	0.23	3.76	0.90	0.35
Breit-Wigner Width	-	-	-	-	1.89	4.75	1.72	0.96
Bkgd Slope	-	-	-	-	0.03	0.36	0.00	0.00
m_X Parameters								
$\mu(\chi_{c1})$ (mean)	0.20	0.19	0.33	0.02	2.78	3.64	0.44	0.03
$\sigma_1(\chi_{c1})$ (core width)	0.31	0.91	0.41	2.16	2.26	8.68	0.87	0.34
$\sigma_2(\chi_{c1})$ (non-core width)	0.16	1.72	0.84	1.49	1.21	51	0.05	0.06
Core fraction	0.35	0.50	1.11	2.14	3.31	4.6	1.21	0.10
$\mu(\chi_{c2})$ (mean)	0.01	0.91	0.03	4.27	0.03	100	0.03	1.55
$\sigma(\chi_{c2})$ (width)	0.00	3.22	0.01	2.27	0.00	11.8	0.01	1.38
Total	0.55%	3.98%	1.49%	5.98%	5.66%	205%	2.52%	2.73%

Table 6.8: Summary of the systematic uncertainties due to uncertainties in the properties of $X(3872)$.

Decay	$X(3872)$ mass	$X(3872)$ width
$X(J\psi\gamma)K^{\pm}$	1.1%	0.8%
$X(J\psi\gamma)K^0_S$	3.2%	1.6%
$X(J\psi\gamma)K^{*\pm}$	7.2%	5.0%
$X(J\psi\gamma)K^{*0}$	12.3%	5.6%
$X(\psi(2S)\gamma)K^{\pm}$	3.0%	0.2%
$X(\psi(2S)\gamma)K^0_S$	3.9%	4.6%
$X(\psi(2S)\gamma)K^{*\pm}$	144%	44%
$X(\psi(2S)\gamma)K^{*0}$	6.4%	9.8%

6.3.6 Bias and Efficiency

The bias on the signal extraction was measured by conducting repeated signal extraction trials using truth-matched MC events. It was defined as the difference between the number of events input and the average number found by the fit. This quantity has a statistical error associated to it based on the number of MC trials conducted. The values of the bias corrections can be found in Tables 5.7, 5.19, and 5.23. In the summary tables to follow, uncertainty in the bias is expressed as a percentage of the total corrected number of events extracted.

There is an uncertainty on the signal extraction efficiency related to two systematic quantities. The cut and reconstruction efficiency was calculated by dividing the number of events passing reconstruction and selection cuts by the number of events generated in MC. In the case where the exact number of generated events was unknown ($\chi_{c1,2}$), it was estimated using the BF from the EvtGen decay parameter definitions file, and is assigned an error of $\sqrt{N}$. The fit efficiency was calculated by dividing the number of events returned from repeated MC signal extraction trials by the number of events input. The uncertainty on this quantity was given by the statistical uncertainty of the MC trials. The values are found in Tables 5.8, 5.20, and 5.23.

6.3.7 PID Correction and Systematics

The *BABAR* PID Working Group generates correction tables to assign each reconstructed particle a weight in order improve the correspondence of MC and data. The total PID correction for an event is the product of the individual particle PID weights, and the total correction to the MC sample is the average of all of the event weights in the sample.

The systematic uncertainty on the particle identification is assigned in *BABAR* as 0.7% per electron, 1.8% per muon, 0.2% per pion, and 1.2% per kaon [83]. The total PID systematic for each decay mode is found by summing the systematic uncertainties, and in the case of more than one possible decay chain (i.e. $J\psi \to \ell^+\ell^-$ can have $\ell = e, \mu$), is weighted by the number of events for each decay found in the data.

The PID corrections and systematics uncertainties for each mode are listed in Table 6.9.

6.3.8 Tracking Systematics

The *BABAR* Tracking Efficiency Task Force has a recipe for calculating the systematic uncertainty due to tracking [84]. The systematic uncertainty per track is combined in quadrature with a correction factor and the total is taken as the systematic error. The particles in this analysis derive from the ChargedTracks list, for which the tracking correction factor is 0.312% with a systematic uncertainty of 0.142% per track.

For the decay channels with a $\psi(2S)$, the total tracking correction is the sum of the corrections for the $\ell^+\ell^-$ and $J/\psi\pi^+\pi^-$ modes weighted by their branching fractions and cut/reconstruction efficiency from Table 4.4. Table 6.9 lists the tracking systematic for each mode.

6.3.9 Photon Corrections

The *BABAR* Neutrals Working Group recipe for correcting MC photons to match data involves a small smearing and shifting correction applied to the energy [85]. There is no additional correction required to the single photon

Table 6.9: Summary of the PID and tracking (TRK) corrections and systematic uncertainties applied to the efficiency for each decay mode.

Mode	PID	PID	TRK
	Correct.	Syst. (%)	Syst. (%)
$\chi_{c1}K^{\pm}$	0.9880	3.68	1.03
$\chi_{c1}K^0_S$	0.9966	4.05	1.37
$\chi_{c1}K^{*\pm}$	0.9961	4.26	1.71
$\chi_{c1}K^{*0}$	1.003	3.85	1.37
$\chi_{c2}K^{\pm}$	0.9861	3.68	1.03
$\chi_{c2}K^0_S$	0.9956	4.05	1.37
$\chi_{c2}K^{*\pm}$	0.9984	4.26	1.71
$\chi_{c2}K^{*0}$	0.9970	3.85	1.37
$X(J/\psi\gamma)K^{\pm}$	0.9917	3.63	1.03
$X(J/\psi\gamma)K^0_S$	0.9972	4.04	1.37
$X(J/\psi\gamma)K^{*\pm}$	0.9968	4.24	1.71
$X(J/\psi\gamma)K^{*0}$	1.007	3.83	1.37
$X(\psi(2S)\gamma)K^{\pm}$	0.9905	4.01	1.45
$X(\psi(2S)\gamma)K^0_S$	0.9989	4.46	1.79
$X(\psi(2S)\gamma)K^{*\pm}$	0.9980	4.55	2.12
$X(\psi(2S)\gamma)K^{*0}$	1.008	4.16	1.78

efficiency, but there is a systematic uncertainty of 1.8% per photon (i.e. per event) [86].

6.3.10 Total Systematic Error

The total systematic errors derived in this section are summarized in Tables 6.10 – 6.13.

Table 6.10: Summary of total systematic uncertainties for the $X(3872) \to J/\psi\gamma$ decay modes.

Systematic	$B \to X(3872)(J/\psi\,\gamma)K$ Decay			
	$K^{\pm}$	K^0_S	$K^{*\pm}$	K^{*0}
$B\overline{B}$ count	1.1%	1.1%	1.1%	1.1%
Branching Fractions	1.9%	1.9%	2.2%	2.8%
Fit Parameters	1.4%	0.9%	1.6%	1.3%
Signal m_{miss}	3.0%	2.5%	139%	10.4%
$X(3872)$ Mass	1.8%	3.2%	7.2%	12.4%
$X(3872)$ Width	0.2%	1.6%	5.0%	5.6%
m_X Background	0.0%	10.0%	0.4%	9.2%
Bias	0.7%	0.9%	11.3%	4.7%
Efficiency	0.8%	1.0%	4.1%	1.4%
PID	3.6%	4.0%	4.2%	3.8%
TRK	1.0%	1.4%	1.7%	1.4%
Photons	1.8%	1.8%	1.8%	1.8%
Total	6.2%	12.1%	140%	20.8%

Table 6.11: Summary of total systematic uncertainties for the $X(3872) \to \psi(2S)\gamma$ decay modes.

Systematic	$B \to X(3872)(\psi(2S)\gamma)K$ Decay			
	$K^{\pm}$	K^0_S	$K^{*\pm}$	K^{*0}
$B\overline{B}$ count	1.1%	1.1%	1.1%	1.1%
Branching Fractions	2.7%	2.7%	3.0%	3.4%
Fit Parameters	0.6%	0.7%	6.9%	1.6%
Signal m_{miss}	5.8%	2.1%	22.2%	119%
$X(3872)$ Mass	1.2%	3.9%	144%	6.4%
$X(3872)$ Width	1.2%	4.6%	44%	9.8%
m_X Background	4.9%	4.9%	0.0%	146%
Bias	0.7%	1.3%	5.8%	14.5%
Efficiency	0.8%	1.5%	4.6%	2.1%
PID	4.0%	4.5%	4.6%	4.2%
TRK	1.4%	1.8%	2.1%	1.8%
Photons	1.8%	1.8%	1.8%	1.8%
Total	10.0%	10.0%	153%	190%

Table 6.12: Summary of total systematic uncertainties for the χ_{c1} decay modes.

Systematic	$\chi_{c1}K^{\pm}$	$\chi_{c1}K^0_S$	$\chi_{c1}K^{*\pm}$	$\chi_{c1}K^{*0}$
$B\overline{B}$ count	1.1%	1.1%	1.1%	1.1%
Branching Fractions	5.6%	5.6%	5.7%	6.0%
Fit Parameters	0.6%	1.5%	5.7%	2.5%
Signal m_{miss}	0.0%	0.0%	0.1%	0.0%
χ_{c1} Mass	1.0%	0.1%	8.0%	0.3%
m_X Background	0.1%	0.8%	1.3%	1.0%
Bias	0.7%	1.7%	5.7%	3.3%
Efficiency	1.1%	2.6%	6.1%	3.5%
PID	3.7%	4.0%	4.3%	3.9%
TRK	1.0%	1.4%	1.7%	1.4%
Photons	1.8%	1.8%	1.8%	1.8%
Total	7.3%	8.2%	15.1%	9.4%

Table 6.13: Summary of total systematic uncertainties for the χ_{c2} decay modes.

Systematic	$\chi_{c2}K^{\pm}$	$\chi_{c2}K^0_S$	$\chi_{c2}K^{*\pm}$	$\chi_{c2}K^{*0}$
$B\overline{B}$ count	1.1%	1.1%	1.1%	1.1%
Branching Fractions	5.3%	5.3%	5.4%	5.7%
Fit Parameters	4.3%	6.2%	217%	2.8%
Signal m_{miss}	2.5%	2.5%	54.0%	0.0%
χ_{c2} Mass	1.7%	0.2%	13.1%	0.1%
m_X Background	15.9%	43.0%	52.0%	5.1%
Bias	6.2%	16%	455%	0.8%
Efficiency	7.1%	9.1%	33.2%	2.0%
PID	3.6%	4.0%	4.3%	3.9%
TRK	1.0%	1.4%	1.7%	1.4%
Photons	1.8%	1.8%	1.8%	1.8%
Total	20.4%	47.9%	511%	9.6%

Chapter 7

Conclusions

This chapter states the final results obtained from this analysis, including statistical and systematic uncertainties. The $B \to \chi_{c1,2}K$ results are compared with previous experimental measurements. The confirmation of $X(3872) \to J/\psi\gamma$, discovery of evidence for $X(3872) \to \psi(2S)\gamma$, and the broader implications for the further understanding of the $X(3872)$ are discussed in detail.

7.1 Analysis Results

The signal extraction method was successfully verified on the χ_{c1} charmonium modes to measure the branching fractions

$$\mathcal{B}(B^{\pm} \to \chi_{c1}K^{\pm}) = (4.5 \pm 0.1(stat.) \pm 0.3(syst.)) \times 10^{-4},$$

$$\mathcal{B}(B^{0} \to \chi_{c1}K^{0}) = (4.2 \pm 0.3(stat.) \pm 0.3(syst.)) \times 10^{-4},$$

$$\mathcal{B}(B^{\pm} \to \chi_{c1}K^{*\pm}) = (2.6 \pm 0.5(stat.) \pm 0.4(syst.)) \times 10^{-4},$$

$$\mathcal{B}(B^{0} \to \chi_{c1}K^{*0}) = (2.5 \pm 0.2(stat.) \pm 0.2(syst.)) \times 10^{-4}.$$

For the χ_{c2} decay modes, the following branching fractions were measured:

$$\mathcal{B}(B^{\pm} \to \chi_{c2}K^{\pm}) = (1.0 \pm 0.6(stat.) \pm 0.2(syst.)) \times 10^{-5},$$

$$\mathcal{B}(B^{0} \to \chi_{c2}K^{0}) = (1.5 \pm 1.0(stat.) \pm 0.7(syst.)) \times 10^{-5},$$

$$\mathcal{B}(B^{\pm} \to \chi_{c2}K^{*\pm}) = (1.1 \pm 4.3(stat.) \pm 5.6(syst.)) \times 10^{-5},$$

$$\mathcal{B}(B^0 \to \chi_{c2} K^{*0}) = (6.6 \pm 1.8(stat.) \pm 0.6(syst.)) \times 10^{-5}.$$

The upper limit on the branching fractions is defined by assuming a Gaussian distribution for the number of signal events and its uncertainty, and integrating over the physically-allowed region from 0 to 90% of the total area around the mean. The total uncertainty is taken as the statistical and systematic uncertainties added in quadrature. These results are:

$$\mathcal{B}(B^\pm \to \chi_{c2} K^\pm) < 1.7 \times 10^{-5}$$

$$\mathcal{B}(B^0 \to \chi_{c2} K^0) < 2.8 \times 10^{-5}$$

$$\mathcal{B}(B^\pm \to \chi_{c2} K^{*\pm}) < 10.0 \times 10^{-5}$$

$$\mathcal{B}(B^0 \to \chi_{c2} K^{*0}) < 9.0 \times 10^{-5}.$$

For $X(3872) \to J/\psi\gamma$, this analysis finds:

$$\begin{aligned}\mathcal{B}(B^\pm \to X(3872)K^\pm) \cdot (X(3872) \to J/\psi\gamma) \\ = (2.8 \pm 0.8(stat.) \pm 0.2(syst.)) \times 10^{-6},\end{aligned}$$

$$\begin{aligned}\mathcal{B}(B^0 \to X(3872)K^0) \cdot (X(3872) \to J/\psi\gamma) \\ = (2.6 \pm 1.8(stat.) \pm 0.3(syst.)) \times 10^{-6},\end{aligned}$$

$$\begin{aligned}\mathcal{B}(B^\pm \to X(3872)K^{*\pm}) \cdot (X(3872) \to J/\psi\gamma) \\ = (0.7 \pm 2.6(stat.) \pm 1.0(syst.)) \times 10^{-6},\end{aligned}$$

$$\begin{aligned}\mathcal{B}(B^0 \to X(3872)K^{*0}) \cdot (X(3872) \to J/\psi\gamma) \\ = (0.7 \pm 1.4(stat.) \pm 0.2(syst.)) \times 10^{-6}.\end{aligned}$$

There is 3.5σ evidence for $X(3872) \to J/\psi\gamma$ in $B^\pm \to X(3872)K^\pm$. Finding no significant signal in the other modes, 90% confidence level upper limits are calculated as described above:

$$\mathcal{B}(B^0 \to X(3872)K^0) \cdot (X(3872) \to J/\psi\gamma) < 4.9 \times 10^{-6},$$

$$\mathcal{B}(B^\pm \to X(3872)K^{*\pm}) \cdot (X(3872) \to J/\psi\gamma) < 4.8 \times 10^{-6},$$

$$\mathcal{B}(B^0 \to X(3872)K^{*0}) \cdot (X(3872) \to J/\psi\gamma) =< 2.8 \times 10^{-6}.$$

In the search for $X(3872) \to \psi(2S)\gamma$, this analysis finds:

$$\begin{aligned}\mathcal{B}(B^\pm \to X(3872)K^\pm) \cdot (X(3872) \to \psi(2S)\gamma) \\ = (9.5 \pm 2.7(stat.) \pm 0.9(syst.)) \times 10^{-6},\end{aligned}$$

$$\begin{aligned}\mathcal{B}(B^0 \to X(3872)K^0) \cdot (X(3872) \to \psi(2S)\gamma) \\ = (11.4 \pm 5.5(stat.) \pm 1.2(syst.)) \times 10^{-6},\end{aligned}$$

$$\begin{aligned}\mathcal{B}(B^\pm \to X(3872)K^{*\pm}) \cdot (X(3872) \to \psi(2S)\gamma) \\ = (6.4 \pm 9.8(stat.) \pm 9.7(syst.)) \times 10^{-6},\end{aligned}$$

$$\begin{aligned}\mathcal{B}(B^0 \to X(3872)K^{*0}) \cdot (X(3872) \to \psi(2S)\gamma) \\ = (-1.3 \pm 3.1(stat.) \pm 2.5(syst.)) \times 10^{-6}.\end{aligned}$$

This analysis measures 3.3σ significance for $X(3872) \to \psi(2S)\gamma$ in $B^\pm \to X(3872)K^\pm$. This is the first evidence for this decay channel. The 90% confidence level upper limits for the other decay modes are measured to be:

$$\mathcal{B}(B^0 \to X(3872)K^0) \cdot (X(3872) \to \psi(2S)\gamma) < 1.9 \times 10^{-5},$$

$$\mathcal{B}(B^\pm \to X(3872)K^{*\pm}) \cdot (X(3872) \to \psi(2S)\gamma) < 2.8 \times 10^{-5},$$

$$\mathcal{B}(B^0 \to X(3872)K^{*0}) \cdot (X(3872) \to \psi(2S)\gamma) < 0.4 \times 10^{-5}.$$

These results for the $\chi_{c1,2}$, $X(3872) \to J/\psi\,\gamma$, and $X(3872) \to \psi(2S)\gamma$ decay modes are displayed concisely in Figures 7.1, 7.2, and 7.3, respectively.

7.2 Discussion and Implications

The $\chi_{c1,2}$ results and their comparison with previous *BABAR* and Belle measurements are summarized in Table 7.1. It is important to note that the *BABAR* data set used in this analysis overlaps somewhat with previous *BABAR* results while the Belle measurements are entirely independent. Furthermore,

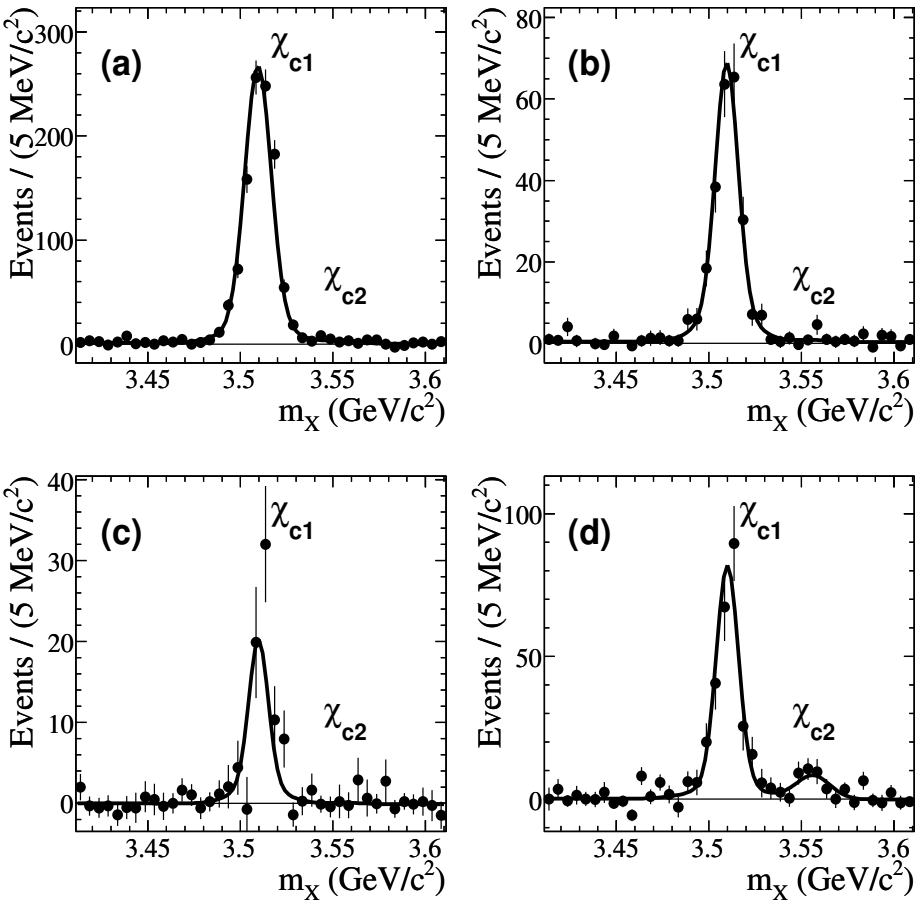

Figure 7.1: $_s$Plot of the number of signal events versus m_X for (a) $B^{\pm} \to \chi_{c1,2}K^{\pm}$, (b) $B^0 \to \chi_{c1,2}K^0_S$, (c) $B^{\pm} \to \chi_{c1,2}K^{*\pm}$, and (d) $B^0 \to \chi_{c1,2}K^{*0}$. The solid curve is the fit to the data.

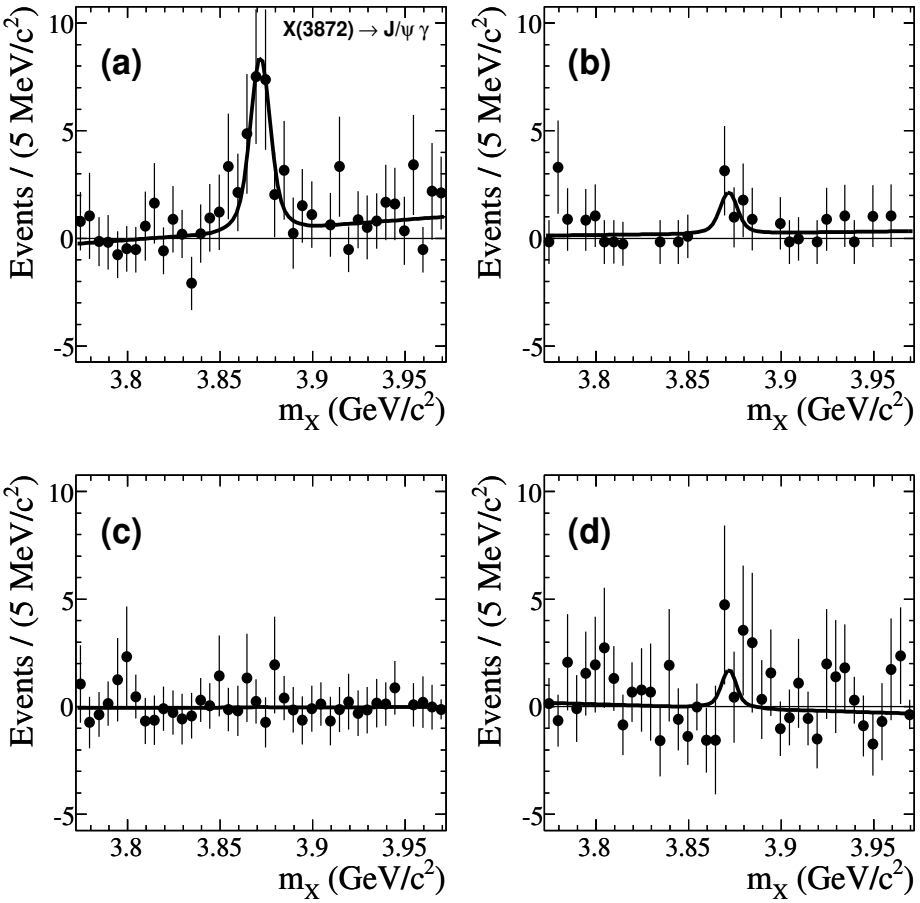

Figure 7.2: $_s$Plot of the number of extracted signal events versus m_X for (a) $B^{\pm} \to X(3872)K^{\pm}$, (b) $B^0 \to X(3872)K^0_S$, (c) $B^{\pm} \to X(3872)K^{*\pm}$, and (d) $B^0 \to X(3872)K^{*0}$, where $X(3872) \to J/\psi\gamma$. The solid curve is the fit to the data.

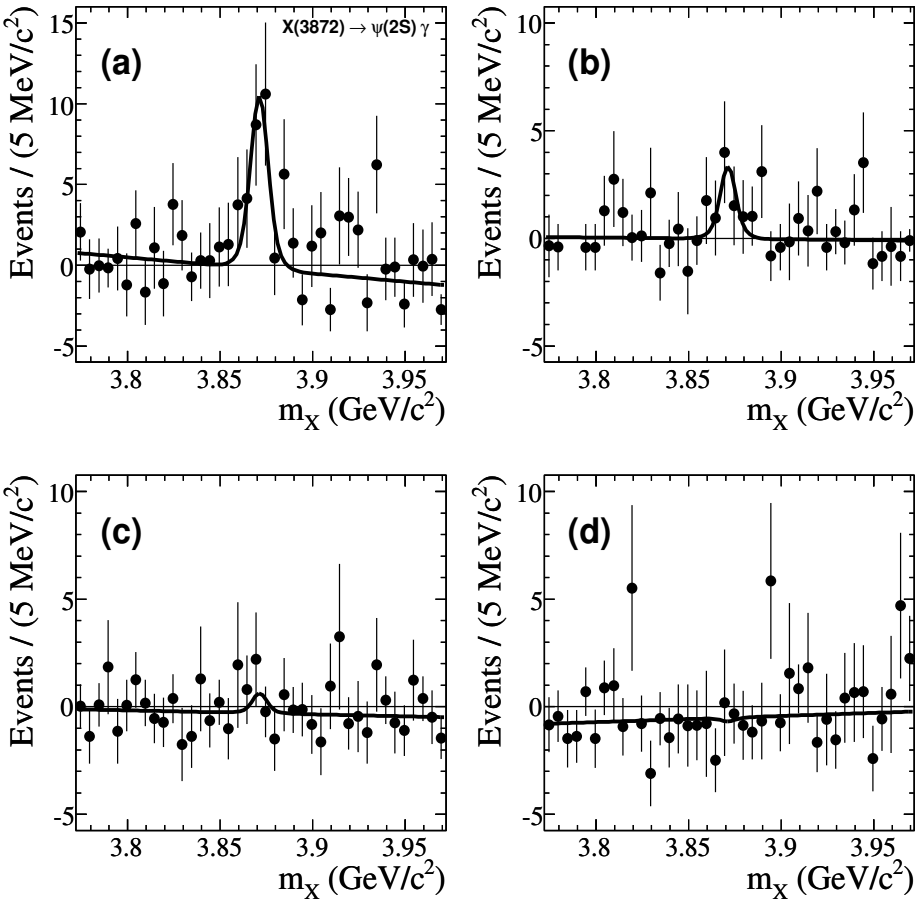

Figure 7.3: $_s$Plot of the number of extracted signal events versus m_X for (a) $B^{\pm} \to X(3872)K^{\pm}$, (b) $B^0 \to X(3872)K^0_S$, (c) $B^{\pm} \to X(3872)K^{*\pm}$, and (d) $B^0 \to X(3872)K^{*0}$, where $X(3872) \to \psi(2S)\gamma$. The solid curve is the fit to the data.

the previous measurements used daughter branching fractions taken from older versions of the PDG [71, 88], which have been rescaled[22] here to allow direct comparison to the results of this analysis.

Table 7.1: Comparison of the present $B \to \chi_{c1,2}K$ signal extraction results with previous measurements. Previous *BABAR* and Belle results have been rescaled to use the most up-to-date daughter BFs. Such corrections have apparently not been applied to the χ_{c1} results appearing in the latest version of the PDG.

Decay	Belle	*BABAR* Old	PDG [33]	Present
	$\times 10^{-4}$	$\times 10^{-4}$	$\times 10^{-4}$	$\times 10^{-4}$
$\chi_{c1}K^{\pm}$	(3.8 ± 0.5) [19]	(4.7 ± 0.4) [37]	(4.9 ± 0.5)	(4.5 ± 0.4)
$\chi_{c1}K^{0}$	(3.2 ± 0.5) [19]	(4.1 ± 0.6) [87]	(3.9 ± 0.4)	(4.2 ± 0.4)
$\chi_{c1}K^{*\pm}$	(3.0 ± 1.0) [19]	(2.5 ± 1.2) [87]	(3.6 ± 0.9)	(2.6 ± 0.6)
$\chi_{c1}K^{*0}$	$(1.8^{+0.4}_{-0.3})$ [60]	(3.0 ± 0.7) [87]	(3.2 ± 0.6)	(2.5 ± 0.3)
$\chi_{c2}K^{\pm}$	< 0.28 [19]	< 0.29 [16]	< 0.29	< 0.17
$\chi_{c2}K^{0}$	< 0.27 [19]	< 0.42 [16]	< 0.26	< 0.28
$\chi_{c2}K^{*\pm}$	< 1.23 [19]	< 0.12 [16]	< 0.12	< 1.0
$\chi_{c2}K^{*0}$	< 0.74 [19]	< 0.37 [16]	< 0.36	(0.66 ± 0.19)

The χ_{c1} measurements are in excellent agreement with and supercede all previous *BABAR* results. These measurements generally agree with Belle results. This analysis provides the single best measurements of all $B \to \chi_{c1}K$ decay modes except for Belle's very recently published measurement of $B^0 \to \chi_{c1}K^{*0}$ [60]. This analysis also provides a substantial statistical improvement over previous PDG $\chi_{c1}K^*$ world average results.

Regarding the χ_{c2} decay modes, this analysis is in agreement with previous $\chi_{c2}K$ results, and provides the best $B^{\pm} \to \chi_{c2}K^{\pm}$ measurement to date. These results for $B \to \chi_{c2}K^*$ are somewhat of a departure from previous measurements. The measurement of $B^{\pm} \to \chi_{c2}K^{*\pm}$ does not improve over the previous *BABAR* result but it is at least in agreement with Belle's measurement for $B \to \chi_{c2}K^{*\pm}(K^0_S\pi^{\pm})$. In the case of $B^0 \to \chi_{c2}K^{*0}$,

[22] In particular, improvements in the measurement of $\mathcal{B}(\chi_{c1} \to J/\psi\gamma)$ and $\mathcal{B}(J/\psi \to \ell^+\ell^-)$ and correcting for the assumption of an equal ratio of charged and neutral B pair production in $\Upsilon(4S)$ decays.

the branching fraction is surprisingly larger than previous upper limits, and somewhat in disagreement with the former *BABAR* measurement of $(1.4 \pm 1.1 \pm 1.4) \times 10^{-5}$ [16]. The previous result was based upon 124×10^6 $B\overline{B}$ events with a similar efficiency for the $K^{*0} \to K^+\pi^-$ decay mode $(7.1 \pm 0.1\%)$, and measured 2.0 ± 1.6 events. As a cross-check, a fit was performed to the Run 1-3 dataset (the previous *BABAR* sample) using the analysis technique described herein, and found 5.4 ± 5.7 events corresponding to $\mathcal{B}(B^0 \to \chi_{c2}K^{*0}) = (6.9 \pm 7.3) \times 10^{-5}$. This result is consistent with the previously measured branching fraction. The only Belle measurement of this decay mode set a limit of $< 1.27 \times 10^{-4}$ [19], which is also consistent with this result.

Theoretical studies of the branching fractions for the $B \to \chi_{c2}K$ decay modes have contradictory predictions, ranging from zero to $\mathcal{O}(10^{-4})$. Based on the most recent theoretical treatments, one could possibly expect $\mathcal{B}(B \to \chi_{c2}K)$ ranging from $\sim (0.2 - 4.0) \times 10^{-4}$ [12, 20, 21]. Given this uncertainty, the first evidence for the factorization-suppressed $B^0 \to \chi_{c2}K^{*0}$ decay presented here is perhaps consistent. However, there is no plausible explanation for the lack of observation of decays to $B \to \chi_2 K$ in the $K^\pm$, K^0_S, and K^{*0} modes; thus this result may not represent more than a statistical fluctuation.

The value of $\mathcal{B}(B^\pm \to X(3872)K^\pm) \cdot (X(3872) \to J/\psi\gamma) = (2.8 \pm 0.8) \times 10^{-6}$, with a total significance of 3.6σ, confirms and supercedes the previous *BABAR* value of $(3.3 \pm 1.0) \times 10^{-6}$ [37], and represents the ultimate measurement of this quantity in *BABAR*. The only Belle measurement[23] to date finds $(1.8 \pm 0.6 \pm 0.1) \times 10^{-6}$ by assuming $\frac{\mathcal{B}(B^\pm \to XK^\pm)}{\mathcal{B}(B^0 \to XK^0_S)} = 1$ and combining the neutral and charged decay modes [36]. The measurement of $\mathcal{B}(B^\pm \to X(3872)K^\pm) \cdot (X(3872) \to \psi(2S)\gamma) = (9.5 \pm 2.9) \times 10^{-6}$ is the first discovery of evidence (3.3σ) for this decay. The ratio of the branching fractions for the two decay modes is $\frac{\mathcal{B}(X(3872) \to \psi(2S)\gamma)}{\mathcal{B}(X(3872) \to J/\psi\gamma)} = 3.5 \pm 1.4$. Comparing to $\mathcal{B}(B^\pm \to X(3872)K^\pm) \cdot \mathcal{B}(X(3872) \to J/\psi\pi^+\pi^-)$ [34] with the errors again in quadrature, one calculates the ratio $\frac{\mathcal{B}(X(3872) \to \psi(2S)\gamma)}{\mathcal{B}(X(3872) \to J/\psi\pi^+\pi^-)} = 1.1 \pm 0.4$. For the kaon decay modes with smaller branching fractions and lower efficiency,

[23] Unpublished.

the lack of evidence is not unusual given the the size of the data sample. Radiative decays to $J/\psi\,\gamma$ and $\psi(2S)\gamma$ of standard higher-mass states in the charmonium model are likewise unexpected and unobserved.

This discovery of evidence for the radiative decays to $J/\psi\,\gamma$ and $\psi(2S)\gamma$ is an important contribution towards the understanding of the $X(3872)$ mystery. The C-parity of the $X(3872)$ is almost certainly determined to be positive. Regarding the $D^0\overline{D}^{*0}$ molecular interpretations of the $X(3872)$, the presence of a $X(3872) \to \psi(2S)\gamma$ decay is difficult to explain. Few theoretical $D^0\overline{D}^{*0}$ molecular models make explicit predictions for the existence of this decay, and it is expected to be suppressed in those that do. If the $X(3872)$ is a charmonium state, observing $c\overline{c} \to J/\psi\,\gamma$ and $c\overline{c} \to \psi(2S)\gamma$ disfavour the 2^{-+} assignment, since these would represent suppressed higher-order multipole transitions. Based on these radiative decays, 1^{++} is the most likely charmonium assignment. The large branching fraction of $\psi(2S)\gamma$ compared to $J/\psi\,\gamma$ is consistent with charmonium model predictions for the 1^{++} $\chi_{c1}(2P)$ state. However, several outstanding problems exist for this conclusion, namely that the $\chi_{c1}(2P)$ state is expected to be very broad, have a mass $\sim 100\,\mathrm{MeV}/c^2$ above that of the $X(3872)$, and decay far more dominantly (orders of magnitude greater) to other final states. The results of this analysis are generally inconsistent with both a purely $D^0\overline{D}^{*0}$ molecular or purely charmonium model interpretation of the $X(3872)$, and may indicate a state containing an admixture of both components, and that an improved theoretical treatment or perhaps even a new interpretation is required.

Bibliography

[1] J.J. Aubert *et al.*, "Experimental Observation of a Heavy Particle J", Phys. Rev. Lett. **33**, 1404 (1974); J.-E. Augustin *et al.*, "Discovery of a Narrow Resonance in e^+e^- Annihilation", Phys. Rev. Lett. **33**, 1406 (1974).

[2] For example, see E. Eichten *et al.*, "Charmonium: The model", Phys. Rev. **D17**, 3090 (1978).

[3] S.-K. Choi *et al.*, Belle Collarboration, "Observation of a Narrow Charmoniumlike State in Exclusive $B^{\pm} \to K^{\pm}\pi^+\pi^- J/\psi$ Decays", Phys. Rev. Lett. **91**, 262001 (2003).

[4] B. Aubert *et al.*, *BABAR* Collaboration, "Study of the $X(3872)$ and $Y(4260)$ in $B^0 \to J/\psi\,\pi^+\pi^- K^0$ and $B^- \to J/\psi\,\pi^+\pi^- K^-$ decays", Phys. Rev. **D73**, 011101 (2006).

[5] V.M. Abazov *et al.*, DØ Collaboration, "Observation and Properties of the $X(3872)$ Decaying to $J/\psi\,\pi^+\pi^-$ in $p\overline{p}$ Collisions at $\sqrt{s} = 1.96$TeV", Phys. Rev. Lett. **93**, 162002 (2004).

[6] D. Acosta *et al.*, CDF Collaboration, "Observation of the Narrow State $X(3872) \to J/\psi\,\pi^+\pi^-$ in $p\overline{p}$ Collisions at $\sqrt{s} = 1.96$TeV" Phys. Rev. Lett. **93**, 072001 (2004).

[7] M. Kreps, CDF Collarboration, "New Results on $X(3872)$ from CDF", XXXIII International Conference on High Energy Physics, Moscow, Russia, hep-ex/0611004 (2006).

[8] G.S. Abrams *et al.*, "Discovery of a Second Narrow Resonance in e^+e^- Annihilation", Phys. Rev. Lett. **33**, 1453 (1974).

[9] S. Godfrey and N. Isgur, "Mesons in a relativized quark model with chromodynamics", Phys. Rev. **D32**, 189, (1985).

[10] T. Barnes, S. Godfrey, and E.S. Swanson, "Higher charmonia", Phys. Rev. **D72**, 054026 (2005).

[11] G.S. Bali, "QCD forces and heavy quark bound states", Phys. Rept. **343**, 1 (2001).

[12] For example, see G.T. Bodwin, E. Braaten, and G.P. Lepage, "Rigorous QCD analysis of inclusive annihilation and production of heavy quarkonium", Phys. Rev. **D51**, 1125 (1995) [Erratum: *ibid.* **D55**, 5853 (1997)].

[13] A detailed derivation can be found in J.H. Kühn, S. Nussinov, and R. Rückl, "Charmonium production in B-decays", Z. Physik **C5**, 117 (1980).

[14] M. Diehl and G. Hiller, "New ways to explore factorization in B decays", JHEP **06**, 067 (2001).

[15] B. Aubert *et al.*, *BABAR* Collaboration, "Measurement of the branching fraction for $B^{\pm} \to \chi_{c0} K^{\pm}$", Phys. Rev. **D69**, 071103 (2004).

[16] B. Aubert *et al.*, *BABAR* Collaboration, "Search for Factorization-Suppressed $B \to \chi_c K^{(*)}$ Decays", Phys. Rev. Lett. **94**, 171801 (2005).

[17] B. Aubert *et al.*, *BABAR* Collaboration, "Observation of $B^0 \to \chi_{c0} K^{*0}$ and evidence for $B^+ \to \chi_{c0} K^{*+}$", Phys. Rev. **D78**, 091101(R) (2008).

[18] K. Abe *et al.*, Belle Collaboration, "Observation of $B^{\pm} \to \chi_{c0} K^{+}$", Phys. Rev. Lett. **88**, 031802 (2002).

[19] N. Soni *et al.*, Belle Collaboration, "Measurement of Branching Fractions for $B \to \chi_{c1(2)} K(K^*)$ at Belle", Phys. Lett. **B634**, 155 (2006).

[20] For example, see P. Colangelo, F. De Fazio, and T.N. Pham, "$B^- \to K^- \chi_{c0}$ decay from charmed meson rescattering", Phys. Lett. **B542**, 71 (2002), and the references therein.

[21] For example, see M. Beneke and L. Vernazza, "$B \to \chi_{cJ}$ decays revisited", arXiv:0810.3575 (2008), and the references therein.

[22] S. Okuba, "ϕ-meson and unitary symmetry model", Phys. Lett. **5**, 165 (1963); G. Zweig, "An SU_3 model for strong interaction symmetry and its breaking", CERN Report TH-401 and TH-412, (1964); J. Iizuka, "A Systematics and Phenomenology of Meson Family", Prog. Theor. Phys. Suppl. **37 & 38**, 21 (1966).

[23] W. Kwong and J.L. Rosner, "D-wave quarkonium levels of the Υ family", Phys. Rev. **D38**, 279 (1988).

[24] For example, see L. Micu, "Decay rates of meson resonances in a quark model", Nucl. Phys. **B10**, 521 (1969); A. Le Yaouanc, *et al.*, "Naive Quark-Pair-Creation Model of Strong-Interaction Vertices", Phys. Rev. **D8**, 2223 (1973).

[25] A thorough review of the latest theoretical and experimental results regarding the new exotic mesons is available in S. Godfrey and S.L. Olsen, "The Exotic XYZ Charmonium-like Mesons", Ann. Rev. Nucl. Part. Sci. **58**, 51 (2008).

[26] N.A. Tornqvist, "From the deuteron to deusons, an analysis of deuteronlike meson-meson bound states", Z. Phys. **C61**, 525 (1994).

[27] A survey of the new mesons with an exceptional focus on the molecular interpretation for the $X(3872)$ is presented in E.S. Swanson, "The New Heavy Mesons: A Status Report", Phys. Rept. **429**, 243 (2006).

[28] L. Maiani *et al.*, "Diquark-antidiquark states with hidden or open charm and the nature of $X(3872)$", Phys. Rev. **D71**, 014028 (2005).

[29] T. Barnes, F.E. Close, and E.S. Swanson, "Hybrid and conventional mesons in the flux tube model: Numerical studies and their phenomenological implications", Phys. Rev. **D52**, 5242 (1995).

[30] N. Isgur and J.E. Paton, "Flux-tube model for hadrons in QCD", Phys. Rev. **D31**, 2910 (1985).

[31] S.-K. Choi *et al.*, Belle Collaboration, "Observation of the $\eta_c(2S)$ in Exclusive $B \to KK_S K^- \pi +$ Decays", Phys. Rev. Lett. **89**, 102001 (2002); B. Aubert, *et al.*, *BABAR* Collaboration, "Measurements of the Mass and Width of the η_c Meson and of an $\eta_c(2S)$ Candidate", Phys. Rev. Lett. **92**, 142002 (2004).

[32] J.L. Rosner *et al.*, CLEO Collaboration, "Observation of the $h_c(^1P_1)$ State of Charmonium", Phys. Rev. Lett. **95** 102003 (2005); P. Rubin, *et al.*, CLEO Collaboration, "Observation of the $^1P_1$ State of Charmonium", Phys. Rev. **D72**, 092004 (2005).

[33] C. Amsler *et al.*, Particle Data Group, "Review of Particle Physics", Phys. Lett. **B667**, 1 (2008).

[34] B. Aubert *et al.*, *BABAR* Collaboration, "Study of $B \to X(3872)K$, with $X(3872) \to J/\psi \pi^+ \pi^-$", Phys. Rev. **D77**, 111101 (2008).

[35] I. Adachi *et al.*, Belle Collaboration, "Study of $X(3872)$ in B meson decays", 34th International Conference on High Energy Physics, Philadelphia, PA, USA, arXiv:0809.1224 (2008).

[36] K. Abe *et al.*, Belle Collaboration, "Evidence for $X(3872) \to \gamma J/\psi$ and the sub-threshold decay $X(3872) \to \omega J/\psi$", International Symposium on Lepton-Photon Interactions at High Energy, Uppsala, Sweden, hep-ex/0505037 (2005).

[37] B. Aubert *et al.*, *BABAR* Collaboration, "Search for $B^+ \to X(3872)K^+$, $X(3872) \to J/\psi \gamma$", Phys. Rev. **D74**, 071101 (2006).

[38] D. Abulencia *et al.*, CDF Collaboration, "Measurement of the Dipion Mass Spectrum in $X(3872) \to J/\psi \pi^+ \pi^-$ Decays", Phys. Rev. Lett. **96**, 102002 (2006).

[39] K. Abe *et al.*, Belle Collaboration, "Experimental constraints on the possible J^{PC} quantum numbers of the $X(3872)$", International Symposium on Lepton-Photon Interactions at High Energy, Uppsala, Sweden, hep-ex/0505038 (2005).

[40] B. Aubert *et al.*, *BABAR* Collaboration, "Observation of $Y(3940) \to J/\psi\,\omega$ in $B \to J/\psi\,\omega K$ at *BABAR*", Phys. Rev. Lett. **101**, 082001 (2008).

[41] G. Gokhroo *et al.*, Belle Collaboration, "Observation of a Near-Threshold $D^0\overline{D}^0\pi^0$ Enhancement in $B \to D^0\overline{D}^0\pi^0 K$ Decay", Phys. Rev. Lett. **97**, 162002 (2006).

[42] B. Aubert *et al.*, *BABAR* Collaboration, "Study of resonances in exclusive B decays to $\overline{D}^{(*)}D^{(*)}K$", Phys. Rev. **D77**, 011102 (2008).

[43] N. Zwahlen *et al.*, Belle Collaboration, "Study of the $B \to X(3872)(D^{*0}\overline{D}^0)K$ decay", 34th International Conference on High Energy Physics, Philadelphia, PA, USA, arXiv:0810.0358 (2008).

[44] W. Dunwoodie and V. Ziegler, "A Simple Explanation for the $X(3872)$ Mass Shift Observed for Decay to $D^{*0}\overline{D^{*0}}$", Phys. Rev. Lett. **100**, 062006 (2008).

[45] C. Hanhart *et al.*, "Reconciling the $X(3872)$ with the near-threshold enhancement in the $D^0\overline{D}^{*0}$ final state", Phys. Rev. **D76** 014007.

[46] B. Aubert *et al.*, *BABAR* Collaboration, "Observation of the Decay $B \to J/\psi\,\eta K$ and Search for $X(3872) \to J/\psi\,\eta$", Phys. Rev. Lett. **93**, 041801 (2004).

[47] R. Chistov *et al.*, Belle Collaboration, "Observation of $B^+ \to \psi(3770)K^+$", Phys. Rev. Lett. **93**, 051803 (2004).

[48] B. Aubert *et al.*, *BABAR* Collaboration, "Search for a charged partnet of the $X(3872)$ in the B meson decay $B \to X^-K$, $X^- \to J/\psi\,\pi^-\pi^0$", Phys. Rev. **D71**, 031501 (2005).

[49] K. Abe *et al.*, Belle Collaboration, "Observation of a Charmoniumlike State Produced in Association with a J/ψ in e^+e^- Annihilation at $\sqrt{s} \approx 10.6\,\mathrm{GeV}$", Phys. Rev. Lett. **98**, 082001 (2007).

[50] K. Abe *et al.*, Belle Collaboration, "Search for new charmonium states in the processes $e^+e^- \to J/\psi\,D^{(*)}D^{(*)}$ at $\sqrt{s} \sim 10.6\,\mathrm{GeV}$", European

Physical Society Conference on High Energy Physics, Manchester, UK, arXiv:0708.3812 (2007).

[51] S.-K. Choi *et al.*, Belle Collaboration, "Observation of a Near-Threshold $\omega J/\psi$ Mass Enhancement in Exclusive $B \to K\omega J/\psi$ Decays", Phys. Rev. Lett. **94**, 182002 (2005).

[52] S. Uehara *et al.*, Belle Collaboration, "Observation of a χ'_{c2} Candidate in $\gamma\gamma \to D\overline{D}$ Production at Belle", Phys. Rev. Lett. **96**, 082003 (2006).

[53] B. Aubert *et al.*, *BABAR* Collaboration, "Observation of a Broad Structure in the $\pi^+\pi^- J/\psi$ Mass Spectrum around $4.26\,\mathrm{GeV}/c^2$", Phys. Rev. Lett. **95**, 142001 (2005).

[54] T.E. Coan *et al.*, CLEO Collaboration, "Charmonium Decays of $Y(4260)$, $psi(4160)$, and $\psi(4040)$", Phys. Rev. Lett. **96**, 162003 (2006); Q. He *et al.*, CLEO Collaboration, "Confirmation of the $Y(4260)$ resonance production in initial state radiation", Phys. Rev. **D74**, 091104 (2006).

[55] C.Z. Yuan *et al.*, Belle Collaboration, "Measurement of the $e^+e^- \to \pi^+\pi^- J/\psi$ Cross Section Via Initial-State Radiation at Belle", Phys. Rev. Lett. **99**, 182004 (2007).

[56] B. Aubert *et al.*, *BABAR* Collaboration, "Evidence of a Broad Structure at an Invariant Mass of $4.32\,\mathrm{GeV}/c^2$ in the Reaction $e^+e^- \to \pi^+\pi^-\psi(2S)$", Phys. Rev. Lett. **98**, 212001 (2007).

[57] X.L. Wang *et al.*, Belle Collaboration, "Observation of Two Resonant Structures in $e^+e^- \to \pi^+\pi^-\psi(2S)$ via Initial-State Radiation at Belle", Phys. Rev. Lett. **99**, 142002 (2007).

[58] S.-K. Choi *et al.*, Belle Collaboration, "Observation of a resonance-like structure in the $\pi^\pm\psi'$ mass distribution in exclusive $B \to K\pi^\pm\psi'$ decays", Phys. Rev. Lett. **100** 142001 (2008).

[59] B. Aubert *et al.*, *BABAR* Collaboration, "Search for the $Z(4430)^-$ at *BABAR*", Phys. Rev. Lett. **100** 112001 (2008).

[60] R. Mizuk *et al.*, Belle Collaboration, "Observation of two resonancelike structures in the $\pi^+\chi_{c1}$ mass distribution in exclusive $\overline{B}^0 \to K^-\pi^+\chi_{c1}$ decays", Phys. Rev. **D78**, 072004 (2008).

[61] T. Barnes and S. Godfrey, "Charmonium options for the $X(3872)$", Phys. Rev. **D69**, 054008 (2004).

[62] E.S. Swanson, "Diagnostic decays of the $X(3872)$", Phys. Lett. **B598**, 197 (2004).

[63] *BABAR* Collaboration, "*BABAR* Technical Design Report", SLAC-R-457 (1995).

[64] B. Aubert *et al.*, *BABAR* Collaboration, "The *BABAR* Detector", Nucl. Instrum. Meth. **A479**, 1 (2002).

[65] G. Benelli *et al.*, "The *BABAR* LST detector high voltage system: design and implementation", Nuclear Science Symposium Conference Record, 2005 IEEE, **2**, 1145 (2005); W. Menges, "The *BABAR* muon system upgrade", Nuclear Science Symposium Conference Record, 2005 IEEE, **3**, 1470 (2005).

[66] M.R. Convery *et al.*, "A novel technique for the production of large area Z-coordinate readout planes for the *BABAR* muon system", Nucl. Instrum. Meth. **A556**, 134 (2006).

[67] A.V. Telnov, private communication.

[68] D.J. Lange, "The EvtGen particle decay simulation package", Nucl. Instrum. Meth. **A462**, 152 (2001).

[69] S. Agostinelli *et al.*, GEANT4 Collaboration, "GEANT4 – a simulation toolkit", Nucl. Instrum. Meth. **A506** 250 (2003).

[70] R. Brun and F. Rademakers, "ROOT – An object oriented data analysis framework", Nucl. Instrum. Meth. **A389** 81 (1997).

[71] W.-M. Yao *et al.*, Particle Data Group, "Review of Particle Physics", J. Phys. G. **33**, 1 (2006).

[72] B. Aubert *et al.*, *BABAR* Collarboration, "Study of inclusive production of charmonium mesons in B decays", Phys. Rev. **D67**, 032002 (2003).

[73] T. Brandt, "Likelihood Based Electron Identification", *BABAR* Analysis Document 391, (2002).

[74] A. Mohapatra, J. Hollar, and H. Band, "Studies of A Neural Net Based Muon Selector for the *BABAR* Experiment", *BABAR* Analysis Document 474, (2004).

[75] G.C. Fox and S. Wolfram, "Event shapes in e^+e^- annihilation", Nucl. Phys. **B149**, 413 (1979).

[76] S. Brandt *et al.*, "The principal axis of jets – an attempt to analyse high-energy collision as two-body processes", Phys. Lett. **12**, 57 (1964).

[77] J. Bjorken and S. Brodsky, "Statistical Model for Electron-Position Annihilation into Hardons", Phys. Rev. **D1**, 1416 (1970).

[78] A. Drescher *et al.*, "The ARGUS electron-photon calorimeter III. Electron-hadron separation", Nucl. Instrum. Meth. **A237**, 464 (1985).

[79] R. Sinkus and T. Voss, "Particle identification with neural networks using a rotational invariant moment representation", Nucl. Instr. Meth. **A391**, 360 (1997).

[80] M. Pivk and F.R. Le Diberder, "$_s$Plot: A statistical tool to unfold data distributions", Nucl. Instrum. Meth. **A555**, 356 (2005).

[81] J.E. Gaiser, "Charmonium Spectroscopy from Radiative Decays of the J/Psi and Psi-Prime", SLAC-R-255, Appendix F (1982).

[82] H. Albrecht *et al.*, ARGUS Collaboration, "Reconstruction of B mesons", Phys. Lett. **B185**, 218 (1987).

[83] J. Hollar and J. Berryhill, "PID systematics studies in $B \to K^{(*)}\ell^+\ell^-$", http://www.slac.stanford.edu/BFROOT/www/Organization /Workshops/2005/bbr_analtools/Sat02/hollar.pdf (2005).

[84] Tracking Efficiency Task Force, "Tracking Efficiency for Run 1 – Run 5 in R22", http://www.slac.stanford.edu/BFROOT/www/Physics TrackEfficTaskForce/TrackingTaskForce-2007-R22.html (2007).

[85] V. Tisserand, "Energy shift/smearing corrections for SP MC vs. data CM2", http://www.slac.stanford.edu/BFROOT/www/Physics /Analysis/AWG/Neutrals/meet04/15Jun/Vincent.pdf (2004).

[86] M. Allen *et al.*, "A Measurement of π^0 Efficiency Using $\tau \to \rho\nu$ and $\tau \to \pi\nu$ Decays", *BABAR* Analysis Document 870 (2004).

[87] B. Aubert *et al.*, *BABAR* Collaboration, "Measurement of Branching Fractions and Charge Asymmetries for Exclusive B Decays to Charmonium", Phys. Rev. Lett. **94**, 141801 (2005).

[88] S. Eidelman *et al.*, Particle Data Group, "Review of Particle Physics", Phys. Lett. **B592**, 1 (2004).